IRDCs to Star Clusters: In Depth Study of the Structure, Evolution and Kinematics of Few Southern Massive Star Forming Regions

A thesis submitted
in partial fulfillment for the degree of

Doctor of Philosophy

by

VEENA V. S

Department of EARTH & SPACE SCIENCES

INDIAN INSTITUTE OF SPACE SCIENCE AND TECHNOLOGY
Thiruvananthapuram - 695547

JUNE 2018

CERTIFICATE

This is to certify that the thesis entitled **"IRDCs to Star Clusters: In Depth Study of the Structure, Evolution and Kinematics of Few Southern Massive Star Forming Regions"** submitted by **Veena V. S**, to the Indian Institute of Space Science and Technology, Thiruvananthapuram, in partial fulfilment for the award of the degree of **Doctor of Philosophy**, is a bonafide record of the project research work carried out by her under my supervision. The contents of this report, in full or in parts, have not been submitted to any other Institute or University for the award of any degree or diploma.

Dr. Sarita Vig
Associate Professor
Department of Earth & Space Sciences

Counter signature of HOD with seal

Place: Thiruvananthapuram
June 2018

DECLARATION

I declare that this thesis titled **"IRDCs to Star Clusters: In Depth Study of the Structure, Evolution and Kinematics of Few Southern Massive Star Forming Regions"** submitted in partial fulfilment of the Degree of **"Doctor of Philosophy"** is a record of original work carried out by me under the supervision of **Dr. Sarita Vig**, and has not formed the basis for the award of any degree, diploma, associateship, fellowship, or other titles in this or any other Institution or University of higher learning. In keeping with the ethical practice in reporting scientific information, due acknowledgements have been made wherever the findings of others have been cited.

Veena V. S

Place: Thiruvananthapuram
June 2018

Research Scholar
Department of Earth & Space Sciences
Roll No. : SC13D007

Acknowledgment

There are many people to whom I owe a huge debt of gratitude for my academic, intellectual and emotional development during the past few years.

My research advisor Dr. Sarita Vig deserves respect and admiration for many things. It has been an honour to be her first Ph.D. student. I often marvelled at her ever growing enthusiasm and passion for research, which was highly contagious and inspirational for me. She has opened the windows for me to the amazing world of astronomy and the wonders of star formation. She is responsible for making this thesis and all those exciting projects, a reality. Thank you for your dedication, time, patience, and constant support, even during tough times in the Ph.D. pursuit.

I would also like to thank Dr. Anandmayee Tej for her immense help and support during my research. Being my doctoral committee member and collaborator, her encouragement was invaluable. I would like to express my gratitude to my collaborators: Prof. T. Chandrasekhar (PRL, Ahmedabad), Dr. C. H. Ishwara-Chandra, Dr. N. G. Kantharia, Dr. D. V. Lal (NCRA, Pune), Dr. B. Mookerjea (TIFR, Mumbai), Dr. A. Sánchez-Monge (University of Cologne, Germany), Biny Sebastian (NCRA, Pune) and Dr. W. P. Varricatt (UKIRT, USA) for their help with data reduction and analysis.

I thank the members of my doctoral committee: Prof. S. K. Ghosh (NCRA, Pune), Prof. N. M. Ashok (PRL, Ahmedabad) and Dr. Nirmala R. James (IIST) for a critical evaluation of my work, which significantly improved the quality of my research. I wish to thank the faculty members of the Astronomy and Astrophysics group of IIST, Dr. Anand Narayanan, Dr. Jagadheep D., Dr. Resmi Lekshmi, and Dr. Samir Mandal, for their motivation and fruitful discussions. I am thankful to Dr. K. S. Dasgupta, former Director and Dr. V. K. Dadhwal, present Director of IIST, for the academic support and the facilities provided to carry out the research work at IIST. I am also thankful to Dr. Raju K. George, Dean, Research and Development and Dr. Kuruvilla Joseph, Dean, Student Activities for their encouragement and support. I also thank the Research Council of IIST for their support at various phases of the PhD. program.

I thank the staff members of GMRT who helped me with the radio observations that have been extensively used in my research work. I also thank S. Bardeau and P. J Barnes

for helping me with the analysis of molecular line data. I thank Joe, Honey, Jessy chechi and Nayana for great conversations that helped me gain a broader view of my research. I would like to thank Mr. Sai Krishnan, lab tutor, for his constant help. Thanks to all department staff members for their support. I thank administrative, library, and canteen staff members of IIST, for their help and support.

My time at IIST was made memorable due to many friends who became a part of my life. I thank all the Ph.D, Master, and project students in our department, for making our research environment enjoyable and collaborative. Thanks to Govind, Dinil, Ashish, Varsha, Suma, Joel, Jim, Amrita, Bikram, Hirishabh, Karthika, Kshitija, Sonu, Ruskin, Somnath, Kausthubh, Shlesha, Geethu, Sreelakshmi, Rashi, Gopika, Prem, Sreelekshmi and Aditya. I am grateful for the time spent with my food and travel buddies, the comrades of our lab, Swagat, Sachin, Aneesha, and Namitha. I will treasure those wonderful moments with Reshma and Aswathy, with whom, I share so many fun memories. I thank my guardian angel Jayalekshmi, for always finding a way to make me smile.

The influence of those with whom I worked before coming to IIST is pivotal. Special thanks to Prof. G. Markandeyulu (IIT Madras) who was my thesis supervisor during Master's program and to Dr. Sreedhar B. Dutta (IISER-TVM). These people helped me revive my confidence when I struggled to survive in IITM.

I express my deep gratitude and respect to my spiritual mentor, Mammen sir. It would be impossible to list all the ways that he has helped me in my life. I thank Nitheesh, whom I can always count on, for being my true spiritual friend.

I would not be who or where I am today without the unconditional love and support I have received from my family. My parents always encouraged me to pursue my dreams and never questioned my passion for astronomy. There are no words that can express my gratitude for everything they have done for me. I also thank my little brother Vinayak for being with me through thick and thin. Finally, I thank all my friends and cousins who believed in me when I didn't believe myself.

Veena V. S

Thiruvananthapuram, India

Abstract

The formation and the evolution of massive stars ($M \geq 8\ M_{\odot}$) are found to dominate the fate of their parental clouds and the host galaxies. This is primarily due to the enhanced feedback mechanisms from these stars that alter the environments on local, global and cosmic scales. The radiative feedback from massive stars causes the ionisation of neutral gas whereas the mechanical feedback effects such as supernovae explosions impart mechanical energy into the ambient interstellar medium (ISM), and can even vent energy into the galactic halo. The nucleosynthesis processes in massive stars and their core collapse supernovae play a crucial role in the chemical enrichment of the ISM that drive the chemical evolution in galaxies. While theoretical formulations have been proposed to explain their formation, observational studies of the early phases remain limited. Most of these observational works are designed to examine the large scale properties of a sample of massive star forming regions. While there are studies that focuses on individual regions, majority of them probe the northern Galactic sky.

In this context, we have carried out a multiwavelength study towards a selected number of massive star forming regions in the southern Galactic sky that are in different evolutionary stages. Our intention is to examine the properties and initial conditions related to the formation of massive stars across different evolutionary phases. We investigate the structure and kinematics of these star forming regions that gives a better insight into the complex interaction mechanisms between massive stars and their parental clouds. In this study, we have considered three star forming regions: a filamentary IRDC (G333.73+0.37) and two H II regions (IRAS 17256–361 and IRAS 17258–3637). In addition to these, we have also probed the star forming complex associated with IRAS 17256–3631 and IRAS 17258–3637, to investigate the large scale environment of massive stars.

We have conducted our observational study at infrared, submillimeter and radio wavelengths. Radio observations serve as a powerful tool to discern regions associated with newly formed massive stars as well as to identify the nature of the ionising sources. Far-infared and millimeter continuum data traces the emission from the cold and dense regions of molecular clouds that often appear as dark extinction features in the optical

images. Near and mid-infrared data on the other hand, are useful in examining the warm dust emission and young stellar objects (YSOs) in these regions. Spectral line data such as radio recombination lines and molecular lines are excellent for probing the complex kinematics of the ionised gas and molecular cloud.

The star formation activity in G333.73+0.37 and IRAS 17256–3631 has been scrutinized using a diverse range of tracers such as the presence of H II regions, infrared YSOs, maser spots etc. We find these regions to be in a star formation flurry. The molecular clouds associated with the regions are massive (M $\sim 10^4$ $M_\odot$). The typical dust temperatures and column densities are $15 - 35$ K and $\sim 10^{22}$ cm^{-2}, respectively. Molecular line studies reveal signatures of infall and/or outflow activity in both the clouds, consistent with results obtained from continuum analysis. We also detect an embedded infrared cluster in IRAS 17256–3631.

We have also used low frequency radio recombination lines (H172α and C172α) and molecular line data in an attempt to sample the velocity structure of the H II regions IRAS 17256–3631 and IRAS 17258–3637. We have successfully mapped the H172α RRL emission across these H II regions and we find velocity gradients in the ionised gas. Our findings suggest that the observed morphologies are governed by strong density gradients prevailing in the molecular clouds. We also observe signatures of pressure and dynamical broadening in the line widths of H172α RRLs. This is the first ever RRL mapping study of H II regions at low frequency bands.

Using low radio frequency wide band observations, we have detected large scale diffuse emission towards the star forming complex associated with the H II region IRAS 17256–3631 and IRAS 17258–3637. The emission has a shell-like morphology. Using radio spectral index analysis and complementary archival data, we identify this feature to be a previously unknown supernova remnant candidate SNR G351.7–1.2. The findings emphasize on the importance of low frequency observations in segregating the emission from SNRs that are associated with H II regions and molecular clouds.

TABLE OF CONTENTS

LIST OF TABLES

LIST OF FIGURES

Chapter 1

Introduction

Massive stars (M$\geq$8 $M_{\odot}$) play a significant role in the evolution of galaxies. They inject energy into the interstellar medium (ISM) through various mechanisms such as radiation pressure, stellar winds and outflows, and are responsible for the generation and dissemination of heavy elements. In the early stages of evolution, the radiation from a massive young stellar object (YSO) can heat the ambient gas and dust and photo-dissociate molecules, while the stellar wind sweeps out the circumstellar material and further erodes the natal molecular cloud. During the main-sequence phase, the intense radiation from the massive star photo-ionises and heats the ISM to 10^4 K and its stellar wind dynamically interacts with the ISM, blowing bubbles and generating turbulence. During the violent death of massive star as a supernova, it releases $\sim$ 10^{51} ergs of kinetic energy into the ISM, forming a supernova remnant (SNR) in a dense medium (Chu & Gruendl, 2011). The energy input from massive stars can sculpt the ISM of host galaxies, creating enormous structures that can even vent mass and energy in to the galactic halo (e.g., Scutum supershell, Henize 70).

The energy feedback from massive stars profusely alters ISM structure, creating multiphase components with varying physical conditions. As stars are formed within the dense regions of ISM, any change in the physical conditions of ISM heavily influence the formation of future generation of stars. Fig. 1.1 shows example of a massive star forming region in our Galaxy.

1.1 Overview of star formation

1.1.1 Large scale: Giant molecular clouds

Giant Molecular Clouds (GMCs) are of prime importance as the initial phase of star formation occurs in cold and dense molecular gas within them. Despite a small volume fraction, nearly a half of the Milk Way's ISM mass within the solar circle is found

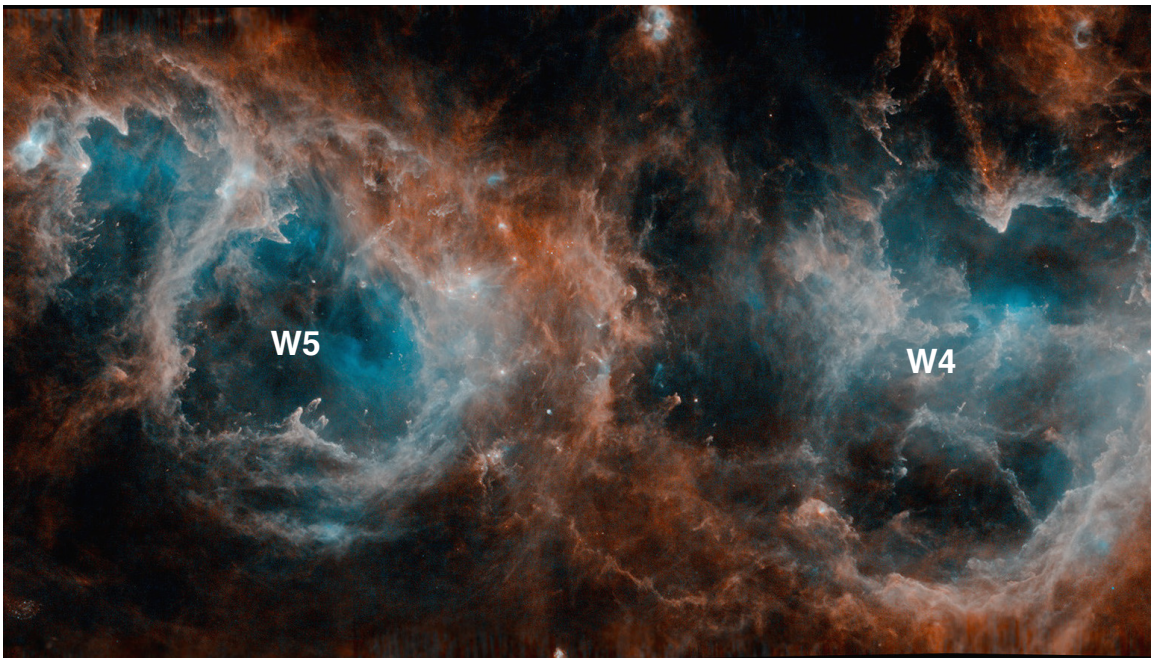

Figure 1.1: Massive star forming complex associated with the regions W4 and W5. Image credit and copyright: ESA/Herschel/NASA/JPL-Caltech; acknowledgement: R. Hurt (JPL-Caltech), CC BY-SA 3.0 IGO

in molecular gas (Williams & McKee, 1997). The typical mass of GMCs ranges between $10^4 - 10^6$ $M_\odot$ whereas the size ranges from few tens of parsecs to few hundred parsecs (Murray, 2011). The average surface mass density of GMCs is found to be $\Sigma \sim 100\ M_\odot\ pc^{-2}$ (Murray, 2011; Tan et al., 2013).

GMCs are believed to form in the disk of the Milky Way when the molecular gas enters the spiral wave pattern of the gravitational potential energy of the Galactic disk (Elmegreen, 1994). Tidal forces among GMCs are relatively weaker in the spiral arms than in the inter-arm regions making gravitational collapse more feasible in the spiral arms (Elmegreen, 1994). GMCs contain clumps that may form star clusters and cores (Tan et al., 2013). Massive star formation occurs in regions with high molecular gas density, roughly coincident with the line-of-sight tangent to spiral arms (Luna et al., 2006). Studies suggest that at smaller scales, GMCs harbour most of the high mass star formation in the Galaxy (e.g., Mac Low & Klessen, 2004; McKee & Ostriker,

2007; Zinnecker & Yorke, 2007). The high column density regions of GMCs known as Infrared dark clouds (IRDCs) block most of the infrared and shorter wavelength background radiation and cover broad ranges gas masses from low mass to high mass star forming regions. On the upper mass end, they harbour massive star forming cores in their earliest evolutionary phases (Chira et al., 2013).

1.1.2 Smaller scale: Fragmentation into clumps and cores

GMCs are observed to be clumpy and the star formation within a GMC is initiated in parsec-scale molecular clumps that collapse and fragment, leading to the formation of a cluster of stellar objects. Cores are regions out of which single stars and binaries form and are gravitationally bound (Williams et al., 2000). These cores are much smaller in size compared to the molecular clumps. In the simplistic case where there is only thermal support of an isothermal sphere, the mass at which the system will undergo a gravitational collapse is given by Jeans mass M_J defined as Shu et al. (1987)

$$M_J = \left(\frac{5\,k_b\,T}{\mu\,m_{\rm H}{\rm G}}\right)^{3/2}\left(\frac{3}{4\pi\rho}\right)^{1/2} \tag{1.1}$$

where ρ and T are the density and temperature of the cloud, $m_{\rm H}$ is the mass of the hydrogen atom, μ is the mean molecular weight and G is the gravitational constant. Once gravity dominates the internal support, spherical collapse occurs on a timescale given by the free-fall timescale

$$\tau_{ff} = \left[\frac{3\,\pi}{32\,G\,\rho}\right]^{1/2} = 3.4\,\left[\frac{100}{n_{\rm H2}}\right]^{1/2}\,{\rm Myr} \tag{1.2}$$

where $n_{\rm H2}$ is the number density of H_2 molecules (Dobbs et al., 2014). For molecular clouds, the typical density is $\sim$100 cm^{-3}, giving rise to a free-fall timescale of few Myr. As a result of the angular momentum conservation during the collapse of the rotating core, a flattened disc structure is formed around the protostar. The mass of the central core increases as material is transported through the accretion disc into the collapsing central protostar. For low mass stars, this accretion phase lasts until the star enters the hydrogen burning phase. The young stars are often associated with prominent bipolar outflows. This ejection of material along the axis of rotation is believed to remove an-

gular momentum from the protostellar system. Once the star begins the thermonuclear fusion in its core, strong stellar wind is produced, preventing further accretion of matter.

1.2 Pre-main sequence evolution of low mass stars: Classification based on observations

The pre-main sequence evolutionary stages observed in the case of sun-like stars have been divided into four major classes: Class 0, I, II and III, based on the continuum spectral energy distribution (SED). This classification makes use of α, the slope of the log-log plot of SED in the infrared wavelengths (Adams et al., 1987), and is defined as

$$\alpha = \frac{d\log(\lambda\, S_\lambda)}{d\log(\lambda)} \tag{1.3}$$

where S_λ is the flux density measured at wavelength λ. Class 0 objects are sources that are extremely faint in the optical and near-infrared wavelengths and possess a significant submillimeter luminosity. They are very young protostars (age $\leq 10^4$ yrs) with high accretion rates. Class I objects ($\alpha > 0$) correspond to a relatively evolved class of embedded sources with circumstellar disks and envelopes (age $\sim$10^5 yrs). The SEDs of Class I sources peak at mid- and far-infrared wavelengths. They are optically invisible. Class II objects also known as classical T Tauri stars ($-2 < \alpha < 0$) have significant circumstellar disks, strong emission lines and are optically bright (age $\sim$10^6 yrs). The accretion disks of Class II objects are still optically thick. This results in a large infrared excess. Class III sources ($\alpha < -2$) are close to the main sequence phase and have weak or no emission lines and negligible excess as they are no longer accreting significant amount of matter (age $\sim$10^7 yrs). A schematic showing the four stages of low mass protostellar evolution and the corresponding SEDs are presented in Fig. 1.2.

1.3 Our understanding of the formation of massive stars

A proper understanding of the formation mechanism of massive stars has been a challenge (Beuther et al., 2007; Tan et al., 2014). The key differences involved in the forma-

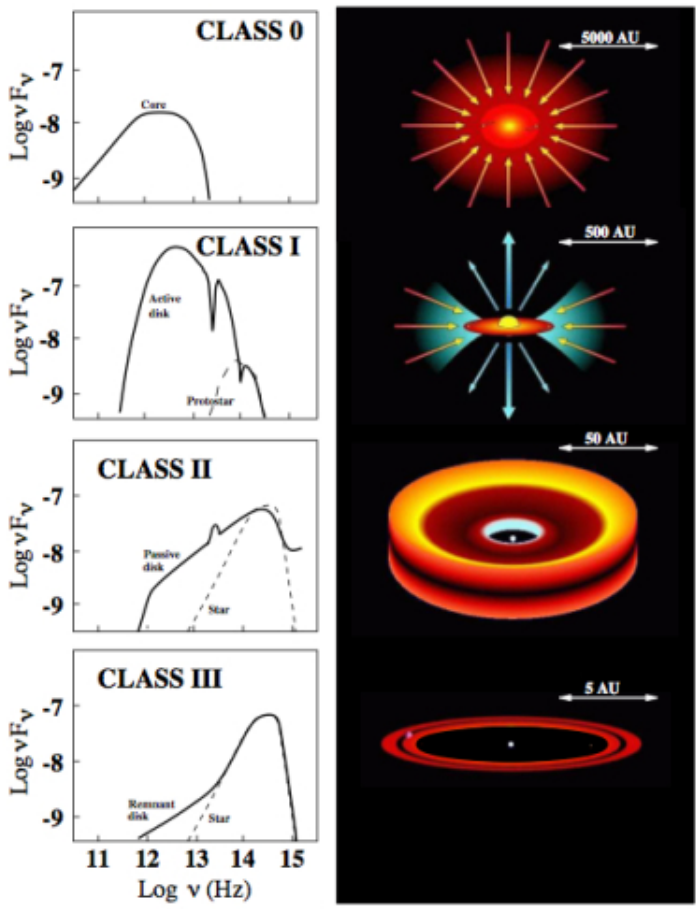

Figure 1.2: A graphical overview of the four stages of low mass protostellar evolution. A typical SED of each class is shown in the left column and a corresponding cartoon of the geometry is shown in the right column. Picture credit: Ph.D thesis of Andrea Isella (2006).

tion of high and low mass stars are: (1) timescales involved in their formation and (2) extreme radiation pressure halting/preventing accretion in the case of massive stars. The timescale required for a protostar to reach the main-sequence phase varies substantially with the mass of the protostar. The characteristic time for this collapse is known as the Kelvin-Helmholtz time. For high mass stars, the Kelvin-Helmholtz timescale is much lower than the free-fall timescale. For a 30 $M_\odot$ star, the Kelvin-Helmholtz timescale is 3×10^4 yrs, which corresponds to 1% of its main-sequence life time (Maeder, 2009). Hence, the massive stars enter the zero-age main-sequence (ZAMS) phase while still undergoing accretion. The extreme radiation pressure of these stars inhibit the accretion beyond $\sim$8 $M_\odot$ (Wolfire & Cassinelli, 1987; Palla & Stahler, 1993). Regardless of the theoretical limitations, stars with masses of 100 $M_\odot$ or greater have been observed (e.g., Heap et al., 1991; Crowther et al., 2010).

1.3.1 Theoretical models

Several models have been proposed to explain the formation mechanisms of massive stars. These models have been largely categorised in to two major groups: core accretion and competitive accretion models.

The most fundamental characteristic of core accretion model is that it assumes both high and low mass stars form by a top-down fragmentation process in which a molecular cloud breaks down in to smaller fragments under the combined influence of turbulence and magnetic field. A massive star forms from a massive core, which does not undergo further fragmentation (McKee & Tan, 2002, 2003). Core accretion models involve varying initial conditions and dust properties to form a massive star. For example, the enhanced accretion rates of the order of $\sim 10^{-3}$ $M_{\odot} yr^{-1}$ compared to $\sim 10^{-6}$ $M_{\odot} yr^{-1}$ for low mass stars (Hosokawa & Omukai, 2009; Hosokawa et al., 2010) and alternative methods for escape of radiation such as wind blown cavities (Krumholz et al., 2005b) or radiatively driven Rayleigh-Taylor instabilities (Krumholz et al., 2005a). The major challenges involved in the core accretion model is that it fails to explain how a massive star can form via direct collapse of the core which is several hundreds of Jean mass. Why the fragmentation does not continue to 1 Jean mass and form a cluster of low mass stars instead of a single high mass star?

According to the competitive accretion model (Bonnell et al., 2001; Smith et al., 2011), massive stars are formed within clusters and the protostars that are destined to become massive settle in the protocluster centres, where high ambient gas densities are maintained by a global clump infall. A gravitational potential well exists in the centre of the protocluster and the gas is funnelled down to the cluster centre, increasing the amount of gas a protostar in the centre can accrete (Bonnell & Bate, 2006). The accretion rate is determined by the location of the protostar in the cluster potential. As the stars have to compete for resources and the most massive star wins the competition because of its mass and location, the model is known as "competitive accretion". According to Krumholz et al. (2005c), the competitive accretion requires a virial parameter $\alpha = E_{turb}/E_{grav} \ll 1$, while molecular observations of massive star forming regions suggest α to be close to unity. Moreover, the radiative feedback from the accreting massive star would disrupt the accretion in altogether.

In an alternative scenario now considered obsolete, Bonnell et al. (1998) and Bonnell (2002) proposed that massive stars can form through the collision and merging of protostars with lower masses in dense systems. However, the model requires very high densities ($\sim 10^8$ pc^{-3}) that are not typically observed in star forming clusters. Using the numerical suggestions, Takahira et al. (2014) have shown that more massive cores are produced in the cloud collisions than those formed through gravitational collapse. This indicates that cloud-cloud collisions play a crucial role in the formation of massive stars. The coexistent infall in filaments, clumps and cores observed in some of the massive star forming regions suggests that pre-assembled mass reservoirs may not be required to form high-mass stars (e.g., Yuan et al., 2018).

Studies also show that collisions could play a minor role in the formation of a massive star (e.g., Baumgardt & Klessen, 2011).

1.3.2 Observational constraints

In order to constrain the models, it is essential to use the observational data and obtain an accurate picture of massive star formation. However, observational studies are challenging as the massive stars remain in an embedded phase that lasts about 15% of their lifetime before evolving into the optically visible main-sequence phase (Churchwell, 2002; Zinnecker & Yorke, 2007). The resulting high dust obscuration makes it difficult to examine the early phases of massive star formation. Additional constraints include their rarity, faster evolution compared to the lower mass counterparts and relatively large distances, apart from being born in a clustered environment.

Once the deeply embedded high mass protostars evolve into ultracompact and compact H II regions that are bright in UV and optical, the circumstellar dust in the vicinity absorbs the stellar radiation and re-emit the absorbed energy in the near, mid and far-infrared. The infrared and longer wavelength maps of such regions with embedded massive stars can be used as a potential tool for studying the physical properties of the massive star forming regions. For carrying out observational studies of massive star forming regions, high resolution instruments in the infrared and radio wavelengths are, therefore, crucial.

1.4 Evolutionary sequence in massive star formation

Establishing a firm evolutionary sequence for high mass stars similar to their lower mass counterparts (Sect. 1.2) is observationally challenging. The evolution of massive protostars is believed to proceed in a sequence where the protostellar embryo heats and subsequently ionises the surrounding gaseous envelope, creating an H II region which eventually blows away the ambient cloud (Motte et al., 2017). A schematic view of the early evolutionary stages in the formation of massive stars is shown in Fig. 1.3 and Fig. 1.4. Objects in the earliest phases of massive star formation are known as massive starless clumps that are associated with IRDCs. In a later stage, they evolve into high mass protostellar objects (HMPOs) and hot molecular cores (HMCs). The final phase corresponds to H II regions. Each of these stages are discussed briefly below.

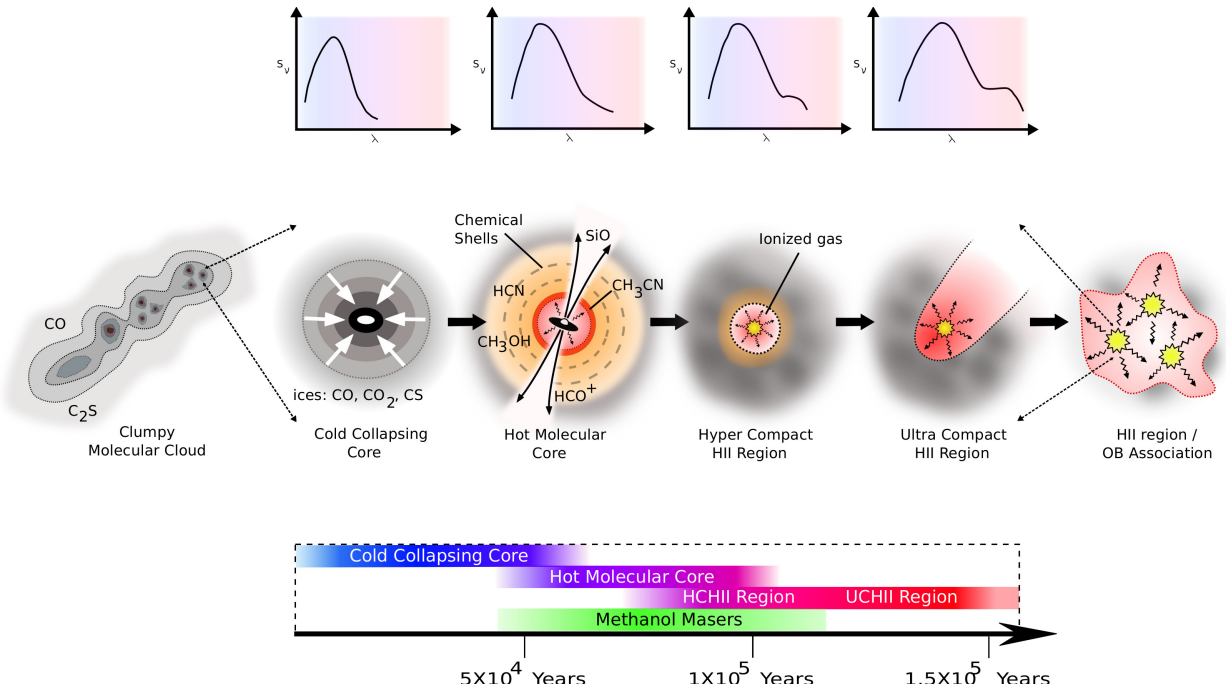

Figure 1.3: A schematic view of the early evolutionary stages in the formation of massive stars. Image shows the proposed evolutionary sequence evolving from left to right. Image courtesy: C. Purcell

1.4.1 IRDCs and massive starless clumps

IRDCs are believed to be the progenitors of massive stars and star clusters, that are characterized by dark extinction features seen against the bright-infrared Galactic back-

ground (Rathborne et al., 2006; Chambers et al., 2009). Initially detected by *ISO* and then by *MSX* (Perault et al., 1996; Egan et al., 1998), these massive clouds ($10^2 - 10^4$ $M_\odot$) vary widely in their morphology from elongated to compact structures. On larger scales, IRDCs are associated with filamentary structures and their sizes are seen to range from a few to hundreds of parsecs (Jackson et al., 2010; Ragan et al., 2014). On smaller scales, they fragment into dense clumps and cores (Battersby et al., 2010; Shipman et al., 2014; Zhang et al., 2016). IRDCs are dense ($n > 10^5$ cm^{-3}), cold (T < 20 K), and bright at submillimeter wavelengths (Carey et al., 2000). These extreme properties make them quintessential objects in the quest of earliest phases in massive star formation.

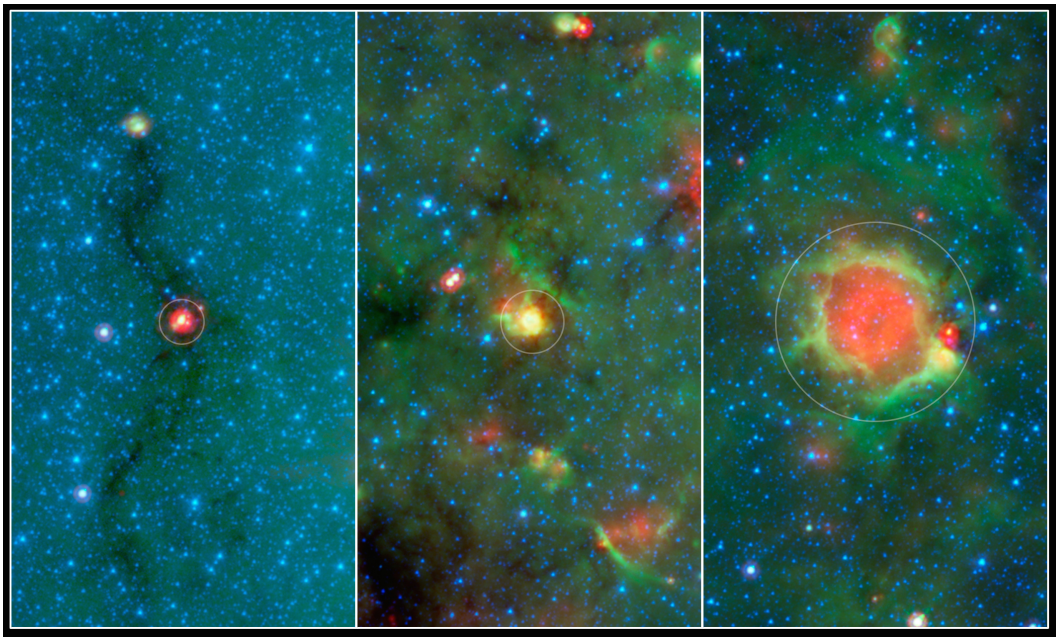

Figure 1.4: This series of images show three evolutionary phases of massive star formation, as pictured in infrared images from NASA's Spitzer Space Telescope. The stars start out in thick cocoon of dust (left), evolve into hotter features (center); and finally, blow out cavities in the surrounding dust and gas, resulting in green-rimmed bubbles with red centers (right). In this image, infrared light of 3.6 μm is blue; 8 μm is green; and 24 μm is red. Image credit: NASA/JPL-Caltech.

Comprehensive analyses at far-infrared and submillimeter wavelengths show that IRDCs possess significant substructures within them. Molecular line emission from these clumps and cores often exhibit signatures of protostellar activity such as infall

and outflow (Beuther & Sridharan, 2007; Jin et al., 2016), characterized by asymmetric line features. While some IRDCs harbour objects of different evolutionary stages such as maser spots, starless cores, ultracompact H II regions and YSOs, there are others that are devoid of any star formation activity (e.g., Busquet et al., 2016; Beuther et al., 2013). The latter serve as good targets to probe the earliest phases prior to collapse. The presence or absence of 70 μm emission has been used to distinguish protostellar and starless cores (e.g., Dunham et al., 2008, 2014). Based on their study towards a sample of IRDCs, Ragan et al. (2012a) suggest that cores lacking 70 μm emission are potentially less evolved than those IRDCs with 70 μm counterpart.

1.4.2 HMPOs and HMCs

HMPOs are a class of objects in the early stages of massive star formation (Molinari et al., 1996) where the central star is surrounded by a massive envelope with a centrally peaked temperature distribution (van der Tak et al., 2000; Sridharan et al., 2002). They are characterized by weak emission from ionized gas despite a high total luminosity ($L>10^3$ $L_\odot$). This suggests that they are at very early evolutionary stages. HMPOs are found to have a higher mass-to-luminosity ratio than ultracompact H II regions (Sridharan et al., 2002). They exhibit evidence of accretion activity such as molecular bipolar outflows, H_2O and CH_3OH masers and large scale infalls etc (e.g., Beuther et al., 2002a,b; Herpin et al., 2009).

HMCs are small (size≤ 0.1 pc) pockets of warm (≥ 100 K) and dense ($\geq 10^6$ cm^{-3}) molecular gas that are characterised by a rich chemistry observable in molecular lines (van der Tak, 2004). According to De Buizer et al. (2003), the basic observational characteristics of HMCs are: 1) they are compact sources seen in radio wavelength ammonia and (or molecular line) maps but show little or no radio continuum emission, 2) they lie in massive star forming regions near ultracompact H II regions (size < 0.1 pc), 3) they are very young and embedded to be detected in the optical or near-infared and 4) are often associated with H_2O masers. In a HMC, the central protostar heats up the surrounding environment, evaporating molecular ices leading to formation of complex molecules such as long carbon chains. HMCs represent the evolutionary stage in massive star formation where the protostars are actively accreting and ultracompact H II regions are yet not formed (Kurtz et al., 2000; Beuther et al., 2007). However,

Table 1.1: Physical parameters of H II regions (Kurtz, 2002)

Class of Region	Size (pc)	Density (cm^{-3})	EM (pc cm^{-6})	Ionized mass ($M_\odot$)
Hypercompact	~ 0.003	$\gtrsim 10^6$	$\gtrsim 10^{10}$	$\sim 10^{-3}$
Ultracompact	$\lesssim 0.1$	$\gtrsim 10^4$	$\gtrsim 10^7$	$\sim 10^{-2}$
Compact	$\lesssim 0.5$	$\gtrsim 5 \times 10^3$	$\gtrsim 10^7$	~ 1
Classical	~ 10	~ 100	$\sim 10^2$	$\sim 10^5$
Giant	~ 100	~ 30	$\sim 5 \times 10^5$	$10^3 - 10^6$
Supergiant	> 100	~ 10	$\sim 10^5$	$10^6 - 10^8$

many studies suggest that some of the classified HMCs may have already reached the ultracompact H II region phase (Cunningham, 2015).

1.4.3 H II regions

Massive OB stars emit most of the radiation in ultraviolet (UV). These UV photons have a profound effect on the surroundings as they convert hydrogen into its ionised (H II) form. H II regions are photoionized nebulae formed around massive young stars. As these young stars are embedded in their parent molecular clouds, H II regions are visible mostly in the infrared and longer wavelengths as they can penetrate the thick layers of gas and dust in the surrounding cocoons. They are classified as hypercompact (HC), ultracompact (UC), compact and classical/extended H II regions (see Table. **??**). HC H II regions have sizes less than 0.01 pc and very high densities ($n_e \geq 10^5$ cm^{-3}) and are the smallest H II regions around massive stars. Many of them have broad radio recombination lines (RRLs) with large line widths, ΔV> 40 km s^{-1} (e.g., Sewilo et al., 2004). UC H II regions have typical sizes of ~ 0.1 pc and low densities ($n_e \sim 10^4$ cm^{-3}) compared to HC H II regions. Compact H II regions have larger sizes ($0.1 - 0.3$ pc) and lower densities compared to UC H II regions and are located in more evolved regions of the clouds. Extended H II regions have sizes upto several parsecs and represent a more evolved state (Kurtz & Franco, 2002).

High resolution radio interferometric observations of H II regions reveal that they appear in a wide range of morphological classifications such as spherical, core-halo,

shell, irregular and cometary (Wood & Churchwell, 1989). An additional morphology designated as bipolar has been also included recently in the classification scheme (de Pree et al., 1994; Deharveng et al., 2015). The diverse morphologies of H II regions depend on several factors such as age, ionized and molecular gas dynamics, density structure of the ISM and relative motion of the H II region with respect to the ambient medium (Churchwell, 2002). However, the details of such interaction mechanisms are not clearly understood. The common appearance of a specific morphology hints that there are ordered physical processes associated with massive star formation (Hoare et al., 2007).

1.5 Formation of massive clusters and OB associations

Massive star formation in a GMC often leads to the formation gravitationally bound OB clusters or loose OB associations (Garmany, 1991, 1994; Lada & Lada, 2003). In our Galaxy, $\sim$ 70% of the O-type stars reside in young clusters and associations (Gies, 1987) and $\sim$ 50% of the remaining population are identified as runaways (de Wit et al., 2005). Some of the famous massive clusters include Orion nebula cluster and Westerlund 2 (see Fig. 1.5). The estimated total mass in these clusters are found to range between $10^3 - 10^5$ $M_\odot$ (e.g., Hillenbrand, 1997; Bosch et al., 2009; Portegies Zwart et al., 2010). An OB association is a large, gravitationally unbound group consisting of a large number of B and few O-type stars. Recent studies also reveal the presence of a population of low mass stars in these associations (Brown, 2001, and references therein). They are typically few parsecs in diameter and often show substructures. A close inspection of these substructures show that they consists of several stellar groups with different ages and kinematics (Garmany, 1994). Whether the OB associations are superpositions of expanded young clusters or not is still a question of debate (Kroupa et al., 2001; Bastian & Goodwin, 2006).

In the initial stages, the massive clusters are heavily embedded within molecular clouds and are visible only in the infrared wavelengths. The embedded phase lasts between $2 - 3$ Myr and clusters with ages larger than 5 Myr are rarely associated with molecular gas (Leisawitz et al., 1989). Studies indicate high infant mortality rate in embedded clusters which is mostly attributed to low star formation efficiency and rapid gas

dispersal which characterizes their birth (Lada & Lada, 2003). The embedded clusters are quintessential in studying the origin and early evolution of stars and planetary systems and provide vital clues about many fundamental properties of the Galactic stellar population, such as the age, initial mass function (IMF), stellar multiplicity, dynamical interactions etc.

Figure 1.5: Hubble Space Telescope image of the cluster Westerlund 2 and its surroundings. Image credit: NASA, ESA, A. Nota (ESA/STScI), and the Westerlund 2 Science Team.

1.6 Impact of massive stars on ISM: Feedback and triggered star formation

The properties of the ISM such as the morphology, turbulence and formation/dispersal of molecular fragments are heavily influenced by the stellar feedback from massive stars. Such feedback mechanisms play a significant role in the evolution of galaxies. In massive clusters and OB associations that contain tens to hundreds of O-type stars, the star formation is found to be hierarchical, with structures extending over a wide range of length and mass scales. The dynamics of these regions are found to be subjugated by feedback from massive O stars in the form of H II regions, wind-blown bubbles and supernova shells (e.g., Cappa et al., 2007; Lopez et al., 2011; Camps-Fariña et al., 2016).

The global mechanical feedback from the massive star population is mostly dominated by supernova explosions. Stellar winds play a significant role only for the youngest populations (Oey & Clarke, 2007).

Feedback from massive stars can have a positive or negative impact on its surroundings. If there is mechanical feedback, the imparted momentum can drive winds that carry material away from the star. For a radiative feedback, the heated gas blows out bubbles of ionised H II gas (Krumholz et al., 2014, and references therein). These effects can drive turbulence through the whole cloud. Sufficiently large feedback effects could disrupt the cloud, halting future star formation in the cloud (Murray, 2011). Using numerical simulations, Shima et al. (2017) concluded that the efficiency of feedback is heavily dependent on the gas structure, with negative feedback dominating when the density is high.

Alternatively, feedback is also thought to be a key mechanism responsible for triggered star formation in many regions (e.g., Deharveng et al., 2003; Zavagno et al., 2006; Koenig et al., 2008; Xu et al., 2014). According to Elmegreen & Lada (1977), Lyman continuum radiation from an OB cluster can drive ionisation fronts into ambient neutral material. The resulting shock front heats and compresses the adjacent layer of molecular gas, leading to gravitational collapse of the shocked neutral layer and subsequent triggered star formation. The stars formed as a result of triggering tend to be massive stars. This effect of positive feedback on future star formation has been explored in many studies (e.g., Whitworth et al., 1994; Vanhala & Cameron, 1998; Koenig et al., 2012). Gas heating due to radiative feedbacks could also increase the Jeans mass, reducing the fragmentation to produce more massive stars forming in place of a larger number of smaller objects (Bate, 2009; Urban et al., 2010).

Detailed observational studies of individual massive star forming regions are therefore crucial for a better comprehension of various feedback effects and how it influences the future generation of stars.

1.7 Motivation of the thesis work

The physical properties involving the formation and evolution of massive stars is not clearly understood till date. Although there are numerous surveys and studies that have

investigated the chemistry and physical conditions of large sample of mass star forming regions (e.g., Chini et al., 1987; Minier et al., 2001; Faúndez et al., 2004; Thompson et al., 2006; Klaassen & Wilson, 2007; Svoboda et al., 2016), studies focussing on individual regions are limited and most of them probe the northern Galactic sky. The main advantage of studying individual regions is that it enables one to understand the various aspects of a particular region such as the star formation activity, physical properties, chemistry, kinematics etc. in its entirety, contrary to large surveys that examine few general properties of these regions. Our aim is to carry out a detailed investigation of the conditions prevailing in some of the southern massive star forming regions. The major questions we attempt to address in this thesis are:

1. What are the initial conditions of massive star formation (temperature, density, mass etc.) and how do they change with evolution?

2. Does the interaction between the ionized gas and the ambient cloud affect the morphology and kinematics of H II regions?

3. How does the massive star formation influence the local environment and the region in its entirety?

As our motivation is to understand the star formation activity, structure and kinematics of massive star forming regions, we use multiwavelength observations ranging from optical to radio wavelengths to understand different facets of massive star formation. While the study of IRDCs is essential for understanding the evolution of fragmentation process in pre-cluster clouds, clumps in later evolutionary stages are useful in examining the advanced stages of high mass star formation. For this, H II regions serve as an ideal tool that acts as a lodestar for identifying regions of recent massive star formation activity. We also use other tracers such as masers, near and mid-infrared YSOs etc.

Our knowledge of the physical environments of H II regions can be improved by a thorough understanding of their morphologies. High resolution observations of RRLs being excellent tracers of velocity distribution in the ionized gas can be used to map the velocity field of the H II region (e.g., Pankonin et al., 1979; Lang et al., 2001; Keto & Klaassen, 2008; Sewiło et al., 2008). The detailed analysis of RRLs enables the estimation of the physical properties of ionized gas such as kinematic distance, electron temperature, electron density and metallicity (Hjellming & Davies, 1970; Shaver,

1980; Mehringer, 1994; Konovalenko & Stepkin, 2005). On the other hand, using submillimeter molecular line observations, one can get an understanding of the complex kinematics of the associated molecular cloud. Apart from tracing the cloud kinematics, other advantages of molecular line observations include probing the temperature, internal dynamics and excitation conditions in these regions (e.g., Blake et al., 1987; Helmich et al., 1994; Zernickel et al., 2012). Velocity information provided by molecular lines can also be used, due to Galactic rotation, to estimate the distance to the source (e.g., Fich et al., 1989). A comparative study of the ionised gas velocity with the velocity field of the molecular cloud can shed light on the interaction mechanisms between the H II region and the associated cloud.

In this thesis, we carry out a detailed investigation of few massive star forming regions that are in different stages of evolution. We first investigate the elongated IRDC G333.73+0.37 (hereafter, G333.73), using an assortment of markers to probe the diverse traits of the star forming activity in the cloud. Based on the results, we attempt to comment on the evolutionary stage of the cloud. We also examine the cometary H II region IRAS 17256–3631 using our multiwavelength approach. Sensitive radio continuum observations at 1300, 610 and 325 MHz are useful in analysing the morphology and properties of ionised gas associated with newly formed massive stars. In addition, we have utilised the archival infrared and submillimeter data along with the molecular line emission from various surveys to probe the molecular cloud. This helps us understand the chemistry, kinematics as well as the evolutionary stages of these regions. In addition, we have also mapped the low frequency RRL emission from IRAS 17256–3631 and the neighbouring bipolar H II region IRAS 17258–3637 to map the velocity field of ionised gas and hence understand the kinematics of these regions. Finally, we use the broadband capabilities of Giant Metrewave Radio Telescope (GMRT), India, to map and study the large scale diffuse emission (angular size $\sim 10'$) from the star forming complex associated with the H II regions IRAS 17256–3631 and IRAS 17258–3637. Our aim is to investigate the large scale radio emission seen towards star forming regions, in an attempt to understand the morphology of ionised gas on large scales.

1.8 Outline of the thesis

The thesis is structured as follows:

- Chapter 2 presents the details of radio and near-infrared observations, various data reduction techniques and archival data.
- In Chapter 3, the star formation activity and structure of the filamentary IRDC G333.73 is analysed using data from near-infrared to radio wavelengths.
- Chapter 4 presents the multiwavelength investigation of the cometary H II region IRAS 17256–3631 and its associated embedded cluster.
- In Chapter 5, the structure and kinematics of two H II regions: IRAS 17256–3631 and IRAS 17258–3637 are probed using low frequency RRLs and complementary molecular line data.
- In Chapter 6, the origin of large scale radio emission associated with the star forming complex comprising of the two H II regions IRAS 17256–3637 and IRAS 17258–3637 is examined.
- In Chapter 7, the summary of the main conclusions from this study and a section on future work are presented.

Chapter 2

Observations and Data Reduction

This chapter describes the observations and data reduction techniques used in this thesis. The radio observations were carried out using the GMRT. For near-infrared observations, Mt. Abu Infrared Telescope and United Kingdom Infrared Telescope (UKIRT) were used. Additionally, archival data from various surveys were used to complement these observations.

2.1 Low frequency radio interferometric observations using GMRT

The ionised gas emission from newly formed massive stars were mapped using GMRT, India (Swarup et al., 1991) from $300 - 1372$ MHz. GMRT consists of 30 antennas each having a diameter of 45 m arranged in a Y-shaped configuration. Twelve antennas are distributed randomly in a central array within an area ~ 1 km^2 and the remaining 18 antennas are stretched out along three arms, each of length ~ 14 km. The minimum and maximum baselines are 105 m and 25 km respectively that allows the simultaneous mapping of small and large scale structures. For example, the angular sizes of the smallest and largest structures observable at 610 MHz are $5''$ and $20'$ respectively. The radio data reduction is performed using the NRAO Astronomical Image Processing System (AIPS) software package. A detailed description of the radio data reduction is given in the next section.

2.1.1 Radio continuum data reduction

The radio data consists of observations of the target source, a primary flux calibrator and a secondary phase calibrator. The raw UV data obtained from the GMRT archive is in a binary format with the extension '.lta'. To convert this to FITS format, two programs called 'LISTSCAN' and 'GVFITS' were used. This resulting FITS file is given

Figure 2.1: Four antennas of the Giant Metrewave Radio Telescope (GMRT, Pune, India). Image courtesy: `http://http://www.mso.anu.edu.au/$~$plah/Home$_$Page$_$Stuff/GMRT$_$2006/GMRT$_$images$_$2006.html`.

as input to the AIPS software. The sequence of steps used for data reduction are given below and the flowchart is shown in Fig. 2.2.

1. **Loading and indexing the data**: Data reduction begins by loading the FITS file into AIPS using the task FITLD. The task reads standard images and UV data from FITS files. This will create a file with extension '.FITLD' in AIPS. A set of extension tables containing information such as the history, antenna names, coordinates, frequency, bandwidth, source list, etc. are created in this file. Next, the task INDXR is run to create an index (NX) table that indexes the UV data file.

2. **Flagging and calibration**: Due to slewing of the telescope, data can get corrupted at the beginning of each scan. The initial 0.25 minutes of data is flagged (i.e. removed) using the task QUACK to remove this corrupted data. The data is then displayed using the task TVFLG to identify non-working antennas and subsequent flagging is carried out

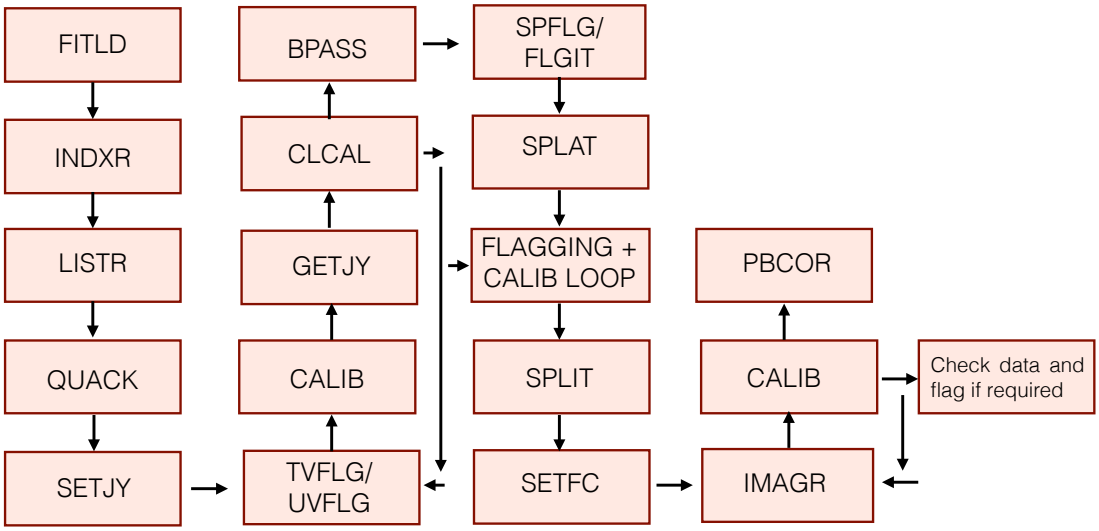

Figure 2.2: Schematic illustrating the sequence of steps for radio continuum data reduction using AIPS.

using TVFLG or UVFLG. As the frequency band is subdivided into multiple channels (128/256/2048), a reference channel (typically near the middle of the band) is selected for initial flagging and calibration purposes. After preliminary flagging, the data is then calibrated. At first, the flux density of the flux calibrator assigned using the task SETJY. Then, the task CALIB is used to create a solution (SN) table. Following this, the task GETJY is used to determine the flux density of the secondary (phase) calibrator. Finally, the task CLCAL is used to apply solutions from SN table to create a new CL table. This completes one cycle of calibration. The calibrated data is inspected using UVPLT, VPLOT and TVFLG to identify data corrupted by radio frequency interference, bad baselines etc. and is flagged further. After every set of flagging, the calibration process is repeated to improve the solutions. The flagging-calibration loop is repeated until the data is cleaned thoroughly. Finally, a bandpass calibration is performed to correct for the frequency dependence of antenna gains. The task BPASS is used for this purpose, which creates a BP table, that contains the bandpass response functions of the antennas. The bandpass functions are examined using the task POSSM to identify bad channels and are removed, if required.

3. **Channel averaging and subsequent calibration**: The channels are averaged to improve the signal-to-noise ratio. This is performed using the task SPLAT. The total number of channels that can be averaged together are limited by the band width smear-

ing effect. When visibilities from a finite bandwidth are gridded as if monochromatic, it will result in aberrations in the image. This causes sources to smear along the radial direction. The effects of bandwidth smearing can be reduced by dividing a large band into smaller subsets. The maximum number of channels that can be safely averaged at GMRT frequencies are given below.

1280 MHz: $40 - 48$ channels ($5 - 6$ MHz)

610 MHz: $24 - 32$ channels ($3 - 4$ MHz)

325 MHz: $8 - 12$ channels ($1 - 1.5$ MHz)

The output file from SPLAT has fewer number of channels compared to the initial UV file. The flagging-calibration loop is re-run to obtain improve the calibration solutions and to remove the bad data.

4. **Imaging and self-calibration of the target**: The calibrated SPLAT file is a multi-source file and includes the target as well as the calibrators. First, the target data is separated out from the calibrators using the task SPLIT. The output of SPLIT is a single source file and can be given to the imaging task IMAGR as input. For wide field imaging, the standard assumptions that the relevant sky area is approximately flat and the third baseline coordinate (w term) is constant across the field of view are no longer valid. This is significant at low frequencies (ν $\leq$610 MHz). To account for this, the whole field corresponding to the primary beam is divided into multiple facets that individually satisfy the assumptions given above and imaged separately. The task SETFC is used to compute the facets (or sub-fields) and the output boxfile is given as an input to the IMAGR. IMAGR then performs a visibility based clean deconvolution of the type devised by Barry Clark and enhanced by Bill Cotton and Fred Schwab. The clean algorithm (Högbom, 1974) assumes that the radio sky can be represented by a small number of point sources. It uses an iterative procedure to find the positions and strengths of these sources. Boxes are drawn around sources and the iteration cycles by cleaning the brightest parts of the residual image. Fourier transform of the clean components are computed and subtracted out from the visibility data at the end of each major iteration cycle. A dirty image is computed from the residuals. The accumulated source model is then convolved with a clean beam and the residuals of the dirty image are added to the clean image. The output consists of a set of images corresponding to

multiple facets and these can be combined to a single image using the task FLATN.

The quality of the image can be improved significantly by minimizing the phase errors. This is achieved by carrying out a phase self-calibration in the visibility data based on a model image, which is the output image created by IMAGR. The method involves minimizing the difference between observed phases and model phases by solving for antenna-based instrumental phases (Pearson & Readhead, 1984). The improved visibility data is used to generate a new model image. The imaging-self-calibration process is iterated several times until the phase variations are minimal.

5. **Primary beam correction and flux rescaling**: The image has to be corrected for reduction in sensitivity at the edges of the primary beam. For this, the image has to be divided by the response of the primary beam. The task PBCOR is used to carry out this primary beam correction. For sources lying in the Galactic plane, there is a significant contribution from the Galactic diffuse emission to the system temperature. This is particularly important at low frequency bands. As the flux calibration is performed using a calibrator that is located away from the Galactic plane, proper scaling of fluxes in the final images is necessary. A system temperature correction to account for the Galactic plane emission, $(\mathrm{T_{gal}} + \mathrm{T_{sys}})/\mathrm{T_{sys}}$ has been used to scale the fluxes at each frequency where $\mathrm{T_{sys}}$ is the system temperature corresponding to the flux calibrators that are located away from the Galactic plane. To estimate $\mathrm{T_{gal}}$, the temperature map of Haslam et al. (1982) at 408 MHz is used. Scaling factor is calculated by extrapolating $\mathrm{T_{gal}}$ to observed frequency by assuming a spectral index of -2.6 (Roger et al., 1999; Guzmán et al., 2011) which is then applied to the self-calibrated image. Typical scaling factors at 325, 610 and 1280 MHz are 5, 2 and 1, respectively. The details of radio continuum observations are given in Table. 2.1.

2.1.2 Radio recombination line data reduction

The 172α RRLs towards two star forming regions IRAS 17256–3631 and 17258–3637 were probed using the L-band (1280 MHz) spectral mode of GMRT. The observed field was centered at IRAS 17256–3631 (α_{J2000}: $17^h29^m01.1^s$, δ_{J2000}: -36°33′38.0″). The second H II region IRAS 17258–3637 is located within the field of view of the pri-

Table 2.1: Details of GMRT radio continuum observations.

	G333.73+0.37		IRAS 17256–3631			SNR G351.7–1.2
Details	1300	610	1372 MHz	610 MHz	325 MHz	$300-500$ MHz
Date of observation	2014 Aug 31	2014 Aug 7	2004 Jan 25	2002 Jan 6	2003 Oct 10	2017 Mar $21-22$
On-source integration time (sec)	164	150	414	83	61	405
Bandwidth (MHz)	32	32	0.5	16	16	200
Primary beam	$21.8'$	$46.6'$	$20.4'$	$46.6'$	$85'$	$52.5'-87.5'$
Synthesized beam	$5.5'' \times 2.0''$	$14.5'' \times 5.4''$	$7.3'' \times 5.2''$	$11.5'' \times 7.9''$	$21.7'' \times 8.5''$	$19.9'' \times 10.5''$
RMS noise (mJy/beam)	0.08	0.3	1.0	1.5	2.5	$0.8-2$
Flux calibrator	3C286	3C286	3C286, 3C48	3C286	3C286	3C286, 3C48
Phase calibrator	1626-298	1626-298	1622-297	1626-298	1830-360	1830-360

mary beam ($\sim$20$'$). The rest frequency of H172α line is 1281.175 MHz and C172α is 1281.815 MHz. We selected the central frequency as 1281.69 MHz, and the total bandwidth of 2 MHz was divided into 512 channels. The observable frequency was determined keeping in view the LSR velocity of the observed regions as well as the motions of Earth and Sun. These settings correspond to a spectral resolution of 4.06 kHz (or velocity resolution of 0.95 km/s). 3C286 and 3C48 were used as the primary flux calibrators while 1626-298 and 1830-360 were used as phase calibrators. The latter was also used for bandpass calibration. As our targets lie in the southern sky and are available for only $\sim$7 hours per day above the elevation limit of GMRT, the targets were observed for 5 days (28 February, 01-03 March and 21 July, 2015). The total on-source integration time was 23.2 hrs. The calibration and flagging of each day's data was carried out separately before co-adding the UV data. The steps for spectral line data reduction are explained below.

1. **Construction of a continuum map**: Before proceeding to the spectral line cube generation, a continuum map has to be made. The steps for continuum image generation are the same as those described in Section 2.1.1.

2. **Continuum subtraction and line map generation**: For the continuum subtraction, the FITLD file that contains 512 channels is used (and not SPLAT or SPLIT file that contains the averaged channels). The task UVLIN is used to subtract the continuum emission by making linear fits to the real and imaginary components versus channel number for each visibility in the line free channels. The appropriate values are then subtracted out from all channels. Of the 5 data sets taken on different days, one dataset was found to be very noisy. This dataset was excluded from further analysis (leading to a total on-source integration time of 18.8 hrs). The remaining four data sets were combined together using the task DBCON and a line map was generated using the task IMAGR. In order to improve the signal-to-noise ratio (SNR), a lower resolution map was generated by selecting UVTAPER of 10 kλ in IMAGR. The primary beam correction was applied and the image rescaling was applied (factor of 1.3) to correct for the contribution of Galactic plane emission to the system temperature. The final resolution of the spectral cube is $27.4'' \times 18.2''$ (low resolution image) while that of the high resolution radio continuum map is $6.7'' \times 4.5''$.

2.2 Near-infrared observations

Imaging and spectroscopic observations in the near-infrared were carried out with the 3.8-m UKIRT, Hawaii and 1.2-m Mt. Abu Infrared Telescope, India.

2.2.1 Data from UKIRT

The region associated with the IRAS source 17256-3631 was observed in the broad-band JHK filters and the narrow-band H_2 filter (centered on the H_2 (1-0) S1 line at 2.12 μm) using the UKIRT Wide-Field Camera (WFCAM; Casali et al., 2007). WFCAM consists of four 2048×2048 HgCdTe Hawaii-2 arrays. With a pixel size of $0.4''$, each array has a field of view of $13.5' \times 13.5'$. A 2×2 microstepping gives a final pixel scale of $0.2''$ pixel^{-1}. Observations were obtained in the 9-point dithered mode with offsets of $20''$. The observing log for the WFCAM observations are given in Table. 2.2.

The data reduction was carried out by the Cambridge Astronomical Survey Unit (CASU). Pipeline photometric calibrations were done using 2MASS sources in the field, and the magnitudes derived were converted to the UKIRT system. The photometric system, calibration, pipeline processing and science archive are described in Hodgkin et al. (2009) and Hambly et al. (2008) and references therein. The pipeline reduction did not detect many sources located within the nebulosity in the field of interest. For such sources, particularly towards the central region of IRAS 17256-3631, aperture photometry was carried out using the QPHOT task in the Image Reduction and Analysis Facility (IRAF) software (Tody, 1986). Photometric magnitudes of saturated sources were replaced by those from the 2MASS Point Source Catalog after converting to the WFCAM photometric system. Care was taken to identify and appropriately subtract out the components if an unresolved 2MASS single source was seen as a resolved binary or multiple sources, one component of which was saturated in the UKIRT-WFCAM images. The 2MASS source magnitude was converted to the UKIRT system (Hodgkin et al., 2009) before performing the subtraction. Finally, a combined catalog was generated by converting to the Bessell & Brett system (Bessell & Brett, 1988) using the transformation equations given in Carpenter (2001).

To obtain the emission in H_2 line in the field, continuum emission was subtracted out

Table 2.2: Details of UKIRT near-infrared observations

Observation date	Filter	Exposure time of each frame (sec)	Total integration time (sec)	FWHM ($''$)
2014 June 05	K	5	180	0.9
2014 June 06	H_2	40	1440	0.87
2014 June 20	J	10	720	1.14
2014 June 20	H	5	360	1.22
2014 June 20	K	5	360	1.14

from the H_2 images using scaled K-band images (Varricatt et al., 2005). We have used the K-band image taken on 05 June 2014 for continuum subtraction as the seeing was comparable to that of H_2 image. Integrated counts using circular apertures of diameter three times the average full width at half-maximum (FWHM) of isolated point sources in each mosaic were used to estimate the scaling factors. The K-band image was scaled using this factor and subtracted from the H_2 image to give the continuum subtracted H_2 image. This method removes the diffuse continuum emission efficiently but improper PSF matching between the narrow and broad band images results in residuals seen in stars.

Apart from imaging, spectroscopic observations of a near-infrared bright source in the same field as above, G351.6921-01.1515 (hereafter IRS-1) was carried out using the UKIRT $1-5$ micron Imager Spectrometer (UIST). UIST employs a 1024×1024 InSb array, and has a pixel scale of $0.12''$ pixel^{-1} for spectroscopy. The observations were performed using a 4-pixel-wide and $1.9'$-long slit. The HK grism covers a wavelength regime of $1.395 - 2.506$ μm. The 4-pixel slit gives a spectral resolution of 500. The slit was oriented 16.5° west of north and centered on IRS-1 ($\alpha_{\rm J2000}$: $17^h29^m01.389^s$, $\delta_{\rm J2000}$: -36°33′54.21″). This ensures sampling of the associated nebulosity in the NW direction. Given the spatial extent of the nebulosity, the observations were performed by nodding to a relatively less crowded region of the sky ($\sim 3.5'$ SE of the source). The sequence of object-sky pairs gave a total on-source integration time of 800 s, with an exposure time of 40 s per frame.

The preliminary data reduction for spectroscopy was done using the UKIRT pipeline

ORACDR. Flat fielding and wavelength calibrations were performed using the flat and arc spectra obtained prior to the target observations. The atmospheric air glow lines were removed by subtracting the sky frame from the target frame. Finally, the flat fielded, wavelength calibrated and sky subtracted frames were combined to give the resultant target spectral image. For telluric and instrumental corrections, a spectroscopic standard BS 6454, that is a F9V star, was observed. Subsequent reduction was performed using the starlink packages FIGARO and KAPPA. The spectrum of the standard star was extracted and the photospheric absorption lines were removed by interpolating across the wavelength range under consideration. Blackbody curve with appropriate temperature is used to fit the continuum of the standard and was then used to divide the target spectrum for telluric and instrumental corrections. The wavelength calibration was further refined using the arc spectra, and flux calibration carried out anew using the 2MASS magnitudes of the standard star, assuming that the seeing did not significantly vary between the observations of the target and the standard star. The flux calibration is expected to be accurate upto $\sim 20\%$. IRAF spectral extraction task APALL was also used to extract the spectra of the central star and the nebulosity.

2.2.2 Data from Mt. Abu Infrared Telescope

The region associated with IRAS 17256–3631 was imaged in the narrow-band Brγ and broad-band K filters using the Near Infrared Camera and Spectrograph (NICS) on the Mt. Abu Infrared Telescope. NICS is equipped with a 1024 $\times$ 1024 HgCdTe detector array giving a pixel scale of $0.5''$ pixel^{-1} and a field of view of $8' \times 8'$. The observations were carried out by dithering in five positions with offsets of $20''$. The field is relatively crowded with faint extended nebulosity. Hence, for better sky subtraction, a nearby relatively sparse region of the sky was observed with the same pattern. The individual frame exposure times in the Brγ and K bands were 90 s and 10 s, respectively. The sky subtracted frames were aligned and co-added to give resultant Brγ and K band images with total on-source integration times of 1350 s and 250 s, respectively. Continuum subtraction was carried out as discussed in Sect. 2.2.1 .

2.3 Archival datasets

Apart from radio and near-infrared observations, we have used archival data to investigate emission of the star forming regions at different wavebands. The properties of the warm dust associated with these regions are investigated using mid-infrared *Spitzer Space Telescope* and the Midcourse Space Experiment (MSX) data. The cold dust emission is analysed using far-infrared and submillimeter maps from *Herschel* Hi-GAL and APEX+Planck surveys, respectively. In addition, we have used the MALT90 and ThruMMS spectral line surveys to examine the chemical properties and kinematics of the regions. The optical emission is probed using SuperCOSMOS H-alpha survey (SHS).

2.3.1 *Spitzer Space Telescope*

The mid-infrared maps from *Spitzer Space Telescope*, with a primary mirror of size 85 cm, is used to probe the warm dust emission and YSOs. The Infrared Array Camera (IRAC) is one of the three focal plane instruments that obtain simultaneous broadband images at 3.6, 4.5, 5.8 and 8.0 μm. The pixel size is $1.2''$ in all four bands and achieved resolutions are $1.7''$, $1.7''$, $1.9''$ and $2.0''$ at 3.6, 4.5, 5.8 and 8.0 μm respectively (Fazio et al., 2004). We used the Level-2 Post-Basic Calibrated data (PBCD) images from the Galactic Legacy Infrared Mid-Plane Survey (GLIMPSE; Benjamin et al., 2003) to study the nature of diffuse emission. In addition, we have also made use of The Multiband Imaging Photometer(MIPS) 24 μm image obtained as a part of the MIPSGAL survey (Carey et al., 2009). The pixel size and resolution at 24 μm are $2.5''$ and $6''$, respectively.

2.3.2 MSX Survey

MSX mapped the entire Galactic plane within $|b| \leq 5^{\circ}$ in four mid-infrared wavebands: 8.3, 12.1, 14.7 and 21.3 μm at a resolution of $\sim 18.3''$ (Price et al., 2001). The image tiles were obtained from NASA/IPAC infrared image archive.

2.3.3 *Herschel* Hi-Gal Survey

We have used images from the *Herschel Space Observatory* to study the cold dust emission from the molecular clouds. The *Herschel Space Observatory* is a 3.5 m telescope capable of observing in the far-infrared and submillimeter spectral range: 55-671 μm (Pilbratt et al., 2010). The images are part of the *Herschel* Hi-Gal Survey (Molinari et al., 2010b). The instruments used in the survey are the Photodetector Array Camera and Spectrometer (PACS; Poglitsch et al., 2010) and the Spectral and Photometric Imaging Receiver (SPIRE; Griffin et al., 2010). The Hi-Gal observations were carried out in parallel mode covering wavelength range of $70 - 500$ μm. We used Level-2.5 PACS images at 70 and 160 μm and Level-3 SPIRE images at 250, 350 and 500 μm for our analysis. The pixel sizes are $2''$, $3''$, $6''$, $10''$ and $14''$ and the corresponding resolutions are $5''$, $13''$, $18.1''$, $24.9''$ and $36.4''$ at 70, 160, 250, 350 and 500 μm respectively. We used the *Herschel* Interactive Processing Environment (HIPE) to download and process the data.

2.3.4 ATLASGAL Survey

The 870 μm images from the APEX Telescope Large Area Survey of the Galaxy (ATLASGAL; Schuller et al., 2009) is used to investigate the cold dust emission from molecular clouds. The observations were performed using the Large Apex Bolometer Camera (LABOCA), a 295-element bolometer array and the pixel size and resolution achieved are $6''$ and $18.2''$, respectively.

2.3.5 APEX+Planck data

The Apex+Planck image is a combination of 870 μm data from the ATLASGAL survey (Schuller et al., 2009) and 850 μm map from the Planck/HFI instrument. The data covers emission at larger angular extent scales, thereby revealing the structure of cold Galactic dust in greater detail (Csengeri et al., 2016). The pixel size and resolution achieved in these images are $3.4''$ and $21''$, respectively.

2.3.6 MALT90 Molecular Line Survey

We have used Millimetre Astronomy Legacy Team 90 GHz Pilot Survey (Foster et al., 2011; Jackson et al., 2013) to understand the properties of the molecular gas. This survey has mapped transitions of 16 molecular species near 90 GHz. The observations were carried out using the 8 GHz wide Mopra Spectrometer (MOPS). The data reduction was conducted by the MALT90 team using an automated reduction pipeline. The spatial and spectral resolutions are $72''$ and 0.11 km s^{-1} respectively. The data cubes available from the website (http://malt90.bu.edu/) are images of size $\sim 4'$.

2.3.7 ThrUMMS Molecular Line Survey

In order to sample the CO line emission, we have used ^{12}CO and ^{13}CO maps from The Three-mm Ultimate Mopra Milky way Survey (ThrUMMS; Barnes et al., 2015). The survey mapped $J = 1 \rightarrow 0$ transition of ^{12}CO, ^{13}CO, C^{18}O, and CN lines near 112 GHz at a spectral resolution of 0.1 km s^{-1} with a spatial resolution of $66''$. The data reduction was performed by ThruMMS team and the calibrated data is made available to the public through the website (https://www.astro.ufl.edu/ peterb/research/thrumms/rbank/).

2.3.8 SuperCOSMOS H-alpha survey

The SuperCOSMOS H-alpha Survey (Parker et al., 2005) is used to compare the optical emission with emission from other wavelength bands. The interference filter used has a central wavelength at 6950 ± 25 Å and FWHM of 70 ± 3 Å. Hence apart from the Hα line, [NII] emission lines at 6548 and 6584 Å are included. These components can be deconvolved only through spectroscopy. The image tiles are accessible through the SHS website (http://www-wfau.roe.ac.uk/sss/halpha/).

Chapter 3

Star Formation activity in the Infrared Dark Cloud G333.73+0.37

IRDCs are reservoirs of dense gas and dust. They are believed to be the progenitors of massive stars and star clusters. In this chapter, we investigate the filamentary IRDC G333.73+0.37 (hereafter, G333.73) using an assortment of markers to probe the earliest stages of massive star formation and to analyse the diverse traits of star forming activity of the cloud. G333.73 is located at a distance of 2.6 kpc (Beltrán et al., 2006; Sánchez-Monge et al., 2013). The infrared luminosity of this region is 2.7×10^4 $L_\odot$. Previous studies have reported signatures of massive star formation within this IRDC. Beltrán et al. (2006) mapped the dust emission at 1.2 mm and identified 8 massive ($14-472$ $M_\odot$) cold dust clumps in this region. High frequency radio continuum observations at 18 and 22.8 GHz by Sánchez-Monge et al. (2013) identified two sources in this region (beam size $\sim 30''$). The ZAMS spectral types of the ionising sources are found to be B0 and B1 respectively, implying the ongoing massive star formation in the region. This IRDC is also associated with an infrared bubble (MWP1G333726+003642) identified by Simpson et al. (2012).

These results are chiefly the outcomes of various surveys and hence provide limited information about the IRDC in its entirety. The motivation of this study is to examine the star forming activity across the entire IRDC. To achieve this, multiwavlength tracers are used to carry out a deep and detailed investigation. As the IRDCs have been identified as dark structures against the nebulous mid-infrared emission, the analysis is initiated with warm dust emission in this region. Subsequently, the properties of cold gas and dust are probed using far-infrared to submillimeter wavelengths. The locations of star-forming flurry are realised using the distribution of ionised gas emission. Using photometric analysis, the population of YSOs and their distribution across the cloud is examined in detail. Such a plethora of observational data enables a fair visualization of the physical properties, chemistry, kinematics as well as the evolutionary stage of G333.73.

3.1 Mid-infrared emission from warm dust

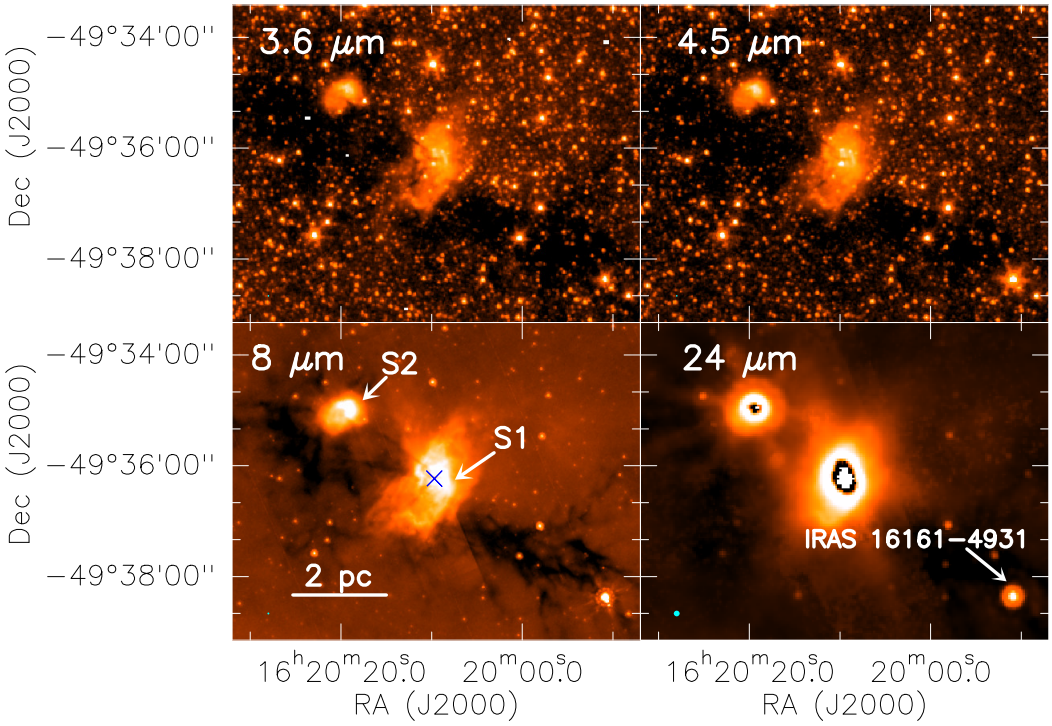

Figure 3.1: Mid-infrared emission from the IRDC G333.73 at 4 wavelength bands from *Spitzer*: 3.6, 4.5, 8.0 and 24.0 μm. The dark extinction filaments are clearly seen in the images. We have also marked the locations of two bright infrared sources S1 and S2 in the 8 μm image. The IRAS peak corresponding to S1 is indicated with a $\times$. The position of the IRAS source 16161-4931 is marked in the 24 μm image. The corresponding beam sizes are 1.7″, 1.7″, 2.0″ and 6.0″ and are shown (cyan) at the bottom left corner of all panels.

The mid-infrared maps of the filamentary IRDC G333.73 at 3.6, 4.5, 8.0 and 24 μm bands from *Spitzer Space Telescope* are shown in Fig. 3.1. Two prominent features visually discernible from the maps are the bright infrared objects that are designated as S1 and S2. S1 is also catalogued as an infrared bubble (MWP1G333726+003642; Simpson et al., 2012). These sources appear to be connected by dark filamentary structures silhouetted against nebulous emission. We have not been able to deduce any previously reported information about S2 from our literature survey. We proceed with the assumption that both these regions belong to the same IRDC and the kinematic distance towards S2 is the same as that of S1, that is 2.6 kpc. The assumption receives support from the molecular line study towards this region which is discussed in a later

section (Sect. 3.3). In the 24 μm image, S1 and S2 are bright and saturated towards the central regions. S1 is also identified as IRAS 16164–4929 indicated by a $\times$ symbol in the 8 μm map. In addition to S1 and S2, multiple point sources are also observed in the 24 μm map towards the IRDC elongation. A bright 24 μm source, associated with IRAS 16161–4931 is located towards the south-west of the IRDC filament. We discuss more about this source in Sect.3.6 .

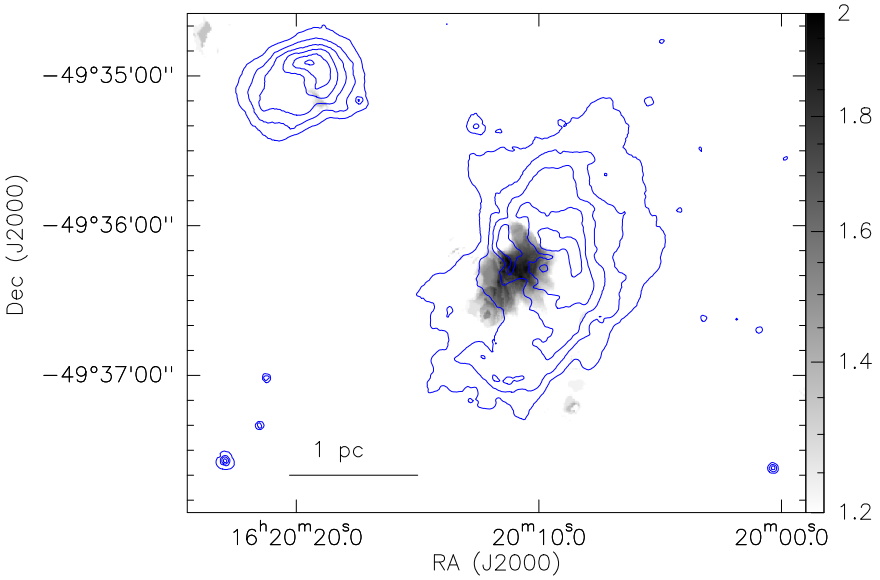

Figure 3.2: Flux ratio map of *Spitzer* [4.5]/[3.6] overlaid with 8 μm warm dust contours. The contour levels are 100, 200, 400, 800, 1600 and 3200 MJy/Sr.

The mid-infrared emission is mostly ascribed to small dust grains and could have contributions from (i) thermal emission from warm dust in the circumstellar envelope heated by direct stellar radiation, (ii) heating of dust due to Lyman-α photons resonantly scattering in the ionised region (Hoare et al., 1991), and (iii) emission due to excitation of polycyclic aromatic hydrocarbons (PAHs) by UV-photons in the photodissociation regions (PDRs, Battersby et al., 2011; Nandakumar et al., 2016). The emission in the 4.5 μm band is believed to be dominated by Brα (4.05 μm) line and molecular H_2 (4.69 μm) and CO emission (4.60 μm), that traces the shocked molecular gas in active protostellar outflows (Noriega-Crespo et al., 2004; Davis et al., 2007). As the point response functions (PRFs) of 4.5 and 3.6 μm bands are similar, we have constructed a ratio map of [4.5 μm]/[3.6 μm] to study the signatures of outflow within the region. The [4.5]/[3.6] ratio map towards S1 is presented in Fig. 3.2. It has been found that the [4.5]/[3.6] ratio is $\sim$1.5 or larger for jets and outflows whereas it is lower for stellar

sources ($\ll$1.5; Takami et al., 2010; Liu et al., 2013a). In our map, we notice excess [4.5]/[3.6] ratio towards S1, that is located $\sim$20$''$ east of the millimeter peak. If the large [4.5]/[3.6] does trace the distribution of shocked gas from the outflow, then it is possible that G333.73 harbours a protostellar outflow (or shocks/winds). We investigate this scenario further in Sect 3.3. where we examine emission from molecular gas.

3.2 Properties of cold dust emission

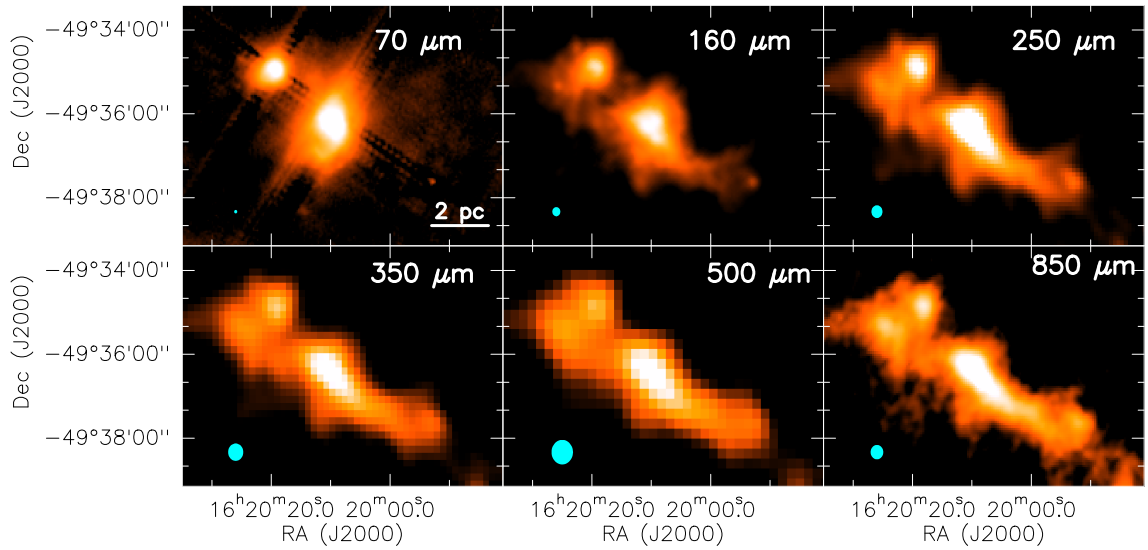

Figure 3.3: Distribution of cold dust emission towards the G333.73 region at 6 wavelength bands: 70, 160, 250, 350 and 500 μm from *Herschel* and 850 μm from APEX+Planck. The corresponding beam sizes (cyan) are shown towards bottom left of individual panels.

The cold dust emission towards the IRDC is examined using far-infrared and sub-millimeter maps at seven wavelength bands (70, 160, 250, 350, 500, 850 μm and 1.2 mm). The wavelength dependent variation of emission towards this region is apparent from the *Herschel* and APEX+Planck maps ($70 - 850$ μm), presented in Fig. 3.3. The cold dust emission maps exhibit a clumpy structure of the IRDC that spans a region $9'.3 \times 1'.9$, which corresponds to 7.2 pc $\times$ 1.5 pc. The 70 μm map is morphologically similar to that of the 24 μm warm dust emission. Unlike the longer wavelength emission maps, the resemblance of the 70 μm emission to the warm dust emission at 24 μm can be attributed to the fact that apart from the thermal emission due to cold dust, the emission at 70 μm also has contribution from very small dust grains (VSGs, Russeil

et al., 2013). The regions S1 and S2 appear to be connected by cold dust filaments as perceived from the longer wavelength emission maps.

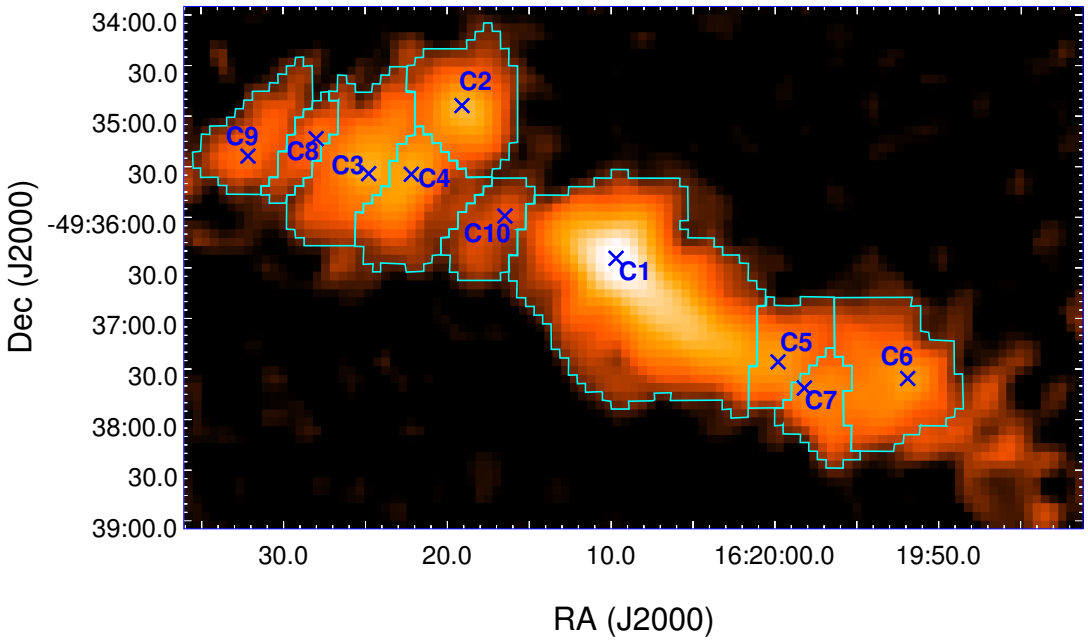

Figure 3.4: Distribution of cold dust emission towards the G333.73 region at 1.2 mm from SEST-SIMBA. The apertures of 10 millimeter clumps identified using the FellWalker algorithm are marked in cyan and the corresponding peak positions are denoted by $\times$ points.

A visual inspection of the 1.2 mm map shows that there are cold dust peaks towards this region in addition to the eight dust clumps identified by Beltrán et al. (2006). We have used the FellWalker algorithm (Berry, 2015) to identify clumps in this region. In the FellWalker algorithm, every pixel with a data value above a user-specified threshold is used as the start of a 'walk'. It then implements a gradient-tracing watershed scheme to identify local peaks and assigns a pixel to a peak that the local gradient point towards. We used a detection threshold of 5σ for identification of peaks and all the pixels outside the 5σ contour are considered as noise. We also set the parameter MinPix as 5 which excluded all clumps with pixels less than 5. Using this algorithm, we detected 10 clumps in G333.73. The peak positions of the clumps are shown in Fig. 3.4. These clumps are labelled as C1, C2...C10 in order of their decreasing peak brightness. Overplotted on the image are the apertures corresponding to the area covered by each clump using the FellWalker algorithm.

In order to characterise individual clumps that can be regarded as sites of local star formation, we have constructed their SEDs. This is achieved by integrating the flux densities within the clump apertures for the wavelengths: 70 μm to 1.2 mm. An average sky background, estimated from a nearby field that is $\sim 3.5'$ away (centred at $\alpha_{J2000} = 16^h\ 19^m51.36^s$,$\delta_{J2000} = -49^\circ\ 34'\ 53.5''$), and devoid of bright diffuse emission is appropriately subtracted to account for the zero offsets at each wavelength. We fitted the flux densities (F_ν) of the clumps using a modified blackbody function of the form (Gordon, 1987; Ward-Thompson & Robson, 1990):

$$F_\nu = \Omega B_\nu(T_\mathrm{d})(1 - e^{-\tau_\nu}) \tag{3.1}$$

where

$$\tau_\nu = \mu\, m_\mathrm{H}\, \kappa_\nu\, N(\mathrm{H}_2) \tag{3.2}$$

Here, Ω is the solid angle subtended by the clump, $B_\nu(T_\mathrm{d})$ is the blackbody function at dust temperature T_d, μ is the mean weight of molecular gas taken to be 2.86 assuming that the gas is 70% molecular hydrogen by mass (Ward-Thompson et al., 2010), m_H is the mass of hydrogen atom, κ_ν is the dust opacity and $N(\mathrm{H}_2)$ is the molecular hydrogen column density. The dust opacity is estimated using the expression (Ward-Thompson et al., 2010),

$$\kappa_\nu = 0.1 \left(\frac{\nu}{1000\,\mathrm{GHz}}\right)^\beta \tag{3.3}$$

where ν is the frequency and β is the dust emissivity index. We have assumed β = 2 in our analysis (Anderson et al., 2012; Russeil et al., 2013). The best fits were obtained using non-linear least squares Marquardt-Levenberg algorithm, considering T_d and $N(\mathrm{H}_2)$ as free parameters. We have assumed a flux density uncertainty of 15% in all bands (Beltrán et al., 2006; Schuller et al., 2009; Launhardt et al., 2013). We find that the fits that include the 70 μm show larger χ^2_{red} (upto a factor of 3) as well as larger errors in the parameters (upto 60%) when compared to fits carried out by excluding the 70 μm flux densities. This is evident from the fits to the SEDs displayed in Fig. 3.5. It is evident that the 70 μm point exhibits excess emission. Such excess has been observed

in other star forming clouds and has been attributed to the contribution from transiently heated very small grains (e.g., Shetty et al., 2009; Compiègne et al., 2010; Russeil et al., 2013) and its inclusion could overestimate the dust temperature. We proceed with the parameters of fits that exclude the 70 μm emission as this characterises the cold dust in the IRDC. The values of the derived parameters for all the clumps are listed in Table 3.1. We also note that the ground-based SEST-SIMBA observations failed to pick up large scale diffuse emission at low flux levels owing to poor sensitivity. Clump 10, being the faintest of all the clumps, has relatively lower flux at 1.2 mm compared to the other bands (Fig. 3.5). We have, therefore, excluded this 1.2 mm data point from the SED fit in order to get more robust estimate of parameters for this clump.

Table 3.1: Dust clumps identified in this region.

Clump	$\alpha_{\rm J2000}$	$\delta_{\rm J2000}$	Area	Temperature	Column density	χ^2_{red}	Mass	Σ
	(^{h} ^{m} ^{s})	($^\circ$ $'$ $''$)	(pc^2)	(K)	(10^{22} cm^{-2})		(M$_\odot$)	(g cm^{-2})
C1	16:20:09.693	−49:36:24.99	2.3	20.8 ± 1.7	2.8 ± 0.6	2.4	1530	0.1
C2	16:20:19.091	−49:34:53.54	0.6	22.3 ± 1.9	1.9 ± 0.6	4.0	266	0.1
C3	16:20:24.837	−49:35:34.14	0.6	16.1 ± 3.2	3.2 ± 0.9	4.8	456	0.2
C4	16:20:22.226	−49:35:34.16	0.6	16.4 ± 1.4	2.9 ± 0.9	5.8	420	0.2
C5	16:20:00.287	−49:37:25.91	0.4	15.1 ± 1.1	3.7 ± 0.9	4.2	350	0.2
C6	16:19:51.925	−49:37:36.01	0.7	14.3 ± 1.2	3.7 ± 0.1	7.2	612	0.2
C7	16:19:58.196	−49:37:41.13	0.3	15.6 ± 1.4	2.5 ± 0.8	6.1	180	0.1
C8	16:20:27.990	−49:35:13.52	0.2	15.9 ± 1.5	1.8 ± 0.6	7.1	87	0.1
C9	16:20:32.144	−49:35:23.76	0.5	16.4 ± 1.4	3.8 ± 1.1	5.4	451	0.2
C10	16:20:16.481	−49:35:59.42	0.3	15.1 ± 0.7	4.9 ± 0.9	1.5	353	0.3

The temperature in the clumps lie in the range: $14.3 - 22.3$ K whereas the column density values lie between $1.8 - 4.9 \times 10^{22}$ cm^{-2}. Clump C2 exhibits highest dust temperature whereas the clump C10 possesses the highest column density. Note that these estimates represent average values over the entire clump. We have also used the column densities of the clumps to estimate their masses (M_c), using the following expression:

$$M_c = N(\mathrm{H_2})\, \mu\, m_{\rm H}\, A \tag{3.4}$$

Here A represents the physical area of the clump. The clump masses lie in the range

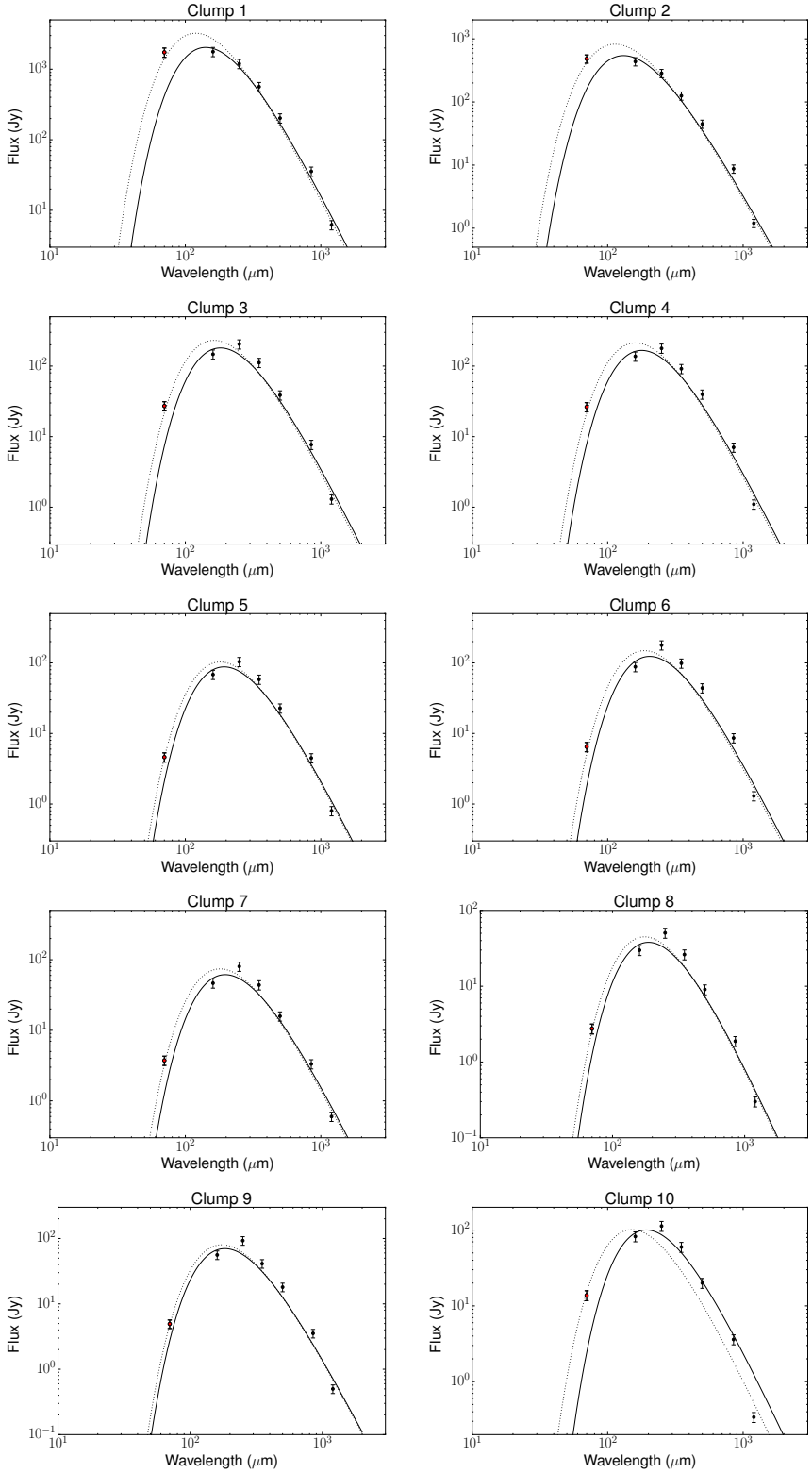

Figure 3.5: SEDs of the cold dust clumps in G333.73. Flux densities from 160 μm $-$ 1.2 mm are represented as solid circles and 70 μm flux is represented as red dot. The best-fit modified blackbody function for each SED excluding 70 μm is shown as a solid line curve and the fit including 70 μm flux is shown as dotted line. The error bars correspond to 15% uncertainties in flux densities.

$87 - 1530$ $M_\odot$. The total cloud mass is estimated to be $\sim$4700 $M_\odot$. This is nearly ~ 5 times larger than the 992 $M_\odot$ obtained by Beltrán et al. (2006). This difference could be attributed to the following: (i) our estimate of cloud mass is based on the modified blackbody fits using 6 far-infrared wavelength bands unlike the latter obtained from only the 1.2 mm map, and (ii) Beltrán et al. (2006) used a value of dust opacity $\kappa_\nu \sim 1$ cm^{2}g^{-1} at 1.2 mm, whereas we have used a different form of dust opacity law whose value depends on β. Note that $\beta = 2$ leads to $\kappa_\nu \sim 0.6$ cm^{2}g^{-1} at 1.2 mm.

We have also estimated the surface density (Σ) of the individual clumps, defined as M_c/A, a parameter that can be used to probe massive star formation in the clumps. According to Krumholz & McKee (2008), clouds with a minimum surface density of $\Sigma \sim$1 g cm^{-2} would be able to form massive stars by suppressing fragmentation. The surface density values for clumps in G333.73 are listed in Table 3.1. The values of Σ for the ten clumps lie in the range $0.1 - 0.3$ g cm^{-2}. The maximum Σ is observed towards clump C10 that also displays the largest column density among clumps. Observational studies towards a large sample of massive star forming cores, such as those by López-Sepulcre et al. (2010), Miettinen & Harju (2010) and Giannetti et al. (2013) have shown that massive star forming cores possess lower surface densities of the order of $\sim$0.2 g cm^{-2}. According to this latter gauge, six of our clumps have the potential to form massive stars. This is substantiated by our assertion that the surface density value of a clump represents a sort of average, and the actual surface density could be higher near the peak emission or dense core considering that the size of clumps are large (> 0.6 pc).

3.2.1 Maps of Column density and Dust Temperature

In addition to the clump SEDs, we have constructed the line-of-sight averaged molecular hydrogen column density and dust temperature maps of this region with the intention of understanding the small scale variations across the IRDC, in addition to comparing this with molecular line emission maps. The maps are created by carrying out a pixel-by-pixel greybody fit in the selected wavelength regime (160 μm-1.2 mm) using the equations discussed earlier. If we consider all the wavelengths, the resolution of the map is limited by emission at the wavelength that has the lowest resolution, i.e. 36.4$''$ at 500 μm. As the longer wavelength data is well sampled, we prefer to construct

higher resolution maps. To achieve this, we excluded the 500 μm image from the analysis. First, the flux units of the remaining maps are converted to Jy/pixel using the task 'Convert Image Unit'. As the pixel scales and beam sizes are different in different bands, the maps are projected to a common Nyquist-sampled pixel grid with a common pixel size and resolution. The plug-in 'ConvolvePhotometric' is used for this purpose. The convolution is performed using azimuthally averaged $Herschel$ convolution kernels provided by Aniano et al. (2011). For the convolution of 850 μm and 1.2 mm maps, we used a Gaussian convolution kernel. The final maps have a pixel size and resolution of 350 μm i.e.,10$''$ and 25$''$ respectively. The relation between the extended large-scale emission of the final $Herschel$ maps and the absolute flux levels of the background are not understood clearly. This background mostly comprises of the cosmic microwave background and the diffuse Galactic background. In order to remove the contribution of the background emission, background subtraction is performed on the $Herschel$ images. We are unable to sample the diffuse emission extending beyond the high density regions owing to poorer sensitivity of 1.2 mm map compared to $Herschel$ and ATLASGAL+Planck maps. For these pixels, the values of $\chi^2_{\rm red}$ are larger. To obtain better fits, the pixels with $\chi^2_{\rm red}$ >2 due to noisy 1.2 mm emission, were fitted anew by excluding the 1.2 mm data point from the SED fit.

The dust temperature, column density and reduced chi-square ($\chi^2_{\rm red}$) maps are presented in Fig. 3.6. For further analysis, we have considered pixels within the 5σ contour of 1.2 mm map. The peak column density is 5.5×10^{22} cm^{-2} whereas the mean column density is 2.4×10^{22} cm^{-2}. The column density distribution is clumpy in nature exhibiting multiple peaks. The temperature within the IRDC ranges from $14.8 - 25.4$ K with a mean value of 18 K. The temperature map peaks towards the location of S1. The temperature map also reveals an additional peak that matches with the location of S2. These temperature peaks can be understood based on the morphology of 160 μm emission. The 160 μm emission is the shortest wavelength used in the SED construction and traces the warmest dust emission components. Hence, pixels with significant emission at 160 μm is weighted by the corresponding flux density leading to a higher dust temperature that signifies higher levels of star formation activity here. The low values of dust temperature are observed towards the dark filaments in the 8 μm map.

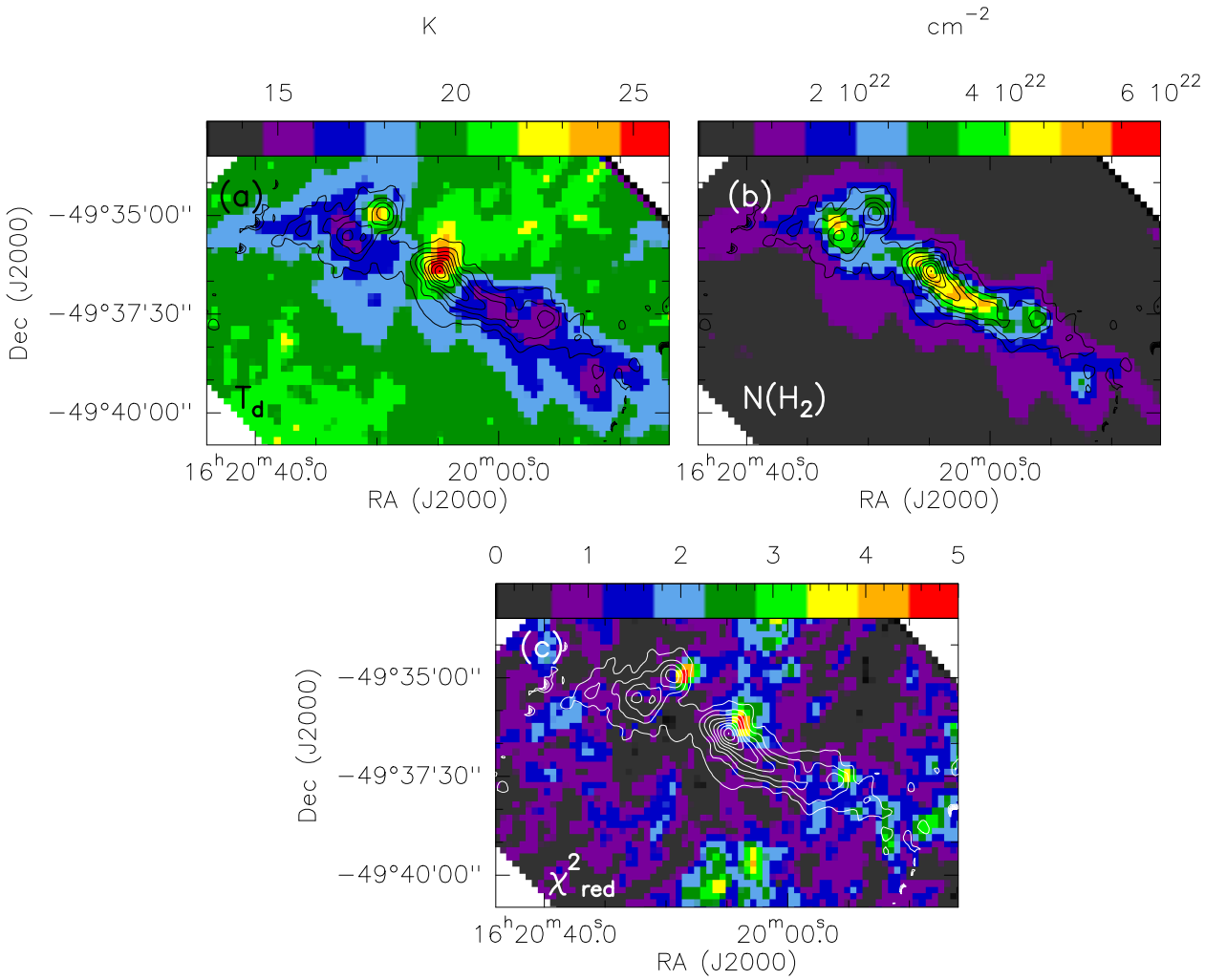

Figure 3.6: (a) Dust temperature (T_d) (b) column density ($N(H_2)$) and (c) reduced chi-square (χ^2_{red}) maps of G333.73 region obtained from the modified blackbody fit towards individual pixels overlaid with 1.2 mm cold dust contours. The contour levels are from 75 mJy/beam to 1200 mJy/beam in steps of 100 mJy/beam.

3.2.2 Extinction maps

An examination of the 8 μm image shows the presence of high extinction filamentary structures in this region. To get an idea of the extinction within the IRDC and thereby study in detail the properties of high density filaments, we have constructed a visual extinction map (A_v) of this region using emission at 8 μm. We followed the procedure described by (Vig et al., 2007) to construct the A_v map. For this, we have initially estimated the optical depth at 8μm (τ_8) in this region using the expression

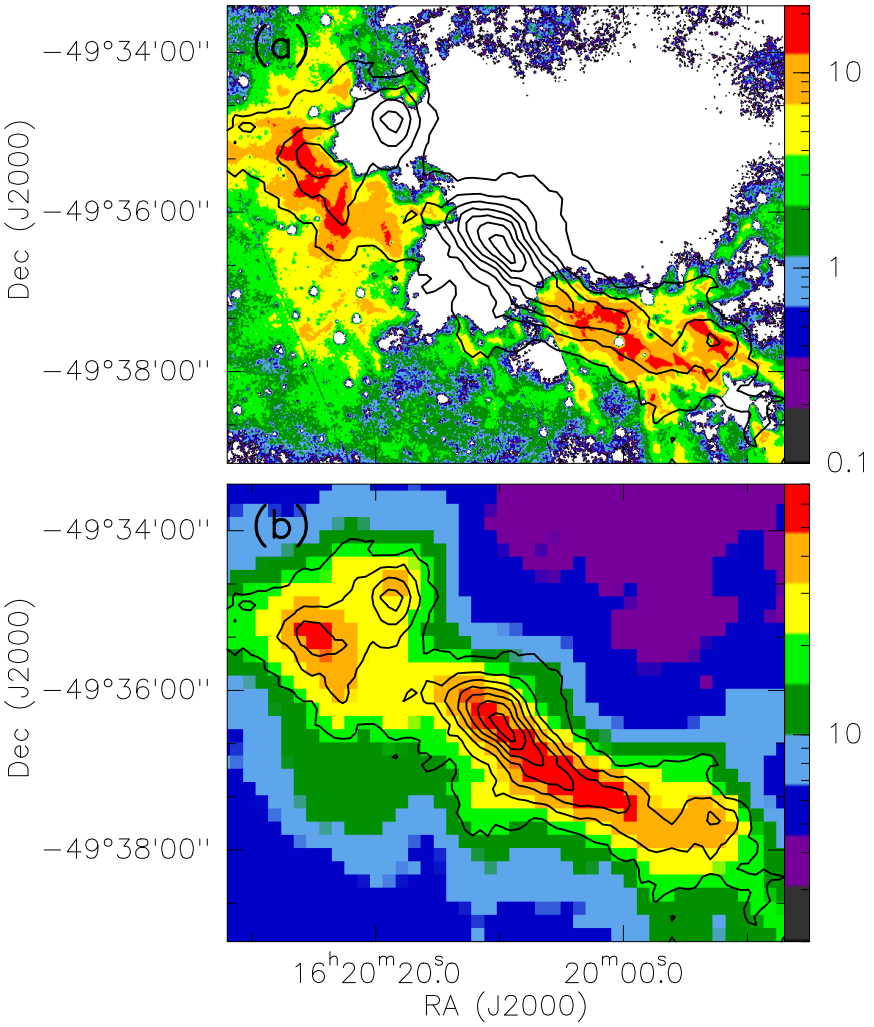

Figure 3.7: Visual extinction (A_v) maps of G333.73 region obtained by (a) estimating the visual extinction from 8 μm dust opacity. (b) conversion of column density map to visual extinction map. Contours represent the 870 μm cold dust emission where the levels are from 0.2 to 2.2 Jy/beam in steps of 0.3 Jy/beam.

$$I = I_0\, e^{-\tau_8} \tag{3.5}$$

where I_0 is the background intensity (estimated near the IRDC) and I is the observed intensity. As I_0 is found to vary across the image, we have assumed a different I_0 for each pixel as follows. A median filter image has been constructed using a window size of 199 pixels ($2'$). Using the median value at the corresponding pixel as I_0 we have estimated τ_8. This has been converted to A_v using the relation A_v/τ_8=22.5 (Vig et al., 2007), and a visual extinction map has been created. We have masked all the pixels

where the pixel value is higher than the median value towards that particular pixel. The resultant map is shown in Fig. 3.7(a). The resolution of this extinction map is $2''$. The extinction within the IRDC ranges from 5-20 A_v. Since S1 and S2 are bright in 8 μm, the pixels corresponding to these regions are masked in the extinction map. The high extinction regions coincide with the cold dust emission contours, but with finer structures that extend to low levels of emission.

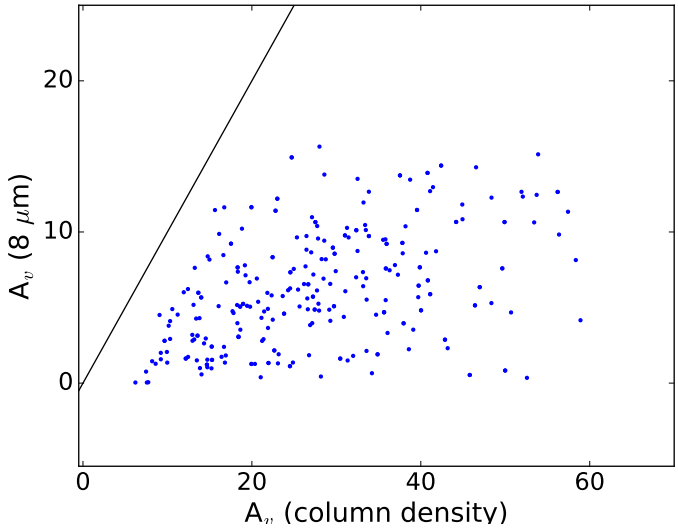

Figure 3.8: Comparison of visual extinction values obtained from 8 μm map and column density map. Line of unit slope is also shown in the plot.

Another method to estimate the extinction within a region is to directly convert the column density to corresponding A_v. For this, we have used the column density map constructed using the far-infared and submillimeter data. We have used the relation A_v = $N(\mathrm{H})/2.21 \times 10^{21}$ (Güver & Özel, 2009) to generate the extinction map from the column density map. The A_v map is shown in Fig. 3.7(b). The resolution of extinction map is same as that of column density map, which is $25''$. The range of visual extinction within the IRDC is higher (8-62 A_v) than that obtained using the other method. The morphology of extinction filaments is similar in both these maps. The major advantage of the second method is that we are able to sample the extinction towards S1 and S2. The A_v is $\sim$55 mag towards S1 whereas it is $\sim$34 mag towards S2.

We have compared the two extinction maps of this region. For this we have first convolved and regridded the 8 μm map to the resolution and pixel size of the column density map. We have then proceeded with the method described in the first paragraph

of this section to construct a low resolution visual extinction map. For the comparison, we have considered all pixels which are within the 5σ contour of 1.2 mm emission. Fig. 3.8 shows the comparison between A_v (8 μm) and A_v (column density). The A_v (8 μm) values are lower than A_v (column density). This could be attributed to the fact that the extinction values obtained from the 8 μm map image are lower limits. This is because in Equation 3.5, we assume the emitting dust is behind the high extinction filaments. However, this may not represent the actual case and there could be considerable mid-infrared emission from S1 and S2. Moreover, this IRDC is located in the Galactic plane at a heliocentric distance of 2.6 kpc. Hence, the derived A_v values at 8 μm serve as underestimates.

3.3 Molecular line emission from G333.73

The kinematics and chemistry of IRDCs can be investigated using molecular line emission. For the IRDC G333.73, we use molecular line data from the MALT90 pilot survey that covers a region of size $\sim 4'$ centred on S1 in clump C1. Six molecular species have been detected towards this region: HCO^+, $H^{13}CO^+$, HCN, HNC, N_2H^+ and C_2H. The spectra of these molecules at the location of emission peak of HCO^+ are shown in Fig. 3.9. The LSR velocity of the region (hence IRDC) is estimated using a single transition of $H^{13}CO^+$ assuming the line to be optically thin. We have fitted a single Gaussian profile to the spectrum and determined the LSR velocity to be -33.2 km s^{-1}. This is consistent with the LSR velocity of -33.0 km s^{-1} estimated from the CS(2-1) line (Bronfman et al., 1996). The hyperfine components of HCN and N_2H^+ molecules are clearly discerned in the velocity profiles. HCN has 3 hyperfine components which are well separated (+5 and -7 km s^{-1} with respect to LSR velocity respectively). N_2H^+ has 7 hyperfine components. The profiles of HCO^+ and HNC lines exhibit a blue asymmetric feature characterized by self-absorption dips in the lines, with relatively strong blue peaks with respect to red peaks. We explore the likely origin of the asymmetric profile in the next section.

As the MALT90 survey has limited coverage, we are unable to sample the molecular gas kinematics of the entire IRDC filament. We, therefore, utilise the ^{12}CO and ^{13}CO data from ThrUMMS survey for this purpose. The CO spectrum towards the peak

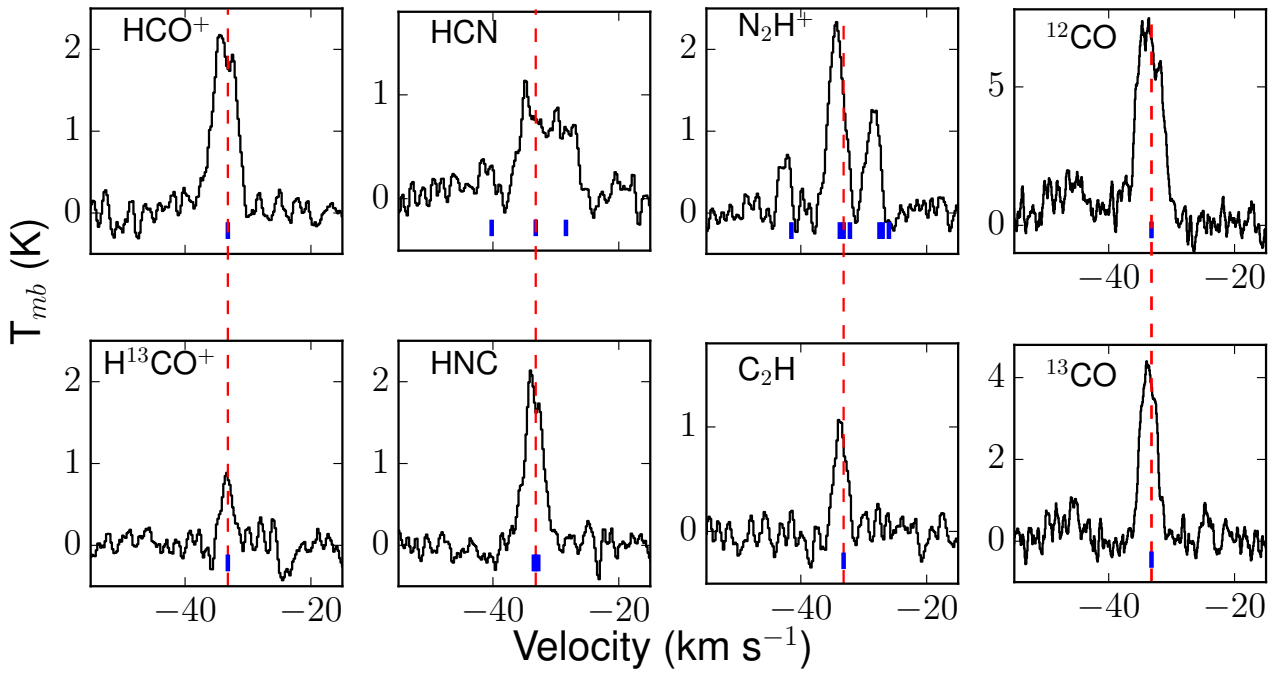

Figure 3.9: The spectra of 8 molecular lines towards the HCO^+ peak position smoothed to a velocity smoothing of 0.4 km s^{-1}. The LSR velocity of the cloud is estimated from $H^{13}CO^+$ line as -33.2 km s^{-1}, indicated by a red dashed line in all the six panels. The hyperfine components of each species are marked as blue lines in individual panels. The velocities of hyperfine components are estimated assuming an LSR velocity of -33.2 km s^{-1}.

position of HCO^+ emission is shown in Fig. 3.9 (last column). This spectrum exhibits blue asymmetric profiles similar to those of HCO^+ and HNC. The distribution of CO emission with respect to warm dust emission is shown in Fig. 3.10. From the maps, it is evident that the CO emission extends well beyond the apparently dark filamentary structure. This is in accordance with expectations as the ^{12}CO and ^{13}CO lines being low density tracers, also sample the diffuse envelope.

3.3.1 Blue asymmetry of HCO^+ and HNC profiles

The HCO^+ line is optically thick based on the expected ratio of line intensties of HCO^+ and $H^{13}CO^+$. Similarly, we proceed with the supposition that HNC is optically thick. Although both display a double peaked structure, HCO^+ is a single transition line whereas HNC has three hyperfine components within 0.5 km s^{-1}, marked in Fig 3.9.

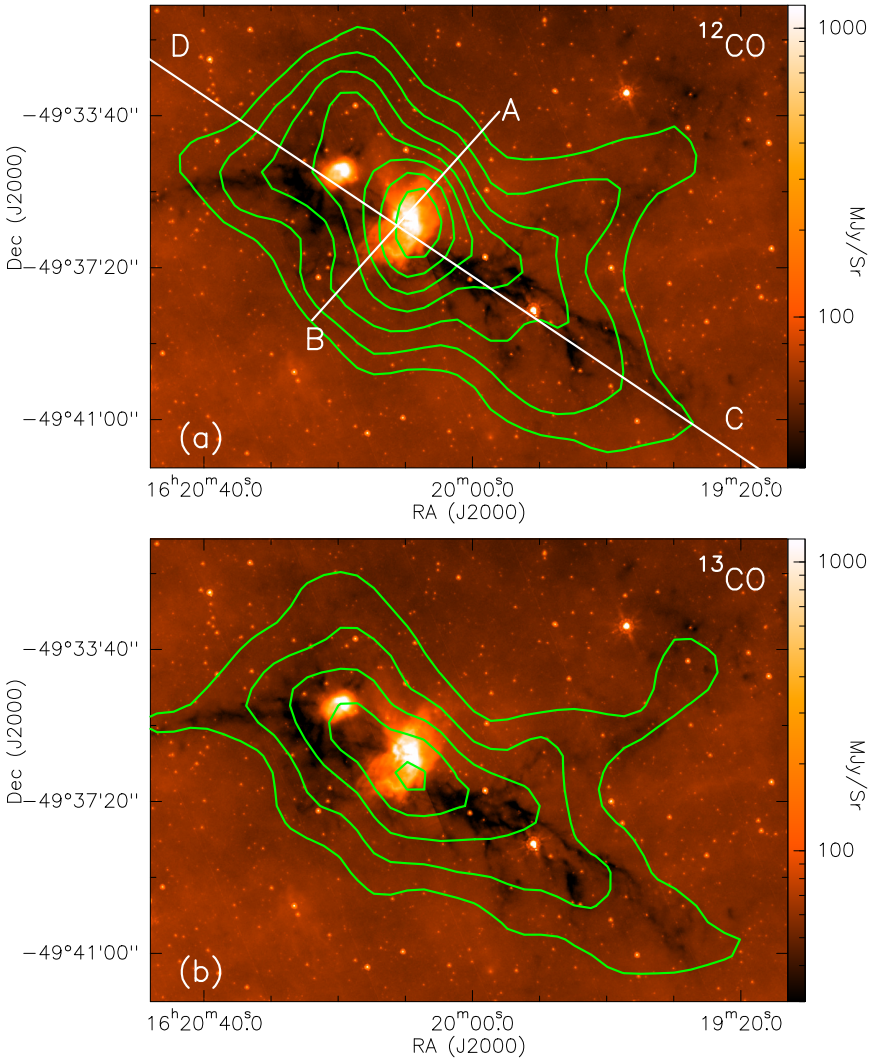

Figure 3.10: *Spitzer* 8 μm map overlaid with (a)^{12}CO and (b) ^{13}CO contours. Contour levels for (a) are 13 to 35 K km s^{-1} in steps of 3.1 K km s^{-1} and for (b), 4.5 to 15 K km s^{-1} in steps of 2.1 K km s^{-1}. Lines AB and CD are the lines along which PV diagrams are constructed.

These lines are considered as good infall and outflow tracers. An examination of the HCO$^+$ and HNC velocity profiles show that they exhibit significant blue asymmetry in their profiles indicative of infall in this region (Miettinen, 2012; Jin et al., 2016). Blue asymmetry could also arise from rotation and outflow (e.g., Redman et al., 2004). The velocity of the absorption dip agrees well with that of the LSR velocity estimated from the H^{13}CO$^+$ line. The velocities of the blue shifted peaks of the HCO$^+$ and HNC lines relative to the LSR velocity are -0.9 km s^{-1} and -0.8 km s^{-1}, respectively. Similarly, the velocities of the red shifted peaks with respect to the LSR velocity are 1.0 km s^{-1} and 0.8 km s^{-1}, respectively. These values indicate that the red and blue peaks are quite

symmetric with respect to the LSR velocity.

We next scrutinise the intensities, and to quantify the blue-skewed profile, we have used the asymmetry parameter δV. This is defined as the difference between the peak velocities of optically thick line, $V_{\rm thick}$ (of HCO^+/HNC in our case), and optically thin line, $V_{\rm thin}$ (of $H^{13}CO^+$), divided by the FWHM of the optically thin line represented as ΔV (Yu & Wang, 2013):

$$\delta \mathrm{V} = \frac{V_{\rm thick} - V_{\rm thin}}{\Delta V_{\rm thin}}$$

Using $\mathrm{V_{thin}}$ as -33.2 km s^{-1} and $\Delta \mathrm{V_{thin}}$ as 2.2 km s^{-1} from the Gaussian fit to the $H^{13}CO^+$ profile, we obtain δV as -0.4 for both the lines. This is characterised as a blue profile according to the criterion of Mardones et al. (1997), who use $\delta V < -0.25$ to assign a profile as blue.

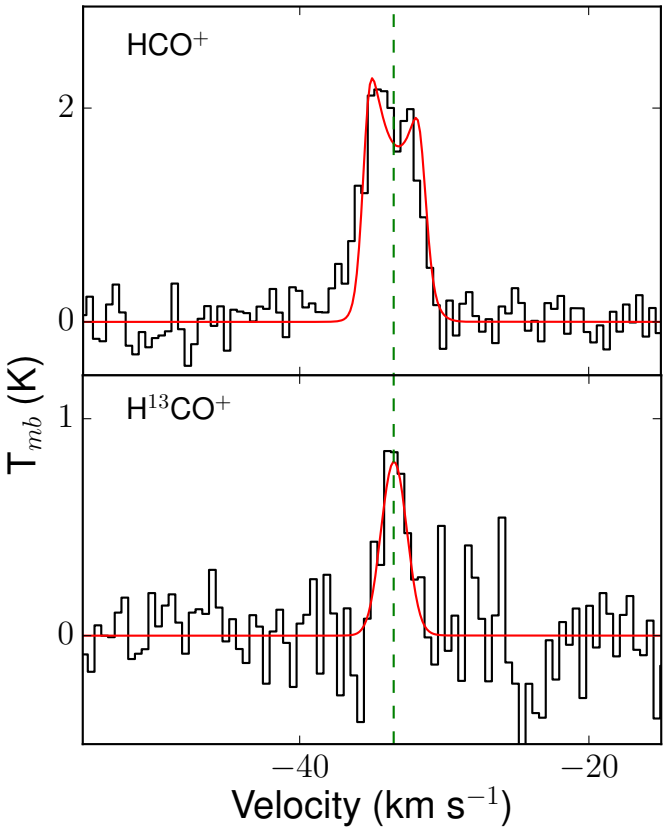

Figure 3.11: Spectrum towards the peak of HCO^+ and $H^{13}CO^+$ emission. The red line represents the best-fit model using the two-layer infall process for optically thick HCO^+ line and its optically thin isotopologue $H^{13}CO^+$ line. The dashed line (green) indicates the LSR velocity of -33.2 km s^{-1}.

3.3.2 HCO^+ line profile analysis using LTE modelling

To study the likely mechanisms responsible for the observed blue asymmetry in the HCO^+ line, we carried out a two-component LTE modelling in CASSIS software (Caux et al., 2011). For the modelling, we considered the HCO^+ line as well as its isotopologue, $H^{13}CO^+$. The observed self-absorbed profile of HCO^+ line can be explained if we use a two-layer model where there is a warm emitting component and a cold absorbing component. For a better signal-to-noise ratio, we have integrated the emission within $20''$ of the HCO^+ peak for both HCO^+ and $H^{13}CO^+$ lines. The best fit to the profiles is obtained by varying the parameters such as linewidth, V_{LSR}, excitation temperature, column density and source size. The $[HCO^+]/[H^{13}CO^+]$ abundance ratio is assumed as 50 (Purcell et al., 2006). The fitted spectrum is shown in Fig. 3.11 and the results of the radiative analysis are presented in Table 3.2. The characteristics of the two components are: a warm component has an excitation temperature of 31.1 K and column density of 1.6×10^{15} cm^{-2}, while the cold, absorbing component has lower excitation temperature (7.1 K) and column density (2.0×10^{13} cm^{-2}). The velocity of the cold component is red shifted by 0.4 km s^{-1} with respect to the warm component. This could be construed as cold molecular gas in the outer envelope receding towards the inner warmer regions and interpreted as protostellar infall. The overall blue asymmetric profile fits well using LTE modelling although we see some additional red and blue components that cannot be explained through the infall scenario alone (see Fig. 3.12). These additional peaks require multiple components suggesting the presence of small scale outflows in the region. Observations with better spatial resolution and sensitivity are essential to enhance our understanding of the profiles.

3.3.3 Mass infall rate

Considering that the blue asymmetry of HCO^+ and HNC lines suggests protostellar infall, the mass infall rate ($\dot{M}_{inf}$) of the circumstellar envelope can be estimated using the expression: $\dot{M}_{inf} = 4\pi R^2 V_{inf} \rho$ (López-Sepulcre et al., 2010), where $V_{inf} = V_{thin} - V_{thick} = V_{H^{13}CO^+} - V_{HCO^+}$ is an estimate of the infall velocity, $\rho = M/(4/3\,\pi R^3)$ is the average clump volume density and R is the radius of the clump, calculated using the dust continuum emission. We estimate V_{inf} as 0.9 km s^{-1} and M$\sim$1530 $M_\odot$ and

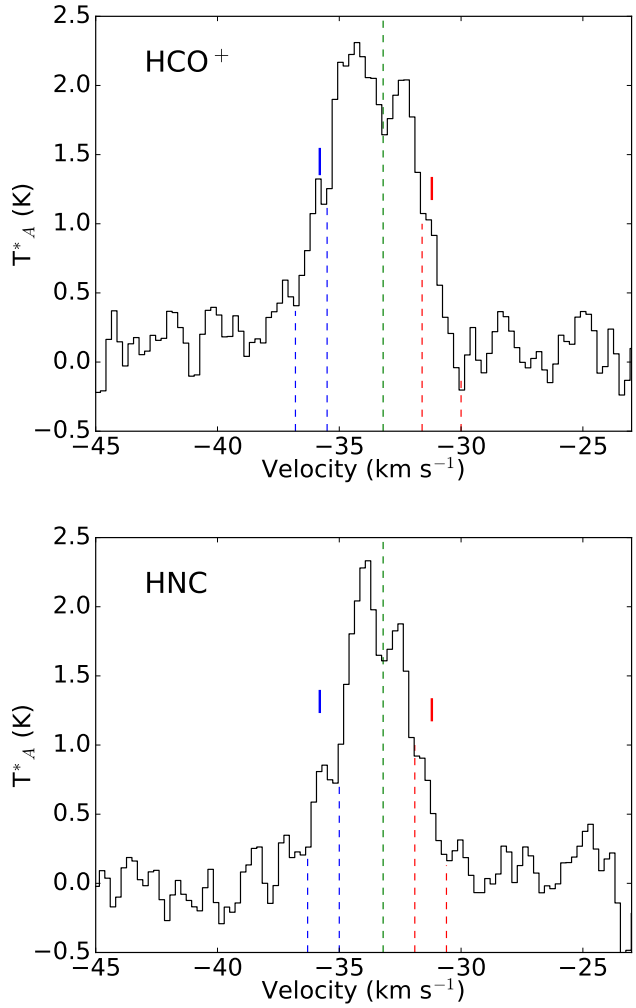

Figure 3.12: Spectrum of HCO^+ and HNC molecules towards peak emission. Location of blue and red wings seen towards both the spectra are indicated with solid lines.

R$\sim$0.9 pc for clump C1 and we obtain $\dot{M}_{inf}$ as 4.7×10^{-3} $M_\odot$ yr^{-1}. This is in congruence with that estimated towards other infall candidates. For example López-Sepulcre et al. (2010) obtained infall rates ranging from $10^{-3} - 10^{-1}$ $M_\odot$ yr^{-1} for a sample of high mass star forming clumps. He et al. (2015) inferred median mass infall rates of $7 - 8 \times 10^{-3}$ $M_\odot$ yr^{-1} for pre-stellar, proto-stellar and ultracompact H II region stages from their sample of massive star forming regions. They concluded that the infall rate is independent of the evolutionary stage.

Table 3.2: Best fit parameters for the two layer infall model.

Parameter	Component 1	Component 2
Column density (10^{14} cm^{-2})	16.1 ± 2.7	0.2 ± 0.03
T_{ex} (K)	31.1 ± 0.5	7.1 ± 0.5
FWHM (km s^{-1})	1.9 ± 0.1	2.8 ± 0.2
Size ($''$)	23.7 ± 1.4	31.1 ± 4.1
V_{LSR} (km s^{-1})	-33.4 ± 0.1	-33.0 ± 0.1

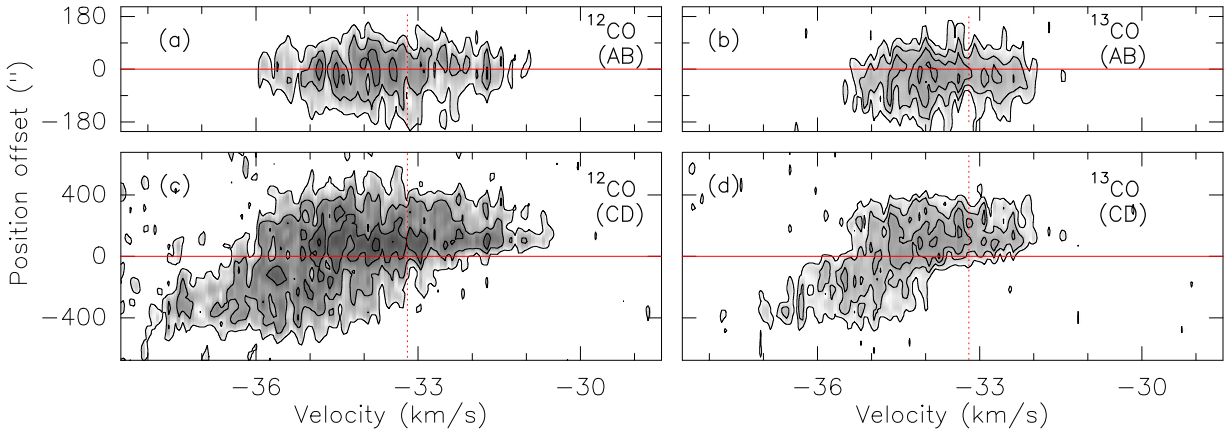

Figure 3.13: Position-velocity diagrams of ^{12}CO and ^{13}CO molecules. (a) and (b) are along the cut AB shown in Fig. 3.10(a) and (c) and (d) along CD shown in Fig. 3.10(a). Solid line marks the location of zero offset and dashed line denotes the LSR velocity.

3.3.4 Velocity structure of the cloud

The position-velocity (PV) diagram serves as useful tool to understand the large scale kinematics of a region. The PV diagrams of ^{12}CO and ^{13}CO are constructed along two directions: (i) AB, perpendicular to the long-axis of the cloud (P.A=47.3°) and (ii) CD, that is parallel to the IRDC long axis (P.A=134.2°). These directions are shown in Fig. 3.10(a). The PV plots are presented in Fig. 3.13. The zero offset in the PV diagrams corresponds to the position $\alpha_{J2000} = 16^h\ 20^m 10.7^s$ and $\delta_{J2000} = -49^\circ\ 36'\ 18.8''$. Along AB towards the centre position, the blue and red components are clearly visible in both species, with the blue component brighter than red, suggesting infall. Along

CD, we observe a velocity gradient from C to D (i.e. south-west to north-east). The overall velocity gradient is approximately 5 km s^{-1} in magnitude, spanning a region of 10′ from west to east i.e. 0.7 km s^{-1} pc^{-1}. We also detect few additional substructures in velocity, evident from the ^{13}CO velocity map shown in Fig. 3.14. Velocity gradients of this nature have been observed in other star forming regions. For example, Sokolov et al. (2017) find a velocity gradient of 0.2 km s^{-1} pc^{-1} in the IRDC filament G035.39-00.33 of length 6 pc. From their study towards a sample of 54 filaments in the northern Galactic plane, Wang et al. (2016) estimate a mean velocity gradient of 0.4 km s^{-1} pc^{-1} towards the filaments. The systematic velocity gradient observed in the IRDC studied here could hint at the rotation and/or accretion flows along the cloud. This is explored in detail in Sect.3.11.

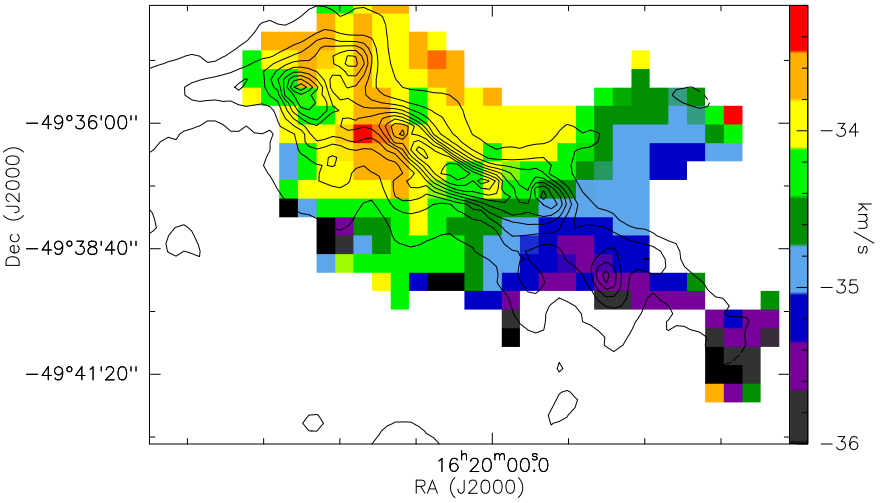

Figure 3.14: Velocity (first moment) map of ^{13}CO line overlaid with column density contours. The contour levels are from 1×10^{22} cm^{-2} to 6×10^{22} cm^{-2} in steps of 7.3×10^{21} cm^{-2}.

3.3.5 Intensity distribution of molecular gas

In this section, we examine the morphology of the molecular line emission associated with the IRDC. The distribution of CO is apparent from Fig. 3.10 while Fig. 3.15 shows the integrated intensity (zeroth moment) maps of the six molecular species from MALT90 survey. The peak of the molecular line emission appears shifted towards the south of the column density peak (estimated from dust continuum emission) by $\sim 15''$ (within Clump C1). This could be attributed to resolution effects as the beam size of

the molecular gas emission is nearly three times larger than that of dust continuum emission. Besides, the role of optical depth effects cannot be ruled out. The detailed properties of individual species are discussed below.

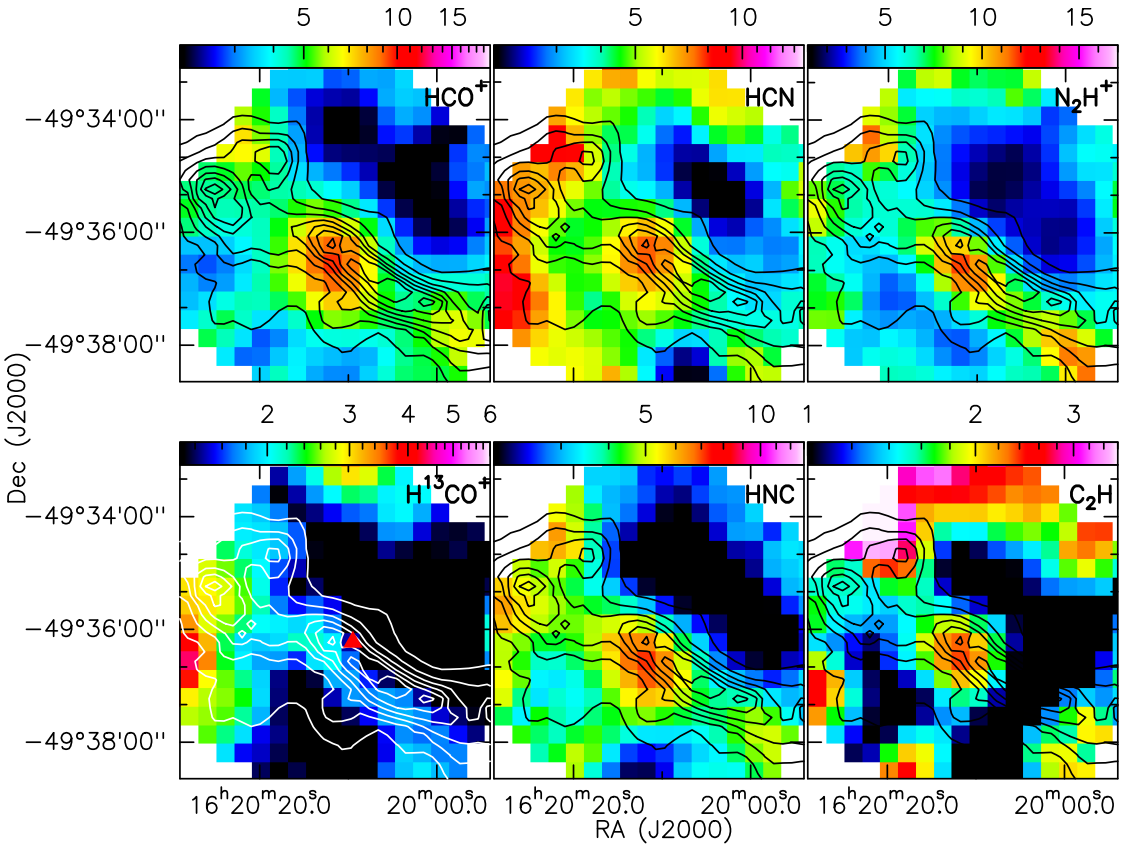

Figure 3.15: Integrated intensity maps of 6 molecular lines (labelled in the top right corners) detected towards G333.73 overlaid with column density contours. The contour levels are from 1×10^{22} cm^{-2} to 6×10^{22} cm^{-2} in steps of 7.3×10^{21} cm^{-2}. We show the integrated intensity maps of HCO^+ (V=$[-38.5, -29.5]$ km s^{-1}, $H^{13}CO^+$ (V=$[-35.5, -30.7]$ km s^{-1}, HCN (V=$[-37.7, -23.9]$ km s^{-1}, HNC (V=$[-38.5, -29.0]$ km s^{-1}, N_2H^+ (V=$[-44.5, -25.2]$ km s^{-1} and C_2H (V=$[-36.3, -31.5]$ km s^{-1}. The colour intensity scale is in units of K km s^{-1}. Triangle in panel 4 ($H^{13}CO^+$) corresponds to IRAS peak position.

^{12}CO and ^{13}CO (Carbon monoxide)

CO is the most easily observed molecular line in the interstellar medium and is present even in fairly tenuous gas (Dame et al., 2001). Generally, the ^{12}CO line is optically thick and ^{13}CO being relatively optically thin, can trace higher density gas ($n_{\rm H2} > 10^3$ cm^{-3}) in molecular clouds. In the present case, ^{13}CO is also optically thick as evident from Fig. 3.9. The distribution of ^{12}CO and ^{13}CO emission in G333.73 is shown in Fig. 3.10 and displays elongated morphology consistent with cold dust emission and column density maps. The aspect ratio of ^{13}CO ($\sim$5) is more than twice that of ^{12}CO ($\sim$2). Moreover, the ^{12}CO emission towards S2 is extended compared to ^{13}CO. This could be due to the fact that ^{12}CO is a low density gas tracer compared to the latter and hence traces the extended envelope surrounding the dense gas. We also see an extension towards the north-west in both the CO maps that overlaps with an extinction filament in the warm dust emission.

HCO$^+$ and H^{13}CO$^+$ (Formylium)

The HCO$^+$ ion is mainly formed through the gas-phase ion-neutral interaction $\mathrm{H_3^+ + CO \rightarrow HCO^+ + H_2}$ (Herbst & Klemperer, 1973). Studies of Sanhueza et al. (2012) and Hoq et al. (2013) suggests that HCO$^+$ abundance increases as a function of evolution. HCO$^+$ abundance is also found to increase in regions where shocks are generated (Miettinen, 2014). The HCO$^+$ ion has been used to investigate the infall and outfall motions (e.g., Codella et al., 2001; Fuller et al., 2005; Cyganowski et al., 2011) and hence, the HCO$^+$ $J = 1 - 0$ is believed to be a good tracer of kinematics in star forming regions (e.g., Sun & Gao, 2009; Rygl et al., 2013). However, this transition could be optically thick as a result of contributions from various mechanisms and gas motions within the clumps. Consequently, higher transitions of HCN, HNC and HCO$^+$ have been suggested as more favourable infall tracers (Chira et al., 2014).

HCO$^+$ is detected close to the peak of the cold dust emission and the distribution is nearly spherical (see Fig. 3.15). Weak HCO$^+$ emission is detected towards the other millimeter peaks of the IRDC (C2, C7) within the sampled region. The formation mechanism of H^{13}CO$^+$ is similar to that of HCO$^+$ except there is ^{13}C instead of ^{12}C. It can also form via the isotope transfer process $\mathrm{HCO^+ + {}^{13}CO \leftrightarrow H^{13}CO^+ + {}^{12}CO}$

(Langer et al., 1984). $H^{13}CO^+$ is a high density tracer and is generally assumed to be optically thin. The distribution of $H^{13}CO^+$ is morphologically different as compared to the HCO^+ emission and we discern that the intensity is relatively weak towards the peak location of other molecular species such as HCO^+. This is a region where most of the ionised gas emission is distributed. The lower intensity of $H^{13}CO^+$ emission towards S1 could be attributed to the destruction of this species by UV radiation and high density electrons as the abundance of $H^{13}CO^+$ is a factor of 50 lower than that of HCO^+ (e.g., Goicoechea et al., 2009; Veena et al., 2017).

HCN (hydrogen cyanide) and HNC (hydrogen isocyanide)

The HCN molecule and its metastable geometrical isomer HNC are primarily formed through the dissociatve recombination reaction $HCNH^+ + e^- \rightarrow HCN + H$ or $HNC + H$ (Herbst, 1978). Reactions with H_3^+, H_3O^+ and HCO^+ are believed to be the dominant destruction mechanisms of these molecules. They are optically thick lines that are typically used as the dense gas tracers in analysing the chemistry of star forming regions (e.g., Miettinen, 2014; Liu et al., 2013b). In particular, HNC molecule is considered as a good tracer of infall motion (Kirk et al., 2013). In the IRDC G333.73, we detect both HCN and HNC molecules with optically thick profiles. The morphologies of HCN and HNC emission are similar to that of HCO^+ emission. The hyperfine components of HCN are visible in the spectrum, but display heavy self-absorption. HNC exhibits a strong blue asymmetry similar to the HCO^+ line. Similar to HCO^+ integrated intensity map, additional peaks (associated with clumps) are also seen towards north-east and south-west directions.

N_2H^+ (diazenylium) and C_2H (ethynyl)

N_2H^+ ion is observed to be a good tracer of dense gas as it is more resistant to freeze out on to dust grains compared to the carbon bearing species (Bergin & Langer, 1997; Charnley, 1997). Thus, it is highly useful in studying cold molecular clumps and cores where other species such as CO and CS are depleted. N_2H^+ is formed through the gas phase interaction $H_3^+ + N_2 \rightarrow N_2H^+ + H_2$. The dominant hyperfine interactions between the molecular electric field gradient and the electric quadrupole moments of the two nuclei produce a splitting of the J=1$\rightarrow$0 line in to seven hyperfine components.

It is mainly destroyed through the electron recombination reactions. The distribution of N_2H^+ emission in G333.73 is similar to the HCO^+, HCN and HNC molecules, but the shape of the clump is elongated (similar to continuum emission from dust) unlike the other species that show a spherical distribution.

The species C_2H is believed to form through photodissociation of acetylene molecule $C_2H_2 + h\nu \rightarrow C_2H + H$ (Fuente et al., 1993) and is acknowledged as a good tracer of PDRs (Ginard et al., 2012). A recent study by Beuther et al. (2008) has shown that C_2H is observed in all stages of high mass evolution from infrared dark clouds to massive protostellar objects to ultracompact H II regions. The distribution of C_2H is spherical in morphology and similar to other molecules such as HCO^+, HCN and HNC towards the peak emission region. However, unlike the other species, the emission is not extended in the direction of filament but appears rather confined to the clump C1. The lack of C_2H emission towards the immediate south-west of peak emission, where the extinction is high, is noticeable. Evidence of secondary peaks are observed towards S2 and towards the south-west of the IRDC. As the location of peak emission matches with that of other high density tracers, we infer that the C_2H emission close to the continuum peak is possibly originating from the molecular cloud itself rather than from the PDR.

3.4 Ionised gas emission

The radio continuum emissions from G333.73+0.37 at 1300 and 610 MHz are shown in Fig. 3.16. The ionised gas emission at 1300 MHz towards S1 reveals a shell-like structure surrounded by a low surface brightness diffuse envelope as seen in Fig. 3.16(a). The shell structure is more evident in the high resolution map, displayed in Fig. 3.16(b) with two peaks separated by lower flux density towards the center that gives the appearance of a cleft ring. The angular diameter of the shell-structure is $\sim$30.5$''$ that corresponds to 0.4 pc at a distance of 2.6 kpc. The radio emission at 610 MHz shown in Fig. 3.16(c) shows a more compact structure and traces of the shell are not evident. While resolution effects could play a role, the data quality is poor compared to the higher frequency image as the diffuse structure is not visible either. There, however, exists a possibility that optical depth effects could hamper our viewing of the shell structure. We also detect radio emission towards the source S2 where the emission is highly compact. This

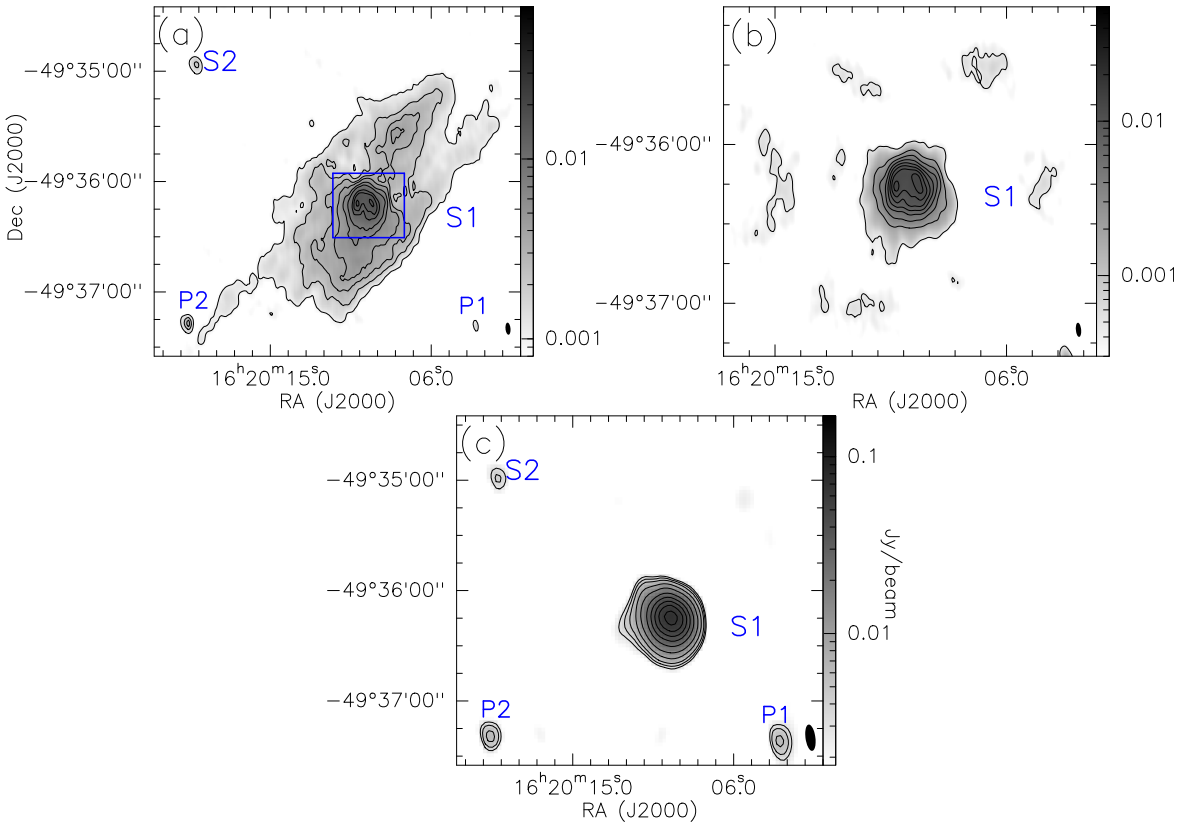

Figure 3.16: (a) Low resolution radio continuum map of G333.73+0.37 at 1300 MHz. The contour levels are at 1.4, 2.1, 3.1, 4.1, 6.1, 8.1, 10.1, 12.1, 14.1 and 16.1 mJy/beam with beam size of $6.6'' \times 2.7''$. The compact shell structure is enclosed within the rectangle. (b) High resolution map of the rectangular region shown in (a). The contour levels are from 2 mJy/beam to 19 mJy/beam in steps of 2.2 mJy/beam. The corresponding beam size is $5.5'' \times 2.0''$. (c) Radio continuum map of G333.73+0.37 at 610 MHz. The contour levels are from 3.5 mJy/beam to 98 mJy/beam in steps of 10 mJy/beam. The corresponding beam size is $14.5'' \times 5.4''$. The beams are represented as filled ellipses towards bottom right of all panels.

suggests that S2 is relatively young and or excited by a lower mass zero age main sequence (ZAMS) star. The radio sources S1 and S2 have been previously identified by Sánchez-Monge et al. (2013). Additionally, two point-like sources, designated P1 and P2, are detected towards the south-west and south-east of S1, marked in Fig. 3.16(a). These are not positionally coincident with any infrared emission/source.

We have computed the spectral indices ($\alpha_{610-1300}$) of the compact sources by integrating flux densities at 610 and 1300 MHz. For S2, we estimate the spectral index as -0.28. For P1 and P2, we obtain steeper spectral indices of -2.0 and -0.4, respectively. These values are indicative of non-thermal contribution to the radio emission (Kobulnicky & Johnson, 1999) as thermal emission from H II regions typically falls in the range $-0.1 \leq \alpha \leq 2$ (Olnon, 1975). The latter two are likely to be background sources of extragalactic origin and we exclude them from further analysis in this work.

We estimate the radio properties of both the H II regions, S1 and S2, to learn about the source(s) of excitation as well as the physical conditions such as ionised gas densities within these regions. The emission measure (EM), electron density (n_e) and the Lyman continuum photon rate ($\dot{\mathrm{N}}_{\mathrm{Lyc}}$) under the assumptions of optically thin emission and negligible absorption by dust are given by the following relations (Schmiedeke et al., 2016).

$$\left(\frac{\mathrm{EM}}{\mathrm{pc\ cm^{-6}}}\right) = 3.217 \times 10^{7} \left(\frac{S_\nu}{\mathrm{Jy}}\right) \left(\frac{T_e}{\mathrm{K}}\right)^{0.35} \left(\frac{\nu}{\mathrm{GHz}}\right)^{0.1} \left(\frac{\theta_{src}}{\mathrm{arcsec}}\right)^{-2} \tag{3.6}$$

$$\left(\frac{n_e}{\mathrm{cm^{-3}}}\right) = 2.576 \times 10^{6} \left(\frac{S_\nu}{\mathrm{Jy}}\right)^{0.5} \left(\frac{T_e}{\mathrm{K}}\right)^{0.175} \left(\frac{\nu}{\mathrm{GHz}}\right)^{0.05} \left(\frac{\theta_{src}}{\mathrm{arcsec}}\right)^{-1.5} \left(\frac{d}{\mathrm{pc}}\right)^{-0.5} \tag{3.7}$$

$$\left(\frac{\mathrm{N_{Lyc}}}{\mathrm{s^{-1}}}\right) = 4.771 \times 10^{42} \left(\frac{S_\nu}{\mathrm{Jy}}\right) \left(\frac{T_e}{\mathrm{K}}\right)^{-0.45} \left(\frac{\nu}{\mathrm{GHz}}\right)^{0.1} \left(\frac{d}{\mathrm{pc}}\right)^{2} \tag{3.8}$$

where S_ν is the flux density at frequency ν, T_e is the electron temperature, θ_{src} is the angular source size, and d is the distance to the source. In order to estimate the electron temperature in this region, we apply the electron temperature gradient curve across the Galactic disk (Churchwell et al., 1978; Quireza et al., 2006b) and obtain a value of 6800 K for a Galactocentric distance of 6.3 kpc. To determine the properties of S2, we use the same kinematic distance of 2.6 kpc as S1, since the LSR velocity of molecular gas close to S2 is similar to what we measured towards S1. The radio properties of S1 and S2 determined from the above equations are listed in Table 3.3. Assuming

that the HII regions are excited by a single ZAMS star, S1 is ionised by a late O or early B type star while S2 is powered by an early B star (Panagia, 1973). The electron density towards S2 is nearly factor of two larger than that towards S1. Equipped with the knowledge of the Lyman continuum flux as well as electron density, we estimate the radius of the Strömgren sphere, defined as the radius at which the rate of ionization equals that of recombination under the assumption that the H II region is expanding in a homogeneous medium. The radius of the Strömgren sphere, R_s is given by the expression

$$R_s = \left(\frac{3\, N_{Lyc}}{4\,\pi\, n_0^2\, \alpha_B} \right)^{1/3} \tag{3.9}$$

Here α_B is the radiative recombination coefficient assumed to be 2.6×10^{-13} cm^3 s^{-1} (Osterbrock, 1989). n_0 represents the mean number density of atomic hydrogen which is estimated from the column density map using the expression n_0 = $3N(\mathrm{H_2})$/2R where R is the radius of the clump, n_0 is 1.6×10^4 cm^{-3} and 2.3×10^4 cm^{-3} for clumps C1 and C2 corresponding to S1 and S2, respectively. From the above expression, we find R_s to be 0.03 and 0.02 pc for S1 and S2, respectively. If we compare this with the observed radius of S1 and S2, we find that the observed radii are an order of magnitude higher compared to R_s values determined. This signifies that the H II regions have expanded beyond the Strömgren spheres and are in the second expansion phase, where pressure disturbances from within the H II region are able to cross the ionization front and create an expanding shock. We can estimate the dynamical age, t$_{dyn}$ of these HII regions based on a simple model of expanding photoionised nebula, in a homogeneous medium using the size of radio emission (Dyson & Williams, 1980). The expression for t$_{dyn}$ is given by

$$t_{dyn} = \left[\frac{4\, R_s}{7\, c_i} \right] \left[\left(\frac{R}{R_s} \right)^{7/4} - 1 \right] \tag{3.10}$$

where R represents the radius of the spherical HII region and c_i is the isothermal sound speed in the ionised gas, assumed to be 10 km s^{-1} for typical H II regions (Stahler & Palla, 2005). R is the radius of the H II region. The estimated dynamical ages for S1 and S2 are found to be 0.2 and 0.01 Myr, respectively. This hints at the youth of S2 relative to S1. It is to be noted that the dynamical age has been calculated assuming

Table 3.3: Properties of the sources S1 and S2 from radio continuum data

Source	Diameter (pc)	EM (pc cm^{-6})	n_e (cm^{-3})	N$_{\rm Lyc}$ (10^{46} s^{-1})	Spectral type	R_s (pc)	t_{dyn} (Myr)
S1	0.38	2.4×10^5	734	22.9	O9.5 - B0	0.03	0.2
S2	0.15	2.9×10^5	1313	4.2	B0 - B0.5	0.02	0.01

a medium which is homogeneous. This is unlikely to represent the factual situation. Hence t_{dyn} should be considered as representative at best.

3.5 Young stellar objects associated with G333.73

Color excess at infrared wavelengths has been extensively used to identify the young objects and to broadly categorise them according to evolutionary stages. Recent studies in nearby star forming regions have shown that the *Spitzer* IRAC color-color diagrams are particularly useful in identifying the young stellar population in these regions as the IRAC bands are highly sensitive to the emission from the circumstellar disks and envelopes (e.g., Allen et al., 2004; Megeath et al., 2004; Hartmann et al., 2005). Examining different models and combining them with the observations, they have found that the different classes of YSOs such as Class I (central source+disk+envelope) and Class II (central source+disk) objects occupy distinct regions in the color-color diagram. In addition to this, the color-color diagrams that combine the IRAC and MIPS 24 μm data are often used to identify highly embedded stars and sources with significant inner holes (e.g., Rho et al., 2006; Lada et al., 2006).

In order to study the YSO population within this IRDC, we searched the Glimpse I′07 Archive for mid-infrared point sources. For this, we have considered all sources lying within the 3σ contour of the 1.2 mm emission. By proceeding in this way, we attempt to identify sources associated with the IRDC and eliminate other field objects that are not related to G333.73. However, as the mid-infrared emission from S1 extends be-

Table 3.4: Coordinates and magnitudes of IRAC YSO candidates.

YSO	α_{2000} ($^h\ ^m\ ^s$)	δ_{2000} ($^\circ\ '\ ''$)	J (mag)	H (mag)	K (mag)	3.6 μm (mag)	4.5μm (mag)	5.8μm (mag)	8.0μm (mag)	24.0μm (mag)	Classification*
MIR1	16:19:50.894	−49:38:21.36	-	-	-	7.0 ± 0.03	5.05 ± 0.07	3.84 ± 0.03	3.01 ± 0.02	1.09 ± 0.02	Class I
MIR2	16:19:51.091	−49:37:49.88	-	-	-	11.99 ± 0.07	10.42 ± 0.06	9.53 ± 0.05	9.53 ± 0.08	-	Reddened Class II
MIR3	16:19:52.317	−49:37:55.90	-	-	13.46 ± 0.04	12.30 ± 0.06	11.90 ± 0.10	11.39 ± 0.10	10.20 ± 0.27	-	Class I
MIR4	16:19:52.879	−49:37:37.00	15.71 ± 0.07	13.72 ± 0.05	12.51 ± 0.04	11.15 ± 0.07	10.51 ± 0.09	10.37 ± 0.11	10.09 ± 0.12	$4.74 \pm 0.04^\dagger$	Reddened Class II
MIR5	16:19:53.038	−49:37:34.59	-	-	-	13.31 ± 0.11	11.51 ± 0.10	10.75 ± 0.11	10.08 ± 0.13	$4.74 \pm 0.04^\dagger$	Class I
MIR6	16:19:55.084	−49:37:42.55	-	-	-	12.76 ± 0.10	12.17 ± 0.11	11.09 ± 0.10	10.43 ± 0.31	-	Class II
MIR7	16:19:58.049	−49:37:04.62	-	14.90 ± 0.09	10.75 ± 0.03	7.45 ± 0.04	6.58 ± 0.07	5.87 ± 0.03	5.54 ± 0.03	4.20 ± 0.03	Reddened Class II
MIR8	16:19:58.291	−49:37:47.05	15.10 ± 0.04	13.47 ± 0.02	12.45 ± 0.04	10.76 ± 0.05	10.10 ± 0.05	9.69 ± 0.05	8.88 ± 0.06	5.57 ± 0.07	Class II
MIR9	16:20:00.555	−49:36:06.85	-	14.59 ± 0.06	13.25 ± 0.04	11.88 ± 0.07	11.46 ± 0.08	10.78 ± 0.06	10.24 ± 0.06	7.09 ± 0.69	Class II
MIR10	16:20:00.701	−49:37:14.31	-	-	-	13.71 ± 0.12	12.23 ± 0.10	11.37 ± 0.09	10.92 ± 0.15	-	Class I
MIR11	16:20:01.848	−49:37:28.12	-	-	-	12.20 ± 0.06	10.85 ± 0.06	10.13 ± 0.05	10.26 ± 0.05	-	Reddened Class II
MIR12	16:20:02.657	−49:36:30.42	13.03 ± 0.03	12.47 ± 0.06	12.14 ± 0.04	11.78 ± 0.07	11.75 ± 0.09	11.58 ± 0.11	10.98 ± 0.20	-	Class II
MIR13	16:20:03.535	−49:36:46.71	16.30 ± 0.10	14.95 ± 0.10	14.02 ± 0.09	12.90 ± 0.08	12.68 ± 0.12	12.25 ± 0.27	11.36 ± 0.13	-	Class II
MIR14	16:20:05.035	−49:36:35.31	-	14.53 ± 0.11	13.39 ± 0.05	12.06 ± 0.06	11.46 ± 0.07	10.98 ± 0.08	10.17 ± 0.07	-	Class II
MIR15	16:20:08.602	−49:37:16.20	-	-	-	13.52 ± 0.14	12.86 ± 0.14	11.62 ± 0.26	10.98 ± 0.14	4.60 ± 0.25	Class II
MIR16	16:20:09.786	−49:36:17.02	-	-	12.33 ± 0.06	8.86 ± 0.19	7.44 ± 0.14	6.37 ± 0.06	5.55 ± 0.03	-	Class I
MIR17	16:20:14.246	−49:36:25.56	-	14.01 ± 0.05	12.54 ± 0.04	11.62 ± 0.08	11.34 ± 0.07	11.11 ± 0.13	10.55 ± 0.20	-	Class II
MIR18	16:20:16.272	−49:34:41.82	-	-	14.01 ± 0.07	12.40 ± 0.07	11.58 ± 0.09	10.92 ± 0.09	10.49 ± 0.07	-	Reddened Class II
MIR19	16:20:18.677	−49:36:23.27	-	-	-	12.59 ± 0.07	11.84 ± 0.11	11.04 ± 0.09	10.48 ± 0.15	3.24 ± 0.27	Reddened Class II
MIR20	16:20:21.415	−49:34:36.64	-	-	-	12.74 ± 0.07	11.96 ± 0.08	11.85 ± 0.27	11.31 ± 0.18	-	Reddened Class II
MIR21	16:20:24.991	−49:34:44.93	-	14.31 ± 0.05	11.82 ± 0.02	9.63 ± 0.05	8.91 ± 0.05	8.38 ± 0.04	7.60 ± 0.03	3.94 ± 0.06	Class II
MIR22	16:20:27.422	−49:35:32.74	-	-	-	12.05 ± 0.06	10.83 ± 0.06	10.35 ± 0.08	10.36 ± 0.07	-	Reddened Class II

* : Classification based on IRAC color-color diagram

† : Upper limit

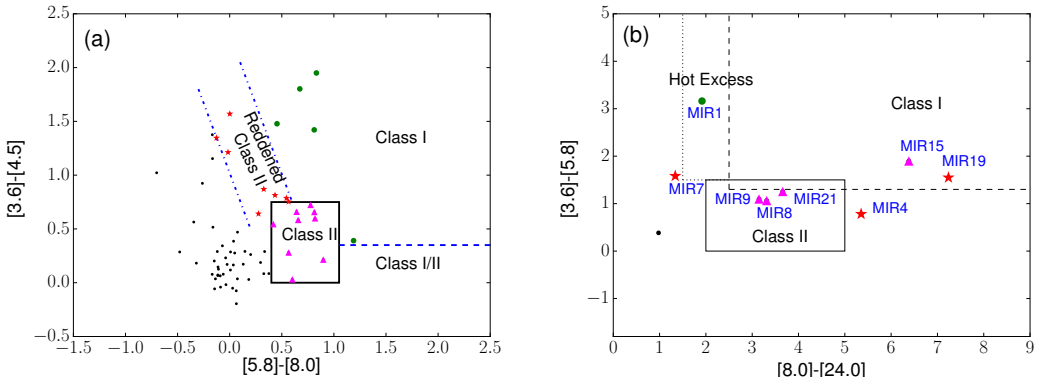

Figure 3.17: (a) *Spitzer*-IRAC color-color diagram using the colors [3.6]-[4.5] versus [5.8]-[8.0]. Solid rectangle indicates the position occupied by Class II objects while parallel dotted lines represent the region occupied by reddened Class II objects. The top-right region of the color-color diagram is occupied by Class I sources and the region to the right of Class II sources is occupied by Class I/II objects. Filled circles (green) represent Class I YSO candidates and triangles (magenta) denote Class II objects. Reddened Class II objects are represented with star symbol (red). Other sources are marked as filled circles (black). (b) Color-color diagram of [3.6]-[5.8] versus [8.0]-[24.0] using mid-infrared magnitudes from *Spitzer*-IRAC and MIPS. Solid line box indicates the region occupied by Class II objects whereas region marked by dashed line represents the region occupied by Class I objects. Dotted line indicates the location of "hot excess" sources (see text).

yond the 3σ contour of the 1.2 mm emission, we have also considered sources within a circular region of radius $1.5'$ around S1 (centred at $\alpha_{\rm J2000}$=$16^h20^m09.4^s$, $\delta_{\rm J2000}$=$-49°36'21''$). Among these two groups of *Spitzer* sources, we find that 73 are detected in all the four IRAC bands. We have also carried out a visual inspection of this region in all the IRAC images by scaling the images to identify sources embedded in mid-infrared nebulosity and find that 16 sources were not identified in the GLIMPSE catalog. Hence we have performed aperture photometry on these sources using the task `qphot` in IRAF software. For this, we have selected an aperture of radius $5''$. The inner and outer radii of the sky annulus are $6''$ and $8.5''$ respectively. Aperture corrections taken from IRAC instrument handbook are used to correct the measured fluxes. These factors are

found to be 1.060, 1.063, 1.063 and 1.084 at 3.6, 4.5, 5.8 and 8.0 μm respectively. The aperture-corrected zero-magnitude fluxes are 297.7, 370.7, 122.2 and 70.3 Jy at 3.6, 4.5, 5.8 and 8.0 μm. In order to identify the YSO candidates, we used the methods prescribed by Megeath et al. (2004) and Allen et al. (2004). For the sources detected in all IRAC bands, we employed the [5.8]-[8.0] versus [3.6]-[4.5] color-color diagram to locate the YSO sources. The color-color diagram is shown in Fig. 3.17(a). The regions occupied by Class I, Class II and reddened Class II sources, based on the predictions of existing models for disks and envelopes (Megeath et al., 2004), are also shown in the image. A total of 22 YSO candidates are detected in the color-color diagram. Of these, 5 are Class I sources, 9 are Class II sources and 8 are reddened Class II sources. We have searched for possible contaminants (PAH and AGNs) in our sample using the criteria given by (Gutermuth et al., 2008) and none of the identified YSOs are classified as contaminants.

The 24 μm data, if available, serves as an additional tool to discriminate between Class I and Class II objects. The SED of Class II objects are flat or declining near 24 μm whereas it is rising for Class I YSOs (Kerton et al., 2013). We have, therefore, employed the flux densities from the 24 μm point source catalog of Gutermuth & Heyer (2015) to plot the IRAC-MIPS color-color diagram. From the catalog, we have identified 7 sources within both our regions of interest. We again carry out a visual inspection of the MIPS 24 μm image and find that there are 5 additional sources that are not listed in the catalog. We performed aperture photometry on these sources using the task `qphot` in IRAF. The parameters for the photometry are taken from Gutermuth & Heyer (2015). This leads to a total of 12 sources at 24 μm. Of these, 9 sources have IRAC magnitudes in all the 4 bands. Among the 12, two sources whose photometry is carried out by us are detected only in the 24 μm band. These sources are likely to be Class 0 protostellar objects although we cannot exclude the possibility of these being background objects.

We have constructed a color-color diagram, [3.6]-[5.8] versus [8.0]-[24.0], based on IRAC and MIPS colors which is used to identify the Class 0/I and Class II sources. This color-color diagram is shown in Fig. 3.17(b). The class I YSO MIR1, lies in the "hot excess" region and is of interest as this region is occupied mostly by Herbig AeBe stars. Class II YSOs with large extinction (A_v >25) or Class 0/I objects with an extra hot component from unusually active accretion, can also fall in the "hot excess" region (Rho et al., 2006). The reddened Class II YSO, MIR7, also lies just outside the boundary of

Table 3.5: Coordinates and magnitudes of near-infrared pre-main sequence sources.

YSO	α_{2000} ($^{h}\ ^{m}\ ^{s}$)	δ_{2000} ($^{\circ}\ ^{\prime}\ ^{\prime\prime}$)	J (mag)	H (mag)	K (mag)
NIR1	16:19:48.421	−49:38:13.39	16.02 ± 0.09	13.54 ± 0.04	12.23 ± 0.03
NIR2	16:19:48.693	−49:37:02.60	15.01 ± 0.07	14.46 ± 0.11	13.99 ± 0.08
NIR3	16:19:50.237	−49:37:28.78	15.70 ± 0.08	14.64 ± 0.09	13.94 ± 0.07
NIR4	16:19:51.425	−49:37:16.62	14.47 ± 0.05	13.84 ± 0.05	13.42 ± 0.06
NIR5	16:20:00.259	−49:36:27.51	14.69 ± 0.05	13.98 ± 0.05	13.58 ± 0.05
NIR6	16:20:01.816	−49:36:47.06	16.05 ± 0.09	14.58 ± 0.13	13.61 ± 0.08
NIR7	16:20:01.850	−49:36:20.02	15.35 ± 0.07	13.93 ± 0.07	13.07 ± 0.04
NIR8	16:20:03.207	−49:35:22.64	11.49 ± 0.02	11.31 ± 0.05	11.09 ± 0.06
NIR9	16:20:03.534	−49:36:01.26	16.07 ± 0.09	15.08 ± 0.13	14.33 ± 0.12
NIR10	16:20:03.731	−49:36:24.67	13.73 ± 0.03	13.24 ± 0.04	12.98 ± 0.04
NIR11	16:20:04.090	−49:36:30.99	13.10 ± 0.02	12.78 ± 0.04	12.52 ± 0.04
NIR12	16:20:04.112	−49:36:12.82	14.43 ± 0.02	13.99 ± 0.02	13.72 ± 0.05
NIR13	16:20:05.813	−49:35:19.74	13.13 ± 0.05	12.80 ± 0.04	12.63 ± 0.03
NIR14	16:20:06.003	−49:35:26.97	11.66 ± 0.03	11.35 ± 0.04	11.19 ± 0.03
NIR15	16:20:07.787	−49:35:26.88	16.48 ± 0.13	14.52 ± 0.06	13.28 ± 0.04
NIR16	16:20:08.299	−49:36:24.99	14.93 ± 0.04	14.33 ± 0.11	13.37 ± 0.14
NIR17	16:20:08.346	−49:35:55.60	12.98 ± 0.03	12.63 ± 0.06	12.38 ± 0.07
NIR18	16:20:08.824	−49:36:03.85	15.33 ± 0.19	13.38 ± 0.20	11.34 ± 0.07
NIR19	16:20:08.843	−49:36:30.29	14.09 ± 0.04	13.41 ± 0.07	12.85 ± 0.09
NIR20	16:20:09.049	−49:36:37.69	14.78 ± 0.04	14.15 ± 0.08	13.64 ± 0.08
NIR21	16:20:09.214	−49:35:05.28	12.66 ± 0.03	12.26 ± 0.05	11.74 ± 0.03
NIR22	16:20:09.456	−49:36:34.86	13.06 ± 0.03	12.53 ± 0.04	12.19 ± 0.05
NIR23	16:20:09.683	−49:36:01.66	12.24 ± 0.03	11.44 ± 0.06	10.82 ± 0.05
NIR24	16:20:09.836	−49:36:27.91	14.82 ± 0.13	14.24 ± 0.22	13.36 ± 0.12
NIR25	16:20:12.553	−49:36:44.04	14.83 ± 0.02	14.26 ± 0.07	13.57 ± 0.06
NIR26	16:20:14.118	−49:37:32.91	13.99 ± 0.02	13.63 ± 0.04	13.43 ± 0.05
NIR27	16:20:14.949	−49:37:17.82	14.04 ± 0.05	13.68 ± 0.05	13.39 ± 0.07
NIR28	16:20:15.384	−49:36:43.86	14.36 ± 0.09	13.88 ± 0.08	13.60 ± 0.07
NIR29	16:20:15.470	−49:36:51.72	13.82 ± 0.03	13.58 ± 0.06	13.40 ± 0.06
NIR30	16:20:15.827	−49:37:11.98	15.67 ± 0.08	14.34 ± 0.05	13.36 ± 0.06
NIR31	16:20:19.361	−49:34:58.80	11.25 ± 0.04	10.43 ± 0.04	9.91 ± 0.05
NIR32	16:20:22.523	−49:35:40.19	13.96 ± 0.02	13.55 ± 0.03	13.31 ± 0.03
NIR33	16:20:23.306	−49:35:46.32	14.72 ± 0.03	14.28 ± 0.05	14.01 ± 0.06
NIR34	16:20:27.642	−49:35:13.01	14.78 ± 0.04	14.24 ± 0.05	13.94 ± 0.05

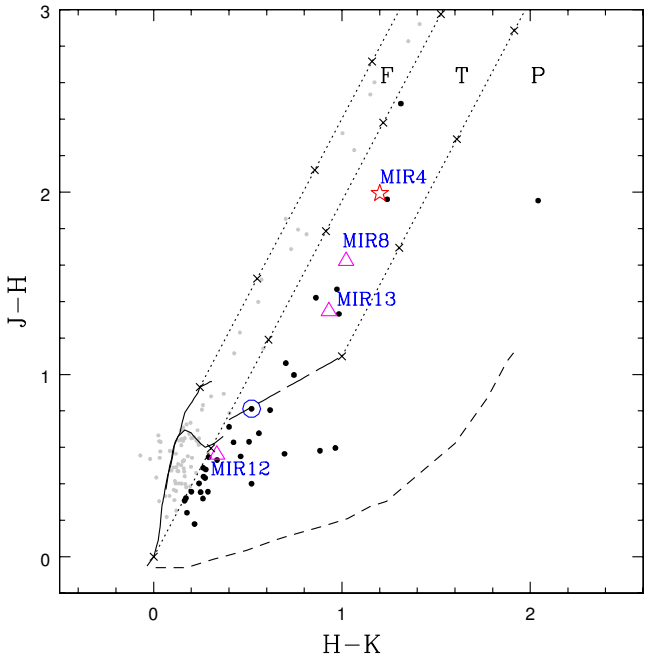

Figure 3.18: Color-color diagram of the 2MASS sources in the G333.73 region. The two solid curves represent the loci of giant (thick line) and main sequence stars (thin line) derived from Bessell & Brett (1988). Classical T Tauri locus from Meyer et al. (1997) is represented with a long-dashed line. The parallel dotted lines are the reddening vectors with crosses placed at intervals corresponding to 5 magnitudes of visual extinction. We have assumed the interstellar reddening law of Rieke & Lebofsky (1985) (A_J/A_v=0.282, A_H/A_v=0.175 and A_K/A_v=0.112). Short-dashed line represents the locus of the Herbig AeBe stars (Lada & Adams, 1992). The plot is classified into "F", "T" and "P" regions (see text for details). The colors and the curves shown in the figure are transformed to Bessell & Brett (1988) system. Sources that are classified as main sequence or giants are represented by gray dots whereas pre-main sequence sources are denoted by black dots. IRAC YSOs identified from mid-infrared color-color diagram having 2MASS counterparts are also shown and labeled in the image. Circled dot denotes central object corresponding to source S2.

"hot excess" objects. The object MIR4 lies in the region to the right of Class II objects. This source has a large [8.0]-[24.0] excess compared to [3.6]-[5.8] color. A visual inspection of MIR4 reveals that another YSO, designated MIR5 (Table 3.5) lies in close vicinity of this source (angular separation of $3''$). Hence the flux attributed to MIR4 in that catalog apparently has contribution from MIR5 due to resolution effects as the resolution of IRAC maps is $\sim 2''$ whereas for 24 μm MIPS data, it is $6''$.

Even though we have identified the YSO population associated with this region using the mid-infrared color-color diagrams, not all sources are detected in all the four IRAC bands. This is due to the fact that the [3.6] and [4.5] bands are more sensitive compared to others (Fazio et al., 2004). Moreover, [5.8] and [8.0] bands traces emission from PAHs that can confuse the detection and photometry of point sources. Hence, we have resorted to the near-infrared (NIR) 2MASS ($H - K_s$) versus ($J - H$) color-color diagram to identify the young population of sources. We have selected sources with good photometric magnitudes (read flag = 2) which are detected in all the three bands. A total of 127 sources are detected within both the regions described earlier. This color-color diagram, shown in Fig. 3.19, is classified into three distinct regions (Sugitani et al., 2002; Tej et al., 2006). The "F" sources are located within the reddening bands of main sequence and giant stars and are believed to be either field stars, Class III objects or Class II objects with small NIR excess. "T" sources occupy the region towards the left of "F" region, and right of the reddening vector corresponding to T Tauri locus. The sources in this region are mostly classical T Tauri stars (Class II) with large NIR excess although there could be a few Herbig AeBe stars with small NIR excess. Towards the right of "T" is the "P" region that is occupied by sources which are relatively younger (Class I or Herbig AeBe stars). From our sample, we find 38 sources that show NIR color excess (i.e. populating the "P" and "T" regions). The details of these YSOs are listed in Table. 3.5 with labels NIR1, NIR2,..., NIR 38. Eleven sources fall in the "T" region and 27 in "P" region. Among the YSOs identified in NIR, 4 objects are already classified as Class II sources based on IRAC colors.

Fig. 3.19 shows the distribution of all the 56 YSO candidates identified in this region: 22 IRAC YSOs and 34 NIR YSO candidates. Nearly 80% of the YSOs detected solely using NIR colors are located in the proximity of S1. This is explicable as the sources away from S1 along the length of the IRDC have low probability of detection due to higher extinction, also evident from the column density map. This YSO sample

is limited by sensitivity as well as nebulosity. Hence we would like to bring attention to the fact that this is a representative sub-sample of the total YSO population in this IRDC.

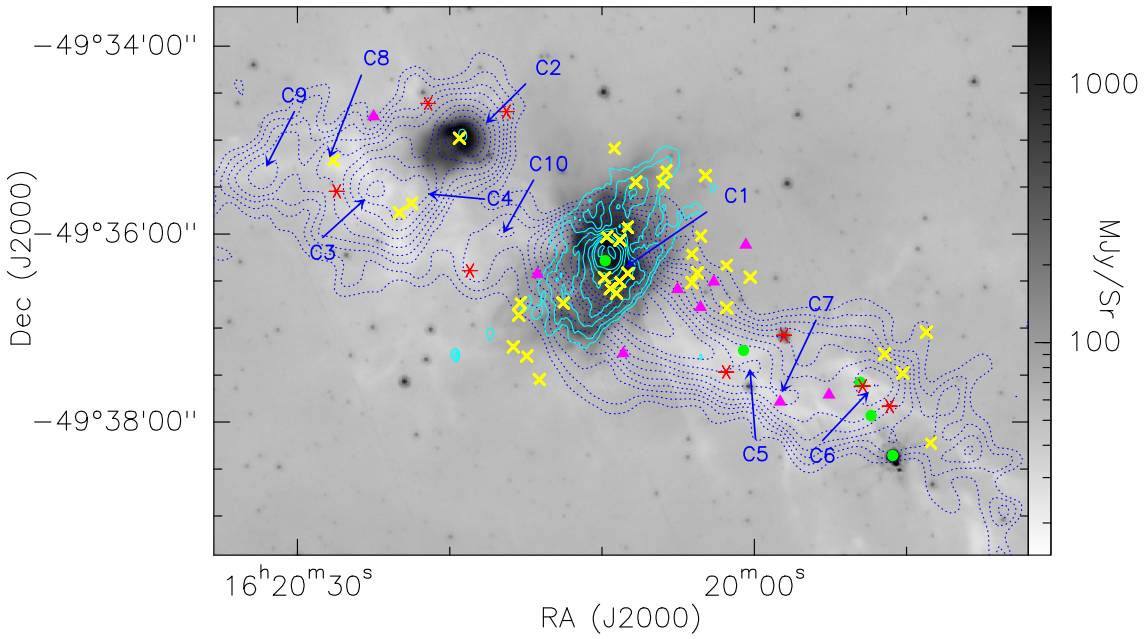

Figure 3.19: IRAC 8 μm image of the IRDC G333.73 overlaid with 1.2 mm cold dust contours (dotted) and low resolution 1300 MHz contours (solid). Also marked in the image are the different classes of YSOs identified from near and mid-infrared color-color diagrams. IRAC Class I YSOs are denoted by filled circles (green) whereas Class II YSOs are marked as triangles (magenta). Asterisk (red) represents reddened Class II objects. Locations of the pre-main sequence objects identified from the 2MASS color-color diagram are indicated by crosses (yellow). The 1.2 mm contour levels are from 40 mJy/beam to 1500 mJy/beam in steps of 70 mJy/beam. 1300 MHz contours levels are the same as those shown in Fig. 3.16(b). Also marked are the locations of the 10 millimeter clumps.

3.6 SED modelling of YSOs

Subsequent to the identification of YSOs, we are interested in gaining an insight into their characteristics such as mass, evolutionary stage, stellar temperature, envelope ac-

cretion rate, disk mass etc. To achieve this, we resort to the radiative transfer models of Robitaille et al. (2007) and use them to fit SEDs of the YSOs. We have fitted SEDs of 9 YSO candidates: MIR1, MIR4, MIR5, MIR7, MIR8, MIR9, MIR15, MIR19 and MIR21, whose 24 μm fluxes are known. The reason for selecting these sources for SED modelling is that the data at longer wavelength, if available, serves as a better tool to constraint the models. For MIR4 and MIR5, only a single common flux density at 24 μm is at hand, and we use it as an upper limit for both these objects. In addition, we have selected a YSO identified based on NIR colors, NIR31, that is in close vicinity ($\sim 3''$) of the radio peak towards S2. Besides, the source is detected at 3.6 and 4.5 μm IRAC bands. It is also detected in the optical bands and we have used the flux densities at B and R bands from USNO catalog (Monet, 1998) and I band from the DENIS catalogue (Epchtein, 1998) in the construction of the SED. As the 24 μm image is saturated, we have used the 12 and 22 μm fluxes from WISE catalog (Cutri & et al., 2012) as upper limits (owing to the poor resolution of these images). Some of the sources appear point-like in the *Herschel* far-infrared images at 70 and 160 μm. For these sources, we have estimated the flux densities within circular apertures of radius $10''$ and $20''$, respectively. These apertures have been taken considering the radial profile of bright point-like sources in this region. For other YSOs as well as other wavelengths, we have considered flux densities of the corresponding clumps as upper limits. The YSO MIR9 lies outside the 3σ threshold of the 1.2 mm map and hence for this object, we carried out the fitting for wavelengths upto 24 μm. The SED fitting of the 10 YSOs described above has been carried out using the command line version of the SED fitting tool. The results are shown in Fig. 3.20. The fitted parameters along with ranges corresponding to first 10 best-fit models are given in Table 3.6.

From the best-fit models, the masses of all sources fall in the range $1.7 \leq \mathrm{M}_\star \leq 10.0$. This suggests that all these sources are intermediate to high mass objects. MIR1, the YSO that has been identified as IRAS 16161–4931 earlier, is the most massive one (10 $\mathrm{M}_\odot$) according to the models. The ages of all the objects other than MIR8, are $\lesssim$2 Myr hinting at the youth of these sources. We have classified the YSO candidates based on their evolutionary stages using the method described by Robitaille et al. (2006). This classification scheme divides the sources into three broad categories based on three physical properties: mass of the central object ($\mathrm{M}_\star$), envelope accretion rate ($\dot{\mathrm{M}}_{\mathrm{env}}$) and disk mass ($\mathrm{M}_{\mathrm{disk}}$). Stage 0/I objects are those with $\dot{\mathrm{M}}_{\mathrm{env}}/\mathrm{M}_\star > 10^{-6}$ yr^{-1}

Table 3.6: Parameters of the models shown in Fig. 3.20. Col. 4 – 9 give Mass, Effective Temperature, Luminosity, Inclination angle, Envelope accretion rate, Disk Mass, Extinction and Age, respectively. The parameters listed are for the best fit model and the range of all the ten best fits.

Source		χ^2	Mass ($M_\odot$)	T_{eff} (K)	Luminosity ($L_\odot$)	Inc. angle (Deg.)	Env. accretion rate ($M_\odot$/yr)	Disk mass ($M_\odot$)	A_V (mag)	Age (Myr)
MIR1 (IRAS 16161–4931)	Best fit	373.8	10.0	25790	6873.0	56.6	0	0.2	55.5	1.00
	Range	$373.8 - 5122.0$	$7.7 - 10.3$	$21850 - 25790$	$2581.0 - 6873.0$	$31.8 - 75.5$	0	$9.6 \times 10^{-3} - 0.3$	$0 - 55.5$	$1.0 - 3.3$
MIR4	Best fit	8.5	3.7	4847	30.3	81.4	1.1×10^{-5}	3.4×10^{-3}	7.2	0.38
	Range	$8.5 - 14.7$	$3.7 - 5.3$	$4153 - 5945$	$14.9 - 31.8$	$56.6 - 81.4$	$0 - 2.4 \times 10^{-5}$	$4.3 \times 10^{-4} - 0.05$	$3.3 - 13.1$	$0.08 - 2.2$
MIR5	Best fit	3.6	4.0	6580	100.1	81.4	3.2×10^{-8}	1.3×10^{-4}	83.3	0.97
	Range	$3.6 - 3.9$	$2.7 - 4.0$	$6580 - 12950$	$55.8 - 118.0$	$49.5 - 81.4$	$0 - 3.2 \times 10^{-8}$	$1.3 \times 10^{-4} - 0.05$	$78.6 - 84.3$	$0.97 - 9.51$
MIR7	Best fit	398.1	5.8	18020	1543.0	63.3	0	0.01	34.0	1.90
	Range	$398.1 - 1267.0$	$4.6 - 6.4$	$15720 - 19240$	$84.2 - 1543.0$	$31.8 - 75.5$	0	$3.3 \times 10^{-3} - 0.1$	$28.2 - 34.0$	$1.53 - 4.38$
MIR8	Best fit	33.6	3.1	12160	83.7	81.4	0	0.02	7.8	9.63
	Range	$33.6 - 66.4$	$1.7 - 3.2$	$4335 - 12160$	$20.6 - 83.7$	$18.2 - 81.4$	$0 - 1.9 \times 10^{-6}$	$2.5 \times 10^{-3} - 0.02$	$5.2 - 12.1$	$0.18 - 9.80$
MIR9	Best fit	8.8	1.7	4401	15.4	18.2	2.7×10^{-6}	0.06	17.1	0.23
	Range	$8.8 - 11.5$	$1.0 - 3.3$	$4134 - 4975$	$8.6 - 19.1$	$18.2 - 69.5$	$6.3 \times 10^{-8} - 2.9 \times 10^{-6}$	$2.9 \times 10^{-5} - 0.06$	$14.5 - 17.8$	$0.18 - 0.71$
MIR15	Best fit	1.8	2.9	4385	66.8	81.4	8.6×10^{-5}	0.01	0	0.07
	Range	$1.8 - 3.7$	$0.6 - 6.4$	$3793 - 4772$	$9.1 - 336.8$	$41.4 - 87.1$	$3.5 \times 10^{-6} - 1.5 \times 10^{-3}$	$4.9 \times 10^{-5} - 0.17$	$0 - 24.9$	$0.01 - 0.20$
MIR19	Best fit	0.8	2.8	4542	36.5	81.4	1.2×10^{-5}	2.0×10^{-4}	5.6	0.18
	Range	$0.8 - 2.4$	$2.7 - 5.6$	$4367 - 5950$	$36.5 - 221.0$	$49.5 - 87.1$	$8.3 \times 10^{-6} - 1.5 \times 10^{-4}$	$2.0 \times 10^{-4} - 0.07$	$0 - 20.9$	$0.05 - 0.31$
MIR21	Best fit	50.8	5.6	4724	158.8	31.8	7.1×10^{-5}	0.02	29.3	0.14
	Range	$50.8 - 83.8$	$4.3 - 5.6$	$4724 - 15130$	$137.8 - 408.4$	$18.2 - 81.4$	$0 - 7.1 \times 10^{-5}$	$1.2 \times 10^{-5} - 0.13$	$20.1 - 29.6$	$0.14 - 1.92$
NIR31 (S2)	Best fit	25.9	5.6	6462	267.0	18.2	1.3×10^{-6}	0.03	4.7	0.30
	Range	$25.9 - 44.6$	$5.1 - 7.1$	$4445 - 6462$	$166.7 - 351.6$	$18.2 - 63.2$	$1.3 \times 10^{-6} - 7.8 \times 10^{-4}$	$1.6 \times 10^{-5} - 0.15$	$1.5 - 4.7$	$0.04 - 0.37$

and are believed to be objects with significant infalling envelopes and possibly disks. If $\dot{M}_{env}/M_{\star} < 10^{-6}$ yr^{-1} and $M_{disk}/M_{\star} > 10^{-6}$, the object is classified as a Stage II source that has an optically thick disk and possible remains of an infalling envelope. If $\dot{M}_{env}/M_{\star} < 10^{-6}$ yr^{-1} and $M_{disk}/M_{\star} < 10^{-6}$, it is a Stage III object with an optically thin disk. The advantage of using this classification scheme along with the classification based on the slope of infrared SED is that it can avoid possible confusion between observable and physical properties and thereby provides a more physical basis for YSO classification. Table 3.7 gives the values for $\dot{M}_{env}/M_{\star}$ and $M_{disk}/M_{\star}$ for the YSOs including the classification based on different methods. We notice that $M_{disk}/M_{\star}$ corresponding to all the 10 YSOs are above the threshold of 10^{-6} for having optically thick disk, suggesting the fledgling nature of these objects.

According to the classification scheme of Robitaille et al. (2006), there is a single Stage I source, there are 5 Stage I/II and 4 Stage II objects. We find that there is a broad corroboration between this classification scheme and those based on infrared colors. Two YSOs that show deviant behaviour between the schemes are MIR1 and MIR7. From the SED modelling, we see that MIR1 and MIR7 fall into Stage II category with zero envelope accretion rate. According to IRAC color-color diagram, they are classified as Class I and Class II objects, respectively. But the IRAC-MIPS colors categorise them as "hot excess" objects. As mentioned earlier, these are suspected to be Class I sources or Class II objects with large extinction ($A_v > 25$ mag). The extinctions estimated from the models are relatively large: 56 and 34 mag for MIR1 and MIR7, respectively. This is consistent with that predicted for a Class II object falling in the "hot excess" region. Hence MIR1 and MIR7 are speculated to be Class II objects with large extinction. The age of these sources are also relatively higher ($1 - 4$ Myr) compared to Stage I and I/II sources (<1 Myr). The object NIR31 that is associated with S2 is classified as a Stage I/II object from SED modelling and has a mass of $\sim$7 $M_{\odot}$. If radio emission from S2 is due to NIR31, we may be probing the radio emission from an intermediate YSO object. We explore this possibility later in Sect 3.7.2. We would also like to point out that although we have applied these models for fitting the SEDs, the parameters are considered as representative at best as the models are based on assumptions that the SEDs of intermediate/massive YSOs are scaled-up versions of their lower mass counterparts.

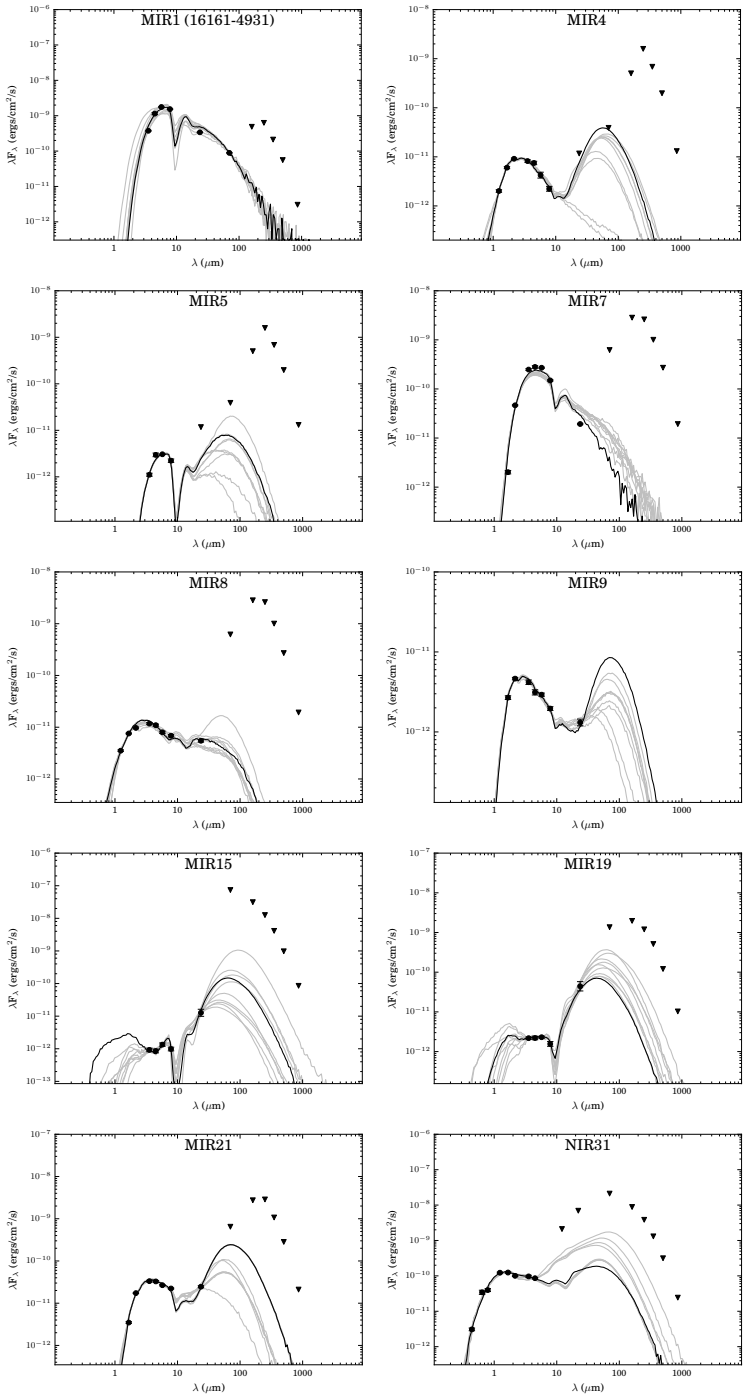

Figure 3.20: Infrared SEDs of YSO candidates MIR1, MIR4, MIR5, MIR7, MIR8, MIR9, MIR15, MIR19, MIR21 and near-infrared source NIR31 fitted with the SED models of Robitaille et al. (2007). The filled circles represent input fluxes and triangles represent upper limits in the far-infrared and submillimeter wavelengths. For NIR31, we have also given the fluxes in the optical bands (B and R). Best fit model is shown as black line while the grey lines represent subsequent nine good fits.

Table 3.7: YSO evolutionary stages based on IRAC color-color diagram and classification scheme by Robitaille et al. (2006).

YSO	$\dot{M}_{env}/M_{\star}$	$M_{disk}/M_{\star}$	Classification (IRAC CC diagram)	Classification (SED modelling)
MIR1*	0	$9.3 \times 10^{-4} - 0.04$	Class I	Stage II
MIR4	$0 - 6.5 \times 10^{-6}$	$8.1 \times 10^{-5} - 0.01$	Red Class II	Stage I or II
MIR5	$0 - 1.2 \times 10^{-8}$	$3.3 \times 10^{-5} - 0.02$	Class I	Stage II
MIR7*	0	$5.2 \times 10^{-4} - 0.02$	Red Class II	Stage II
MIR8	0	$7.8 \times 10^{-4} - 0.01$	Class II	Stage II
MIR9	$1.9 \times 10^{-8} - 2.9 \times 10^{-6}$	$8.8 \times 10^{-6} - 0.06$	Class II	Stage I or II
MIR15	$5.5 \times 10^{-7} - 2.5 \times 10^{-3}$	$7.6 \times 10^{-6} - 0.28$	Class II	Stage I or II
MIR19	$1.5 \times 10^{-6} - 5.6 \times 10^{-5}$	$3.6 \times 10^{-5} - 0.03$	Red Class II	Stage I
MIR21	$0 - 1.7 \times 10^{-5}$	$2.1 \times 10^{-6} - 0.03$	Class II	Stage I or II
NIR31	$1.8 \times 10^{-7} - 1.5 \times 10^{-4}$	$2.2 \times 10^{-6} - 0.03$	-	Stage I or II

* : Hot excess sources based on MIPS-IRAC CC diagram

3.7 Morphology of radio sources

3.7.1 S1

From the radio emission that traces the ionised gas (Fig. 3.16), we perceive that S1 can be categorised as a HII region with a shell-like morphology. According to Wood & Churchwell (1989) and Kurtz et al. (1994), shell-like regions are the rarest (less than 5%) of all the H II regions detected. Recent studies of Sgr B2 and W49 star forming regions (De Pree et al., 2005, and references therein) show a higher percentage (28%) of detection of shell-like H II regions. Strong stellar-winds from the central OB stars as well as the pressure from the ionizing radiation are believed to induce the formation of shell-like/bubble structures in their vicinity (Weaver et al., 1977; Shull, 1980). While radiation pressure on dust grains are capable of producing shell-like structures in ultracompact H II regions (Kahn, 1974), they are generally less important compared to the stellar winds (Turner & Matthews, 1984). An important probe of stellar winds is

the presence or absence of extended 24 μm emission near the center of bubbles. The centrally peaked 24 μm favours the explanation that the grains are mostly heated by the absorption of Lyman continuum photons, that are abundant near the exciting star (Deharveng et al., 2010). In few cases, a void is found to exist in the 24 μm emission towards the centre. This orifice could be produced either by stellar winds or due to the radiation pressure of the central star (Watson et al., 2008, 2009). Towards S1, we anticipate that the overall distribution of 24 μm emission is similar to that of ionised gas although the former is saturated towards the central region. This leads us to believe that the stellar winds have not yet succeeded in clearing out dust from the central region. The emission at 24 μm and radio, is surrounded by 8 μm shell of enhanced emission. Towards the centre, several high extinction filamentary structures are perceived at 8 μm, evident from Fig. 3.21(a).

We first explore the possibility of stellar winds from the central star being responsible for the observed shell-like morphology of the ionised gas. Note that the 8 μm shell envelopes the ionised gas shell. The interaction of massive stellar winds with the ambient medium will sweep up dense shells of gas that expand away from the central source and the swept-up shell(s) are exposed to the ionizing radiation from the newly formed star. This shell material may be partially or completely ionised and the radius of the shell increases as a function of time. The radius (R_{shell}) and expansion velocity (V_{shell}) of the shell can be estimated using the following expressions (Castor et al., 1975; Garay & Lizano, 1999):

$$R_{shell} = 0.042 \left[\frac{L_w}{10^{36}\ \mathrm{erg\,s^{-1}}}\right]^{1/5} \left[\frac{n_0}{10^5\ \mathrm{cm^{-3}}}\right]^{-1/5} \left[\frac{t}{10^3\ \mathrm{yr}}\right]^{3/5} \mathrm{pc} \tag{3.11}$$

$$V_{shell} = 24.7 \left[\frac{L_w}{10^{36}\ \mathrm{erg\,s^{-1}}}\right]^{1/5} \left[\frac{n_0}{10^5\ \mathrm{cm^{-3}}}\right]^{-1/5} \left[\frac{t}{10^3\ \mathrm{yr}}\right]^{-2/5} \mathrm{km\,s^{-1}} \tag{3.12}$$

where L_w is the mechanical luminosity of the stellar wind, n_0 is the density of the molecular cloud and t is the shell expansion time. Based on the 1300 MHz radio image, the radius of the shell is taken as 0.05 pc. We adopt an archetypal shell expansion veloc-

ity of 10 km s^{-1} (e.g., Garay et al., 1986; Bloomer et al., 1998; Harper-Clark & Murray, 2009) and consider the cloud density as 1.6×10^4 cm^{-3}, estimated towards clump C1. Using these values, we estimate the mechanical luminosity and shell expansion time to be 1.5×10^{34} erg s^{-1} and 2.9×10^3 yr, respectively.

The expansion of the H II region could be due to the following: (i) the pressure difference between the ionised gas and ambient medium, and (ii) the stellar wind from the exciting star. A comparison of the expansion rates of both these mechanisms can aid in the determination of the stage of expansion, i.e. whether the stellar wind dominates the classical expansion or vice-versa. From previous studies (Shull, 1980; Garay & Lizano, 1999), it is seen that the stellar wind is more important when the following condition is satisfied.

$$\left[\frac{L_w}{10^{36}\ \mathrm{erg\,s^{-1}}}\right] > 0.33 \left[\frac{\mathrm{N_{Lyc}}}{10^{49}\ \mathrm{s^{-1}}}\right]^{2/3} \left[\frac{n_0}{10^5\ \mathrm{cm^{-3}}}\right]^{-1/3} \tag{3.13}$$

Considering the $\mathrm{N_{Lyc}}$ estimated from radio flux, we estimate right hand side as 4.8×10^{34} erg s^{-1}, that is nearly three times larger compared to the mechanical luminosity of stellar wind $\sim 1.5 \times 10^{34}$ erg s^{-1}. This suggests that the effect of stellar wind is lower than that surmised from classical expansion. However, we would like to allude to the fact that the derived stellar wind luminosity is based on a typical expansion velocity of 10 km s^{-1}. If we increase V_{shell} to 20 km s^{-1}, L_w increases by an order of magnitude, to 1.2×10^{35} erg s^{-1}. On the other hand, if we decrease V_{shell} to 5 km s^{-1}, L_w changes to 1.9×10^{33} erg s^{-1}. Thus, the expansion velocity is a crucial parameter that decides the stage of expansion of the H II region.

We also detect a large scale diffuse emission in the radio waveband associated with S1, which conforms to the morphology of emission from warm dust. The large scale morphology of radio emission can be attributed to the density gradient where the H II region expands out towards regions of lower density (Israel, 1978; Tenorio-Tagle, 1979). Fig. 3.21(b) shows the distribution of ionised gas with respect to the column density map. The large scale radio emission is distributed nearly perpendicular to the long-axis of the cloud where the column density is high. This explains the expansion of ionised gas towards regions of lower density i.e. towards north-west and south-east, whereas towards the east and west of the radio peak, it is constricted by the high density gas,

consistent with the champagne flow model.

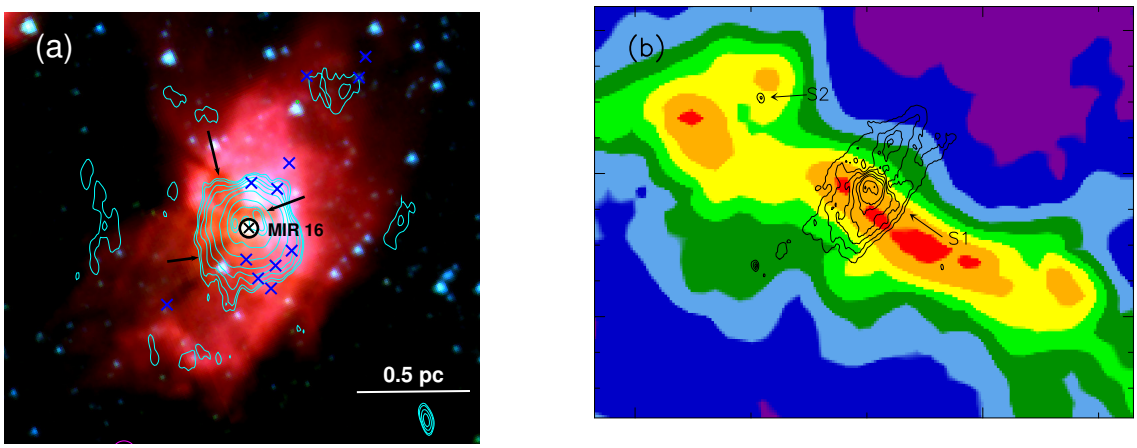

Figure 3.21: (a) *Spitzer*-IRAC color composite image of S1. Blue represents 3.6 μm, green 4.5 μm and red 8 μm. Radio emission at 1300 MHz is overlaid as cyan contours. All YSO candidates within the radio contours are marked as $\times$. The location of the mid-infared Class I object MIR16 which is at the centre of the radio emission is marked and labeled in the image. Arrows point toward high extinction filamentary structures. (b) Smoothed column density map of G333.73 overlaid with 1300 MHz radio contours (black).

To unravel the stars responsible for the ionised gas emission, we probe the region for YSO population, particularly towards the geometric centre (RA: $16^h20^m09.89^s$, Dec: $-49°36'15.32''$) of the bubble/shell. The Lyman continuum flux predicts O9.5-B0 as the single ZAMS star exciting the shell. In this estimate, the diffuse emission is not taken into consideration. While we have been unable to detect any object at the geometric centre (in near or mid-infrared), we have detected a Class I source, MIR16, close to the centre (angular separation of $2''$). The lack of detection of any source at the geometric centre is probably due to the nebulosity and high extinction in this region, reinforced by the high extinction filamentary structures observed in the near- and mid-infrared wavelength bands, visible in Fig. 3.21(a). We cannot rule out the possibility of an ionizing source being deeply embedded in the filamentary structures. In addition, we detect ionised peaks around the shell with lower flux density at 1300 MHz, shown in Fig. 3.21(a). This would suggest that the large scale radio emission could be the result of multiple objects rather than a single ionizing source, although it is possible that this is the fragmented emission from the nebulous gas. We also detect six YSOs around the

radio shell. The distribution of these objects around the radio shell is explicable on the basis of lower extinction as well as nebulosity in these regions.

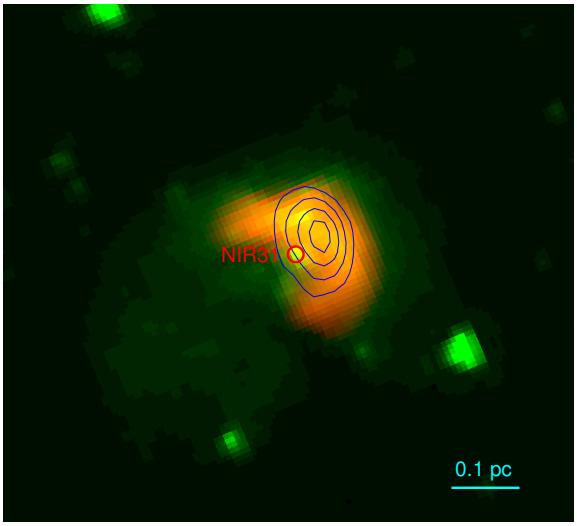

Figure 3.22: *Spitzer*-IRAC color composite image of S2. The 4.5 μm emission is shown in green and 8 μm is in red. Circle marks the YSO source NIR31. High resolution radio map at 1300 MHz is overlaid as blue contours. Contour levels are same as that of Fig. 3.16(b).

3.7.2 S2

In this subsection, we examine the morphology of the compact H II region S2 (see Fig. 3.22), that is located towards the north-east of S1 and possesses an arc-like structure when viewed in the mid-infrared warm dust emission. Diffuse nebulosity at lower flux levels in mid-infrared, spanning a region 0.4×0.3 pc^2, is directed away from the concave edge of the arc. This cometary shaped object is oriented along the NW-SE direction (see Fig. 3.22). At 24 μm, the emission is saturated and hence the distribution of emission is indecipherable. Such mid-infrared arc-shaped features have been observed towards other star forming regions (e.g., Povich et al., 2008; Nandakumar et al., 2016) and could be attributed to (i) expansion of an H II region, (ii) bow-shocks due to high velocity stars (Povich et al., 2008) or (iii) dust or bow-wave (Ochsendorf et al., 2014a). The radio emission towards S2 is compact but shows hints of extension towards the diffuse emission affirming the cometary outlook of the warm dust emission. The radio emission peaks approximately mid-way on the arc. The YSO, NIR31, is located $\sim 3''$ away from the radio peak. This source is classified as a pre-main sequence star based on the

NIR color-color diagram as well as from the SED modelling. The mass of this object is estimated to be $5-7\,\mathrm{M}_{\odot}$, an intermediate mass YSO. Radio emission has been detected from several low and intermediate mass YSOs and are ascribed to stellar winds (Panagia & Felli, 1975; Martin, 1996) or collimated ionised jets (Reynolds, 1986). We look into the possibility of NIR31 being the ionizing source of S2.

We first consider the bow-shock model as the origin of the mid and far-infrared arc-shaped emission (e.g., France et al., 2007; Kobulnicky et al., 2016). Massive stellar objects with energetic winds generate strong shocks in the surrounding medium. If the relative motion between the star and ambient medium is large, the shock will be bent back around the star. For supersonic velocities, the ambient gas is swept up into an arc-shaped bow-shock and has been observed around several massive objects (e.g., Peri et al., 2012, 2015). We use simple analytic expressions to calculate the shock parameters. For a star moving supersonically in the plane of the sky, the bow-shock is expected to trace a parabola. The shock occurs at a stand-off distance R_0 from the star where the stellar wind momentum flux equals the ram pressure of the ambient medium. The stand-off distance in the thin shell limit can be calculated using the expression (Wilkin, 1996):

$$R_0 = \sqrt{\frac{\dot{m}_* v_w}{4\pi \rho_a v_*^2}} \tag{3.14}$$

Here $\dot{m}_*$ is the stellar wind mass-loss rate, v_w is the wind's terminal velocity, ρ_a is the mass density of the ambient gas and v_* is the relative velocity of the star through the medium. The stellar wind mass-loss rate ($\dot{m}_*$) and wind terminal velocity (v_w) are calculated using the expressions (Mac Low et al., 1991)

$$\left[\frac{\dot{m}_*}{10^{-6}\mathrm{M}_{\odot}\mathrm{yr}^{-1}}\right] = 2 \times 10^{-7} \left[\frac{L}{\mathrm{L}_{\odot}}\right]^{1.25} \tag{3.15}$$

$$\log\left[\frac{v_w}{10^{8}\mathrm{cm\,s}^{-1}}\right] = -38.2 + 16.23 \log\left[\frac{\mathrm{T_{eff}}}{\mathrm{K}}\right] - 1.70 \left(\log\left[\frac{\mathrm{T_{eff}}}{\mathrm{K}}\right]\right)^2 \tag{3.16}$$

From the radio continuum emission we estimate the spectral type of the ionizing source as B0-B0.5. Considering a B0.5 type star, we have adopted luminosity $L = 1.1 \times 10^4\ L_\odot$ and effective temperature $T_{eff} = 26,200$ K, (Panagia, 1973). Using these values, we get $\dot{m}_* = 0.23 \times 10^{-7}$ $\mathrm{M_\odot yr^{-1}}$ and $v_w = 1060$ km s^{-1}. We can estimate mass density using the electron number density derived in Sect. 3.4, using the expression $\rho_a = \mu m_{\rm H} n_e$ where $n_e = 1.3 \times 10^3$ cm^{-3}. Here μ is mean nucleus number per hydrogen atom taken as 1.4 and $m_{\rm H}$ is the mass of hydrogen atom. The distance between NIR31 and radio peak is 0.04 pc that corresponds to 8250 AU. Considering this as R_0, we obtain the stellar velocity v_* as 6.2 km s^{-1}. Typical stellar velocities observed in bow shock regions are $\sim$10 km s^{-1} (van Buren & Mac Low, 1992; Nakashima et al., 2016) which is similar to our estimate. The arc-shaped emission is also symmetric around MIR31. Therefore, we suggest that the observed mid-infrared arc could be a result of bow-shock due to MIR31. The arc-shaped features resulting from the stellar wind bow shocks are also detected in far-infrared wavelengths (e.g., Cox et al., 2012; Decin et al., 2012). Density gradients present in the cloud can also affect the bow shock symmetries (Wilkin, 2000).

The expansion of the H II region towards a low density medium could result in a cometary or arc-shaped morphology. A close examination of the morphology of S2 in 70 and 160 μm bands reveals that the far-infrared dust emission also follows an arc-like morphology similar to that seen at mid-infrared wavebands. At longer wavebands, the resolution prohibits us from distinguishing the morphology of cold dust emission in detail. If the nebulosity (seen in mid- and far-infrared with an inkling in radio) is due to a local density gradient in this direction, we would expect the constriction of ionised flow by a high density medium on the far side of the head or arc. By comparing the radio emission and column density distribution in Fig. 3.21(b), we observe a local maxima in the column density towards the north of S2. As mentioned earlier, the radio emission is slightly extended towards south of column density peak. Hence density gradients might be responsible for the observed morphology of S2. Apart from pure bow-shocks and density gradients, there are various hybrid models that incorporate the effects of stellar winds into existing models (e.g., Gaume et al., 1994; Arthur & Hoare, 2006). Hence it is also possible that the arc-like morphology of S2 is a combination of bow shock and

density gradient.

An alternate possibility that has been considered to justify the arc-shaped emission is the dust wave model. Ochsendorf et al. (2014a) have shown that the arc-shaped emission around the star σ Ori AB is a dust wave, that is a consequence of the interaction of radiation pressure of the star with the dust carried along by the photo-evaporative flow. Such photo-evaporative flows are initiated when the ionisation front leaks out of a dense confining molecular environment into a surrounding strenuous medium. The bow-wave model has also been applied to arc-like structures interior to the partially broken bubbles RCW120 and RCW82 (Ochsendorf et al., 2014b). We believe that the cometary structure in S2 is unlikely to be the outcome of a bow-wave as we do not perceive any bubble structure around S2.

3.8 Evolutionary stages of clumps

We next examine the star forming properties of the clumps in the IRDC using our multiwavelength approach. We estimate the relative evolutionary stages of clumps based on the evolutionary sequence proposed by Chambers et al. (2009) and Battersby et al. (2010). According to Chambers et al. (2009), in an IRDC, the star formation begins with a quiescent clump which evolves later into an active clump (containing enhanced 4.5 μm emission called "green fuzzy" and a 24 μm point source) and finally becomes a red (enhanced 8 μm emission) clump. Battersby et al. (2010) further modified this classification scheme by incorporating radio emission and suggesting that the red clumps are diffuse ones without associated millimeter peaks. They discuss four important star formation tracers: (1) Quiescent clump (no signs of active star formation), (2) Intermediate clumps that exhibit one or two signs of active star formation (such as shock/outflow signatures or 24 μm point source), (3) Active clumps that exhibit three or four signs of active star formation ("green fuzzies", 24 μm point source, UCH II region or maser emission), and (4) Evolved red clumps with diffuse 8 μm emission. Sánchez-Monge et al. (2013) also proposed an evolutionary sequence where clumps are classified as either Type 1 or Type 2 owing to their detection in infrared/millimeter images. A clump is classified as Type 2 if it has associated mid-infrared emission and Type 1 in the absence of mid-infrared emission. Thus, the quiescent clumps are Type 2 whereas intermedi-

ate/active clumps are Type 1.

We have searched for MIPS 24 μm point sources associated with the clumps within a search radius of $10''$ from the peak position. We also sought the locations of masers in this region in literature. We find that while there has been a search for 22 GHz water maser and 6.7 GHz methanol maser (half power beam widths of $7'$ and $3.3'$) towards this star forming region, the masers were not detected (Braz et al., 1989; Schutte et al., 1993; Walsh et al., 1997). Hence, we have used solely the radio and mid-infrared data to classify the clumps. The results are presented in Table 3.8. The columns in the table list the clump name, association with radio and 8 μm peaks, and 24 μm point source. Column 5 testifies to the clump activity (Q-quiescent, A-active, I-intermediate, E-evolved) and Column 6 shows whether a clump is in Type 1 or Type 2 evolutionary stage. Among the ten clumps considered, two (C1 and C2) are active/evolved clumps, two (C6 and C7) are intermediate clumps and the rest eight are quiescent clumps. The two active/evolved (A/E) clumps, C1 and C2, have higher dust temperatures ($T_d > 20$ K) compared to other clumps. The molecular gas associated with C1 also shows evidence of protostellar infall. The star formation activity in C1 and C2 have already been discussed in previous sections and these clumps corresponds to the star forming regions S1 and S2. The intermediate clumps: Clump C6 harbours two mid-infrared YSOs MIR4 and MIR5 whereas Clump C7 is associated with the YSO MIR8.

3.9 Star forming potential of quiescent clumps

We probe the dynamical state of the quiescent clumps by comparing their free-fall and dynamical timescales. The parameter free-fall time (τ_{ff}) is defined as the timescale over which an object will collapse into a point under its own gravity. We estimate the free-fall time of the quiescent clumps using the expression

$$\tau_{ff} = \left[\frac{3\,\pi}{32\,G\,\rho}\right]^{1/2} = 3.4\,\left[\frac{100}{n_{\rm H2}}\right]^{1/2}\ \text{Myr} \tag{3.17}$$

where ρ is the density of the molecular clump and $n_{\rm H2}$ is the number density of H_2 molecules (Dobbs et al., 2014). The free-fall time of the 6 quiescent clumps are listed in Table 3.9 and they lie in the range $0.1 - 0.2$ Myr. It is to be noted that the estimates of

Table 3.8: The classification of clumps based on multi-wavelength signposts of star formation.

Clump No.	Radio source	IRAC 8 μm peak	MIPS 24 μm source	Clump activity	Evolutionary Stage
C1	✓	✓	Saturated	A/E	Type 2
C2	✓	✓	Saturated	A/E	Type 2
C3	X	X	X	Q	Type 1
C4	X	X	X	Q	Type 1
C5	X	X	X	Q	Type 1
C6	X	X	✓	I	Type 2
C7	X	X	✓	I	Type 2
C8	X	X	X	Q	Type 1
C9	X	X	X	Q	Type 1
C10	X	X	X	Q	Type 1

[a]Q-quiescent, I-intermediate, A-active, E-evolved based on Battersby et al. (2010)

✓- Detection; X - Non detection

τ_{ff} are based on the current density of the cloud and if the clump is undergoing collapse, then the initial free-fall times may not be the same as the present day estimates.

The dynamical or crossing time τ_{dyn}, defined as the time required for the sound waves to cross the clump and can be estimated using the expression (Tan et al., 2006)

$$\tau_{dyn} = \left[\frac{\mathrm{R}}{\sigma_{obs}}\right] \tag{3.18}$$

Here R is the radius of the clump and σ_{obs} is the velocity dispersion of the cloud. We estimate $\sigma_{obs} \sim 0.9$ km s^{-1} using the FWHM of the optically thin $H^{13}CO^{+}$ line. The dynamical times of the quiescent clumps are listed in Column 4 of Table 3.9 and they lie between $0.3 - 0.4$ Myr. The free-fall and dynamical time estimates can be used to predict whether a clump is gravitationally stable or not. A clump becomes gravitationally unstable if $\tau_{ff} < \tau_{dyn}$ (e.g., Contreras et al., 2017; Sanhueza et al., 2017). To analyse the potential of collapse for these quiescent clumps, we specify the ratio τ_{ff}/τ_{dyn}, tabulated in Column 5 of Table 3.9. All the six quiescent clumps have $\tau_{ff}/\tau_{dyn} < 1$ and these are prone to gravitational collapse. We note that these are representative values

and a more rigorous analysis would entail high resolution molecular line observations to gauge the dispersion velocity in each clump.

Under the assumption that the quiescent clumps undergo collapse, we analyse their potential to form high mass stars. For this, we used the formulation of Svoboda et al. (2016) to find the mass of the most massive star ($\mathrm{M_{max}}$), likely to form in the clump, using a stellar IMF of Kroupa (2001). $\mathrm{M_{max}}$ is estimated using the expression

$$\mathrm{M_{max}} = 20 \left[\frac{\sigma_{\mathrm{sf}}\ \mathrm{M_{clump}}}{0.3 \times 1064 \mathrm{M_{\odot}}} \right]^{1/1.3} \mathrm{M_{\odot}} \tag{3.19}$$

Here, σ_{sf} is the star forming efficiency in the clump, taken as 30% in the present work (Lada & Lada, 2003). The estimated $\mathrm{M_{max}}$ for the 6 quiescent clumps are listed in Table 3.9. The mass estimates range from $2.9 - 10.4$ $\mathrm{M_{\odot}}$. This suggests that all the quiescent clumps in this region have the potential to form intermediate to massive stars.

Table 3.9: Properties of the 6 quiescent clumps.

Clump No.	$\mathrm{M_{max}}$ ($\mathrm{M_{\odot}}$)	τ_{ff} (Myr)	τ_{dyn} (Myr)	τ_{ff}/τ_{dyn}
C3	10.4	0.2	0.4	0.5
C4	9.7	0.2	0.4	0.5
C5	8.5	0.2	0.4	0.5
C8	2.9	0.2	0.3	0.7
C9	10.3	0.2	0.4	0.5
C10	8.6	0.1	0.3	0.3

3.10 Fragmentation in the filamentary cloud

From clumps, we move on to the expanse of the cloud in order to assimilate a larger picture of the IRDC. G333.73 is located in the fourth Galactic quadrant where multiple Giant Molecular Filaments (GMFs) are located. GMFs are tremendously long filamentary clouds (aspect ratio $\sim$ 50 or larger) with lengths exceeding 100 pc. A recent study by Goodman et al. (2014) suggests that these GMFs, also designated as 'bones', can be used to constrain the spiral structure of the Milky Way. A number of

bone-like filaments have been identified in our Galaxy (e.g., Zucker et al., 2015; Wang et al., 2016). Large scale PV diagrams (i.e Galactic longitude versus velocity) reveal that many of these GMFs have velocity structures consistent with or close to that of the Scutum-Centaurus arm (see Zucker et al., 2015; Li et al., 2016). For G333.73, based on its Galactic longitude (333.73) and LSR velocity of -33.2 km s^{-1}, we believe that the cloud is located in the inter-arm region, closer to the Scutum-Centaurus arm in comparison to the Sagittarius-Carina arm (Abreu-Vicente et al., 2016) also evident from Fig. 3.23. The smaller size ($\sim$7 pc) and aspect ratio ($\sim$5) of G333.73 suggests that this filament is unlikely to be a GMF itself. This is corroborated by studies where star formation in nearby molecular clouds have demonstrated that the distribution of gas and dust is often filamentary comprising of either a single filament or a network of filaments. These are believed to trace the densest regions of GMFs (Haikala et al., 2005; Myers, 2009; Contreras et al., 2016). Recent surveys have found hundreds of filaments using *Herschel* and ATLASGAL (Schisano et al., 2014; Li et al., 2016). These filaments have lengths in the range $1-30$ pc, typical aspect ratios $\sim 2-30$, and are dense ($N(\mathrm{H_2}) \sim 10^{21}-10^{22}$ cm^{-2}) and massive ($100-10^5$ M$_\odot$). The size, aspect ratio, mass (4700 M$_\odot$) and average column density ($\sim 2.4\times10^{22}$ cm^{-2}) of G333.73 fall well within the range of values observed for other filamentary clouds.

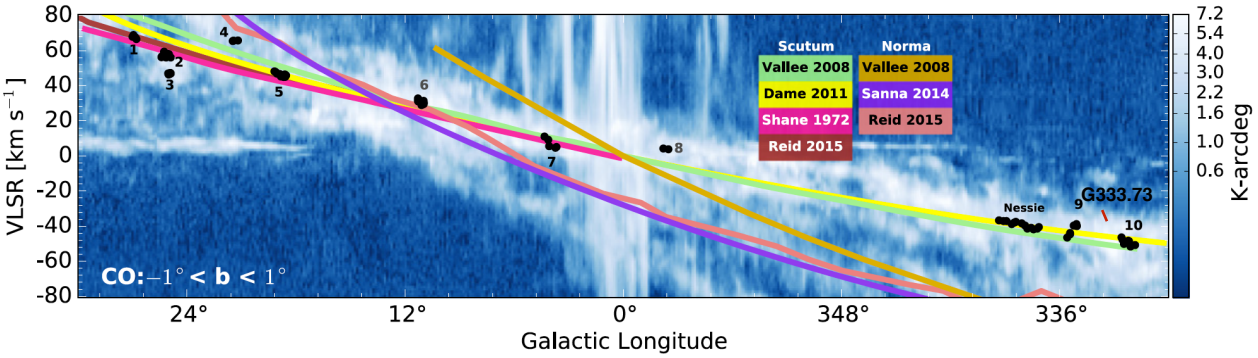

Figure 3.23: Position-velocity digram of the MilkyWay adopted from Zucker et al. (2015). Also shown are the spiral arm models from various studies as well as the location of the bone candidates. The location of the IRDC G333.73 is marked and labelled.

We next compare the clump properties with those expected from the theoretical predictions of fragmentation of a filamentary cloud. Assuming that the clumps are governed by Jeans instability, we estimate the Jeans length of the homogeneous gas

using the expression (Carroll & Ostlie, 1996; Wang et al., 2014)

$$\lambda_{\rm J} = c_s \left(\frac{\pi}{G\rho}\right)^{1/2} = 0.066 \left(\frac{T}{10\ {\rm K}}\right)^{1/2} \left(\frac{n}{10^5\ {\rm cm^{-3}}}\right)^{-1/2}\ {\rm pc} \tag{3.20}$$

where G is the gravitational constant and c_s is the sound speed, T is the temperature of the clump and n is the number density. The expression for Jeans mass is given as

$$M_{\rm J} = \frac{\pi^{5/2}\, c_s^3}{6\sqrt{G^3\rho}} = 0.877 \left(\frac{T}{10\ {\rm K}}\right)^{3/2} \left(\frac{n}{10^5\ {\rm cm^{-3}}}\right)^{-1/2} {\rm M_\odot} \tag{3.21}$$

Employing average values of (i) temperature ~ 16.8 K and (ii) number density $\sim 3.6 \times 10^4$ cm^{-3}, of the clumps in this region (Sect. 3.2), we determine $\lambda_{\rm J} \sim 0.2$ pc and $\rm M_J \sim 3.3\ M_\odot$. Observationally, the radii of the clumps are found to lie between $0.3 - 0.9$ pc while the clump masses range from 87 to 1530 $\rm M_\odot$. The radii of these clumps are consistent with the calculated Jeans length whereas the masses are larger by a factor of $\gtrsim 25$ compared to the Jeans mass. The thermal pressure by itself predicts smaller Jeans mass than the observed clump masses, suggesting the dominance of turbulence in this region. This supports the idea that turbulence achieves greater significance in high mass star forming regions (Lada et al., 2008). As the molecular line width could have contributions from both thermal and non-thermal components, it is possible to estimate the magnitude of each of these effects. The mean thermal broadening can be calculated using the equation $V_{\rm therm} = \sqrt{k\,T_{\rm ex}/\mu\,m_{\rm H2}}$ and is found to be $\sim$0.2 km s^{-1} for the average clump temperature. This is nearly a factor of four lower than the mean velocity dispersion of 0.9 km s^{-1} implying the supersonic nature of the filament.

The clumps in G333.73 appear to be spaced regularly along the filament. The fragmentation along the filaments can explained using the 'sausage instability' model (Chandrasekhar & Fermi, 1953) that can approximate a filamentary cloud to an isothermal cylinder. The self-gravitating cylinder in equilibrium has a critical linear mass density above which it will undergo gravitational collapse. If the turbulent pressure dominates over thermal pressure, the critical linear mass density is given by the expression (Jackson et al., 2010):

$$(M/l)_{crit} = 84\,\Delta V^2\ {\rm M_\odot\ pc^{-1}} \tag{3.22}$$

For ΔV = 2.2 km s^{-1}, $(M/l)_{crit}$ is found to be 407 M$_\odot$ pc^{-1}, whereas the linear mass density of G333.73 is $(4700/7.2) \sim 653$ M$_\odot$ pc^{-1}. We observe that this exceeds the critical limit and hence the cloud may be on the verge of global collapse. This is consistent with the infall motion seen in Clump C1 (Sect. 3.3.3) as well as accretion signatures observed on a larger scale (next section). The presence of YSOs (André et al., 2010) and massive star formation (Li et al., 2016) substantiates the supercritical nature of the filamentary cloud.

3.11 Velocity gradient in G333.73: Rotation or accretion?

As discussed in Sect 3.3.4, we have detected a fairly regular velocity gradient across the length of the filament. We first investigate whether this gradient could be a result of cloud rotation and estimate the ratio of rotational-to-gravitational energies, β, for a cylindrical cloud using the expression (Jiménez-Serra et al., 2014, and references therein)

$$\beta = \frac{E_{\rm rot}}{E_{\rm grav}} \sim \frac{\Omega^2\, L^3}{36\, G\, M} \sim \frac{V_{\rm grad}^2\, L}{36\, G\, M} \tag{3.23}$$

Here, $E_{\rm grav}$ is the gravitational energy of the cylindrical cloud given by $E_{\rm grav} = \frac{3}{2}\frac{G\,M^2}{L}$, for a cloud of mass M and length L and G is the gravitational constant. $E_{\rm rot}$ is the kinetic energy due to the cloud's rotation defined as $E_{\rm rot} = \frac{1}{2} I\, \Omega^2$, where Ω is the angular speed of the cloud and I is the moment of inertia given as $I \sim \frac{M\,L^2}{12}$ when the rotational axis is perpendicular to the long axis of the cylinder. Ω is estimated using the velocity gradient $V_{\rm grad}$ across the length, $V_{\rm grad}/L$. For the case of G333.73, we consider $M \sim 4700$ M$_\odot$, $L \sim 7.2$ pc and $V_{\rm grad} \sim 5/7.2 \sim 0.7$ km s^{-1} pc^{-1}. This gives $\Omega \sim 2.3 \times 10^{-14}$ s^{-1}, and $\beta \sim 0.3$. Ragan et al. (2012b) cite a value of $\beta \sim \frac{1}{3}$ as the breakup speed for rotating clouds, with larger values of β preventing cloud fragmentation and star formation. Our value of β is close to the break-up speed. However this value is estimated using gradients from relatively low density tracers (^{13}CO) that can be dominated by turbulent motions (Arquilla & Goldsmith, 1986; Goodman et al., 1993). This is also in accordance with what is observed by us. Therefore, our estimation of

$\beta \sim 0.3$ using ^{13}CO is plausibly an overestimate. The presence of clumps as evidences of fragmentation suggests that any contribution of rotation to the velocity gradient is likely to be negligible.

An alternate scenario to explain the velocity gradient is accretion flows along the filament (Smith et al., 2013; Tobin et al., 2012). Under this presumption, we estimate the gas accretion rate along the filament ($\dot{M}$) considering a simple cylindrical model (Kirk et al., 2013) using the following expression:

$$\dot{M} = \frac{V_{\rm grad}\, M}{\tan(\alpha)} \tag{3.24}$$

Here, α represents the angle of inclination of the long-axis of the cylinder with respect to the plane of the sky. A value of $\alpha \sim 0^{\circ}$ would prohibit the detection of velocity gradient, whereas $\alpha \sim 90^{\circ}$ would prevent the cylindrical cloud appearing elongated to us. Taking an average value of $\alpha \sim 45^{\circ}$, we find the accretion rate to be 4.6×10^{-3} $\rm M_{\odot}\,yr^{-1}$. This accretion rate is similar to those found in other star forming regions (e.g., Galván-Madrid et al., 2009; Jiménez-Serra et al., 2014). We, therefore, believe that the accretion flows can reasonably explain the large scale velocity gradient found in G333.73, rather than rotation. The findings support the infall motion observed in the high density gas tracers and supercritical linear mass density derived earlier. However, we cannot rule out the residual effect of velocity coherence that has been widely observed in GMFs (Ragan et al., 2014; Wang et al., 2015).

3.12 Age limit of the IRDC

After examining the global traits of G333.73, our motivation is to uncover a limit to the age of the IRDC based on our multiwavelength analysis. The fragmentation of the cloud to clumps and the level of star forming activity within should permit us to ascertain the broad evolutionary state of the IRDC (Jackson et al., 2010). The dark quiescent filaments prior to the hot-core phase are believed to be in the earliest stages (Carey et al., 2000; Wang et al., 2014). The IRDCs that harbour young H II regions are likely to be in the intermediate phase (Xu et al., 2016, 2017). Thereafter, the H II regions evolves with time and disperses the IRDC, leading to the emergence of the embedded cluster

which reveal the active sites of massive star formation such as Orion and NGC 6334. As G333.73 is associated with clumps that harbour H II regions and YSOs, it is consistent with the proposition that IRDCs are the precursors of massive star clusters and can form multiple high mass stars simultaneously. The expanding H II region in G333.73 is in the process of dispersing the natal cloud in its immediate vicinity [Fig. 3.21(b)]. Therefore, we believe that G333.73 is in an intermediate phase as compared to prestellar filamentary clouds and highly evolved regions that harbour massive star clusters in our Galaxy.

In this work, we presented different timescales such as the age of H II region, age of YSOs from SED modelling, free-fall and dynamical timescales of the clumps. We now compare these estimates and attempt to derive a limit for the current age of G333.73. The expansion time scales of the compact H II regions, S1 and S2, are found to be 0.2 and 0.01 Myr respectively. We also estimated the free-fall and dynamical times of the quiescent clumps, that lie within the range: $0.1 - 0.4$ Myr. The ages of YSOs in this region, based on the best fit to the SED using radiative transfer models, fall in the range $0.1 - 9.6$ Myr. All the YSOs except one, MIR8, are younger than 2 Myr according to the best-fit models. For MIR8, we find that the lower limit to the age among ten best fit models is 0.2 Myr. If we consider the YSOs other than MIR8, we could assign a lower limit to the age of G333.73 as 2 Myr. The ages of giant molecular clouds (GMCs) are usually estimated to be nearly two to three times the free-fall timescale (Murray, 2011). The free-fall times of GMCs are estimated using a mean cloud density, based on the CO emission density that is converted directly to a hydrogen column density assuming a constant CO to H_2 abundance ratio (e.g., Scoville & Solomon, 1975; Gordon & Burton, 1976; Sodroski, 1991). We estimated the mean CO density of the cloud from our CO maps and find $n(\mathrm{H_2}) \sim 2300$ cm^{-3}. This corresponds to $\tau_{ff}^{cloud} \sim 0.7$ Myr giving an age estimate of ~ 2 Myr. This is in conformity with those obtained by other means. However, a caveat is that we are sampling the relatively higher density region of the cloud and it may not be prudent to use these densities to obtain a measure of the limit to the age of the cloud.

We reform our goal to estimate the age of the clumps as that can provide a lower limit to the age of the IRDC. In order to carry this out, we refer to the characteristic timescales occupied by the starless and star-forming phases in a cloud. Battersby et al. (2017) carried out a pixel-by-pixel analysis of the cloud complex within a $2^\circ \times 2^\circ$ of the

Galactic plane and noticed that the starless phase occupies nearly $60-70\%$ of the dense molecular region (DMR) lifetime while the star forming phase is approximately $30-40\%$ of the total DMR lifetime. The total lifetime of DMRs $\tau_{\rm tot}$ based on the association with ultracompact H II regions (UCH II) is given by the following expression (Battersby et al., 2017):

$$\tau_{\rm tot} = \frac{\tau_{\rm UCH\,II}}{f_{\rm star}\, f_{\rm UCH\,II}} \tag{3.25}$$

where $\tau_{\rm UCH\,II}$ is the age of the UCH II region, $f_{\rm star}$ is the fraction of starry pixels and $f_{\rm UCH\,II}$ is the fraction of pixels that are associated with UCH II regions. We apply the above expression to clumps themselves in order to secure a limit to the age. Based on our clump analysis, we demonstrated that 4 clumps are in star-forming phase (i.e. active, evolved and intermediate) and rest 6 are in quiescent phase. This gives us the fraction of starry clumps as 40%. Of the 4 star-forming clumps, 2 harbour compact H II regions that leads us to $f_{\rm UCH\,II} \sim 50\%$. $\tau_{\rm UCH\,II}$ is taken as 0.2 Myr, considering the H II region expansion timescale of S1 estimated in Sect. 3.4. This is in agreement with the age of ultracompact H II regions from chemical clocks (Treviño-Morales et al., 2014). We then estimate a lower limit to the lifetime of G333.73 as 1 Myr. This is consistent with the absolute lifetime estimate of Battersby et al. (2017) for massive star forming clouds which is $1-3$ Myr. We also obtained similar estimate based on the age of YSOs. Hence, the age of G333.73 is likely to be 1-2 Myr. An upper limit could be the lifetimes of GMCs in our Galaxy, which is found to lie between $10-20$ Myr (Murray, 2011; Dobbs et al., 2014) although GMFs are expected to be older (Duarte-Cabral & Dobbs, 2017).

3.13 Summary

In this chapter, the star formation activity towards the southern filamentary IRDC G333.73+0.37 was examined. Combining the data at infrared, submillimeter and radio wavelengths, we find that the region harbours a multitude of objects in different evolutionary stages, ranging from quiescent clumps to H II regions. The filament as a whole is supercritical. The expanding H II region S1 is in the process of dispersing the cloud in its immediate

vicinity. Thus, IRDC G333.73+0.37 is in intermediate phase compared to prestellar filamentary clouds and highly evolved regions that harbour massive star clusters. We find a lower limit to the age of this IRDC as $1 - 2$ Myr.

Chapter 4

Star Formation Activity Towards the Southern Cometary H II region IRAS 17256–3631

In this chapter we investigate the star formation activity in an H II region IRAS 17256–3631. A vital phase in the formation of a massive star is that of an H II region that is still embedded in the nascent molecular cloud (i.e. not visible optically) and undergoing expansion. An examination of the H II region and its parental cloud are crucial for the comprehension of the evolution of the H II region and the formation of the next generation of stars (Barbá et al., 1999). While observations of molecular clouds at far-infrared and millimeter wavelengths give an insight into the evolution of precluster clouds and fragmentation process, the ionised gas distribution and young stellar objects help examine the physical conditions in the advanced stages of high mass star formation. One has to carefully look at multiple wavelengths in order to get a collective picture of the massive star formation mechanism and how it acts as a feedback system for the surrounding interstellar medium.

In literature, the distance to IRAS 17256–3631 is given as 2 kpc (Fontani et al., 2005; Beltrán et al., 2006; Sánchez-Monge et al., 2013) and 14.7 kpc (Quireza et al., 2006b). In the present work, we adopt a distance of 2 kpc from Fontani et al. (2005) based on the CS-line kinematics. The infrared luminosity of this region is 6.4×10^4 $L_\odot$ (Fontani et al., 2005). This is classified as a low (L) type region. These L type regions are based on the IRAS color indices $[25-12] < 0.57$ and $[60-12] < 1.30$ and are believed to be optimum targets to search for high mass protostars (Palla et al., 1991). Our new estimate of the luminosity gives a value of 1.6×10^5 $L_\odot$ (discussed later). The molecular line and millimeter continuum studies by Fontani et al. (2005) have identified this region to be associated with massive protostellar candidates. Beltrán et al. (2006) had identified 11 massive dust clumps with masses ranging from 387 – 23 $M_\odot$ from their millimeter wave continuum emission studies. Radio continuum observations by Sánchez-Monge et al. (2013) detected emission at 18.0 and 22.8 GHz from this region (Beam size $\sim 30''$). Bica et al. (2003) have detected an infrared star cluster (No. 166 in

their catalog) with an angular size of $1.6'$ that is located $19''$ away from the luminous IRAS source position.

Here, we present a multiwavelength study of the region using infrared, submillimeter and radio continuum wavelengths. The radio observations using GMRT array enable us to probe the small and large scale structures simultaneously. The highly sensitive data from UKIRT allow us to look deeper into the infrared cluster detected by Bica et al. (2003). In order to locate the clumps of dense gas-dust and to understand the energetics, we use the Herschel Hi-GAL and ATLASGAL data at far-infrared and submillimeter wavelengths .

4.1 Radio emission from ionised gas

The radio continuum emission from IRAS 17256–3631 at 1372, 610 and 325 MHz are shown in Figs. 4.1a, 4.1b and 4.1c respectively. The morphology of the H II region is strikingly similar to that of the cometary-shaped ultracompact H II region described by Wood & Churchwell (1989). There is a steep density gradient towards north-west characterized by a bright, arc-like leading edge (or head) and a low surface brightness tail of emission. The angular size of the radio emitting region is $\sim 5' \times 4'$ (2.9×2.3 pc). The total flux densities (upto 3σ contour level of the peak flux density) at 1372, 610 and 325 MHz are 8.5, 13.2 and 33.6 Jy, respectively. The radio emission at 1372 MHz peaks at $\alpha_{\rm J2000}$: $17^{\rm h}29^{\rm m}02.2^{\rm s}$, $\delta_{\rm J2000}$: $-36°33'30.2''$. The location of radio peak positions at all three frequencies match well (within $3''$). The peak flux densities, synthesized beams, flux densities and rms flux density values are given in Table 5.1.

The Lyman continuum photon flux at 1372 MHz was estimated using the equation (Mezger & Henderson, 1967; Sánchez-Monge et al., 2013),

$$\left[\frac{N_{Ly}}{\rm s^{-1}}\right] = 8.9 \times 10^{40} \left[\frac{\rm S_\nu}{\rm Jy}\right] \left[\frac{\nu}{\rm GHz}\right]^{0.1} \left[\frac{\rm T_e}{10^4 K}\right]^{-0.45} \left[\frac{\rm d}{\rm pc}\right]^2 \quad (4.1)$$

where, S_ν is the flux density at frequency ν, T_e is the electron temperature, and d is the distance to the source. Based on the electron temperature gradient across the Galactocentric distance (Churchwell et al., 1978), the electron temperature for this region is found to be 7500 K. Using this value, the Lyman continuum flux is found to be

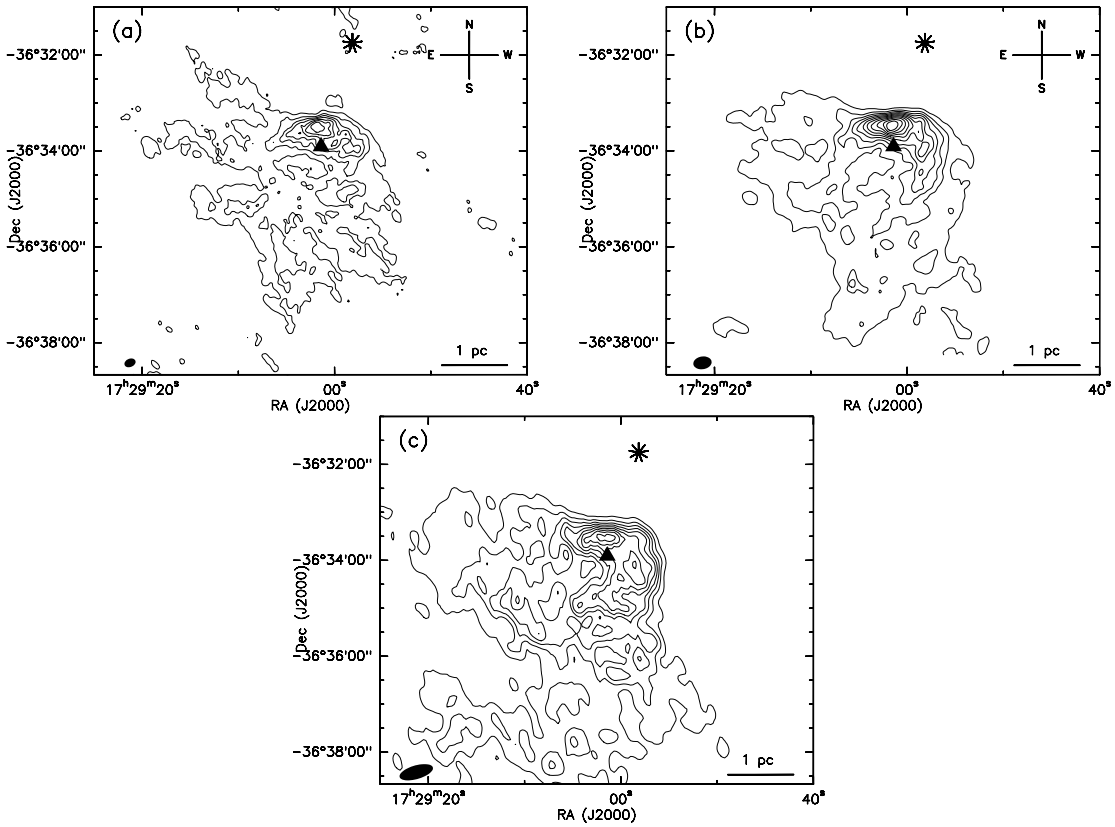

Figure 4.1: (a) Radio continuum map at 1372 MHz. The contour levels are at 3, 11, 19, 27, 36, 44, 52 and 60 mJy/beam with beam size of $7.3'' \times 5.2''$. (b) Radio continuum map at 610 MHz. The contour levels for 610 MHz map are at 8, 19.5, 31.0, 42.6, 54.2, 65.7, 77.2, 88.8, 100, 112, 123 and 135 mJy/beam where the beam size is $11.5'' \times 7.9''$. (c) Radio continuum map at 325 MHz. The contour levels for 325 MHz are 20, 44, 68, 92, 116, 140, 164, 188, and 212 mJy/beam where the beam size is $21.7'' \times 8.5''$. The corresponding beams are shown in the bottom left corner of the images in black. Cross and triangle correspond to EGO-1 and IRS-1 (discussed in text).

3.5×10^{48} s^{-1}. This is a lower limit since the emission may be optically thick at this frequency. If a single ZAMS star is responsible for the ionization of the entire region, from our flux density measurements, we find that the ZAMS spectral type of this star to be earlier than $\mathrm{O7} - \mathrm{O7.5}$ (Panagia, 1973). From the high frequency radio continuum observations, Sánchez-Monge et al. (2013) estimated the spectral type of the ionizing source as O9 that is of later type when compared to our estimate. This is probably because they are not be sampling the diffuse emission completely. An additional reason for their later spectral type is their assumption of electron temperature of 10^4 K com-

pared to our 7500 K. Using the latter temperature would lead to a spectral type that is ~ 0.5 earlier.

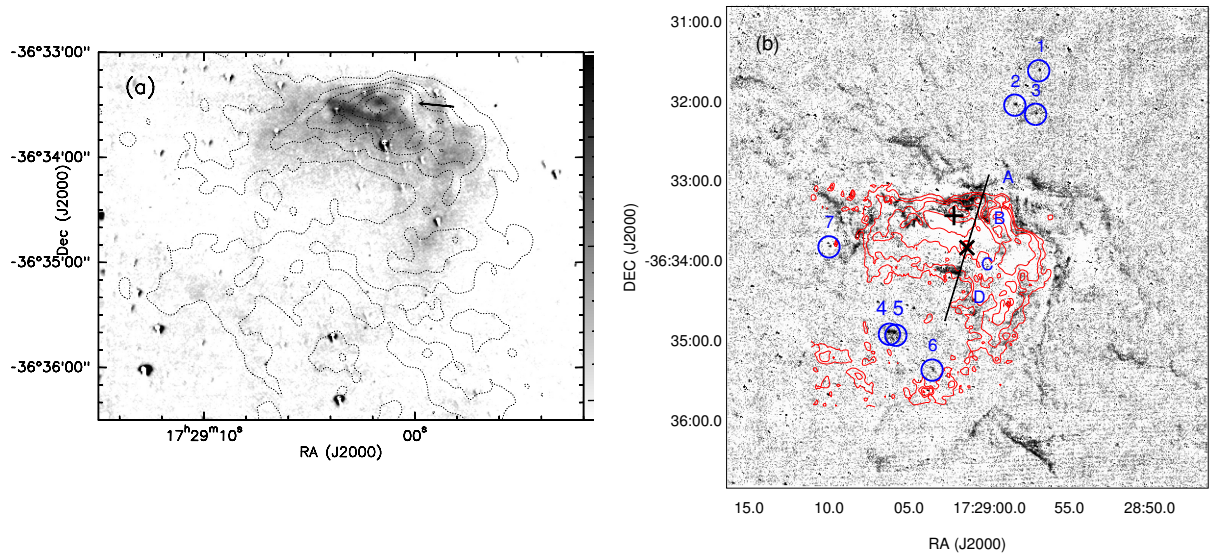

Figure 4.2: (a) The continuum subtracted Brγ image of the field around IRAS 17256–3631 overlaid with 1372 MHz radio contours. The contour levels are at 6, 15, 24, 33, 42, 51 and 60 mJy/beam. Residuals of continuum subtraction around the stars are seen in this image. The arrow point towards a high extinction filamentary structure; (b) The Narrow band H_2 image of the region IRAS 17256–3631 overlaid with Brγ contours. The image has been smoothed to 3 pixels to improve the contrast against the background noise. Emission is seen as black filaments in the image. The detected H_2 knots are encircled and numbered. Radio peak is marked (+ point). The black line represents the UKIRT slit position centered over IRS-1 (cross point). The four regions from which the nebular spectrum were taken are labelled as A, B, C and D in the image.

An alternative gauge of the ionised gas is the Brγ recombination line (2.16 μm) in the near-infrared. The continuum subtracted Brγ image of the field around IRAS 17256–3631 is shown in Fig. 4.2a. The image displays a similar cometary morphology, with the head towards the north-west direction that matches the radio continuum emission. However, being a near-infrared line, this suffers from extinction. This is evident from the high extinction regions seen in the Brγ map.

4.1.1 Spectral Index Maps

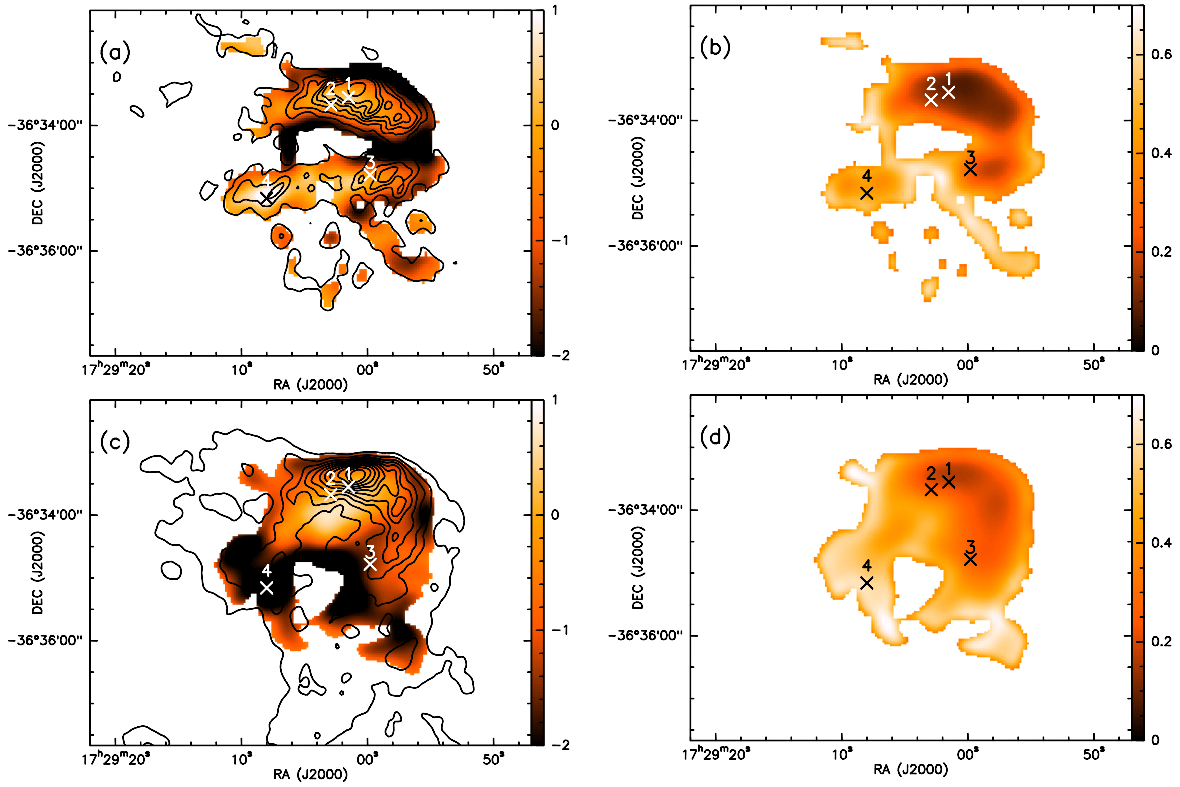

Figure 4.3: (a) The 1372-610 spectral index map overlaid with 1372 MHz radio continuum contours. The four locations at which the spectral indices are computed are also shown in the figure. (b) Error map of 1372-610 spectral index map. (c) 610-325 spectral index map overlaid with 610 MHz radio continuum contours. The four locations shown in (a) are also shown here. (d) Error map corresponding to the 610-325 spectral index map.

The spectral index map is a useful tool to study the variation of spectral index across the H II region and to get an idea about the mechanisms responsible for radio emission. We created two spectral indices maps, corresponding to 1372 - 610 MHz and 610 - 325 MHz. For the generation of spectral index maps, we used visibilities from baselines sensitive to emission at same angular scales. We produced images at the three frequencies using the same UV range: $0.18 - 24$ kλ. As each spectral index map requires the two images to be of the same resolution and pixel size, we convolved and regridded maps to a common pixel size and resolution, corresponding to the lower frequency image. The spectral index maps along with their error maps are shown in Fig. 4.3. Both the spectral index maps are similar in morphology. From these maps, we

see that the spectral indices in this region span a wide range, between -2.0 to 1.0. Regions with spectral index larger than -0.1 are believed to arise from thermal emission (Olnon, 1975) while spectral index < -0.5 is believed to be mostly due to non-thermal mechanisms (Kobulnicky & Johnson, 1999). Both the spectral index maps show evidences of non-thermal emission near the head towards the north and north-west, but the uncertainties are also larger here in both the maps. In the 610 - 325 map, the tail region shows steeper negative indices. One has to bear in mind that spectral indices include contributions from both thermal and non-thermal mechanisms, and spectral indices in both maps are likely to be different due to different mechanisms dominating at different frequencies.

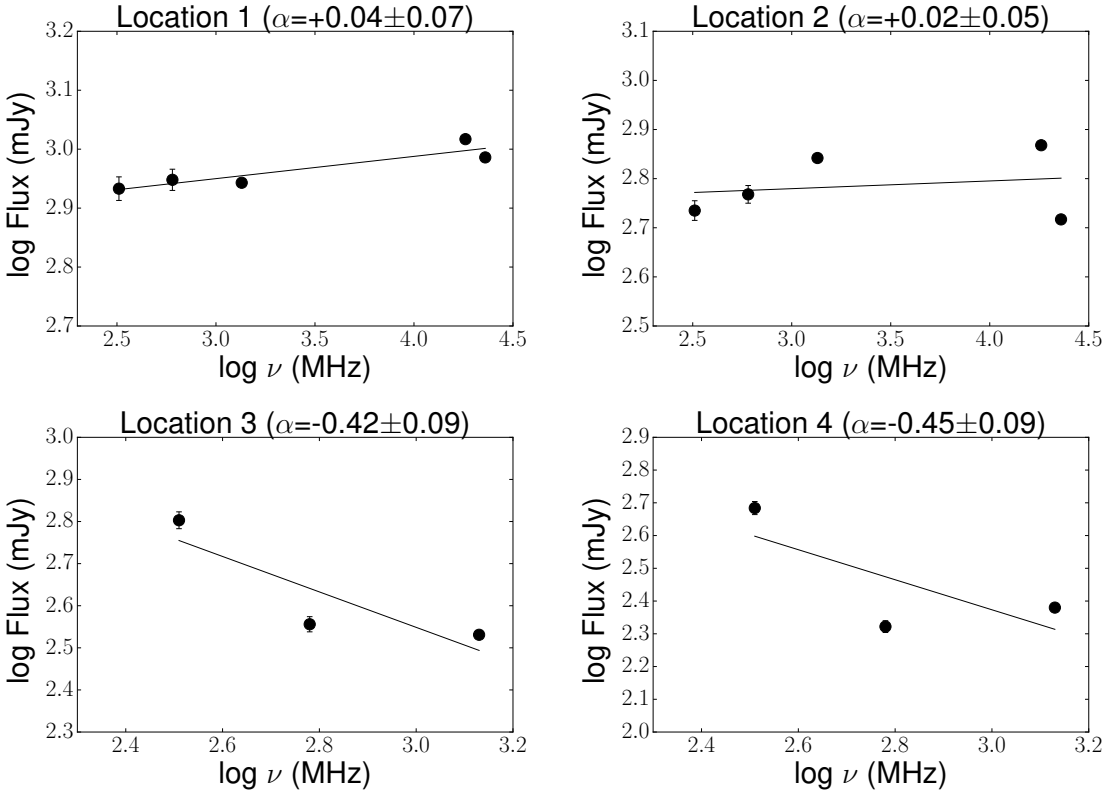

Figure 4.4: The spectral index plots of the four locations shown in Fig. 4.3.

We have compared the spectral indices at different locations using the three GMRT and two ATCA images (Sanchez-Monge et al. 2013), from images convolved to a common resolution of $31'' \times 31''$. The radio SED at 4 representative positions, marked as 1, 2, 3 and 4 in Fig. 4.3 are shown in Fig. 4.4. The spectral indices of these four locations are listed in Table 4.1. Column 1 lists their locations, Column 2 lists the spectral index obtained from fitting to fluxes at five frequencies including ATCA, Column 3 lists the spectral index fitting to fluxes using three GMRT frequencies while Columns 4 and 5

list the spectral indices from 610 - 325 and 1372 - 610 MHz maps, respectively. The positions 1 and 2 have ATCA emission counterparts while positions 3 and 4 have only GMRT fluxes. This is because the ATCA maps are snapshot images of $\sim$10 min integration and we do not see the diffuse emission contribution, particularly towards the south-east. If the ATCA maps do not sample the diffuse emission, then the fluxes at some regions covered by ATCA maps are also likely to be lower than the actual values. While positions 1 and 2 near the radio peak show optically thin thermal emission with positive spectral indices less than 0.1, the other positions (3 and 4) towards the outer envelope show evidences of non-thermal emission. Towards the south-east, near the tail region, the lower frequency (610 - 325) spectral indices are more non-thermal in nature (i.e. steeper negative index) when compared to the higher frequencies, ie. 1372 - 610. This is likely to be because thermal contribution dominates at higher frequencies. IRAS 17256–3631 exhibits a morphology where the spectral indices are nearly flat towards the core and relatively negative towards the diffuse envelope.

Table 4.1: Spectral indices corresponding to the locations shown in Fig. 4.3.

Location	$\alpha_{\rm ATCA+GMRT}$	$\alpha_{\rm GMRT}$	$\alpha_{610-325}$	$\alpha_{1372-610}$
1	0.04±0.07	0.02±0.06	0.13±0.06	-0.01±0.08
2	0.02±0.05	0.18±0.03	0.24±0.08	0.10±0.13
3	-	-0.42±0.09	-0.91±0.15	-0.07±0.16
4	-	-0.43±0.09	-1.25±0.23	0.09±0.25

A similar morphology is observed in other Galactic star forming regions (Curiel et al., 1993; Felli et al., 1993; Garay et al., 1996). In particular, Mücke et al. (2002) have observed non-thermal emission towards the tail of two cometary H II regions. They attribute this to synchrotron emission produced by shocks or magnetic reconnection out of a pool of thermal particles. The combined thermal and non-thermal emission can be present in regions where there is a shock moving through a magnetized medium (Crusius-Watzel, 1990; Henriksen et al., 1991). Garay et al. (1996) proposed that the diffuse non-thermal emission corresponds to synchrotron radiation from electrons that are accelerated in the region of interaction between stellar wind and ambient cloud material. Hence it is likely that shock is responsible for the presence of non-thermal emission around the envelope.

Table 4.2: The positions of identified H_2 knots.

H_2 knot no.	α_{J2000} (^{h} ^{m} ^{s})	δ_{J2000} (^{circ} $'$ $''$)
1	17:28:56.916	-36:31:41.48
2	17:28:58.405	-36:32:07.28
3	17:28:57.109	-36:32:14.24
4	17:29:06.348	-36:34:57.65
5	17:29:05.965	-36:34:58.08
6	17:29:03.565	-36:35:26.19
7	17:29:09.998	-36:33:53.21

4.2 H_2 Emission from molecular gas

The high-excitation molecular gas can be probed using the near-infrared H_2 line. Our continuum-subtracted H_2 image (Fig. 4.2b) shows faint diffuse filamentary emission. A comparison of the H_2 and Brγ emission reveals that the morphology of H_2 is different compared to the ionized gas emission. H_2 is seen at the edges of the ionized gas emission while there is little or no emission in the central region towards the radio peak. This indicates the presence of highly excited molecular gas around the H II region. In addition to the filamentary structures, several H_2 knots are also seen in this region. These are marked in Fig. 4.2b and listed in Table 4.2. All the knots other than knot 7 seem to be aligned towards NW-SE direction with respect to IRS-1 (position angle $\sim$24°. Similar knots are also detected in other star forming regions that are interpreted as shocked emission along the jet axis (Varricatt et al., 2010). One of the H_2 knots (Knot No. 2) is located near the object EGO-1 (discussed later). This knot is likely to be associated with EGO-1.

4.3 Dust emission

4.3.1 Emission from cold dust

Emission at seven wavelength bands have been used to study the physical properties of the cold dust clumps. These include five bands from $Herschel$ Hi-GAL (70, 160, 250, 350 and 500 μm), 870 μm emission from the ATLASGAL survey, and 1.2 mm emission from Beltrán et al. (2006). In order to estimate the dust clump properties, we first identified clumps in 350 μm image as the resolution is optimum, close to the lowest available resolution at 500 μm. Identifying clumps in the higher resolution images at 70 or 160 μm would lead to inappropriate allocation of fluxes in the low resolution images if we use the same apertures in all the wavelength bands. A flip side of identifying clumps using 350 μm image is that more than one clump in a higher resolution image (say 870 μm) could be associated with a single 350 μm image. The clumps are identified using the $2\mathrm{D} - Clumpfind$ algorithm, a two-dimensional variation of the $Clumpfind$ algorithm developed by Williams et al. (1994). The algorithm works by contouring the data at multiples of rms noise in the map and searches for peaks of emission that are identified as clumps. The advantage of $2\mathrm{D} - Clumpfind$ is that it does not $apriori$ assume any clump profile, and the total flux is conserved.

The results from the *Herschel Space Observatory* have shown that filaments are all-prevalent in the Galactic plane, particularly at the longer wavelengths (Molinari et al., 2010a). Such filamentary emission is also seen in the vicinity of this region, IRAS 17256–3631. We are interested in high density clumps characterized by large emission at 350 μm. The threshold and the contour spacing are given as input parameters in terms of the rms. To locate clumps in the 350 μm image, the lowest contour level is set at 830 MJy/Sr corresponding to $\sim 15\sigma$ with a contour step of 2σ. Here σ is 50 MJy/Sr, the uncertainty determined from a region close by ($\sim 3'$ away). A total of eighteen clumps were obtained by this method. They are listed in Table 4.3 and are shown in Fig. 4.5. We have also explored the clump structure using the dendrogram algorithm (Rosolowsky et al., 2008) and find that the tree structure is the same as that obtained using $2\mathrm{D} - Clumpfind$.

In order to obtain the flux densities of clumps at other wavelengths (i.e. 70, 160, 250, 500, 870 μm and 1.2 mm) for clump SED, we adopted arbitrary apertures corresponding

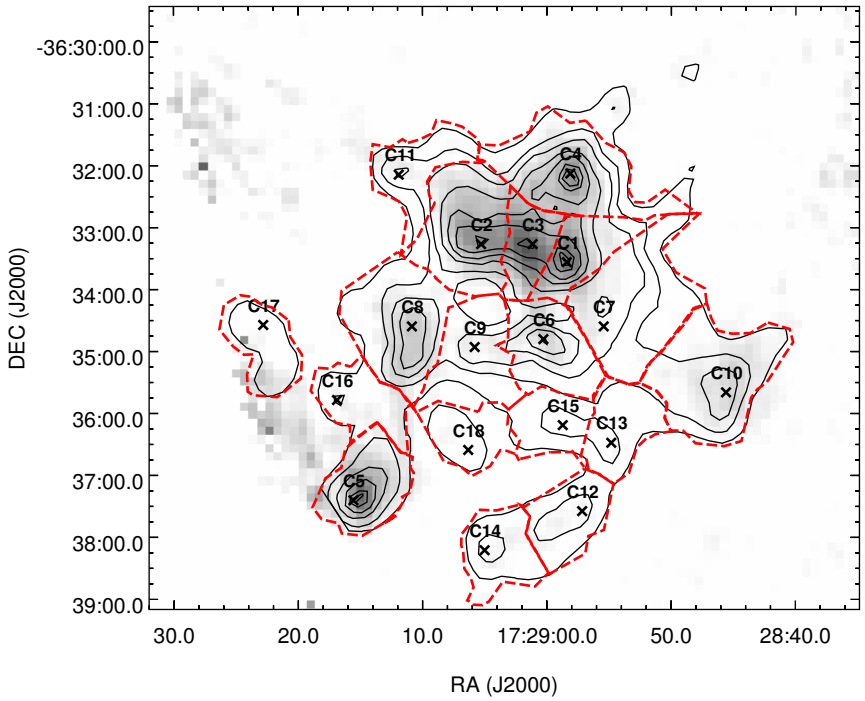

Figure 4.5: 1.2 mm SIMBA map overlaid with clump apertures used for identifying clumps. The peak positions of clumps are indicated. The contours represent SPIRE 350 μm emission with levels at 830, 1260, 1650, 2040, 2430, 2820, 3210, 3600, 3990 MJy/Sr.

to the area covered by each clump in the 350 μm image. The apertures used for the clumps are shown in Fig 4.5. A few clumps do not have PACS coverage while others are not detected in 870 μm or 1.2 mm images. The latter is not surprising considering the poorer sensitivities of ground-based telescopes that would not sample at low flux levels. A clump is considered to be detected at 870 μm and/or 1.2 mm if the flux levels of at least 9 pixels (approximately one beam) towards the clump are above the corresponding 3-σ contour level. For each clump, SEDs are constructed using available wavelength bands. The flux densities for each clump within the arbitrary aperture at wavelengths at which it is detected are estimated. Sky emission within an identical aperture is subtracted from the flux densities by considering a region that is $\sim 15'$ away in the Galactic plane that is devoid of bright diffuse emission. The flux densities are fitted with a modified blackbody function using the method described in Sect. 3.2.

We have set dust temperature, dust emissivity index and column density as free

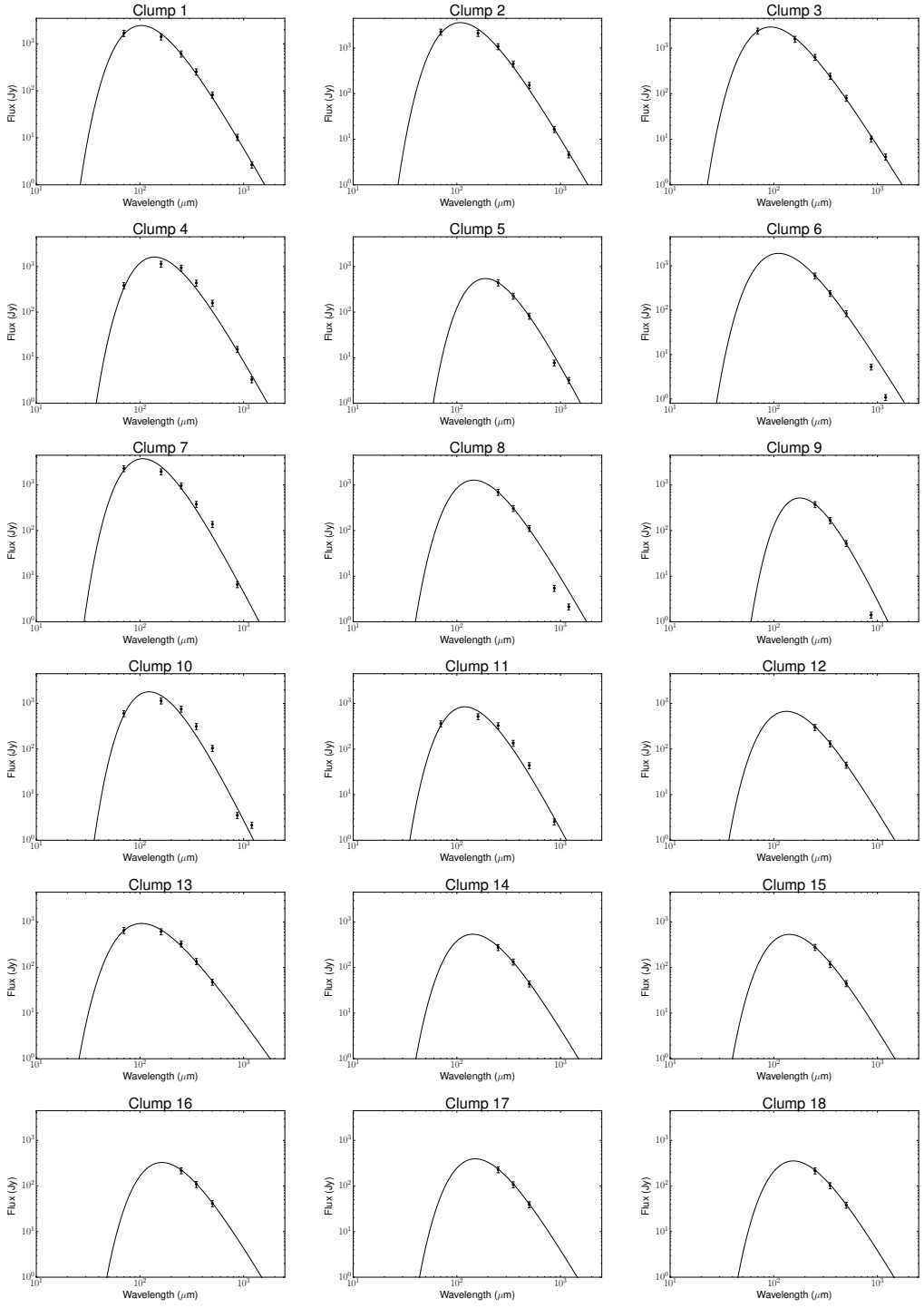

Figure 4.6: Spectral energy distributions of Herschel SPIRE 350 μm clumps. The integrated flux density within each clump aperture is shown on a log-log plot of wavelength versus flux. The data are shown with 15% uncertainty error-bars.

parameters in our fits. Six clumps: C12, C14, C15, C16, C17 and C18 are neither covered by PACS nor are they detected at 870 μm and 1.2 mm. For these clumps, as only three SPIRE wavebands are available, β is constrained to 2. The fitting was carried out using the nonlinear least squares Marquardt-Levenberg algorithm. We assumed flux uncertainties of the order $\sim$ 15% in all bands (Launhardt et al., 2013; Schuller et al., 2009; Faúndez et al., 2004; Brooks et al., 2005). The clump SEDs are presented in Fig. 4.6.

Table 4.3: Molecular clumps identified in this region.

Clump	α_{J2000} ($^{h\ m\ s}$)	δ_{J2000} ($^{c}irc\ ^{\prime}\ ^{\prime\prime}$)	Area (pc^{-2})	β	Temperature (K)	Column density (10^{21} cm^{-2})	Mass ($\times 10^2$ M$_\odot$)	L ($\times 10^2$ L$_\odot$)	Σ (g cm^{-2})
C1	17:28:58.399	-36:33:33.57	0.5	2.0 ± 0.1	28.6 ± 1.4	20.4 ± 3.2	2	102	0.08
C2	17:29:05.286	-36:33:16.16	0.8	2.0 ± 0.2	27.1 ± 1.9	16.7 ± 3.8	4	144	0.09
C3	17:29:01.149	-36:33:19.41	0.3	1.8 ± 0.1	33.2 ± 1.5	16.9 ± 2.2	2	138	0.10
C4	17:28:58.118	-36:32:07.71	1.1	2.3 ± 0.3	20.2 ± 1.7	23.9 ± 8.5	6	49	0.11
C5	17:29:15.564	-36:37:24.28	0.8	2.6 ± 0.2	14.2 ± 1.1	85.3 ± 23.8	12	11	0.31
C6	17:29:00.282	-36:34:48.17	0.8	1.9 ± 0.6	27.1 ± 11.9	15.7 ± 15.2	2	75	0.06
C7	17:28:55.431	-36:34:09.92	1.1	2.6 ± 0.4	24.9 ± 3.3	12.8 ± 5.0	3	143	0.06
C8	17:29:10.854	-36:34:35.85	1.1	2.1 ± 0.6	19.6 ± 6.0	26.7 ± 22.6	6	37	0.12
C9	17:29:05.807	-36:34:55.84	0.5	3.1 ± 0.6	13.9 ± 2.7	75.8 ± 55	10	1	0.43
C10	17:28:45.591	-36:35:39.65	1.1	2.8 ± 0.4	20.6 ± 2.6	14.7 ± 7.9	4	9	0.16
C11	17:29:11.910	-36:32:08.88	0.5	2.5 ± 0.4	22.4 ± 2.7	12.4 ± 5.6	2	4	0.07
C13	17:28:54.820	-36:36:28.52	0.5	1.3 ± 0.2	32.7 ± 2.8	6.6 ± 1.3	2	7	0.08
				SED fit with β=2					
C12	17:28:57.160	-36:37:34.76	0.5	2	21.9 ± 0.2	16.4 ± 0.03	1	3	0.03
C14	17:29:05.008	-36:38:12.65	0.5	2	20.4 ± 1.3	18.8 ± 0.3	2	3	0.10
C15	17:28:58.722	-36:36:11.46	0.5	2	20.5 ± 1.5	19.2 ± 0.4	2	3	0.09
C16	17:29:16.880	-36:35:47.15	0.5	2	17.8 ± 0.01	24.2 ± 0.01	3	1	0.10
C17	17:29:22.812	-36:34:34.38	0.5	2	19.3 ± 0.2	19.5 ± 0.03	2	2	0.09
C18	17:29:06.328	-36:36:35.52	0.5	2	18.8 ± 0.3	20.0 ± 0.1	2	1	0.10

The dust temperature and column density values obtained using the best-fit are listed in Table 4.3 for all the eighteen clumps. For twelve clumps, the best-fit β values are also tabulated. The clump temperatures range from $14 - 33$ K. The central clump C3 has the highest temperature of 33 K. This is also the location of the radio emission peak. The column densities lie in the range $0.7 - 8.5 \times 10^{22}$ cm^{-2}. The highest column density is found towards clump C5, that also has the lowest temperature of 14 K. The value of β lies between $1.8 - 2.3$ for the brightest four clumps: C1, C2, C3 and C4. This is close to the normally accepted value of 2 (Hildebrand, 1983). For the other

eight clumps fitted with variable β, the value of β ranges from 1.3 to 3.1. The β values obtained show an inverse correlation with the dust temperature. We investigate this further in the next section. For dense clumps, other authors find that the values of β range from $0.9 - 3.3$ (e.g., Anderson et al., 2010; Rathborne et al., 2010). Kuan et al. (1996) obtained a value of 3.7 for Sgr B(2)N region and they have interpreted it as a strong evidence for the presence of ice coated dust mantles in the region. The mean column density value of these clumps, 2.5×10^{22} cm^{-2}, is similar to that of other massive star forming regions, eg., mean value of $1 \times 10^{22}\mathrm{cm}^{-2}$ for Gemini OB1 molecular cloud complex (Dunham et al., 2010) and $5.7 \times 10^{22} - 8.6 \times 10^{23}\mathrm{cm}^{-2}$ for 18 young star forming regions (Garay et al., 2007). For $R_V = 3.1$, using the relation $N(H_2)/A_V = 9.4 \times 10^{20}$ cm^{-2}mag^{-1} (Bohlin et al., 1978), we find that $A_V = 26$ mag for the mean column density. Although this is similar to the value of diffuse interstellar extinction for a distance of 14.7 kpc (Sect. 1), this is likely to be a coincidence as extinction estimated from the mean column density includes the effect of the dense clump(s) while the latter refers to diffuse interstellar medium alone.

The column densities are converted to clump masses using the equation given in Sect. 3.2. The area and mass of each clump are listed in Table 4.3. The masses of clumps lie between $\sim 100 - 1200$ M$_\odot$, and the total mass of the cloud is 6700 M$_\odot$. Beltrán et al. (2006) used 1.2 mm continuum data to estimate the total mass of the clumps within this region and they obtained a total mass of 674 M$_\odot$. This is a factor of 10 lower than our value, and can be explained on the basis of the fact that the ground based SEST-SIMBA observations at 1.2 mm do not sample a number of clumps as well as the diffuse emission at low flux levels owing to poorer sensitivity. We estimate clump diameters of 0.6 to 1.2 pc assuming each clump to be spherical. A clump requires $\sim$30 M$_\odot$ to form a high mass star with star formation efficiency of 30% or greater (Lada & Lada, 2003). Similarly, Motte et al. (2007) and Fallscheer et al. (2013) use a lower limit of 40 M$_\odot$ for identifying potential molecular cores that can form a high mass star. The least massive of our clumps is 100 M$_\odot$, and the sizes of our clumps are similar to the sample of these authors: $0.03 - 0.5$ pc (Motte et al., 2007) and $0.4 - 1.1$ pc (Fallscheer et al., 2013). It is likely few of the clumps in this region either harbor or are capable of forming high mass stars.

We have also estimated the surface density (Σ) of the clumps. For this, we divide the mass of each clump by the area and obtain the surface densities of clumps that

are listed in Table 4.3. The surface densities of the clumps range from 0.03 to 0.4 g/cm^2. According to Krumholz & McKee (2008), these values would indicate that fragmentation could be initiated in these clumps with massive star formation being supressed as a result. However, López-Sepulcre et al. (2010) and Giannetti et al. (2013) find lower surface densities even towards massive star forming cores, i.e. those with surface densities of 0.2 g/cm^2 or larger. Similarly, Miettinen & Harju (2010) find that it is possible to have lower surface densities of clumps (i.e. lower than 1 g/cm^2) for massive star formation, but the core densities could be higher. In addition, Chambers et al. (2009) in their analyses comment that lower surface densities of clumps could be attributed to large areas used (i.e large apertures) as they find massive protostars in cores of lower surface densities. In our case, the average surface densities are representative values that could be lower than the surface densities near the core or peak emission of clump as the area of clumps is very large (reaching to $\sim$20% of peak flux in few cases). Further, there are uncertainities associated with the temperature and column density. Hence, it is possible that few clumps in this region with larger average surface densities such as C5, C9 and C10 have the potential to form massive stars.

We have calculated the luminosity of the individual clumps by integrating the flux densities within the best fit curve of the modified blackbody. The estimated luminosities are given in Table 4.3 and range from $10^2 - 1.4 \times 10^4$ L$_\odot$. Clump luminosities provide an insight into embedded young stellar objects as well as the clump evolutionary stage. According to Rathborne et al. (2010), a bolometric luminosity of 10^4 L$_\odot$ can be used as a rough threshold to identify clumps harboring a high-mass protostar. Using this criteria, we find 4 of the clumps (C1, C2, C3 and C7) have luminosities $> 10^4$ L$_\odot$ and may contain a high mass protostar.

4.3.2 Relation between temperature and dust emissivity index

We observe that clumps with higher dust emissivity index β show lower values of dust temperature T_d and vice-versa. Earlier studies have shown an anti-correlation between these parameters (e.g. Dupac et al., 2003; Désert et al., 2008; Paradis et al., 2010; Anderson et al., 2012). In order to investigate this further as the β and T_d parameters obtained from clump SED fitting represent average values, we have constructed the column density, dust temperature and β maps of this region by carrying out pixel-by-pixel fit using a

greybody SED (discussed in Sect. 3.2) to 7 images of this region (70 - 1200 μm). However, we obtain only partial maps of this region owing to partial coverage by PACS. The temperature map is shown in Fig. 4.7(a). The temperature distribution shows a maximum of 47.7 $\pm$ 4.9 K within Clump C3 that also corresponds to the radio emission peak. For estimating the median values and other statistical analysis such as that of β-T_d relation, we have selected pixels lying within the 3-sigma contour of 1.2 mm map as it samples regions (clumps) where the greybody SED fits are expected to be fairly good. For these pixels, we find that the reduced chi-square < 5. The dust emissivity index β, column density and reduced chi-square maps are shown in Fig. 4.8.

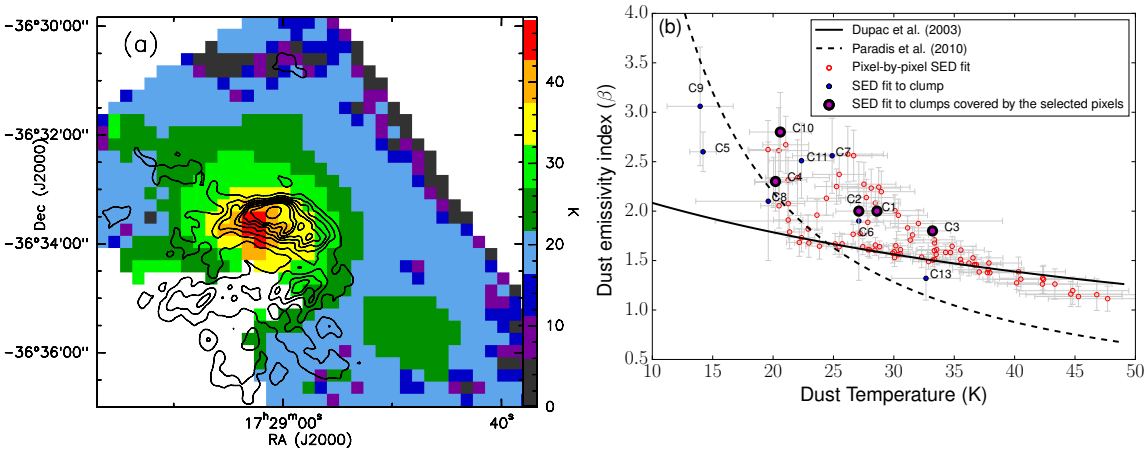

Figure 4.7: (a) Dust temperature map overlaid with 1372 MHz radio contours. (b) The plot of T_d versus β for pixels within 3-σ contour of 1.2 mm map. Also plotted are values for 12 clumps with variable β. The β-T_d relations of (Dupac et al., 2003) and (Paradis et al., 2010) are also shown in the plot.

In order to understand the relation between β and T_d, we have plotted β as a function of T_d for these pixels. This is shown in Fig. 4.7(b). We see an anti-correlation between β and T_d values for these pixels. Also plotted in the figure are the values of individual 12 clumps that have been fitted with variable β (see Table 4.3). Among these, the clumps C1, C2, C3, C4 and C10 are covered within the selected pixels. Their dust temperature and β values lie close to the region occupied by pixels. The clumps seem to show the anti-correlation albeit with larger uncertainties compared to pixels. Clump C9 shows the largest β value of 3.1 ± 0.6. Among the pixels, β values range between $1.1 - 2.7$ in the temperature range $19.5 - 47.7$ K. The inverse correlation between β and T_d observed is similar to that obtained by other studies. Dupac et al. (2003) have observed this

towards numerous regions in our Galaxy and they attribute this to (i) change in grain sizes in cold dense environments, (ii) differences in chemical composition of grains or (iii) intrinsic dependence of β on T_d due to quantum processes that could be dominant. The best-fit hyperbolic function obtained by them has been overplotted on Fig 4.7(b). We have also overplotted the best-fit relations obtained by Paradis et al. (2010) towards the region of Galactic longitude $l = 30^{\circ}$ for comparison.

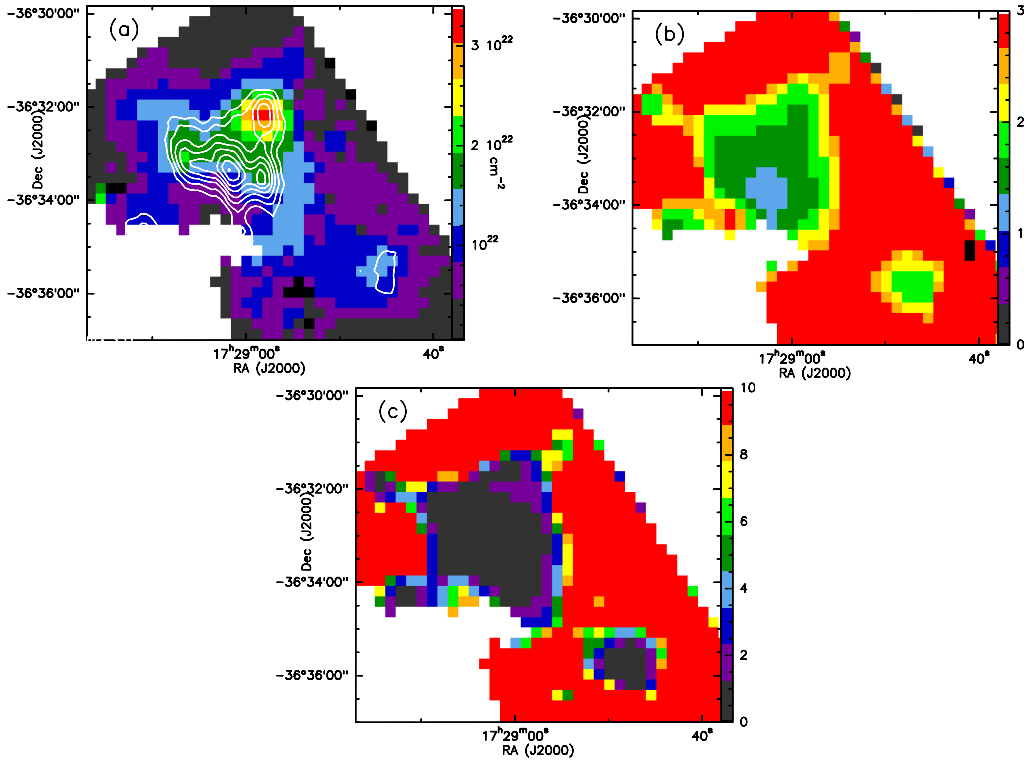

Figure 4.8: (a) Column density map overlaid with 1.2 mm cold dust contours. The contour levels are 250, 380, 510, 640, 770, 900, 1030, 1160, 1290 and 1420 mJy/beam. (b) Dust emissivity index (β) map. (c) Reduced chi-square (χ_{red}) map.

The warmest pixel corresponds to the clump C3 and this matches with the highest average dust temperature obtained for the clump C3. The pixel with the highest temperature 47.7 ± 4.9 K shows the lowest value of $\beta \sim 1.1 \pm 0.1$. Warm regions show lower dust emissivity index, and vice-versa in the outer envelope. Assuming this to be true and intrinsic to grain properties, we can infer that the warmer or active region is comprised of bare silicate grain aggregates or porous graphite grains (Dupac et al., 2003; Mathis & Whiffen, 1989), while the higher emissivity index regions could be interpreted as those with icy mantles (Aannestad, 1975). We, however, cannot exclude the possibility of this effect arising due to different molecular clouds along the same line-of-sight (Shetty

et al., 2009) considering that this region lies along the inner Galactic plane.

4.3.3 Emission from warm dust

The emission from warm dust towards IRAS 17256–3631 is seen as extended diffuse emission in the IRAC 8 μm image. This emission possesses a sharp, arc like edge towards the north. Further, emission in the form of filamentary structures is also seen. The MIR maps in other IRAC bands (3.6 and 4.5 μm) also show similar emission features as in the 8 μm map. Diffuse emission from the warm dust is far more extended than the ionized region in the NE–SW direction as seen in Fig. 4.9a. However, regions of higher flux densities trace the ionized gas morphology towards the north-west.

The 8 μm emission is dominated by mid-infrared radiation from the heated dust as well as emission from the photodissociation regions (PDRs) (Churchwell et al., 2009). Polycyclic Aromatic Hydrocarbons (PAH; Leger & Puget, 1984) are also significant contributors at these wavelengths. The combination of radio and 8 μm show that the H II region is surrounded by the bright mid-infrared filamentary emission that is probably tracing the PDR associated with this region. The emission morphology at 70 μm bears a similarity to that at 8 μm as seen in Fig. 4.9b. The better correlation of 70 μm emission with 8 μm emission as compared to other Herschel wavelength bands can be attributed to the fact that emission at 70 μm is not due to a single dust component. The stochastically heated dust grains as well as grains that are at thermal equilibrium contribute to the 70 μm emission (Compiègne et al., 2010). However, there are some prominent differences between 8 and 70 μm emission that include filamentary emission appearing to emanate from the cometary head.

4.3.4 Emission morphology and spectral energy distribution

The emission from cold dust at far-infrared and submm wavelengths shows a clumpy distribution. The morphology of cold dust emission is different from that of ionized and mid-infrared emission. The three central brightest clumps are along an arc (Clump C1, C2 and C3 in Fig. 4.5). It is along this region where most of the bright mid-infrared emission is located. However, the radio cometary head coincides with the clump peaks and the radio peak is located southwards. There is less near and mid-infrared nebulosity

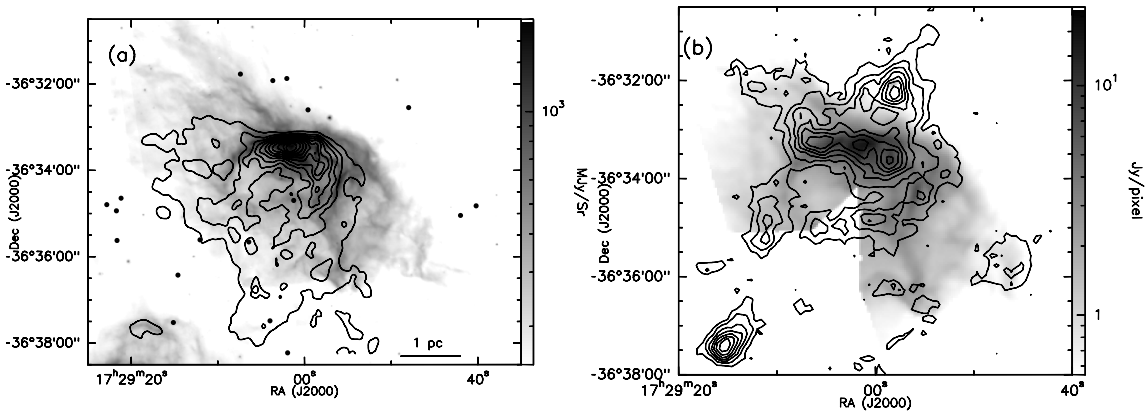

Figure 4.9: (a) Overlay of ionized gas contours at 610 MHz on the *Spitzer* IRAC 8 μm image. The contour levels are at 8, 19.5, 31.0, 42.6, 54.2, 65.7, 77.2, 88.8, 100, 112, 123 and 135 mJy/beam. The positions of 18 YSOs are also marked. (b) Image of PACS 70 μm emission overlaid with 870 μm cold dust contours. The contour levels are at 0.24, 0.54, 0.84, 1.14, 1.44, 1.74, 2.04 and 2.34 Jy/beam.

towards the clumps C4, C5 and C8.

We also obtain total SED of this region using flux densities from IRAS-HIRES (Aumann et al., 1990), Midcourse Space Experiment (MSX Price et al., 2001), Herschel-HiGal, ATLASGAL and SEST-SIMBA within a circular region of radius $1.8'$ centred on the IRAS peak. This is shown in Fig. 4.10. By integrating under the SED, we find the total luminosity of this region to be 1.6×10^5 L$_\odot$. This is marginally larger than the previous estimate, given that we have better wavelength coverage. This bolometric luminosity corresponds to a single ZAMS star of spectral type O6.5.

4.4 Embedded cluster and young stellar objects

We have used the UKIRT (Sect. 2.2.1) and *Spitzer* IRAC point source catalogs for studying the associated cluster and the nature of the stellar population in the region around IRAS 17256–3631. We used two sets of level 2 Post-Basic Calibrated Data images from the Spitzer Heritage Archive for the analysis presented here. The first set of images are from GLIMPSE legacy project (Benjamin et al., 2003) in all the four IRAC bands. However, there is only a partial coverage at 3.6 and 5.8 μm, and the south-eastern portion towards our region of interest is not covered. The second set of

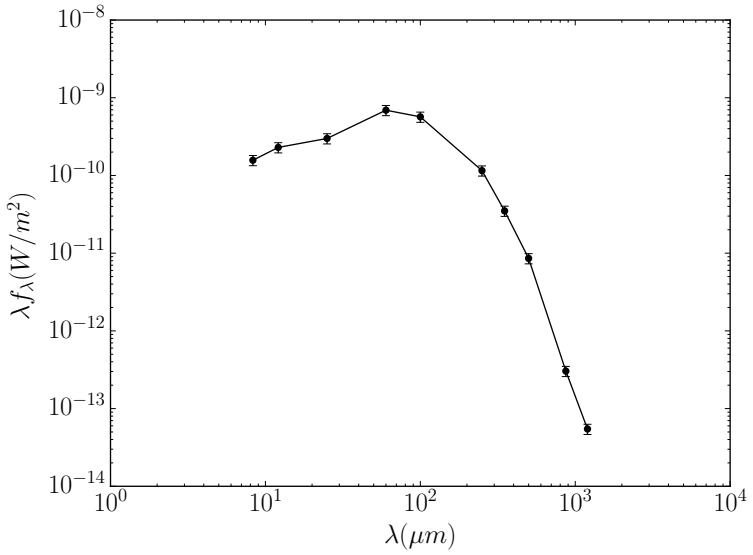

Figure 4.10: Spectral Energy Distribution of this region obtained by integrating fluxes within a circular region of diameter $3.5'$ centred on the IRAS peak.

IRAC images (AOR key: 40231680) are available at two bands only, 3.6 and 4.5 μm, but cover our region of interest fully. As the GLIMPSE point source catalogs do not completely cover our region of interest, we performed photometry for 3.6 and 4.5 μm bands using the second set of images and at 8.0 μm band using the GLIMPSE tile. We considered a $10' \times 10'$ region centered on the IRAS peak ($\alpha_{\rm J2000}$: $17^{\rm h}29^{\rm m}01.1^{\rm s}$, $\delta_{\rm J2000}$: $-36°33'38.0''$).

Aperture photometry was carried out using the SExtractor software (Bertin & Arnouts, 1996). In order to perform the background subtraction, a background map was constructed by estimating the background value in each mesh of a grid that covers the whole frame. The mesh size for each band were given as an input in the algorithm. To check for detection efficiency and photometric accuracy, we took a $100''$ region sufficiently away from the nebulosity, where there is GLIMPSE catalog coverage. We compared the magnitudes obtained using our photometry with values from the GLIMPSE catalogue. By comparing with the GLIMPSE catalog, we found $\sim$80% common sources in all the bands. We also carefully checked for spurious sources and removed them from the catalog. By visual inspection, we see that in regions of strong nebulosity in the 8.0 μm band, the detection rate is lower compared to regions with little or no nebulosity. In these regions, we manually performed photometry for the sources using the aperture photometry task 'qphot' of IRAF. The aperture size was chosen as $6''$ and the

background estimation has been carried out with a 2″ sky annulus. After performing manual photometry and removing the spurious sources, we combined the individual band catalogs to produce a final catalog. We detected 4155, 4163 and 572 sources in the 3.6, 4.5 and 8.0 μm bands, respectively. Of these, 275 sources were detected in all the three bands.

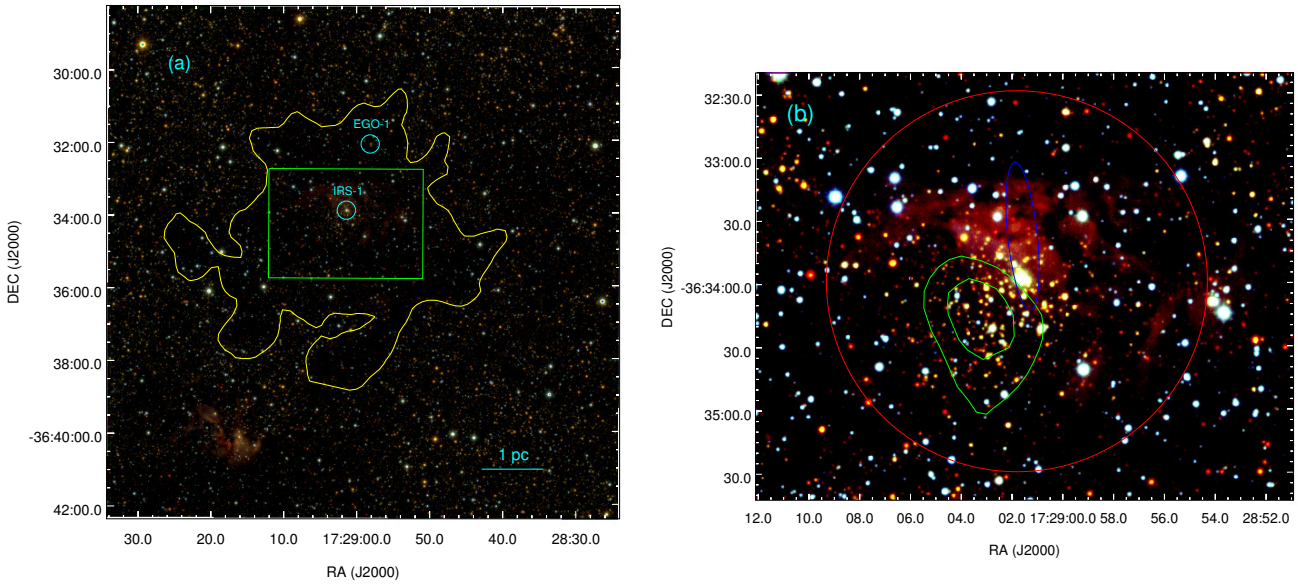

Figure 4.11: (a) UKIRT color composite image of the IRAS 17256–3631 region in JHK bands. Blue represents J band, green represents H band and red represents K band. Lowest contour of 350 μm data is marked as yellow contour. The locations of IRS-1 and EGO-1 are also marked in the image. (b) Colour composite image showing the stellar density contours (green) corresponding to the near-infrared cluster. The region of radius 1.5′ centered on IRS-1 is marked as a red circle. The IRAS error ellipse (blue) is also shown in the figure.

4.4.1 Infrared cluster

A JHK colour-composite image of the region around IRAS 17256–3631 is shown in Fig. 4.11a. Apart from a spatially extended diffuse emission the region also harbours a partially embedded cluster. This cluster has been identified by Bica et al. (2003) based on 2MASS data. Using the source count algorithm outlined in Schmeja (2010) we re-

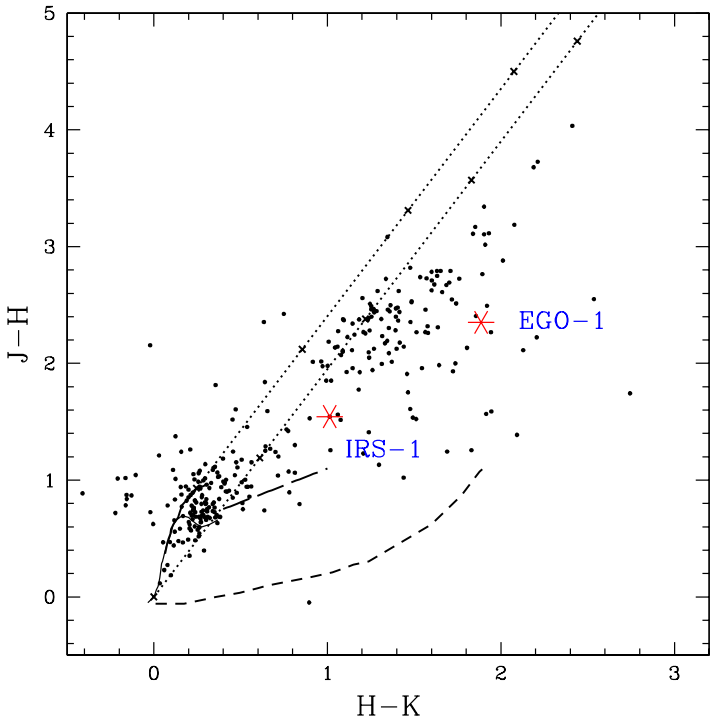

Figure 4.12: The colour-colour diagram of near-infrared sources within 1.5′ radius of IRS-1. Two solid curves represent loci of main sequence (thin line) and giant stars (thick line), respectively, derived from Bessell & Brett (1988). Long dashed lines represents T Tauri locus (Meyer et al., 1997). Short dashed lines represents the loci of Herbig AeBe stars (Lada & Adams, 1992). Parallel dotted lines represent reddening vectors with cross points placed along intervals corresponding to 10 magnitudes of A_V. We have assumed interstellar extinction law of Rieke & Lebofsky (1985). The sources IRS-1 and EGO-1 are represented with asterisks.

visited this cluster with high resolution and deeper UKIRT data. Fig. 4.11b shows the stellar surface density contours for a grid / bin size of 60″ with separation of 30″. The source count method, that identifies density enhancements over a background level, clearly identifies only a part of the cluster that is out of the nebulosity. This implies that the cluster is partially embedded. We investigate the nature of the stellar population associated with the cluster using JHK colour-colour diagram (CCD) shown in Fig. 4.12. For this we have used a region of radius 1.5′ centered on the brightest IR

source (IRS-1) that lies within the positional uncertainty of the IRAS point source position (see Fig. 4.11b). The CCD shows two distinct population of objects. The low extinction group ($A_V = 0 - 5$) is possibly the contamination from field stars and the high extinction population (with an average $A_V \sim 15$ and going upto $A_V \sim 30$) are likely to be the cluster members associated with the cluster identified here. As can be seen from the plot, majority of the candidate cluster members are distributed to the right of the reddening band of the main sequence stars.

This region of the diagram is identified with near-infrared sources (Class II, Class I and Herbig Ae/Be stars). The near-infrared excess in pre-main sequence Class I and II stars is due to the optically thick circumstellar disks/envelopes. These disks/envelopes become optically thin with age; hence the fraction of near-infrared excess stars decreases with age. For very young ($\leq 1\mathrm{Myr}$) embedded clusters the fraction is $\sim 50\%$ (Lada et al., 2000; Haisch et al., 2000) and it decreases to $\sim 20\%$ for more evolved (2 – 3 Myr) clusters (Haisch et al., 2001; Teixeira et al., 2004). Taking the cluster population into consideration, we estimate around 40% of stars with near-infrared excess. This indicates that the cluster is a very young and partially embedded cluster, and as the molecular cloud disperses, the cluster members as well as the shape of the cluster would be revealed.

4.4.2 IRAC YSOs

To identify the young stellar objects in the vicinity of IRAS 17256–3631, we have used the IRAC photometric data from the catalog generated (refer Sect. 2.3.1). We selected point sources within the lowest contour of 350 μm image (830 MJy/Sr), that encompasses most of the diffuse radio, near-infrared, MIR and submm emission. There are 58 sources detected in the three IRAC bands of 3.6, 4.5 and 8.0 μm. Fig. 4.13 shows the ([3.5] - [4.5]) vs ([4.5] - [8.0]) IRAC CCD. Simon et al. (2007) used the following color cuts to isolate YSOs in a given stellar population based on the SED fits.

$$[3.6] - [4.5] > 0.6 \times ([4.5] - [8.0]) - 1.0,$$

$$[4.5] - [8.0] < 2.8,$$

$$[3.6] - [4.5] < 0.6 \times ([4.5] - [8.0]) + 0.3,$$

$$[3.6] - [4.5] > -([4.5] - [8.0]) + 0.85.$$

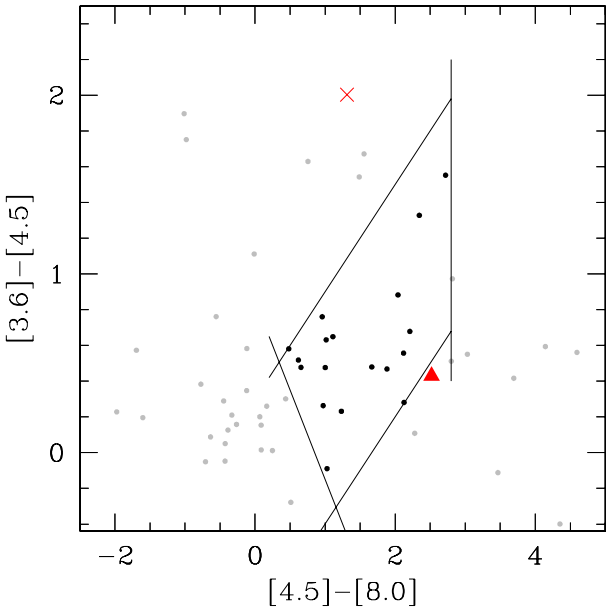

Figure 4.13: IRAC colour-colour diagram of the 58 sources within lowest contour level of 350 μm. The sources which are not classified as YSOs are represented by gray points. Black dots represent the IRAC YSOs identified using the criteria of Simon et al. (2007). The triangle and $\times$ represent IRS-1 and EGO-1, respectively. The criteria for YSO identification are shown as solid lines.

Based on the above criteria, 18 sources were identified as YSOs in our region of interest. These are shown as solid circles in Fig. 4.13. The locations of these sources associated with IRAS 17256–3631 are shown in Fig. 4.9a. The spatial distribution of infrared objects in different evolutionary stages do not show a morphological segregation. This is because of some foreground and large background contamination due to the location of this region, i.e., towards the Galactic centre.

We see a point-like source near the clump C4 at 8 μm and 70 μm. We looked for this in the all-sky survey from Widefield Infrared Survey Experiment (WISE, Wright et al., 2010) and found that it is present in the 12 and 22 μm images as well. It is therefore likely to be in an early evolutionary stage. Although this source (represented by $\times$ in the IRAC colour-colour diagram in Fig. 4.13) does not lie in the region occupied by YSOs, a careful examination of IRAC images reveals that this is likely to be due to the enhanced emission in the 4.5 μm band, that is shown in Fig. 4.14. In fact, two green fuzzies associated with this extended green object (EGO, Cyganowski et al., 2008; Chambers et al., 2009) are seen towards the south of this source that are not detected in either 3.6, 5.8 (GLIMPSE) or 8 μm bands. The locations of these green fuzzies are encircled in Fig. 4.14. EGOs are characterized by their extended green emission in the IRAC three-color composite images. Their angular sizes vary from a few to 30$''$ and are believed to be associated with massive young stellar objects (Cyganowski et al., 2009). We refer to this source as EGO-1.

Table 4.4: The lines detected in the spectrum of IRS1.

Line	Wavelength (μm)	Comment
Brγ	2.165	IRS-1 (absorption), Nebular (emission)
HI (10-4)	1.736	IRS-1 (absorption)
HI (13-4)	1.611	IRS-1 (absorption)
He I	1.736	IRS-1 (absorption)
He I	1.700	IRS-1 (absorption)
HI (8-4)	1.945	Nebular (emission)
He I	2.058	Nebular (emission)
H_2	2.121	Nebular (emission)

4.4.3 Near-infrared spectroscopy

IRS-1 is the brightest near-infrared source in our region marked in the near-infrared CCD and its location is encircled in Fig. 4.11a. It is located $\sim 25''$ away from the radio peak. As described in Sect. 2.2.1, we carried out spectroscopic observations of this source in the wavelength range of 1.4 – 2.5 μm. The extracted spectrum of IRS-1 is shown in Fig. 4.15. The shaded vertical strips represent the spectral region with poor

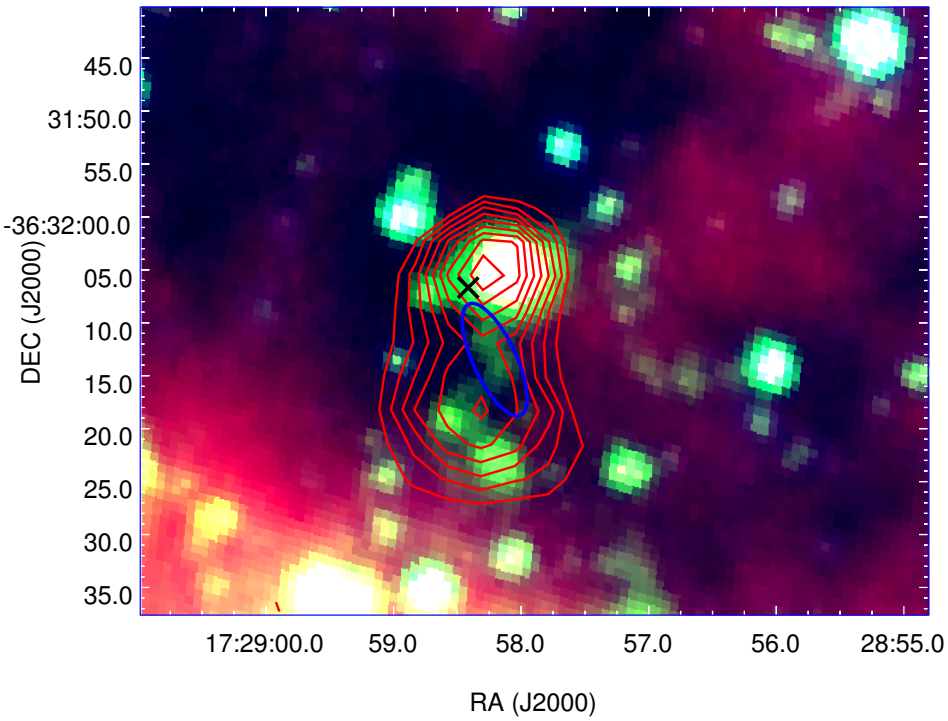

Figure 4.14: IRAC three-color composite image of EGO-1. Blue represents 3.6 μm, green 4.5 μm and red 8 μm. Ellipse marks the extended green emission. The Herschel PACS 160 μm contours are also shown in the image. The $\times$ locates the position of H_2 knot 2 (Fig. 4.2b).

sky transparency. Several hydrogen and helium lines characteristic of massive O and B stars (Bik et al., 2005) are detected in the spectra of IRS-1. The lines detected above 3σ level are listed in Table 4.4. The spectral features seen in IRS-1 are consistent with that of late O type and early B type stars as described in the K-band spectral atlas of Hanson et al. (1996).

In order to probe the nebulosity associated with IRAS 17256-3631, we oriented the slit along the direction shown in Fig. 4.2b. Spectra at positions A, B, C, and D were extracted and presented in the left panel of Fig. 4.16. There is a clear variation of the strength of the Brγ emission along the slit. It initially increases; from A to B as we move southwards, with maximum emission seen in region B that is close to IRS-1. Beyond B it decreases considerably, with very little or no emission in region D. The right panel of Fig. 4.16 shows the spectrum of region B. The spectral features are consistent

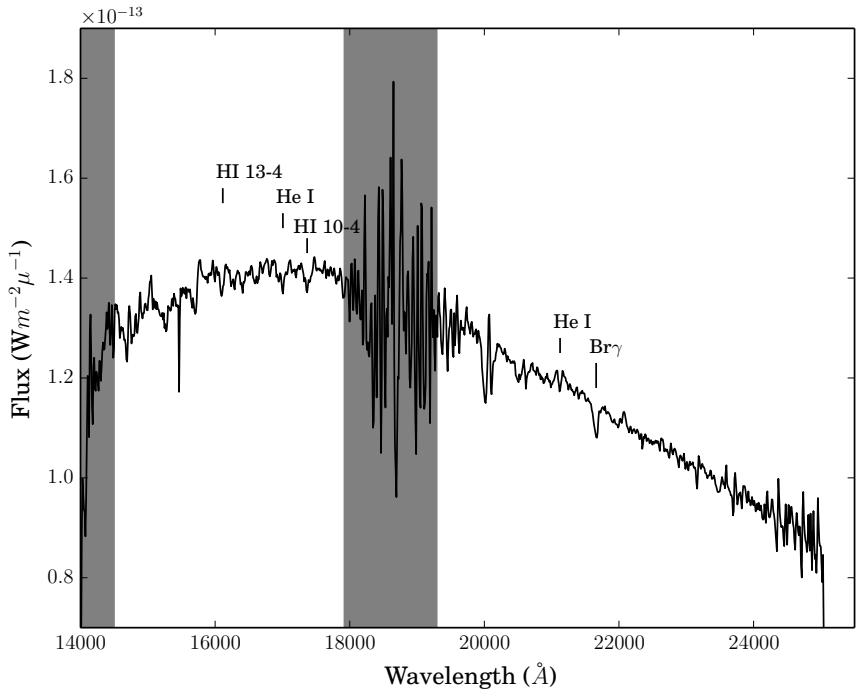

Figure 4.15: The near-infrared HK spectrum of the IRS-1. The shaded area represent the region of poor sky transparency. The near-infrared spectral lines identified are marked over the spectrum.

with those from ultracompact H II regions (Bik et al., 2005; Hanson et al., 1997). The spectrum from region B shows the presence of weak H_2 line at 2.12 μm. This line can be attributed to two excitation mechanisms, namely shock and UV fluorescence. The signatures of shock excited H_2 emission is the absence of transitions from high-ν levels and a high ratio of fluxes (10:1) in the 2.12 and 2.24 μm lines (Smith, 1995). The UV fluorescence, on the other hand, leads to population of both high and low-ν states. The diagnostic tool for UV fluorescence is a ratio of 2:1 for the 2.12 and 2.24 lines (Black & Dalgarno, 1976). The 2.24 μm line is not detected down to 1.5σ level. This appears to favour the shock excitation mechanism although we need better signal-to-noise ratio to ascertain this. It is worth noting that the H_2 image shows the presence of a faint H_2 nebulosity at B consistent with the location of region B (Fig. 4.2b).

4.4.4 SED models of IRS-1 and EGO-1

In order to get a qualitative idea about the evolutionary stage of IRS-1 and EGO-1, we have fitted their SED with the models of Robitaille et al. (2007) (hereafter RWIW).

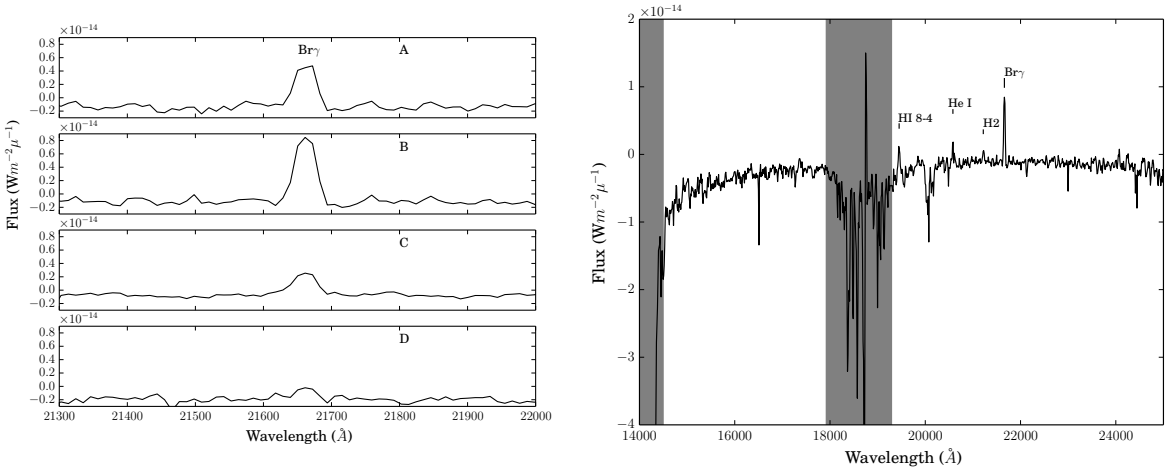

Figure 4.16: (Left) Brγ line across different slit positions labeled as A, B, C and D in Fig.4.2b. (Right) The near-infrared HK spectrum of nebular region in the vicinity of IRS-1. The shaded region represents region of poor sky transparency.

Table 4.5: Infrared magnitudes of IRS-1 and EGO-1.

Source	α_{J2000} ($^h\ ^m\ ^s$)	δ_{J2000} ($^\circ\ '\ ''$)	J (mag)	H (mag)	K (mag)	3.6 μm (mag)	4.5 μm (mag)	8.0μm (mag)
IRS-1	17:29:01.39	-36:33:54.21	11.20 ± 0.01	9.79 ± 0.03	8.86 ± 0.02	8.22 ± 0.01	7.79 ± 0.01	5.27 ± 0.03
EGO-1	17:28:58.13	-36:32:05.10	16.45 ± 0.01	14.29 ± 0.01	12.57 ± 0.01	10.32 ± 0.01	8.32 ± 0.01	7.01 ± 0.02

The assumptions include a given gas and circumstellar dust geometry as well as a dust grain model to carry out radiative transfer modelling. RWIW have pre-computed a large number of radiative transfer models covering a wide range of stellar masses and evolutionary stages. We have used the online version of the fitting tool. The SEDs are constructed using near and mid-infrared wavelength fluxes shown in Table 4.5. The associated clump flux densities at 350 and 870 μm were given as the upper limits for constraining the models. The inputs to the models include distance, visual extinction and source flux densities at various wavebands. The SED and the 10 best fitting models for each are shown in Fig. 4.17. Table 4.6 lists the range of parameters for these models. From the best fit model, the mass of IRS-1 is found to be 14.6 $M_\odot$ and 10 best fit models give a mass range of 6.7– 14.6 $M_\odot$ suggesting IRS-1 as a massive star in this region.

Table 4.6: Parameters of the Robitaille et al. (2007) models for IRS-1 and EGO-1. Col. 4 – 9 gives Mass, Effective Temperature, Luminosity, Inclination angle, Envelope accretion rate, Envelope mass, Disk Mass, Extinction and Age, respectively. The range of parameters given here are for best fit model and subsequent 9 good fits.

Source		χ^2	Mass ($M_\odot$)	T_{eff} (K)	Luminosity ($L_\odot$)	Inc. angle (Deg.)	Env. accretion rate ($M_\odot$/yr)	Env. mass ($M_\odot$)	Disk mass ($M_\odot$)	A_V	Age (Myr)
IRS-1	Best fit	103.5	14.60	30955	19200	31.79	0	1.39×10^{-8}	9.04×10^{-9}	10.0	1.3
	Range	103.5 - 115.9	6.66 - 14.60	4666 - 30935	272 -19200	18.19 - 75.52	0 - 6.03 $\times10^{-5}$	1.39×10^{-8} - 22.8	9.04×10^{-9} - 0.001	10.0	0.07 -1.3
EGO-1	Best fit	71.4	6.83	4530	302	31.79	7.48×10^{-4}	9.19	0.35	14.09	0.05
	Range	71.4 - 206.5	6.83 - 3.49	4223 - 6658	122 - 497	117.2 - 286.6	2.05×10^{-5} - 7.48×10^{-4}	0.3 - 22.6	0.003 - 0.2	2.0 - 13.2	0.005 - 0.2

This is consistent with the spectral type inferred from the near-infrared spectra. The mass of EGO-1 is found to be 6.8 $M_{\odot}$ from the best fit model. The mass ranges from 3.5–6.8 $M_{\odot}$. Although we have attempted to estimate the physical parameters using the RWIW SED fits, we would like to mention that the fitting is based on the assumption that the SEDs of massive YSOs are scaled up versions of their lower mass counterparts.

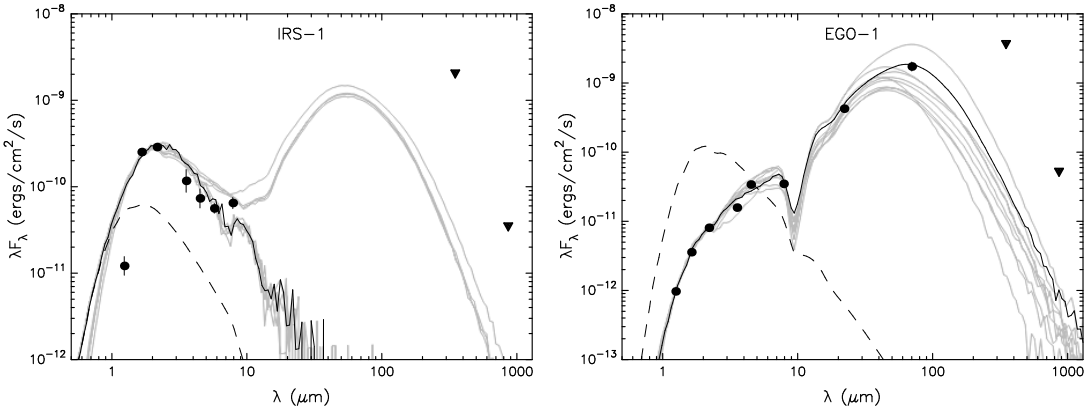

Figure 4.17: RWIW best fit models for (left) IRS-1 and (right) EGO-1. The filled circles represent the input fluxes while triangles represent upper limits. The black line shows the best fitting model, and grey lines show the subsequent 9 good fits. The dashed line marks the SED of the stellar photosphere in the best fitting model.

4.5 Star formation activity

The spatial distribution of dust and ionized material around the infrared cluster is illustrated in Fig. 4.18. This figure shows a colour composite image of the embedded cluster in near infrared K band (blue) and cold dust emission at 870 μm (red), overlaid with contours of ionised gas emission (yellow; at 1372 MHz). The cold dust emission is absent towards the location of the cluster giving an appearance of a void or cavity here (encircled in the figure). It is likely that the parental molecular cloud has dispersed locally, after the formation of the stellar cluster. Even in the radio emission, we observe low flux levels towards the cluster. IRS-1 is located to the north-west of the infrared cluster and appears within the aperture corresponding to clump C3 although it is nearly $35''$ south of dust emission peak. Most of the high density clumps are also situated north and north-west of the cluster. The void in radio emission near the cluster could be due to stellar winds emanating from stars in the cluster (Smith, 1973; Cappa et al.,

2005). Numerical radiaton-hydrodynamical simulations of cometary H II regions by Arthur & Hoare (2006) show that champagne flow models with powerful stellar winds from early type stars can produce limb brightened morphologies. Wind blown broken shell/void kind of structures in radio and mid-infrared around clusters of stars have also been observed in other regions, eg. RCW49 (Whiteoak & Uchida, 1997; Benaglia et al., 2013).

We next attempt to find the relative evolutionary stages of clumps based on the evolutionary sequence proposed by Chambers et al. (2009) and Battersby et al. (2010) discussed in detail in Sect. 3.8. The four important star formation tracers are: (1) Quiescent clump (no signs of active star formation), (2) Intermediate clumps that exhibit one or two signs of active star formation (such as shock/outflow signatures or 24 μm point source), (3) Active clumps that exhibit three or four signs of active star formation ("green fuzzies", 24 μm point source, UCH II region or maser emission), and (4) Evolved red clumps with diffuse 8 μm emission.

In the absence of Spitzer-MIPS 24 μm data, we searched for WISE 22 μm point sources associated with the clumps within a search radius of $5''$ from the peak position (shown in Fig 4.5) and based on association with radio and mid-infrared emission, we have classified the clumps based on the scheme of Battersby et al. (2010). We also searched for 6.7 GHz methanol and H_2O masers, neither being detected here (MacLeod et al., 1998; Sánchez-Monge et al., 2013). There is little information about masers towards all the clumps. The results of clump classification are presented in Table 4.7. The columns in the table list the clump name, association with radio and 8 μm peaks, and 22 μm point source. Column 5 gives the clump activity (Q-quiescent, A-active, I-intermediate, E-evolved). Among the eighteen clumps considered, five clumps (C1, C2, C3, C6, C7) are active or evolved clumps. These lie to the north and west of the infrared cluster. The clump C4 is in intermediate stage as this is associated with EGO-1 and no radio emission is detected here. There is a source associated with EGO-1 seen in the PACS 160 μm image (see Fig. 4.14). The 160 μm source exhibits two peaks separated by $13''$. The northern peak is located $\sim 2''$ away from EGO-1. The southern peak lies near the green fuzzies. This double peaked source is likely to be tracing protostellar outflows. While it is difficult to predict the geometry of this region, the observations indicate that clump C4 harbors very young high mass protostar(s). This is consistent with the RWIW models of EGO-1. The rest of the clumps are quiescent. While few

Table 4.7: Clump activity and classification.

Clump No.	Radio peak	IRAC 8 μm peak	WISE 22 μm source	Clump Activity[a]	Evolutionary Stage[b]
C1	✓	✓	X	A/E	Type 2
C2	✓	✓	X	A/E	Type 2
C3	✓	✓	X	A/E	Type 2
C4	X	X	✓	I	Type 2
C5	X	X	X	Q	Type 1
C6	✓	X	X	A/E	Type 2
C7	X	✓	X	A/E	Type 2
C8	X	X	X	Q	Type 1
C9	X	X	X	Q	Type 1
C10	X	X	X	Q	Type 1
C11	X	X	X	Q	Type 1
C12	X	X	X	Q	Type 1
C13	X	X	X	Q	Type 1
C14	X	X	X	Q	Type 1
C15	X	X	X	Q	Type 1
C16	X	X	X	Q	Type 1
C17	X	X	X	Q	Type 1
C18	X	X	X	Q	Type 1

[a]Q-quiescent, I-intermediate, A-active, E-evolved based on Battersby et al. (2010)

[b]Classification scheme adopted by Sánchez-Monge et al. (2013)

have weak 8 μm diffuse emission from filamentary structures extending from the active/evolved clumps, it is unlikely that these are associated with the clumps themselves. The clump C2 is resolved into two components in the 870 μm map. As the 350 μm map is of lower resolution, there is a chance that some of the clumps actually consists of two or more sources/clumps. The sizes of the clumps range between $0.6 - 1.2$ pc. The evolutionary sequence of clumps is consistent with that proposed by Sánchez-Monge et al. (2013) (see Sect. 3.8).

The differences in evolutionary stages of clumps can also be visualised using a plot of bolometric luminosity versus clump mass (Sridharan et al., 2002; Molinari et al., 2008; Rathborne et al., 2010). For both the low and high-mass regimes, sources in different evolutionary phases have been shown to lie in distinct regions within this di-

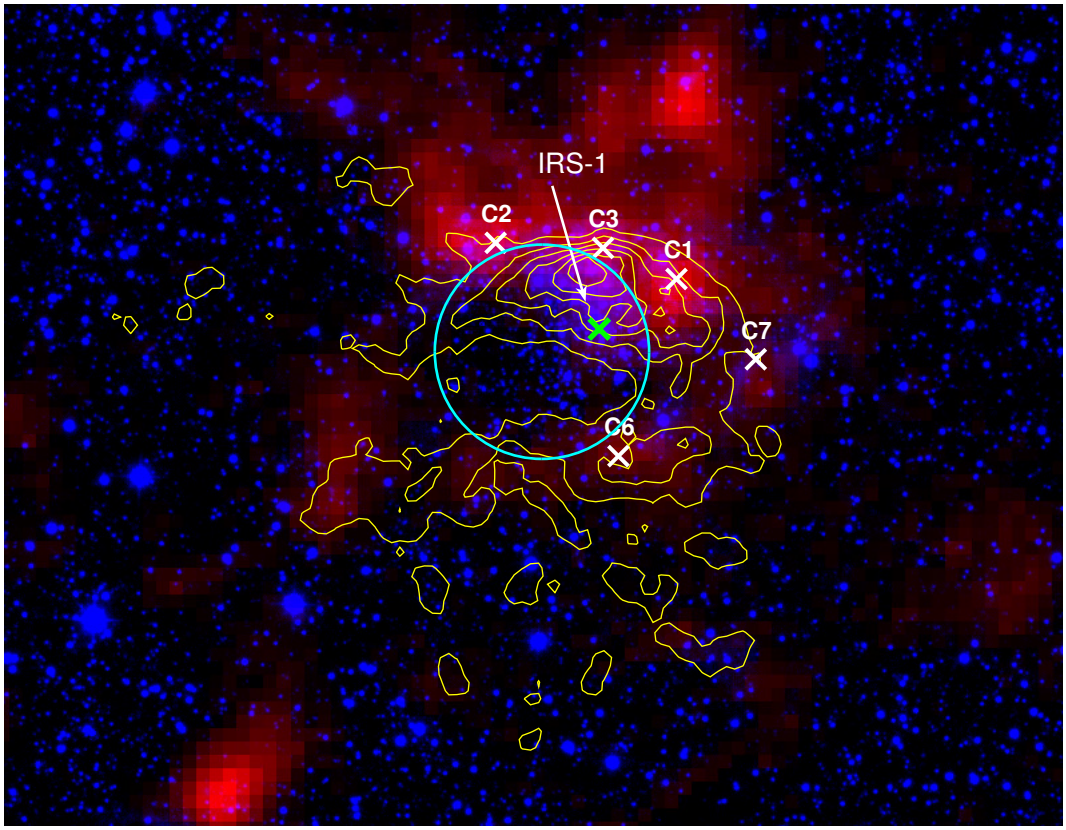

Figure 4.18: Color composite image of the IRAS 17256–3631 region. The size of the field is $6.2' \times 8.1'$. The emission of cold dust appears in red (870 μm) and near-infrared K-band image (2.2 μm) is in blue. The yellow contours correspond to radio continuum emission at 1372 MHz. The star cluster is encircled. IRS-1 is highlighted as a green $\times$. The positions of six active/evolved clumps are also shown.

agram. A plot of the clump masses and luminosities (listed in Table 4.3) is shown in Fig. 4.19. At the initial stages of evolution, the massive clumps occupy the lower region in the plot (towards the right). As the protostellar activity increases the sources move almost vertically upwards, towards the higher luminosity side with no significant variation in their masses. Here, the sources are in the accelerating accretion phase. After they reach the ZAMS stage (solid line in Fig. 4.19), they move horizontally towards the lower mass side (i.e towards left in the plot), maintaining nearly constant luminosities. This phase is known as the envelope clearing phase. If we assume that each clump forms a single star, then the luminosities and masses would indicate that our clumps lie in the massive star regime. The solid black line distinguishes the accelerating accretion phase from the final envelope clearing phase based on the models shown in Figure 9 of

Molinari et al. (2008). For this region, we find that clumps classified as A/E (Type 2) lie in the region occupied by the envelope clearing phase. On the other hand, the quiescent clumps (Type 1) lie below in the earlier evolutionary phase region corresponding to the accelerating accretion phase. The clump classified as intermediate lies between the two groups. This corroborates with the evolutionary stage of clumps obtained by us earlier using multi-wavelength tracers.

The evolutionary stages of clumps obtained support the picture of the H II region described in the last section. The embedded star cluster has cleared its surroundings of dense gas. and star formation is active towards the central clumps and the clump C4 to the north is in an earlier evolutionary stage. Since the active clumps surround the infrared cluster towards the north and west where the ionised gas has propagated, it is not unlikely that the ionisation front has triggered star formation in clumps here. The clumps towards the east and south are likely to be quiescent, probably due to lower densities as this is the direction in which the H II region is expanding.

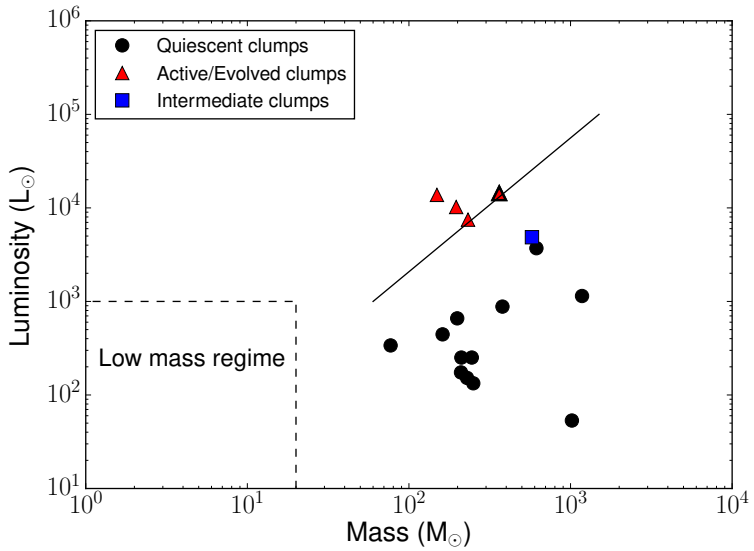

Figure 4.19: Plot of bolometric luminosity versus mass of the clumps. The solid line distinguishes the final-envelope clearing phase (region above) from the accelerating accretion phase (region below) for high mass protostellar objects (Molinari et al., 2008). The triangle with thick line indicates the location of two active/evolved clumps.

4.6 Cometary nature of the H II Region

4.6.1 Ionized gas distribution

IRAS 17256–3631 is a cometary H II region as seen from the radio continuum images. This morphology is observed in 20% of all the known H II regions (Wood & Churchwell, 1989). A cometary H II region comprises of a bright arc-like head and a broad tail of emission. The high resolution 1372 MHz image ($\sim 6''$) shows clumpiness in the ionised gas emission. The lower resolution 610 MHz image ($\sim 10''$), on the other hand, displays a comparatively smooth cometary structure. The 325 MHz image reveals the presence of large scale diffuse emission at lower flux densities spanning a region of $\sim 7'$. The cometary structure is evident in all the frequency bands. The clumpiness of ionized gas can be explained as a result of the local density enhancements in the molecular cloud (Kim & Koo, 2001). If a single ZAMS star is ionizing the entire region, the spectral type of the ionizing source is O7–O7.5 or earlier. This is consistent with the luminosity of 1.6×10^5 $L_\odot$ of this region that corresponds to a single ZAMS O6.5 star (discussed in the next section). Although the radio emission peaks at a location that is $\sim 25''$ away from IRS-1, the radio ZAMS spectral type (O7.5) is consistent with that of IRS-1 estimated from near-infrared spectroscopy (O7.5 or later).

In the near-infrared, the ionised gas has been probed using Brγ line that shows high extinction filamentary features towards the west side of the region. The Brγ emission peak coincides with the radio peak. The cometary nature is also evident from the radio spectral index maps, where the spectral indices are found to be negative towards the head, indicative of shock-excitation. The spectral index-maps match well with the H_2 emission map as the excited molecular hydrogen is found to lie towards region of negative spectral index (non-thermal) emission. However, not all regions of negative spectral indices show H_2 emission, which could be attributed to extinction in the near-infrared. The mechanism for the production of shock excitation across the cometary head is discussed below.

4.6.2 Cometary models

In this subsection, our aim is to understand the origin of the cometary morphology of the H II region under investigation here. Cometary H II regions vary widely in their appearance and several models have been proposed to explain their shape. The two prominent ones are (i) the bow-shock model (Reid & Ho, 1985; van Buren et al., 1990; Mac Low et al., 1991), and (ii) champagne flow model (Israel, 1978; Tenorio-Tagle, 1979).

In the bow shock model, it has been proposed that cometary regions are the result of relative motion of the star against ambient molecular gas. Here, the H II regions are modeled as bow-shocks created by wind blowing massive stars moving supersonically through the molecular clouds. The champagne flow model, on the other hand, explains the cometary shape as a result of density gradient in the molecular cloud, where the ionised gas expands asymmetrically out of a dense clump towards a regions of minimum density. The effect of strong stellar winds have also been included in these models (Gaume et al., 1994; Arthur & Hoare, 2006).

From the contours in our radio maps, we see that there is a steep density gradient towards north-west while it is shallow and spread out towards south-east. This implies that the H II region is density bounded in north-west and ionization bounded towards the south-east. In order to understand the mechanism responsible for the observed morphology of the H II region, we first consider the bow-shock model. We use simple analytic expressions to calculate few shock parameters. According to this model, the stellar wind from a star travelling supersonically through the molecular cloud flows isotropically from the star in all directions, until it encounters a terminal shock. For a star moving in the plane of sky, the bow-shock is expected to trace a parabola. The shock occurs at a stand-off distance l from the star where the momentum flux in the wind equals the ram pressure of the ambient medium. The stand-off distance l is estimated using the expression below (van Buren et al., 1990).

$$\left[\frac{l}{\mathrm{cm}}\right] = 5.50\times10^{16} \left[\frac{\dot{m}_*}{10^{-6}\mathrm{M}_\odot\mathrm{yr}^{-1}}\right]^{1/2} \left[\frac{v_w}{10^8\mathrm{cm\,s}^{-1}}\right]^{1/2} \mu_H^{-1/2} \left[\frac{n_H}{10^5\mathrm{cm}^{-3}}\right]^{-1/2} \left[\frac{v_*}{10^6\mathrm{cm\,s}^{-1}}\right]^{-1} \tag{4.2}$$

where $\dot{m}_*$ is the stellar wind mass loss rate, v_w is the wind's terminal velocity, n_H is the number density of hydrogen nuclei in all forms of the ambient gas and v_* is the relative velocity of the star through the medium. The mean mass per particle in the molecular gas is μ_H=1.4m$_H$ where m$_H$ is taken as one atomic mass unit. The stellar wind mass loss rate ($\dot{m}_*$) and wind terminal velocity (v_w) are calculated using expressions given below (Mac Low et al., 1991).

$$\left[\frac{\dot{m}_*}{10^{-6}\mathrm{M}_\odot \mathrm{yr}^{-1}}\right] = 2 \times 10^{-7} \left[\frac{L}{\mathrm{L}_\odot}\right]^{1.25} \tag{4.3}$$

$$\log\left[\frac{\mathrm{v_w}}{10^8 \mathrm{cms}^{-1}}\right] = -38.2 + 16.23 \log\left[\frac{\mathrm{T_{eff}}}{\mathrm{K}}\right] - 1.70 \left(\log\left[\frac{\mathrm{T_{eff}}}{\mathrm{K}}\right]\right)^2 \tag{4.4}$$

Considering an O7.5 type star, we have assumed a luminosity $L = 8.3 \times 10^4\ L_\odot$ and effective temperature $T_{eff} = 37,500$ K, (Panagia, 1973). With this, we get $\dot{m}_* = 0.28 \times 10^{-6}$ M$_\odot$yr^{-1} and $v_w = 3.0 \times 10^8$ cm s^{-1}. Using these values and taking the number density of hydrogen nuclei to be 1.4$\times$10^5 cm^{-3} (Fontani et al., 2005) and typical velocity of the star (v_*) to be 10 km/s (van Buren & Mac Low, 1992), the stand-off distance is 3.5$\times$10^{16} cm that corresponds to 0.01 pc. The stand-off distance increases by an order of magnitude to 0.12 pc if the velocity of the star is 1 km/s. On the other hand, decreasing the ambient density by an order of magnitude (1.4$\times$10^4 cm^{-2}) within which the star is moving with a velocity 10 km/s changes the stand-off distance to 0.05 pc. Taking stand-off distance as the distance between the steep density gradient at the cometary head and the radio peak (i.e location of embedded exciting star), we estimate l for IRAS 17256–3631 from our radio images as ~ 0.2 pc. If we assume IRS-1 to be the ionizing source, the stand-off distance is $\sim$0.44 pc. If we consider a star moving with a moderate velocity of 1 km/s, we get the theoretical stand-off distance as 0.38 pc, close to the observed value only if we consider an ambient medium of density that is lower by an order of magnitude. We note that the viewing angle could play a role in our estimation of l. An inclination of 45° would lead to a decrease in the theoretical stand-off distance by $\sim 70\%$. However, this would enhance the disparity between the

theoretical and observed values.

Another parameter that we have estimated in the bow-shock model is the trapping parameter (τ_{bow}) for the ionization front. The supersonically moving star sweeps up dense shells of gas that traps the H II region within them and consequently, the ram pressure prevents the H II region from expanding dynamically. The shell traps the H II region when there are more recombinations in the shell than ionizing photons. The trapping parameter is expected to be much larger than 1 ($\tau_{bow} \gg 1$) as computed by Mac Low et al. (1991) for a number of cometary H II regions. They find $\tau_{bow} \sim 15-900$ for 4 ultracompact H II regions. Here, we calculate the trapping parameter and compare with values obtained for other cometary H II regions explained using the bow-shock model. The trapping parameter at the stagnation point is given by the following expression (van Buren et al., 1990)

$$\tau_{bow} = 0.282 \left[\frac{\dot{m}_*}{10^{-6}\mathrm{M}_\odot\mathrm{yr}^{-1}}\right]^{3/2} \left[\frac{v_w}{10^8\mathrm{cms}^{-1}}\right]^{3/2} \left[\frac{v_*}{10^6\mathrm{cms}^{-1}}\right]^{-1} \left[\frac{n_H}{10^5\mathrm{cm}^{-3}}\right]^{1/2} \mu_H^{-1/2} \left[\frac{T_e}{10^4\mathrm{K}}\right]^{-1} \left[\frac{N_{Ly}}{10^{49}\mathrm{s}^{-1}}\right]^{-1} \gamma^{-1} \left[\frac{\alpha}{10^{-13}\mathrm{cm}^3\mathrm{s}^{-1}}\right] \tag{4.5}$$

Here T_e is the electron temperature of the H II region assumed to be 7500 K, and N_{Ly} is the ionizing flux of the star taken as 3.12×10^{48} s^{-1}, calculated from the 1372 MHz data. The recombination coefficient for hydrogen atoms is denoted by α and we assume a value of 3.57×10^{-13} cm^3 s^{-1} at 7500 K. This value is estimated by linear interpolation of the optically thick Case B from Osterbrock (1989). γ is the ratio of specific heats and taking this as 5/3, we obtain the value of trapping parameter as $\tau_{\mathbf{bow}} = \mathbf{1.8}$. This implies that even if there is a bow shock, it is quite weak and the H II region appearance will be amorphous corresponding to ionized quiescent cloud material surrounding the completely ionized bow shock (van Buren et al., 1990). However, in our case we see steep density gradient near the cometary head of the H II region.

From the considerations above, we see that it is unlikely that the cometary appearance of IRAS 17256–3631 can be explained using the bow shock model alone. Further, we note that although the bow-shock model is generally invoked to explain the cometary morphology of H II regions, the origin of the supersonic nature of stellar ve-

locities in young embedded clusters has been under speculation. In fact, bow-shocks from run-away O stars in the interstellar medium have been observed (Kaper et al., 1997; Noriega-Crespo et al., 1997; Comerón & Pasquali, 2007). However, in these cases the velocities are high, of the order of 10-100 km/s as they move in diffuse interstellar medium (Ramspeck et al., 2001; Edelmann et al., 2005; Gvaramadze et al., 2011). In dense molecular clouds, the adiabatic sound speed is ~ 0.3 km/s. Spectroscopic observations have indicated that dispersion velocities of stars in young Galactic clusters that are embedded or just emerged from their natal molecular cloud are typically in the range 0.5-3 km/s (Schmeja et al., 2008; Saurin et al., 2012). Although these are close to or larger than the sound speed, the velocities of stars moving at supersonic speeds producing bow shocks are found to be much higher (5–20 km/s) in the models. It is required that the supersonic motion of the star be in the plane of sky or close to it for the H II region to appear cometary. Therefore, proper motion measurements would be required to determine the stellar velocity, and that is difficult considering that the star is embedded and the distance is large. Another method to confirm the supersonic velocity of star and formation of bow-shock, involves measurement of the relative velocity of ionized gas with respect to the molecular cloud.

An alternative model that explains the cometary morphology is the champagne flow model. A massive star at the center of a molecular clump but close to the edge of the molecular cloud will produce an ionisation front that preferentially expands towards the low density regions (Kim & Koo, 2001). Here, the density gradients along with hierarchical structure of molecular clouds decide the morphology of the H II region. In our case, we propose that the champagne flow plays a prominent role in the morphology of the H II region based on the following reasons. (i) If IRS-1 is the driving source, then the high density clumps C1, C2 and C3 are likely to be constraining the flow of ionised gas. (ii) The ionised cometary head matches with the location of three clumps, C1, C2 and C3 (Fig. 4.18). (iii) The radio emission has more than one emission peak that is expected due to high density clumps (a bright peak at north and another at north-west). (iv) The near-infrared H_2 emission detected in this region lacks the expected bow shock type morphology and is seen as diffuse filamentary structures (Fig. 4.2(b)) above the cometary head. This can be attributed to the density gradient in the dense ISM beyond the cometary head.

We propose the following explanation for the observed morphology based on the

champagne flow model. If we assume that IRS-1 is the massive star that is the ionising source, then the radio emission shows a steep density gradient towards the north-west of IRS-1. However, one cannot exclude the possibility of other massive stars also ionising the medium. The star(s) ionize the ambient molecular gas and the expanding ionization front encounters the high density clumps C1, C2, C3 located to the north-west and distributed in an arc-shaped morphology near the head. Regions of lower density are towards south-east of the exciting source and a champagne flow develops where the ionized gas escapes through this region producing extended emission towards south-east. The displacement of radio peak with respect to the ionising source is likely to be due to density enhancements or clumpy nature of ambient medium. In fact, radio emission peak not coinciding with the ionising source is listed as one of the characteristics for champagne flow in H II regions, although there could be exceptions because of projection effects (Yorke et al., 1983). The amount of dense molecular gas is less in the southern direction as evident from the cold dust emission map. Another interesting feature is the asymmetry of the cometary tail that is clearly seen in the 325 MHz map. The diffuse emission extends towards the north-east and south-west where there is low flux density due to cold dust. This augurs well for the champagne flow model. We, therefore, strongly believe that the cometary appearance of IRAS 17256–3631 can be explained due to the density gradient as predicted by champagne flow models.

4.7 Summary

IRAS 17256–3631 is a massive star forming region currently undergoing a bout of star formation. Using an assortment of star formation tracers, we probed the evolutionary phases of dust clumps in this region. We also identified an embedded cluster associated with this region, harbouring one or more massive stars. An investigation on the origin of cometary morphology of the H II region supports the champagne flow scenario.

Chapter 5

Gas Kinematics in the H II regions IRAS 17256–3631 and IRAS 17258–3637

In this chapter, we investigate the gas kinematics towards two H II regions using RRL observations and complementary molecular line data. RRLs arise from atomic transitions between large principal quantum number levels (typically n$\geq$40), where the small difference between energy levels entails emission of photons that belong to the radio regime. RRLs serve as the best tracers of ionized plasma in the H II regions due to their well-understood physics and high immunity to extinction (Thompson et al., 2015). The molecular line observations can be used to probe the velocity field of the ambient cloud. Such a comparative study is crucial in understanding the different interaction mechanisms between the ionised gas and molecular cloud, which is responsible for the complex morphologies of H II regions.

The two H II regions investigated in this chapter, IRAS 17256–3631 and IRAS 17258–3637 are separated by $\sim 7'$. The structure, morphology and star formation activity towards the cometary shaped IRAS 17256–3631, that is located at a distance of 2 kpc, has been examined across a wide wavelength spectrum in Chapter 4. Towards this H II region, simple analytic calculations had been used in conjunction with the morphology of dust and gas emission to show that the observed cometary morphology is better explained with the champagne flow model. IRAS 17258–3637, on the other hand, is a bipolar H II region located at a distance of 2.4 kpc (Vig et al., 2014). IRAS 17258–3637 harbors an infrared cluster embedded in fan-shaped nebulous emission. Several filamentary structures are visible in the warm dust emission. Earlier studies also reported the presence of a cold dust clump at 1.2 mm in this region (Faúndez et al., 2004). The morphology of ionized gas emission is similar to that of warm dust emission with radio emission comprising six high density regions encompassed in diffuse emission spanning a region 1.5×1.0 pc^2. The ZAMS spectral type of the bright radio core is estimated as O7.5. The bipolar nature is explained as arising due to density gradients within a flat molecular cloud.

The 172α RRL observations of these two H II regions, carried out with the Giant Metrewave Radio Telescope (GMRT) are presented here. RRLs are used to investigate the large scale motion of ionized gas. Complementary molecular line observations from MALT90 survey towards IRAS 17256–3631 has also been used to analyse the motion of the ambient molecular medium. Towards IRAS 17258–3637, far-infrared dust emission observed by the ATLASGAL has been used to infer about the distribution of molecular cloud. These sensitive observations provide a vital clue towards improving our understanding of the morphology of the H II regions.

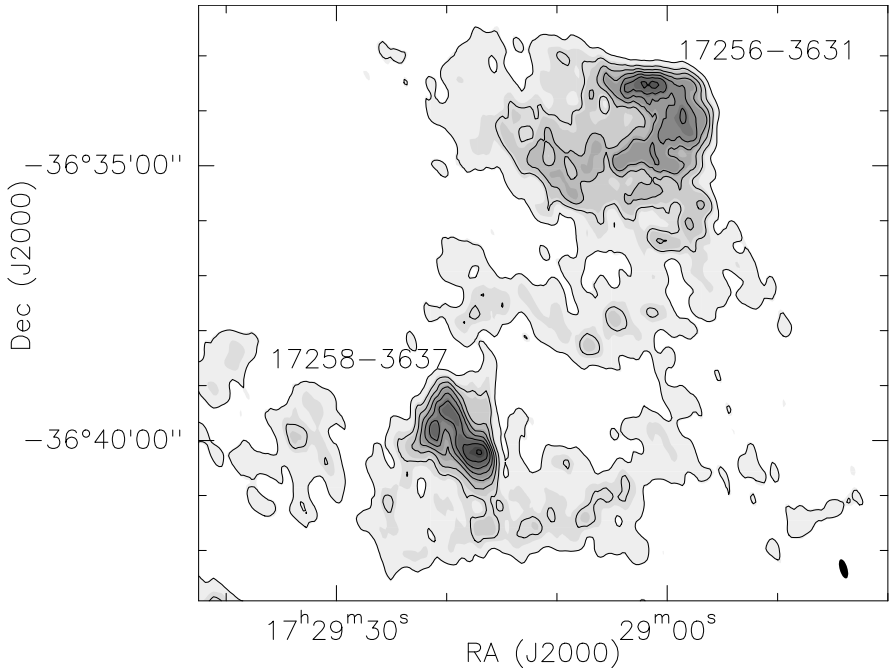

Figure 5.1: Radio continuum map of IRAS 17256–3631 and IRAS 17258–3637 at 325 MHz. The contour levels are from 25 mJy/beam to 250 mJy/beam in steps of 30 mJy/beam. The beam size is 21.7″ × 8.5″ and is shown as a filled ellipse in the bottom right corner of the image.

5.1 Continuum emission

In this section, we discuss the continuum emission arising from ionized gas at radio wavelengths and from dust at far-infrared wavelengths. The latter traces the expanse of the associated molecular cloud. The relative position of the two H II regions is illustrated in the low frequency ionized gas emission at 325 MHz in Fig. 5.1. The large

scale diffuse emission encompasses the H II regions. Considering that the kinematic distances of these regions are similar, it is possible that both of them are associated with the same giant molecular cloud.

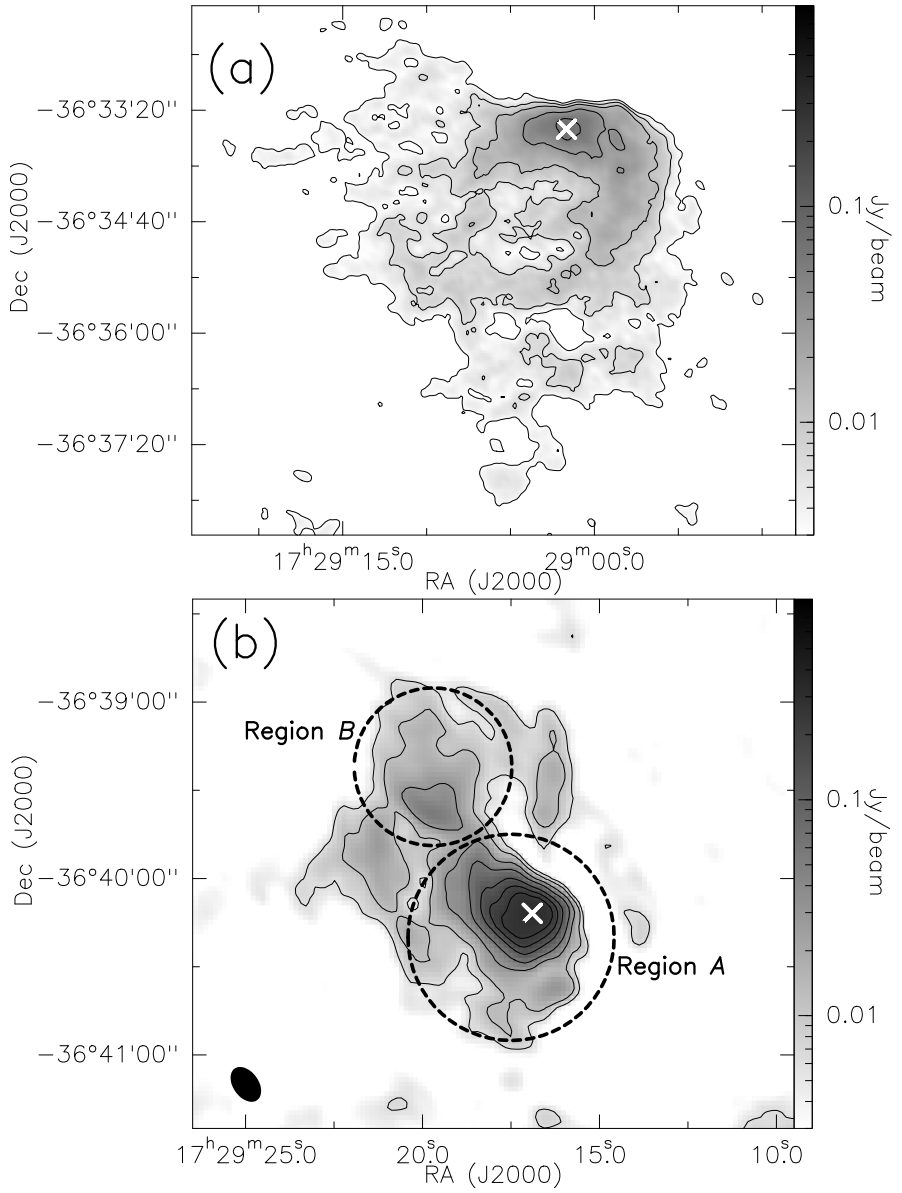

Figure 5.2: (a) Radio continuum map of IRAS 17256–3631 at 1280 MHz. The contour levels are 3, 6, 12, 24, 48, 96 and 192 mJy/beam. (b) Radio continuum map of IRAS 17258–3637 at 1280 MHz. The contour levels are at 6, 12, 24, 48, 96,192 and 272 mJy/beam . The beam size is $6.7'' \times 4.5''$ and is shown as a filled ellipse in the bottom left corner of both panels. Locations of the peak emission are marked with crosses.

5.1.1 IRAS 17256–3631

The radio continuum emission at 1280 MHz towards IRAS 17256–3631 is presented in Fig. 5.2(a). The image displays a sharp, arc-like edge with a nebulous tail characteristic of cometary H II regions. The cometary axis is aligned in the NW-SE direction. Large scale diffuse emission that spans an area of 3×3 pc^2 is perceived towards the southern region. We estimated the zero-age main-sequence (ZAMS) spectral type of the ionizing source to be O7–O7.5 based on the radio flux density (Chapter 4). The distribution of the ionized gas with respect to cold dust emission is shown in Fig. 5.3(a). We identified 18 cold dust clumps in this region and using the extensive multiwavelength analysis (discussed in Chapter 4), established that they represent early stages in the star formation process. These clumps are marked in Fig. 5.3(a).

We have estimated the average electron density of this region from the radio continuum emission using the following expression (Schmiedeke et al., 2016).

$$\left[\frac{\bar{n}_e}{\mathrm{cm^{-3}}}\right] = 2.576 \times 10^6 \left[\frac{F_\nu}{\mathrm{Jy}}\right]^{0.5} \left[\frac{T_e}{\mathrm{K}}\right]^{0.175} \left[\frac{\nu}{\mathrm{GHz}}\right]^{0.05} \times \left[\frac{\theta_{source}}{\mathrm{arcsec}}\right]^{-1.5} \left[\frac{D}{\mathrm{pc}}\right]^{-0.5} \tag{5.1}$$

where $\bar{n}_e$ is the electron density, F_ν is the flux density at frequency ν, T_e is the electron temperature, θ_{source} is the source diameter and D is the distance to the source. We have adopted the value of electron temperature as 7560 K based on the studies of Quireza et al. (2006b). The flux density F_ν is estimated within the 3σ level of radio emission, where σ is the rms noise. This corresponds to a region of area 24 arcmin^2 that gives $\theta_{source} \sim 5.5'$ assuming spherical symmetry. By application of the above expression, we obtain average electron density across the entire region $\bar{n}_e \sim 152$ cm^{-3}. In addition to this, have also estimated the electron density towards the continuum peak by selecting a circular region of radius $10''$ centered on the peak emission. The electron density near the peak emission location is found to be ∼2.0×10^3 cm^{-3}.

5.1.2 IRAS 17258–3637

The 1280 MHz radio continuum map of this region is presented in Fig. 5.2(b). The H II region is aligned in the NE-SW direction. We note the elongated region of ionized gas suggesting a bipolar morphology, consistent with that described in Vig et al. (2014). The two brightest radio regions are designated as *A* and *B* in the present work, shown in Fig. 5.2(b). The ZAMS spectral type assuming a single ionizing source is O7.5 (Vig et al., 2014). Using Eqn. (5.1), we estimated the average electron density from the radio continuum emission towards regions A and B distinctly. For an electron temperature of 6490 K (Quireza et al., 2006b), θ_{source} of $1.1'$ and $1.6'$, for A and B respectively, we estimate $\bar{n}_e(A) \sim 816$ and $\bar{n}_e(B) \sim 326$ cm^{-3}. The electron density at the continuum peak is estimated by considering a circular region of $10''$ radius. The peak n_e is found to be 3.2×10^3 cm^{-3}.

In order to investigate the cold dust emission from this region, we examined the sensitive 870 μm ATLASGAL map presented in Fig. 5.3(b). From the image, we observe that the diffuse emission tracing the large scale molecular cloud extends up to 2.8×2.0 pc^2 in the NE-SW direction. We have used 870 μm cold dust map to identify the dust clumps for two reasons: (i) the 870 μm map has the best possible resolution among dust emission maps available for this region: Herschel maps at 350 & 500 μm, 870 μm ATLASGAL and 1.2 mm map from SEST-SIMBA (Faúndez et al., 2004), and (ii) the emission is optically thin at this wavelength. The *Herschel* maps of this region are shown in Fig. 5.4. We identified two clumps in the cold dust map. This is confirmed by the application of the 2D-*Clumpfind* algorithm (Williams et al., 1994) to this image. We considered a threshold of 0.8 Jy/beam corresponding to 5σ flux level and a step size of 5σ. The peak of the dust emission lies close to the radio peak. The clump masses are estimated using the expression (Beltrán et al., 2006)

$$\mathrm{M}_{clump} = \frac{g\, S_\nu\, d^2}{\kappa_\nu\, B_\nu(T_d)} \tag{5.2}$$

where S_ν is the flux density at frequency ν, d is the distance to the source(2.4 kpc adopted from Vig et al. (2014)), κ_ν is the dust mass opacity coefficient, g is the gas-to-dust ratio ~ 100 and $B_\nu(T_d)$ is the Planck function for a blackbody at dust temperature T_d. We have considered a dust temperature of 42 K from the studies of Faúndez et al.

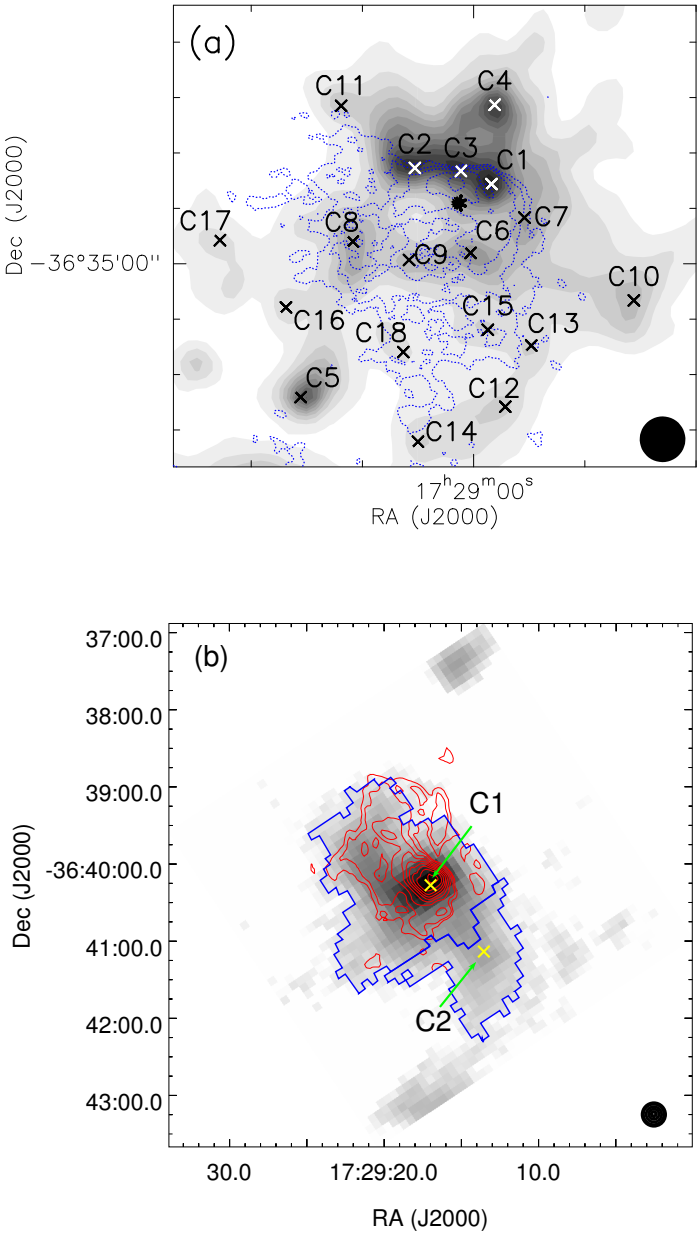

Figure 5.3: (a) Cold dust emission from IRAS 17256–3631 at 350 μm overlaid with 1280 MHz radio contours. The peak positions of 18 clumps identified in Chapter 4 are marked and labeled. The asterisk represents IRS-1 which is believed to be the ionizing source (Paper I). (b) Cold dust emission at 870 μm from IRAS 17258–3637 overlaid with 1280 MHz radio contours. The peak positions of the identified clumps are marked with cross points. The clump apertures from *Clumpfind* algorithm are shown in blue. The contour levels are same as that of Fig. 5.2. The respective beam sizes are given in bottom right of each panel.

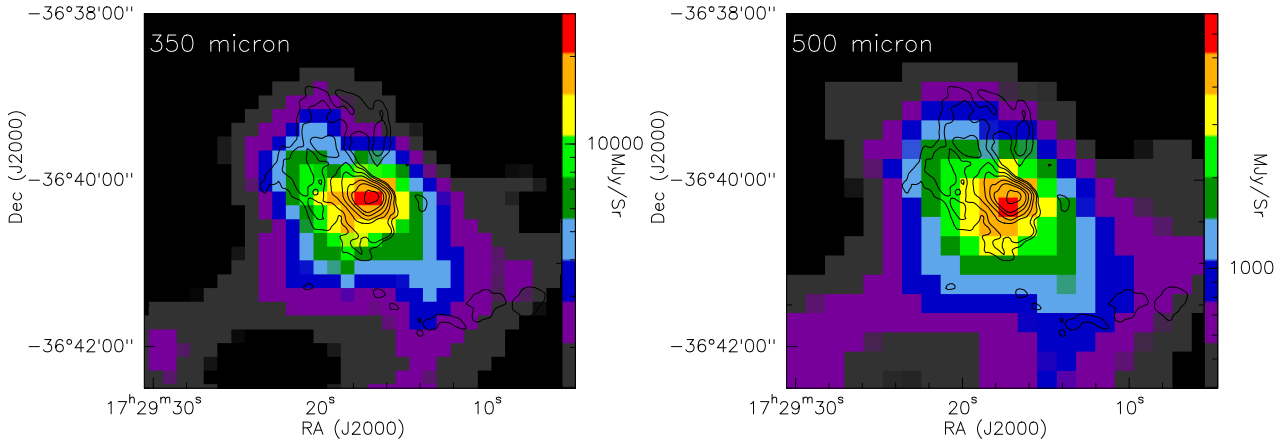

Figure 5.4: (a) Herschel 350 μm dust continuum map of the H II region IRAS 17258–3637 overlaid with 1280 MHz radio contours. (b) Herschel 500 μm cold dust map overlaid with 1280 MHz radio contours.

(2004). The assumed dust opacity is calculated using the expression (Ward-Thompson et al., 2010)

$$\kappa_\nu = 0.1(\nu/1000\ \mathrm{GHz})^\beta \tag{5.3}$$

In the above expression, β is the dust emissivity index, that is taken as 2 (Ward-Thompson et al., 2002, 2010). Using this expression, we find κ_ν as 1.2 cm^{2}g^{-1}. Incorporating this in Eqn. (5.2), the clump masses are estimated as 2480 and 380 M$_\odot$ for clumps C1 and C2 respectively. This is nearly two times larger than the previous mass estimate of 1400 M$_\odot$ by Faúndez et al. (2004) using 1.2 mm observations. This could be attributed to the larger clump aperture considered as a result of better sensitivity of the 870μm map. In addition, we note that Faúndez et al. (2004) have used $\kappa_\nu \sim 1$ cm^2/g at 1.2 mm.

5.2 RRL emission

In this section, we probe the RRL emission from the two H II regions and carry out an investigation of the distribution and observed velocity field of the ionized gas. We also assess the effect of line broadening mechanisms on the velocity profile of H172α RRL.

5.2.1 Moment maps

In this subsection, we discuss the morphology and properties of the line emission towards each H II region.

IRAS 17256–3631

The radio spectrum towards the H II region IRAS 17256–3631 integrated over the entire emission region is presented in Fig. 5.5. We detect both hydrogen as well as carbon RRLs. We fitted Gaussian profiles to the spectra to estimate the velocity and width of the RRLs. The LSR velocity of the hydrogen line is found to be -13.2 km/s and the line width is 26.3 km/s, also listed in Table. 5.1. The spatial distribution and velocity structure of RRLs can be studied by generating the moment maps. We have created the moment maps using the task `MOMNT` in AIPS software. The zeroth, first and second moments correspond to the integrated intensity, central velocity and velocity dispersion σ_v, respectively. To generate these moment maps, the line emission has been integrated within the velocities: $+17$ to -44 km/s. The zeroth moment map of the Hydrogen RRL towards IRAS 17256–3631 is shown in Fig. 5.6(a). We note that the line emission peaks westward of the radio continuum peak. This is attributed to optical depth effects near the continuum peak. From the first moment map shown in Fig. 5.6(b), we see that there appears a velocity gradient in this region, -8 to -20 km/s. This is analyzed and discussed later in Sect. 5.2.3. The second moment map displaying the dispersion in velocity is shown in Fig. 5.6(c). The zeroth and second moment maps are quite similar in appearance where the maximum dispersion is observed towards peak emission of the integrated intensity map. The line emission is not seen in the outer envelope of this H II region owing to poor SNR.

Apart from hydrogen RRL, we also detected emission from the carbon RRL. Carbon RRLs are believed to originate from photodissociation regions (PDRs; Brown et al., 1978). The LSR velocity of the carbon line is in this region is found to be -12.6 km/s while the width of the line is 5.4 km/s. The carbon line has a poorer SNR. Hence, we solely present the spectrum of C172α line from this region, shown in Fig 5.5(b)

Quireza et al. (2006a) detected H92α and C92α RRL emission towards this H II region. The LSR velocity and line width are -12.0 km/s and 23.6 km/s for H92α RRL

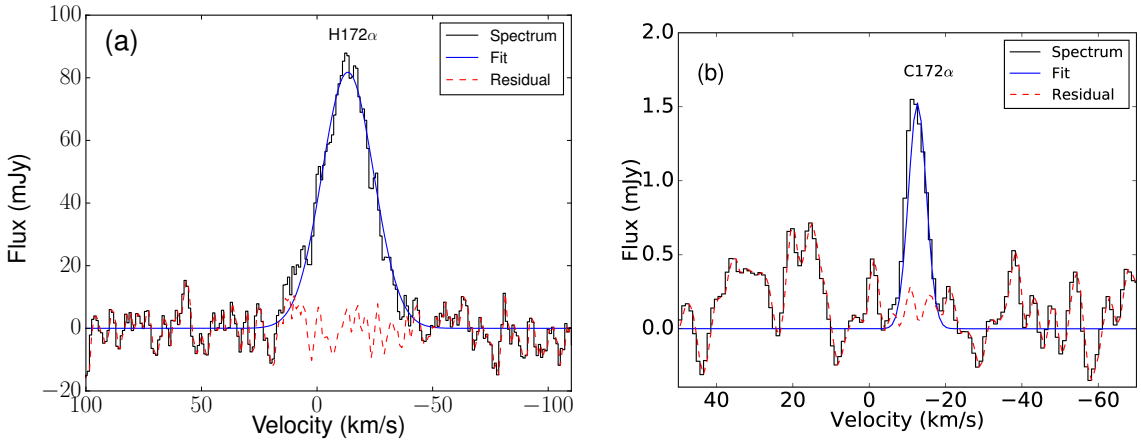

Figure 5.5: Spectra of hydrogen and carbon RRLs towards IRAS 17256–3631. The spectra are boxcar smoothed by 3 channels that corresponds to a velocity resolution of 2.9 km/s.

and -11.9 km/s and 4.7 km/s for the C92α RRL. These values are consistent with values obtained by us (see Table 5.1). Assuming local thermodynamic equilibrium and negligible pressure broadening effects for H172α RRL, we have calculated the electron temperature from the line to continuum ratio using Eqn. (1) of Quireza et al. (2006b). We obtained T_e as 4038 K. This is lower than T_e value of 7960 K obtained using H92α RRL by Quireza et al. (2006b). Our estimate can be considered as a lower limit as the emission is assumed to be optically thick towards the radio continuum peak, evident from Fig. 5.6(a).

IRAS 17258–3637

The RRL emission towards IRAS 17258–3637 is extracted for regions *A* and *B* separately. Our intention is to scrutinize for significant differences in the spectra towards the two regions. Towards IRAS 17258–3637*A*, we detected both hydrogen and carbon RRLs. The spectra towards the entire IRAS 17258–3637 region are shown in Fig. 5.7(a) and (b). The LSR velocity of the hydrogen line is -14.8 km/s whereas it is -12.4 km/s for the carbon line (see Table. 5.1). The line widths ΔV (full width at half maximum: FWHM) are 18.5 and 6.4 km/s, respectively. There is a difference in the velocities of the two lines, of $\sim$ 2.4 km/s. We speculate on this difference in later sections. Apart from the carbon line, we also detect another spectral emission feature blue shifted by 10.8 km/s with respect to the carbon line, visible in the (b) panel of Fig. 5.7. The width

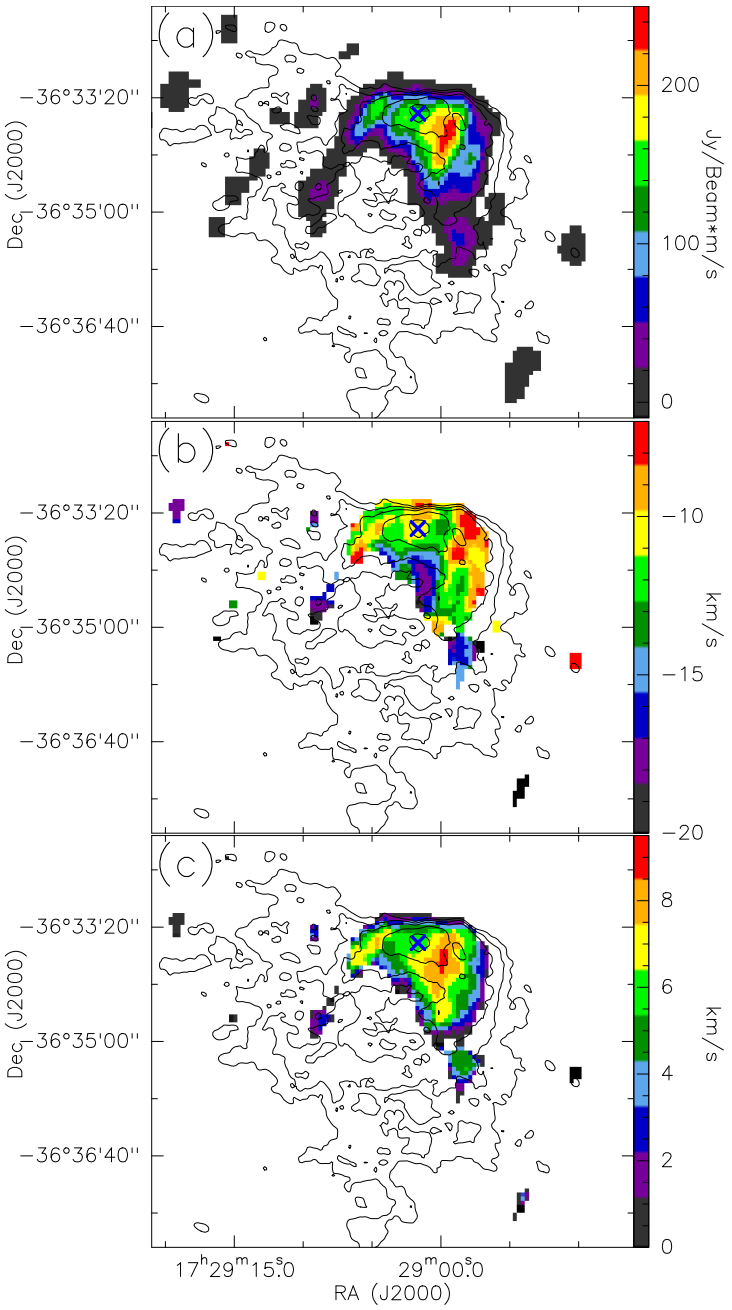

Figure 5.6: (a) Integrated intensity (zeroth moment), (b) Central velocity (first moment), and (c) Velocity dispersion (second moment) of the hydrogen RRL towards IRAS 17256–3631. Contours represent the 1280 MHz continuum emission. The contour levels are the same as those shown in Fig. 5.2(a). The radio continuum peak is marked with a cross in all the three panels.

of this line is 6.2 km/s, that is nearly the same as that of the carbon line. This line could be a RRL feature from an element heavier than carbon or alternately, it could be another

doppler shifted RRL. A similar feature is detected in few other star forming regions and is mostly believed to be a RRL feature originating from the sulfur atom (Chaisson et al., 1972; Pankonin et al., 1977; Roshi et al., 2005). RRL of other heavier elements such as Si, Mg and Fe have also been detected in some H II regions (e.g., Silverglate, 1984). Assuming an LSR velocity of -12.4 km/s, similar to that of the carbon RRL, we estimated the approximate positions of these lines in the spectrum and marked them in Fig. 5.7(b). The line strength of a single, heavy element RRL is expected to be $\sim 1/3$ that of the carbon RRL (Pankonin, 1980). But in our case, this line has nearly the same intensity as that of carbon line. We, therefore, speculate that the origin of the second line is an admixture of multiple elements such as Mg, Si, S and Fe.

The spectrum of IRAS 17258–3637*B*, displayed in Fig. 5.7(c), shows the presence of hydrogen RRL from this region. The carbon RRL is not detected here. The non-detection of carbon RRL towards region *B* could either be due to poor SNR or lack of significant emission from the PDR here. A comparison of the hydrogen RRLs toward regions *A* and *B* shows differences in the spectra in terms of widths and central velocities. This hints at the possibility that *A* and *B* are two distinct regions with different properties. The hydrogen RRL towards region *B* is broader compared to that from region *A* and a single component Gaussian fit to the former is inadequate. We therefore, fit two Gaussian functions to the observed profile: one broad (ΔV=30.1 km/s) and one narrow (ΔV=7.2 km/s). The broad component is believed to arise from the H II region, whereas the narrow component component could be from the much cooler partially ionized medium in the vicinity of the H II region (PIM; Pankonin et al., 1977; Kantharia et al., 1998a). The central velocity of these lines (broad: -8.7 and narrow:-9.9 km/s) are relatively redshifted with respect to that from *A*. The LSR velocity and line width of H92α from Quireza et al. (2006a) using single dish measurements are -13.9 km/s and 28.4 km/s respectively. The LSR velocity and line width obtained by them for the C92α RRL are -10.0 km/s and 9.7 km/s, respectively. The carbon RRL line width obtained by them is larger than that of C172α by 3.3 km/s (Table 5.1). This could be attributed to the sampling of emission from a larger region (beam $\sim 3.2'$). We also estimated the electron temperature for IRAS 17258–3637A region. Our estimate of 5906 K is lower compared to the estimate of Quireza et al. (2006b) which is 6490 K. This could be due to optical depth effects similar to that observed towards IRAS 17256–3631.

The moment maps towards the region associated with IRAS 17258–3637 are shown

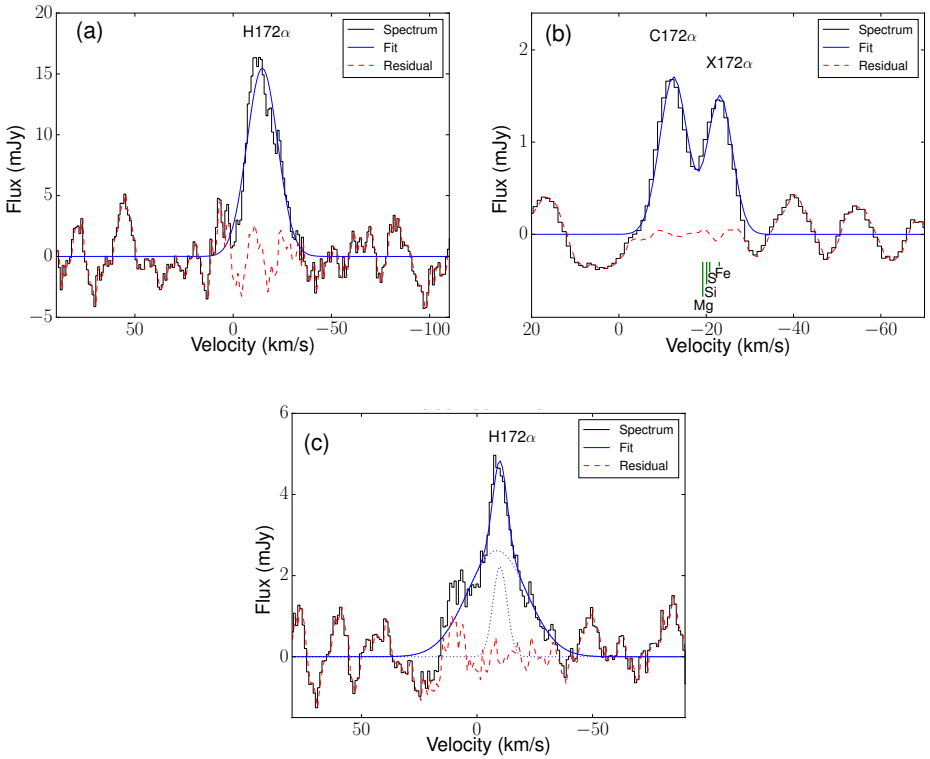

Figure 5.7: (a) H172α RRL towards IRAS 17258–3637*A* (b) C172α RRL towards IRAS 17258–3637*A* and (c) H172α RRL towards 17258–3637*B*. The spectra are boxcar smoothed to a velocity resolution of 6.3 km/s. The expected velocities of Mg, Si, S and Fe RRLs are also marked in panel (b). The estimation of velocities are under the assumption that these lines possess same LSR velocities as that of the carbon RRL.

in Fig. 5.8. The morphology is similar to that of continuum morphology but the spatial extent of line emission is again lower compared to the continuum emission (due to low SNR). Similar to the case of IRAS 17256–3631, the peak of line emission towards IRAS 17258–3637 is shifted with respect to the continuum peak. This suggests that the emission is optically thick at the continuum peak. The velocity distribution is non-uniform in this region, -7.0 to -16.3 km/s. We also notice that the velocity towards *B* is red-shifted with respect to *A*. This is consistent with the velocities obtained from the Gaussian fit to RRL integrated over the entire region and tabulated in Table 5.1. Within IRAS 17258–3637*A*, we observe a gradual increase in velocity as we move from central peak towards the south-east. This could be due to expansion of the H II region. It is difficult to interpret and correlate the velocity structures of regions *A* and *B* owing to

the complex nature of IRAS 17258–3637 but an attempt has been made to explain the observed velocity fields in terms of projection effects later in Sect. 5.4.2.

5.2.2 Line broadening in H172α

In this section, we attempt to estimate the effect of line broadening mechanisms on the observed H172α RRL towards both the H II regions. Apart from natural broadening, three important mechanisms are responsible for the broadening of radio recombination lines (Keto et al., 2008):

1. Thermal/microturbulence broadening arising from the thermal motion of the gas particles and packets of gas that are much smaller than the beam.
2. Dynamical broadening due to large scale gas motions.
3. Pressure broadening originating from the high electron densities in the region.

We investigate the impact of each of these effects on the observed RRL and obtain an estimate of the electron density values. The expression for thermal broadening $\Delta\nu_t$ depends on the line frequency ν_0 and temperature T_e as follows

$$\Delta\nu_t = \sqrt{\frac{8\,k\,T_e\,ln2}{m\,c^2}}\nu_0 \tag{5.4}$$

Here m is the mass of the particle, k is the Boltzmann constant and c is the speed of light. Under the assumption that the line width is predominantly due to thermal broadening and the effects of dynamical and pressure broadening are negligible, we estimate the upper limits to the electron temperature, $T_{e,max}$ corresponding to the H172α, C172α and X172α RRLs for both the H II regions. Substituting $\Delta\nu_t$=ΔV in Eqn. (5.4), the upper limits are calculated. These values are given in Column 6 of Table 5.1. We notice that the upper limit values $T_{e,max}$ obtained for all the regions are high except for the narrow component of hydrogen RRL towards IRAS 17258–3637A and the narrow component towards IRAS 17258–3637B. For the latter, an upper limit of 1145 K implies that this line originates in the cooler region of the PIM. The typical electron

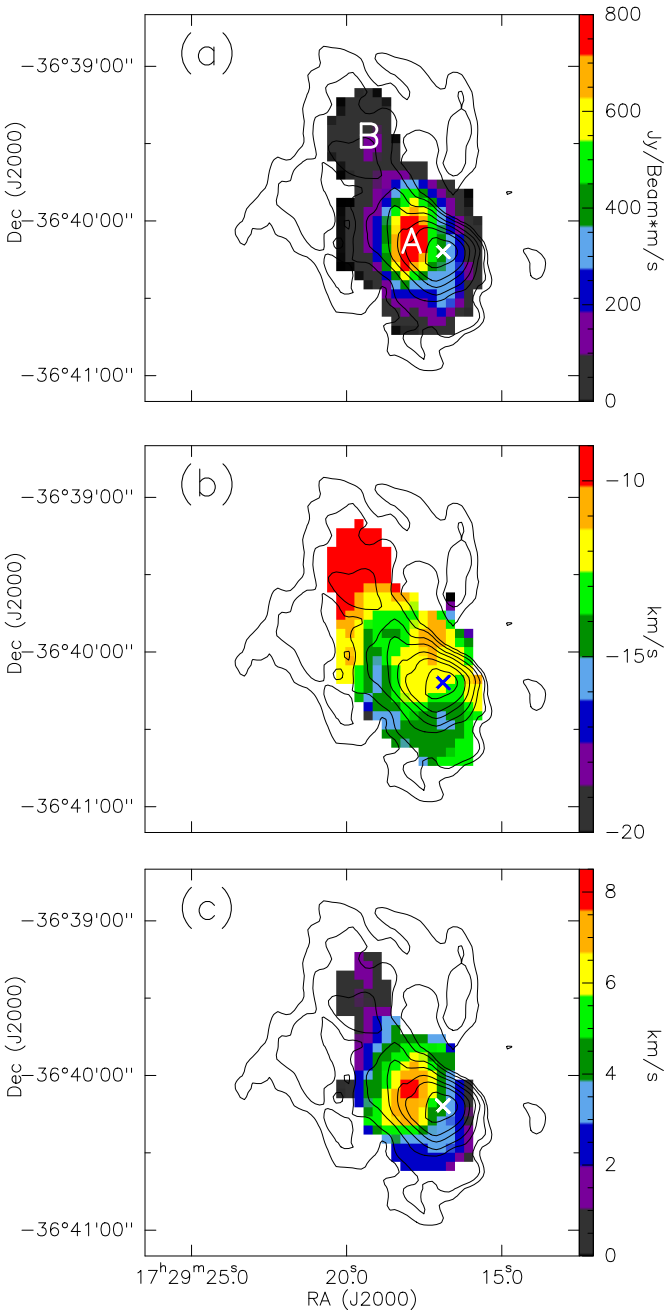

Figure 5.8: (a) Integrated intensity (zeroth moment), (b) Central velocity (first moment), and (c) Velocity dispersion (second moment) of the hydrogen RRL towards IRAS 17258–3637. The contours represent 1280 MHz continuum emission. The contour levels are the same as those shown in Fig. 5.2(b). The two regions *A* and *B* are marked in panel (a). The radio continuum peak is marked with crosses in all the panels.

temperatures of the H II regions are $\leq 10^4$ K. This suggests that the higher values of upper limits obtained for the 172α RRLs except for H172α RRL in IRAS 17258–3637A and narrow component in IRAS 17258–3637B are direct evidences for the effects of dynamical and pressure broadening.

To estimate the effects of dynamical and pressure broadening, we consider the following equations. The thermal width of the RRL is a Gaussian profile. This combines with the dynamical broadening $\Delta\nu_d$ to give a Gaussian profile again $\Delta\nu_{\rm G}$ for the RRL line. The dynamical broadening is the result of large scale gas motions in the H II region.

$$\Delta\nu_{\rm G} = \sqrt{\Delta\nu_t^2 + \Delta\nu_d^2} \tag{5.5}$$

For RRLs with large principal quantum numbers (N) arising from high density gas, pressure broadening due to electron impacts are believed to be a major source of line broadening (Griem, 1967). The line profile arising from the pressure broadening $\Delta\nu_{\rm P}$ is a Lorentzian and it has higher intensity in the line wings compared to the Gaussian profile. The Lorentzian profile combines with the Gaussian to give a resultant Voigt profile $\Delta\nu_{\rm V}$ of the following form (Keto et al., 2008).

$$\Delta\nu_{\rm V} = 0.5343\Delta\nu_{\rm P} + \sqrt{\Delta\nu_{\rm G}^2 + (0.4657\Delta\nu_{\rm P})^2} \tag{5.6}$$

The electron density can be estimated from the ratio of pressure and thermal broadening. For α ($\Delta{\rm N} = 1$) transitions, the expression for electron density is defined as follows (Keto et al., 1995)

$$\frac{\Delta\nu_{\rm P}}{\Delta\nu_t} = 1.2\left(\frac{n_e}{10^5}\right)\left(\frac{\rm N}{92}\right)^7 \tag{5.7}$$

where n_e is the electron density and N is the principal quantum number.

Table 5.1: Line parameters estimated by integrating emission across the full regions

Source		V (km/s)	ΔV (km/s)	$S_I^\star$ (mJy)	$S_C^{\star\star}$ (Jy)	$T_{e,max}^*$ (K)
IRAS 17256–3631	Hydrogen	-13.2 ± 0.2	26.3±0.6	85.5	3.6	15246
	Carbon	-12.6 ± 0.3	5.4±0.7	1.65	0.2	7639
IRAS 17258–3637 *A*	Hydrogen	-14.8 ± 0.9	18.5 ±2.1	16.4	0.8	7544
	Carbon	-12.4 ± 0.6	6.4±1.5	1.96	0.3	10728
	X172$\alpha^\dagger$	-14.6 ± 0.7	6.2±1.6	1.64	0.3	26833
IRAS 17258–3637 *B*	Hydrogen	-8.7 ± 0.9^a	30.1 ±2.8	4.9	0.4	19967
		-9.9 ± 0.5^b	7.2±1.6			1145
	Carbon	...	...	...	...	...

* : RRL flux density

** : Radio continuum flux density

* : Upper limit assuming line width is primarily due to thermal broadening

† : LSR velocity assuming X to be sulphur

^{a} : Broad component

^{b} : Narrow component

IRAS 17256–3631

A comparison of our estimates of the line parameters for H172α RRL with that of H92α RRL by Quireza et al. (2006a) shows that the width (ΔV) of H172α line is larger by $\sim$3 km/s. This could be attributed solely to the pressure broadening effects if we assume both these lines originate within the same volume of gas and hence suffer same amount of dynamical broadening. However, such a comparison is not fully appropriate, as Quireza et al. (2006a) sample a larger region owing to their larger beam size using single dish, 140 foot Green Bank Telescope observations. In addition, there could be differing opacity effects at the distinct frequencies considered.

To analyze the various line broadening mechanisms towards IRAS 17256–3631, we first consider the thermal broadening $\Delta\nu_t$. From the observations of H92α RRLs towards IRAS 17256–3631 by Quireza et al. (2006b), the estimated electron temperature of this region is 7560 K. Using this temperature value and m as the mass of hydrogen atom, i.e. 1.67×10^{-27} kg, we determine $\Delta\nu_t$ from Eqn. (5.4) as $\sim$18.6 km/s. To get

an estimate of the microturbulence present in the region, we have followed the method prescribed by Sewiło et al. (2008). The average molecular line FWHM in this region is $\sim$2.5 km/s (from CO and CS line observations of Fontani et al., 2005). This is similar to the widths of HCO^+ and $H^{13}CO^+$ lines discussed later. Considering that the line width due to thermal broadening in molecular lines is $<$0.5 km/s (Sewiło et al., 2008), the estimated FWHM can be considered as that arising mostly from the turbulence, unless there are large scale effects. Thus, the combined width due to thermal and turbulence broadening (added in quadrature) is 18.8 km/s. This implies that the effect of microturbulence is negligible in this region. We next estimate the effect of pressure broadening along one line-of-sight (i.e single pixel) assuming that the contribution of dynamical broadening is negligible. We select the pixel with peak emission as it corresponds to the maximum SNR. The observed line width towards this line-of-sight as estimated from the second moment map is $\sim$ 21.3 km/s (FWHM = 2.35σ_v). Considering the microturbulence of 2.5 km/s and other gas motions to be negligible towards the single pixel, we substitute $\Delta\nu_{\rm V} \sim 21.3$ km/s and $\Delta\nu_{\rm G} = \Delta\nu_t \sim 18.8$ km/s in Eqn. (5.6) and estimate the pressure broadening term $\Delta\nu_{\rm P} \sim 4.3$ km/s. We use this value of pressure broadening to estimate the dynamical broadening across the entire H II region. This assumes a uniform density across the H II region. From the integrated profile towards the full region, we get $\Delta\nu_{\rm V}$ = 26.3 km/s. Our estimate of pressure broadening from the pixel with the peak RRL emission can be considered as sort of large value as there are density gradients present within the ionized nebula. Using this upper limit and $\Delta\nu_{\rm G} = 18.8$ km/s, the dynamical broadening due to large scale gas motion is found to be $\Delta\nu_d \sim 14.7$ km/s from Eqns. (5.5) and (5.6). This is a conservative estimate and the actual value is expected to be higher.

A comparison of the estimates obtained for the broadening effects shows that the magnitude of pressure broadening is nearly one-third that of dynamical broadening while the magnitude of dynamical broadening is comparable to that of thermal broadening. This is not surprising as we observe a velocity gradient in this region that confirms the presence of high speed gas motions. The reverse has also been observed, where the effect of pressure broadening is larger than that of dynamical broadening (e.g., G01.4–0.4; Keto et al., 2008). However, these mostly correspond to hypercompact H II regions that are characterized by their small sizes and high electron densities (10^5-10^6 cm^{-3}) and pressure broadening due to particle collisions is the dominant mechanism in the

broadening of RRL.

We next endeavour to estimate the electron density using the values obtained earlier for $\Delta\nu_{\rm P}$ and $\Delta\nu_t$. Substituting N=172 in Eqn. (5.7), we obtain n_e as $\sim$241 cm^{-3} for $\Delta\nu_{\rm P}$ of 4.8 km/s. We would like to emphasize that the pressure broadening and hence the electron density values are expected to be larger as the emission is believed to be optically thick towards the continuum peak. Therefore, the line emission detected is predominantly from the outer surface of the H II region. For the same reason, we are unable to probe the electron density gradients, existing within the H II region. The densities towards the continuum peak, therefore, could be orders of magnitude higher than that of average value obtained.

All our calculations are based on a Gaussian fit to the observed profile. Cases have been reported where there is an observable detection of Voigt profile of the RRLs (e.g., Simpson, 1973; Kantharia et al., 1998b; Foster et al., 2007; von Procházka et al., 2010). In few sources, apart from pressure broadening, the Lorentzian profile has a contribution from radiation broadening due to the Galactic background as well as bright background sources (Kantharia et al., 1998b). In these cases, the profile deviates from the Gaussian considerably and is detected observationally. In our case, as the magnitude of pressure broadening is considerably lower than the other broadening mechanisms, it is unlikely to produce an observable effect on our line profile.

IRAS 17258–3637

A comparison of line widths of H172α with H92α is difficult in this region as the line width of the latter has contributions from both the regions A and B. Hence, we cannot draw any conclusions about the line broadening mechanisms apriori. To estimate the effects of various broadening mechanisms and to determine the average electron density towards IRAS 17258–3637, we proceed with the analysis similar to that for IRAS 17256–3631 (Sect. 4.2.1). We carry out the analysis separately for the two distinct regions, *A* and *B*. We first estimate the magnitude of thermal broadening using a temperature of 6490 K estimated by Quireza et al. (2006b). These authors used the the line-to-continuum ratio from the single dish H92α observations from the 140 ft Green Bank Telescope (Half Power Beam Width $\sim 3.2'$) for determining the temperature. With this resolution, they could not distinguish the two regions separated by $0.8'$: *A*

Table 5.2: Properties of the individual H II regions from radio continuum and H172α RRL

Source	$\Delta\nu_t$ (km/s)	$\Delta\nu_d$ (km/s)	$\Delta\nu_{\rm P}$ (km/s)	n_e (cm^{-3})	$\bar{n}_e$ (cm^{-3})	$\Delta\nu_{\rm P,min}$ (km/s)
IRAS 17256–3631	18.6	14.6	4.8	273	152	2.7
IRAS 17258–3637A	17.2	3.3	1.8	110	816	13.4
IRAS17258–3637B	...	...	...	...	326	5.4

$\Delta\nu_t$: Thermal broadening
$\Delta\nu_d$: Dynamical broadening
$\Delta\nu_{\rm P}$: Pressure broadening
n_e : Local electron density estimated from H172α RRL
$\bar{n}_e$: Average electron density from radio continuum emission
$\Delta\nu_{\rm P,min}$: Minimum pressure broadening estimated from average electron density

and *B* implying that they used emission from the entire H II region to estimate the electron temperature. We proceed by using the same electron temperature for both these regions. However, the results are treated with caution as the local electron temperatures for the individual regions may vary from the value considered. Using Eqn. (5.4), we estimate the value of thermal broadening as $\Delta\nu_t \sim 17.2$ km/s.

We first consider IRAS 17258–3637*A*. From the second moment map, the velocity dispersion corresponding to the peak line emission is $\Delta\nu_{\rm V} \sim 18.2$ km/s. Considering that the effect of microturbulence in this region to be similar to IRAS 17256–3631 ($\sim$2.5 km/s), the combined line width due to thermal and microturbulence broadening is 17.4 km/s. Using this, we estimate the upper limit on the pressure broadening as $\Delta\nu_{\rm P} \sim 1.6$ km/s. Now if we consider the integrated profile from the entire *A* region, $\Delta\nu_{\rm V} \sim 18.5$ km/s. Using this, the estimated lower limit of dynamical broadening is $\Delta\nu_d \sim 3.3$ km/s. The scenario here is clearly different from that of IRAS 17256–3631. The thermal broadening is the dominant broadening mechanism in this region. The pressure broadening is negligible while the effect of dynamical broadening is also lower. Also, we could not find large velocity gradients in the first moment map towards *A*. From the pressure and thermal broadening estimates, the lower limit to the electron density is 110 cm^{-3}.

For the northern region IRAS 17258–3637*B*, we do not attempt to interpret the line broadening effects owing to the complex profile of hydrogen RRL. In an earlier section, we speculated that the narrow component originates in the PIM region while the broad component is from the H II region. Comparing the magnitude of thermal broadening $\Delta\nu_t \sim 17.2$ km/s with the width of narrow RRL that is 7.2 km/s (see Table 5.1), it is evident that the narrow component cannot be associated with the H II region. We can estimate the electron temperature of this PIM region assuming that the broadening is entirely due to thermal effects. Hence, a thermal width of 7.2 km/s corresponds to an electron temperature of ~ 1145 K. This is comparable to the electron temperature values observed towards PDRs and PIMs associated with other H II regions (Timmermann et al., 1996; Garay et al., 1998). It is difficult to decipher the broadening mechanisms for the broad component as it is compounded with the narrow component in emission. In addition, the emission from *B* is relatively weak and the noise effects start dominating in the higher order moment maps.

Table 5.2 lists the various parameters obtained for the hydrogen RRLs in both the H II regions. Columns 2, 3 and 4 gives the magnitudes of thermal, pressure and dynamical broadening. Columns 5 and 6 lists the local electron density estimated from the pressure broadening and average electron density from the continuum measurements. We have also used the average column density $\bar{n}_e$ estimated from the radio continuum flux to calculate the minimum pressure broadening suffered by hydrogen RRLs. The estimated lower limits using Eq. (5.7) are given in Column 7 of Table 5.2. For IRAS 17258–3637A, the average electron density from the continuum is much larger (factor of 7) than that estimated using hydrogen RRL. This is likely due to optical depth effects and we may be sampling emission only from the outer layer of H II region where the electron densities are expected to be lower.

5.2.3 Velocity gradient in IRAS 17256–3631

From the velocity map of IRAS 17256–3631, we discern a velocity gradient in the NW-SE direction that is of the order of ~ 12 km/s. In order to correlate the velocity with position along the cometary axis, we consider a region with good SNR. We consider five rectangular apertures: S1, S2, S3, S4 and S5 (shown in Fig. 5.9) within this region,

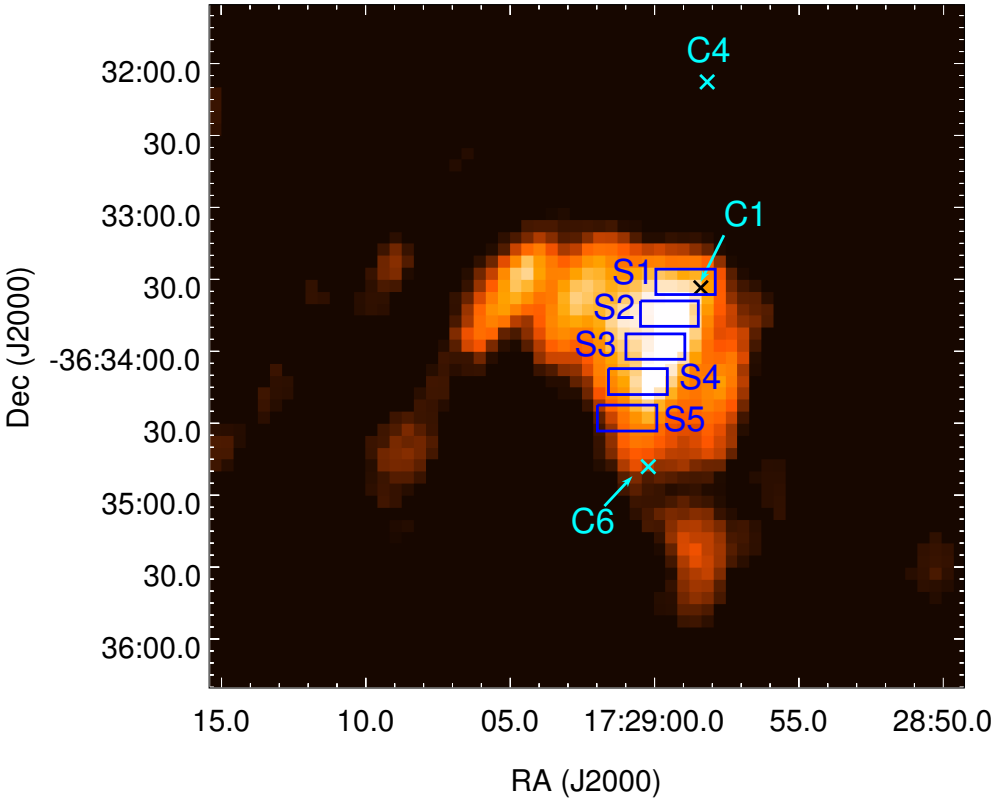

Figure 5.9: Integrated intensity map of hydrogen RRL towards IRAS 17256–3631. The boxes show areas over which emission is integrated to study the velocity gradient across the source. The peak positions of 3 clumps C1, C4 and C6 whose spectrum are presented in a later section are also marked and labeled.

aligned along the axis from the cometary head towards the diffuse tail. We integrated the flux density within each aperture and fitted a single Gaussian profile to each spectrum. The results are shown in Fig. 5.10. It is evident that the velocity is increasingly blue shifted as we move from NW to SE. The shift in velocity is ∼8 km/s as we traverse from S1 to S5 and the LSR velocities of ionized gas regions within the slits are listed in Table 5.3. The presence of a velocity gradient across the cometary axis implies a large scale motion of gas in the H II region. Similar ionized gas motions across few other cometary H II regions have been reported previously. For instance, Garay et al. (1994) found velocity gradients of 4.5, 8 and 12 km/s towards three cometary H II regions, G13.87+0.28, G32.80+0.19 and G61.48+0.09, respectively. Using the near-infrared Brγ line mapping, Lumsden & Hoare (1999) detected a large velocity gradient (∼20 km/s) within the cometary H II region G29.96-0.02. These represent compact and

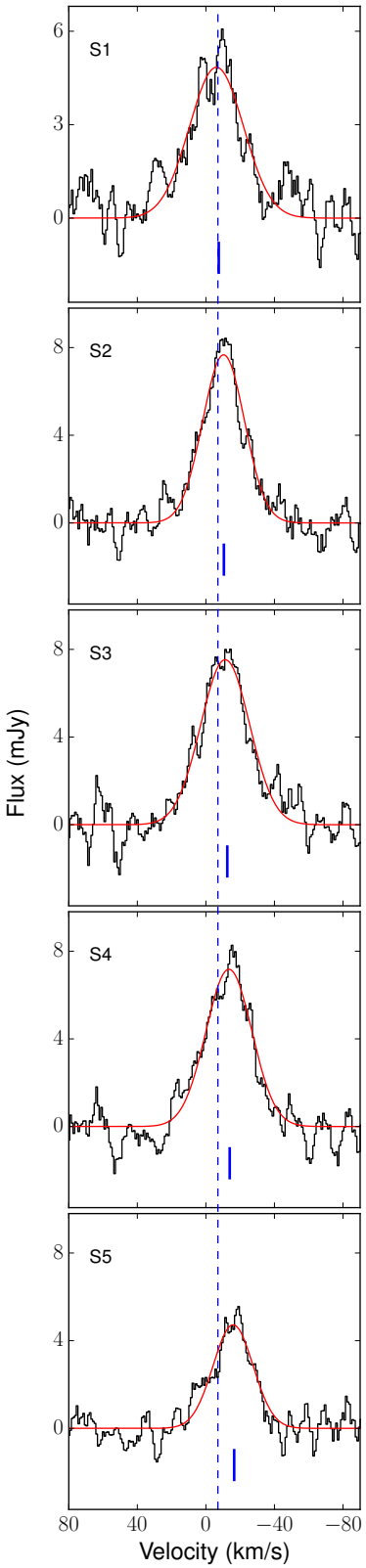

Figure 5.10: Velocity profile of the H172α line towards IRAS 17256–3631 at different aperture positions. The dashed vertical line denotes the central velocity towards location S1 (-8.6 km/s). The small line in the individual panels mark the location of Gaussian peak of individual spectra.

ultracompact H II regions (size $\leq$1 pc) powered by massive stars whose spectral types are earlier than O8. The peak electron densities are of the order of 10^3-10^4 cm^{-3}. The estimated molecular hydrogen column densities towards the cometary-like H II regions G32.80+0.19 and G61.48+0.09 lie within the range $5\times10^{21}-3\times10^{22}$ cm^{-2} (Gomez et al., 1995). These values are similar to the mean column density of 2.5×10^{22} cm^{-2} estimated towards IRAS 17256–3631 (Chapter 4).

In order to understand the mechanism(s) responsible for the ionized gas motion, it is instructive to examine the local density structures as well as the kinematics of the ambient molecular cloud. For this, we use transitions of several molecular species and the results are presented in the next section.

5.2.4 Photodissociation region (PDR)

IRAS 17256–3631

The RRLs of carbon are believed to emanate from the PDRs associated with the H II region (Pankonin et al., 1977). From the fit of the carbon line towards IRAS 17256–3631 with a Gaussian profile, we observe that the velocity of the carbon line is -12.6 km/s while its width is relatively narrow (ΔV=5.4 km/s). The narrow width of the carbon line hints at the emission originating from a relatively cooler medium, i.e., from the PDR. The central velocity of the carbon line is red shifted with respect to that of hydrogen by 0.6 km/s. Comparing the velocity of carbon line with the MALT90 molecular line data (discussed later), we see that the carbon RRL is blue shifted by 4.3 km/s with respect to ambient cloud. Keeping in view the fact that the carbon RRL emission is weak and detected close to the peak of hydrogen RRL, it is possible that the PDR medium is set into motion by the expansion of the H II region and we are likely tracing the carbon RRL emission close to the H II region. The origin of carbon RRL could either be due to the spontaneous emission in the C II region region and/or stimulated emission due to the strong background radiation field of the H II region (Kantharia et al., 1998a). In the case of IRAS 17256–3631, we detect C172α RRL near the continuum peak which could possibly indicate the predominance of stimulated emission. We have not detected carbon RRL towards other regions of the continuum emission. In order to trace carbon RRLs towards the diffuse envelope and to study the velocity structure of PDR, we need

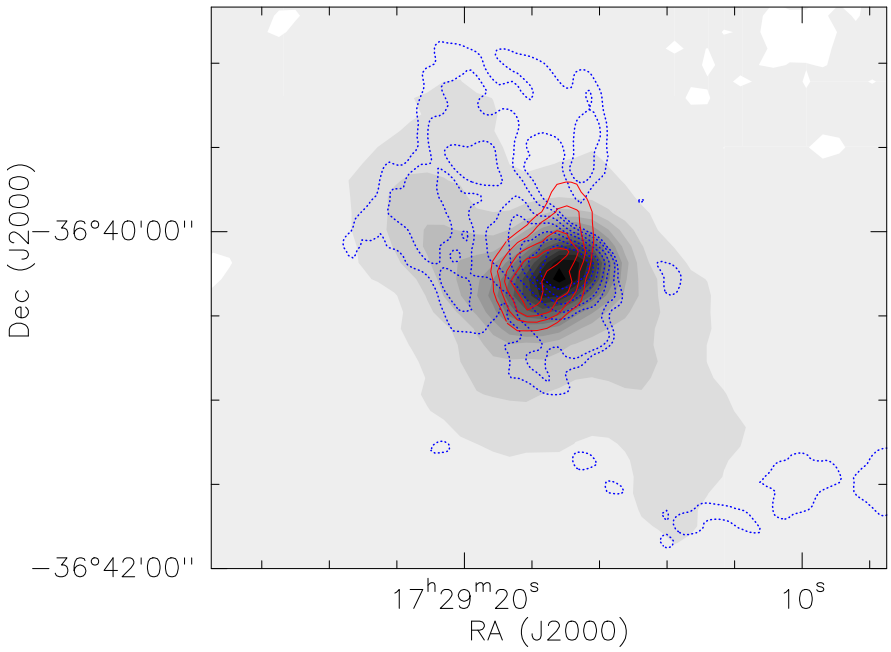

Figure 5.11: 870 μm cold dust emission towards IRAS 17258–3637 overlaid with integrated intensity contours of carbon RRL (red) and 1280 MHz radio continuum contours (dotted blue). The contour levels of the carbon RRL emission are from 7 Jy/beam*m/s to 40 Jy/beam*m/s in steps of 8 Jy/beam*m/s. The contour levels of the 1280 MHz emission are same as that of Fig. 5.2(b).

sensitive, high resolution observations with larger integration times.

IRAS 17258–3637

The integrated intensity map of carbon RRL towards IRAS 17258–3637*A* is shown in Fig. 5.11. The peak of the carbon RRL is shifted from the H172α peak by $\sim$ 7″. Carbon line emission is believed to arise in the PDR and also the partially ionized medium (PIM) located outside the HII region where hydrogen can be partially ionized which gives rise to the narrow hydrogen line. The temperature of this region cannot be larger than 1145K. In addition, we observe that most of the emission overlaps with the radio continuum emission region. This suggests that the carbon RRL could be from the PDR in front of the H II region, along our line-of-sight. We also see a small extension of the emission towards northwest-southeast direction, where there is no hydrogen RRL or continuum emission. If the emission arises in the homogeneous and isotropic partially

Table 5.3: Central velocity towards different aperture positions

Slit	V_{LSR} (km/s)
S1	-8.6 ± 1.2
S2	-10.9 ± 0.6
S3	-12.5 ± 0.7
S4	-13.9 ± 0.6
S5	-16.5 ± 0.9

ionized layer in front of the H II region, the the carbon RRL emission should follow the continuum emission. Detection of C172α emission towards outer regions where there is weak or no radio continuum emission suggests that these originate within regions whose physical properties such as n_e, T_e and emission measure (EM) are different from that of PIM surrounding the H II region (e.g., Kantharia et al., 1998a). From the molecular line data, the velocity of molecular cloud is estimated as ~ -12 km/s (Batchelor et al., 1977; Gardner & Whiteoak, 1978). The carbon line also has a velocity of -12.4 km/s, indicating that the PDR is stationary with respect to the molecular cloud. Alternately, it is possible that we are tracing the PDR emission from the surface layers rather than regions close to the H II region that could involve motion of ionized gas.

5.3 Molecular line emission from IRAS 17256–3631

5.3.1 Velocity profile of the cloud

The properties of the molecular cloud associated with IRAS 17256–3631 are investigated using the molecular line data from MALT90 survey. Six molecular species were detected towards this region: HCO^+, $H^{13}CO^+$, HCN, HNC, N_2H^+ and C_2H. In order to probe the kinematics of the cloud, we have considered the spectra of these molecules towards three different locations, that correspond to the peaks of three cold dust clumps: C4, C1 and C6. These clumps are shown in Fig. 5.3(a). Our justification for considering C1 and C6 is that they lie close to the region covered by the rectangular apertures

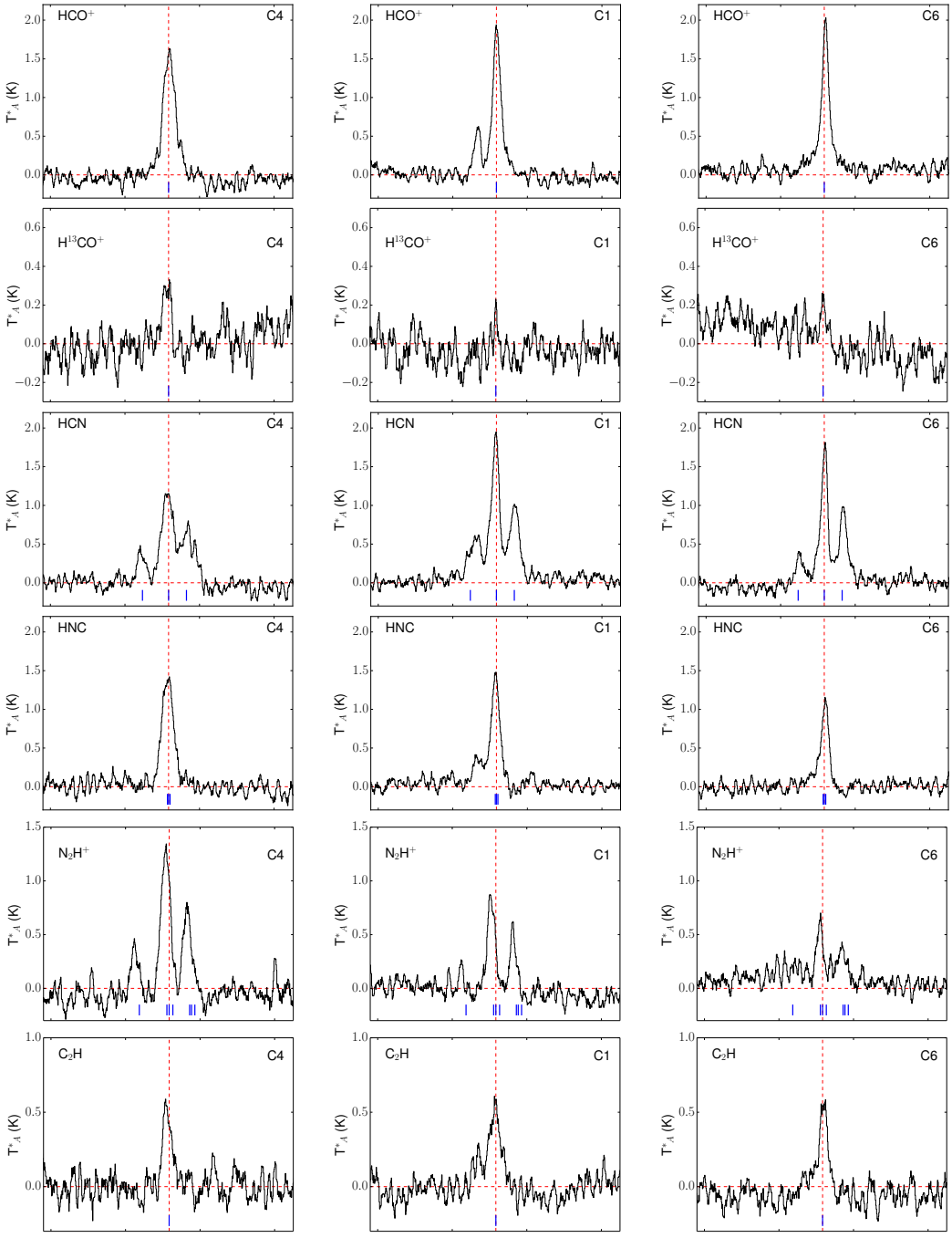

Figure 5.12: Velocity profiles of the molecular lines towards three positions, which are peaks of clump C4, C1 and C6 (Fig.5.15). The spectra are smoothed to a velocity resolution of 0.8 km/s. From top to bottom, the lines are HCO^+, $H^{13}CO^+$, HCN, HNC, N_2H^+ and C_2H. The x-axis is the LSR velocity in units of km/s and y-axis is the antenna temperature corrected for atmospheric attenuation in units of K. The dashed lines represent the central velocity of $H^{13}CO^+$ line (-8.3 km/s; vertical) and zero intensity (horizontal). The hyperfine components are marked with blue vertical lines.

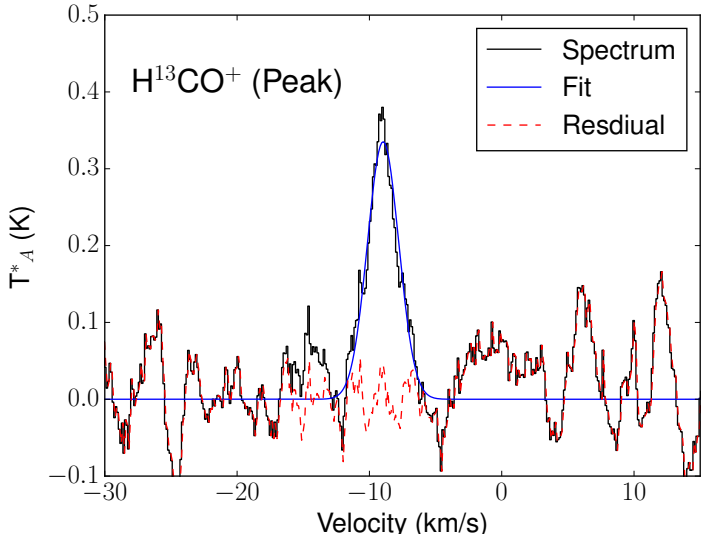

Figure 5.13: Spectrum of $H^{13}CO^+$ line towards the location of its peak ($\alpha_{J2000} = 17^h\ 29^m02.65^s$, $\delta_{J2000} = -36^\circ\ 32'\ 57.6''$) fitted with single component Gaussian function.

for measuring the velocities of ionized gas (Sect. 5.2.3). In addition, we consider the clump C4 as it is devoid of ionized gas emission. While the former two clumps are in active/evolved star formation stage, the latter is in an intermediate stage (Chapter 4). The molecular spectra towards C4, C1 and C6 (clump positions as we move from north to south respectively) are presented in Fig. 5.12.

Among the six molecular species, five are detected at the locations of all the three clumps. $H^{13}CO^+$ is detected solely towards the clump C4. We could estimate the LSR velocity using either HCO^+ or $H^{13}CO^+$ as their spectra involve a single transition, i.e. without any hyperfine components. However, we prefer to use the latter as it is likely to be optically thin. The LSR velocity is ~ -8.3 km/s estimated from the $H^{13}CO^+$ spectrum towards its peak emission (see Fig. 5.13). The hyperfine components of HCN and N_2H^+ are clearly resolved and detected towards the three clumps.

5.3.2 Wing emission and additional velocity components in the HCO^+ spectrum

We carefully examined the HCO^+ spectrum towards the peak positions of three clumps: C1, C4 and C6, as the spectrum towards each location reveals distinct features. To-

wards C4, we observe additional components in close proximity but on either side of the brightest component. We fit three Gaussian profiles to the spectrum of C4. C1 shows an additional well resolved velocity component while C6 shows a spectral line transition that is characterized by broad wings. To the spectrum towards C1, we fitted two Gaussian profiles for the two components. In the case of C6, we fit a narrow as well as a broad component as a single Gaussian profile provides an inadequate fit evident from the large residuals to the spectral line. The results of the fits to the HCO^+ spectra of these clumps are shown in Fig. 5.14 and presented in Table 5.4 . In this section, we present the analysis of these features.

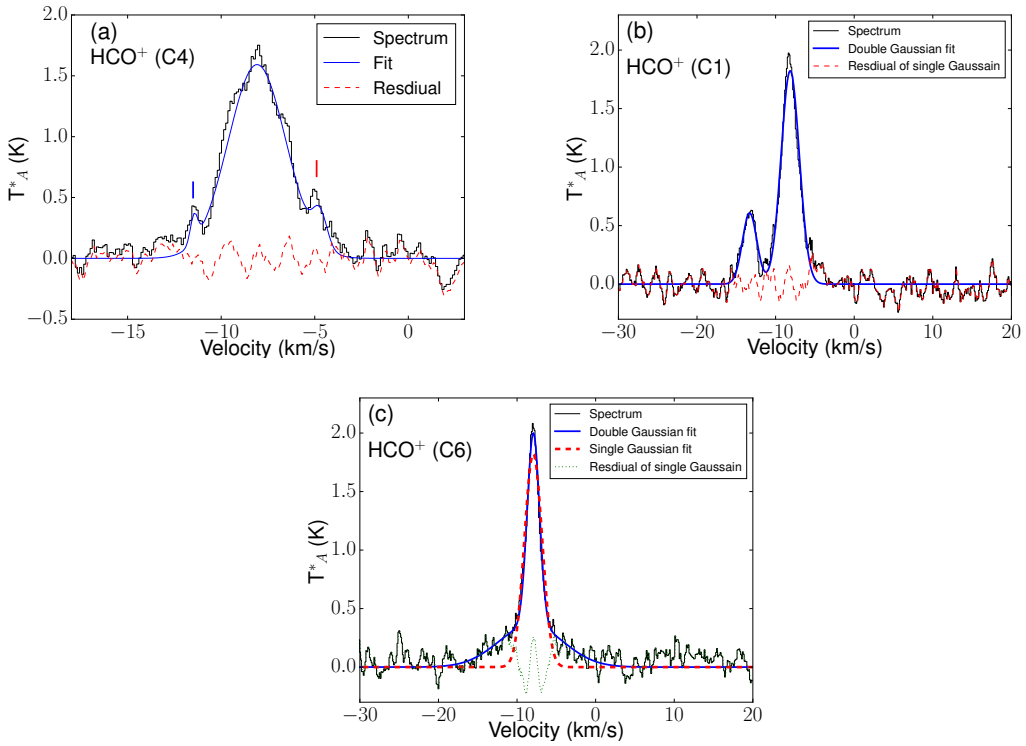

Figure 5.14: (a) The HCO^+ spectrum towards peak of C4 fitted with 3 Gaussians. The red and blue peaks on either side of the central line are marked with vertical lines. (b) The HCO^+ spectrum towards the location C1. Spectrum is fitted with two Gaussians. (c) HCO^+ spectrum towards C6. Fit to the spectrum with a single Gaussian is shown with red dashed line whereas the two component Gaussian fit is represented by blue line. The residual of the single Gaussian fit (green dotted line) is also shown in the spectrum.

C4

The profile of HCO^+ towards C4 shows three components as is evident from Fig. 5.14(a) and the central brightest component is broader than that observed towards the other clumps. We fit three Gaussian profiles to the spectrum and the best fit parameters are listed in Table 5.4. This broadening is also apparent in the HNC spectrum towards C4. The velocity of the central component is -8.1 km/s whereas the velocities of blue and red components are -11.5 and -4.7 km/s, respectively shown in Fig. 5.14(a). Both these components are separated by 3.4 km/s from the central peak. Many star forming regions display broad wings in the HCO^+ profiles that have been interpreted to be the result of molecular outflows (e.g. Gregersen et al., 1997; Zhu et al., 2010). The broadening of a spectral line could arise due to turbulence close to the protostellar object that could be the outcome of outflows, fragmentation, or unresolved velocity gradients (Tackenberg et al., 2014). In addition, hydrodynamic simulations of a collapsing cloud in the absence of outflows could also give rise to optically thick lines (e.g. HCO^+) that become broader with time (Smith et al., 2013). Gorti & Hollenbach (2002) suggest that line broadening of molecules could also originate in flows created by photoevapourating clumps. In Chapter 4, we identified an extended green object (EGO-1) close to the peak emission of the clump C4 that is likely to trace a massive protostellar object. In addition, we detected a H_2 knot near EGO-1. We speculated that this could be the outcome of an outflow. Keeping this in view, we regard the broad features along with the secondary peaks as spectral signatures sampling the proposed outflow close to the protostellar object.

C1

Towards the clump C1, apart from the primary component there is an additional, blue shifted component of HCO^+. This component is also conspicuous among the spectra of HNC and C_2H, towards C1. The velocity of the primary component is -8.2 km/s with a width of $\Delta V\sim$ 2.7 km/s. The velocity of the secondary component is -13.3 km/s and its width is 2.1 km/s. This line is relatively weak with an intensity that is nearly one-third of the primary feature as seen in Fig. 5.14(b). In many cases, an asymmetry in the line intensity is observed that is characteristic of infall or outflow motion (e.g. Walker et al., 1994; Gregersen et al., 1997; Velusamy et al., 2008). In our case, we

Table 5.4: HCO^+ line parameters

Source	V (km/s)	ΔV^a (km/s)	Δv^b(km/s)
C4	-4.72±0.08	0.89±0.18	3.36
	-8.08±0.03	3.62±0.07	0
	-11.45±0.06	0.46±0.16	−3.37
C1	-8.14±0.02	2.73±0.05	0
	-13.3±0.05	2.12±0.12	−5.22
C6	-7.92±0.02	1.83±0.05	0.32
	-8.25±0.19	9.61±0.54	0

^{a} : Line width, ^{b} : separation in velocity from the brightest component

do not observe any noticeable asymmetry in the primary line intensity. Rather, we observe a well separated blue component that could be a potential cloud situated along the same line-of-sight. Such multiple velocity components that are separated by few km/s have also been interpreted as overlapping cores characteristic of high mass star forming regions (Tackenberg et al., 2014).

C6

The HCO^+ spectrum towards the clump C6 displays excess emission in the line wings that cannot be fitted with a single Gaussian. In the single Gaussian fit, the residuals show a distinct pattern with positive values at the line center, and increasingly negative values towards the line wings and positive values thereafter. This pattern manifests the failure of a single Gaussian fit and has been recognized by Dickey et al. (1990) who explain this feature as the result of an additional broad, low-intensity component. Fig.5.14(c) shows the single and double Gaussian fits to the observed profile. From the plot, it is apparent that the spectrum is better fit with the double Gaussian profile. The central velocities of the fitted components are -8.2 and -7.9 km/s respectively, and the corresponding line widths are 9.5 and 1.8 km/s, respectively.

A study of molecular line profiles towards towards nearby star forming regions by Falgarone & Phillips (1990) showed that nearly all the profiles exhibit excess line emission towards the line wings. They argued that the excess emission is not associated with

the protostellar activity, and is the direct observational signature of turbulence within the gas clouds instead. It is possible that the excess line emission towards C6 emanates due to turbulence in the molecular cloud caused by the expansion of ionized gas towards a lower density region.

5.3.3 Column Densities of HCO^+ and $H^{13}CO^+$

We obtain an estimate of the column densities of the isotopologues HCO^+ and $H^{13}CO^+$ towards IRAS 17256–3631 using simplistic assumptions. Under conditions of local thermodynamic equilibrium, these include: (i) $H^{13}CO^+$ line is optically thin, (ii) HCO^+ line is optically thick, and (iii) the excitation temperatures of HCO^+ and $H^{13}CO^+$ species are the same. As the $H^{13}CO^+$ line has a poor SNR across the region, we consider the line intensities towards the peak of $H^{13}CO^+$ emission that is in the vicinity of clump C2 shown in Fig. 5.13. We proceed under the assumption that the $H^{13}CO^+$ profile is optically thin. We would like to remark that the column densities obtained this way would act as lower limits, in case the $H^{13}CO^+$ line is optically thick. The expression for the excitation temperature of an optically thick HCO^+ line is given below (Yu & Wang, 2013).

$$T_{\rm ex} = \frac{h\nu_0}{k}\left[\ln\left(1+\frac{h\nu_0/k}{T_{\rm max}({\rm HCO^+})+J_\nu(T_{\rm bg})}\right)\right]^{-1} \tag{5.8}$$

$$J_\nu(T) = \frac{h\nu_0}{k}\frac{1}{(e^{h\nu_0/kT}-1)} \tag{5.9}$$

Here ν_0 is the rest frequency of the HCO^+ line that is taken as 89188.526 MHz in the present case, $T_{\rm bg}$ is the temperature of the background radiation taken as 2.73 K (Purcell et al., 2006; Yu & Wang, 2015) while h and k represent Planck constant and Boltzmann constant, respectively. $T_{\rm max}(HCO^+)$ is the brighteness temperature of the maximum line intensity and is estimated using $T_{\rm max}(HCO^+)$=T_A^*/η_{MB}, where T_A^* is the antenna temperature corrected for atmospheric attenuation and η_{MB} is the main beam efficiency. We have adopted η_{MB} as 0.49 (Ladd et al., 2005) and estimated $T_{\rm max}(HCO^+)$ as 4.7 K. Using the above expressions and assuming a beam filling factor of unity, we estimated the excitation temperature $T_{\rm ex} \sim 7.7$ K. The excitation temperature is used to

obtain the optical depth of the $H^{13}CO^+$ line in the following way (Yu & Wang, 2013).

$$\tau = -\ln\left[1 - \frac{T_{\rm max}(H^{13}CO^+)}{[J_\nu(T_{\rm ex}) - J_\nu(T_{\rm bg})]}\right] \tag{5.10}$$

The optical depth of the $H^{13}CO^+$ line is determined to be $\tau \sim 0.12$. The total column density of the $H^{13}CO^+$ line, $N(H^{13}CO^+)$, is calculated using Eqn. (2) of Miettinen (2014).

$$N(mol) = \frac{3h\epsilon_0}{2\pi^2}\frac{1}{\mu^2 S}\frac{Z_{rot}(T_{\rm ex})}{g_K g_I} e^{E_{\rm u}/k_{\rm B}T_{\rm ex}} F(T_{\rm ex}) \int \tau(\nu) d\nu \tag{5.11}$$

where h is the Planck constant, ϵ_0 is the vacuum permittivity, μ is the permanent electric dipole moment, S is the line strength, Z_{rot} is the rotational partition function, g_K is the K-level degeneracy, g_I is the reduced nuclear spin degeneracy (Turner, 1991), and $F(T_{\rm ex}) = (e^{E_{\rm u}/k_{\rm B}T_{\rm ex}} - 1)^{-1}$. Here, the electric dipole moment matrix element is defined as $\mid \mu_{ul} \mid \equiv \mu^2 S/g_u$, where g_u = 2J + 1 is the rotational degeneracy of the upper state (Townes & Schawlow, 1975). For linear molecules, $g_K = g_I = 1$ for all levels (Turner, 1991). The values of various parameters used for the estimation of column density are given in Table 5.5.

The $H^{13}CO^+$ column density is estimated to be $\sim 2.3\times10^{13}$cm^{-2}. Assuming the abundance ratio [HCO^+]/[$H^{13}CO^+$] ~ 50 (e.g. Yu & Wang, 2015), the HCO^+ column density is estimated as 1.2×10^{15}cm^{-2}. We compare these values with those towards other molecular clouds. Purcell et al. (2006) estimated the $H^{13}CO^+$ and HCO^+ column density towards 79 massive star forming regions and their derived $H^{13}CO^+$ column densities lie in the range 0.5 - 14.3$\times10^{13}$ cm^{-2}. The HCO^+ column densities lie in the range 2.5 - 71.4$\times10^{14}$ cm^{-2}. Our values fall well within this range. It is to be noted that although we have assumed a beam filling factor ~ 1, if the gas is clumpy within the beam area, the true filling factor will be less than 1. In that case, the beam-averaged column density will be a lower limit to the source-averaged value.

We also estimated the fractional abundances of HCO^+ and $H^{13}CO^+$ molecules by dividing the molecular column density by the H_2 column density, χ=$N(HCO^+)/N(H_2)$. For this, we have considered $N(H_2) \sim 1.7 \times 10^{22}$ cm^{-2} towards clump C2 (Paper I).

Table 5.5: Line parameters for $H^{13}CO^+$

Parameter	Value
Frequency* (MHz)	86754.33
E_u/k^* (K)	4.16
$S\mu^{2*}$ (D^2)	15.2
Rotational constant B* (MHz)	43377
T_{ex} (K)	7.7
τ	0.12
$N(H^{13}CO^+)$ (cm^{-2})	2.3×10^{13}

*Values adopted from SPLATALOGUE spectral line catalog available at http://www.cv.nrao.edu/php/splat/

Based on this, the calculated fractional abundances are 7.2×10^{-8} and 1.4×10^{-9} for HCO^+ and $H^{13}CO^+$ molecules, respectively. A comparison of the HCO^+ abundance with that of other star forming regions is presented in detail in the following subsection.

5.3.4 Virial parameter α_{vir}

We estimate the virial parameter, α_{vir}, to gauge whether or not the clumps are stable against gravitational collapse. The virial parameter, α_{vir} is defined as follows.

$$\alpha_{vir} = \frac{\mathrm{M}_{vir}}{\mathrm{M}_{clump}} \tag{5.12}$$

Here M_{vir} is the viral mass and M_{clump} is the clump mass. For a clump with negligible surface pressure and magnetic field, $\alpha_{vir} = 1$ corresponds to virial equilibrium. Few recent studies indicate that $\alpha_{vir} > 1$ and $\alpha_{vir} < 1$ do not necessarily indicate expansion and contraction (Ballesteros-Paredes, 2006). The value of virial parameter $\alpha_{vir} \sim 2$ is considered an upper limit for a gravitationally bound clump (Kauffmann et al., 2013). The virial mass in Eqn. (5.12) is defined as

$$\mathrm{M}_{vir} = 3 \left[\frac{5-2p}{3-p}\right] \frac{\mathrm{R}\sigma^2}{\mathrm{G}} \tag{5.13}$$

Here R is the clump radius, σ is the average velocity dispersion along the line-of-sight, p is the radial profile index of a core with density profile $\rho \propto r^{-p}$, and G is the gravitational constant (Battersby et al., 2014). We assume $p \sim 1.8$, the mean value of the radial index obtained by Mueller et al. (2002) based on the modelling of a large number of massive dense cores. With this value of p, Eqn. (5.13) takes the form:

$$\left[\frac{\mathrm{M}_{vir}}{\mathrm{M}_\odot}\right] = 0.713 \left[\frac{\theta}{''}\right] \left[\frac{d}{\mathrm{kpc}}\right] \left[\frac{\Delta V}{\mathrm{km/s}}\right]^2 \tag{5.14}$$

In the above expression, d is the distance to the source, θ is the angular radius of the clump and ΔV, the full width at half maximum (FWHM) of the optically thin molecular line.

The selection of a line for estimating the virial mass has often been a matter of scale. The CO line that is normally optically thick has been used in surveys to estimate the virial masses of large scale clouds in the Galaxy (e.g. Solomon et al., 1987). MacLaren et al. (1988) argued that an optically thick line will allow us to probe only the surface layers of the cloud and hence the virial mass could be underestimated. In addition, the radiative transfer effects could also cause additional broadening and distortion, the effects of which cannot be separated easily. Optically thin lines, on the other hand, sample velocities over much smaller scales i.e., deep into the core region of the cloud. Issa et al. (1990) estimated the virial masses of local clouds using the relatively optically thin ^{13}CO line and concluded that using ^{13}CO rather than the optically thick counterpart ^{12}CO gives a better agreement with other methods of mass estimation. Several recent studies that estimate the virial mass adopt line widths obtained from optically thin lines due to the above mentioned reasons (e.g. Reiter et al., 2011; Azimlu et al., 2009; Maud et al., 2015).

Being stronger in intensity, HCO^+ is detected towards most of the clumps in the region covered by MALT90. However, the presence of multiple components and the effects of line broadening towards many clumps (e.g. C4, C6) cannot be overlooked. The line width estimation in such active regions where we we detect the signatures of turbulence, outflows and/or unresolved components is a cumbersome task. For the case of

IRAS 17256–3631, we have therefore used an optically thin line without any additional satellite or hyperfine components, namely the $H^{13}CO^+$. But unlike its optically thick isotopologue (HCO^+), this line is very weak and not detected towards all the clumps. We proceeded with a line width of 2.7 km/s of $H^{13}CO^+$ measured at the position of its peak emission where the SNR is good (Fig. 5.13) and applied this value to estimate the virial mass of all the clumps in the region. Although this is not the most reliable estimate of virial mass, this will atleast provide a preliminary insight into the star formation activity of the individual clumps of parsec scale. Fontani et al. (2005) estimated the virial mass of the entire molecular cloud using the FWHM of CS line ~ 2.6 km/s, consistent with our estimate of the velocity dispersion.

Table 5.6: Virial masses and virial parameters for the 18 clumps in IRAS 17256–3631

Clump No.	M_{vir} ($M_\odot$)	M_{clump} ($M_\odot$)	α_{vir}
C1	402	200	2.0
C2	578	400	1.4
C3	371	200	1.9
C4	609	600	1.0
C5	504	1200	0.4
C6	483	200	2.4
C7	639	300	2.1
C8	596	600	1.0
C9	454	1000	0.5
C10	630	400	1.6
C11	447	200	2.2
C12	423	200	2.1
C13	431	100	4.3
C14	447	200	2.2
C15	411	200	2.1
C16	398	300	1.3
C17	406	200	2.0
C18	419	200	2.1

We estimate the virial mass of the 18 molecular clumps under the assumptions that (i) the clumps are homogeneous and spherically symmetric, (ii) contributions due to surface pressure and magnetic field is negligible. M_{clump} is estimated from the dust continuum emission, the details of which are given in Chapter 4. The clump numbers, virial mass M_{vir}, clump mass M_{clump} and virial parameter α_{vir} values are listed in Table 5.6. Of the eighteen clumps, ten have $\alpha_{vir} \leq 2$, the critical limit below which the clumps are believed to be unstable. Further, the clump C4, that shows several signatures of protostellar activity has α_{vir}=1. From the table, we see that two of our clumps, C5 and C9 have relatively low values ($\alpha_{vir} < 1$). The same clumps possess the highest surface densities (Σ) as compared to other clumps (0.3 and 0.4 g cm^{-2} respectively, Chapter 4). It is therefore likely that these clumps are unstable and undergoing gravitational collapse. The clump C13 has a relatively large virial parameter (α_{vir} ∼4.3). This could be interpreted as the stability of the clump against collapse. However, we would like to remark that this is the least massive clump (with clump mass at least a factor of 2 less than the other clumps). In addition, we emphasize that the absolute values should be treated with caution considering that a single velocity dispersion value has been used for all the clumps. The median α_{vir} for our clump data is 2.0 that is close to the median $\alpha_{vir} \sim 1.9$ obtained by Heyer et al. (2009) for a sample of giant molecular clouds. We stress that the values of virial parameter obtained here are representative and one must keep in view the caveats involved in estimating the virial masses.

5.3.5 Molecular line emission as a chemical tracer of dense gas

In this section we examine the spatial distribution of the molecular emission and attempt to understand the processes or conditions that the molecules trace. The integrated intensity maps of the molecular species detected towards IRAS 17256–3631 are presented in Fig. 5.15. From the zeroth moment map, we can see that the peak emission of the molecular lines is located to the north or north-west of the H II region, above the cometary head. The properties and emission morphology of individual species are discussed below.

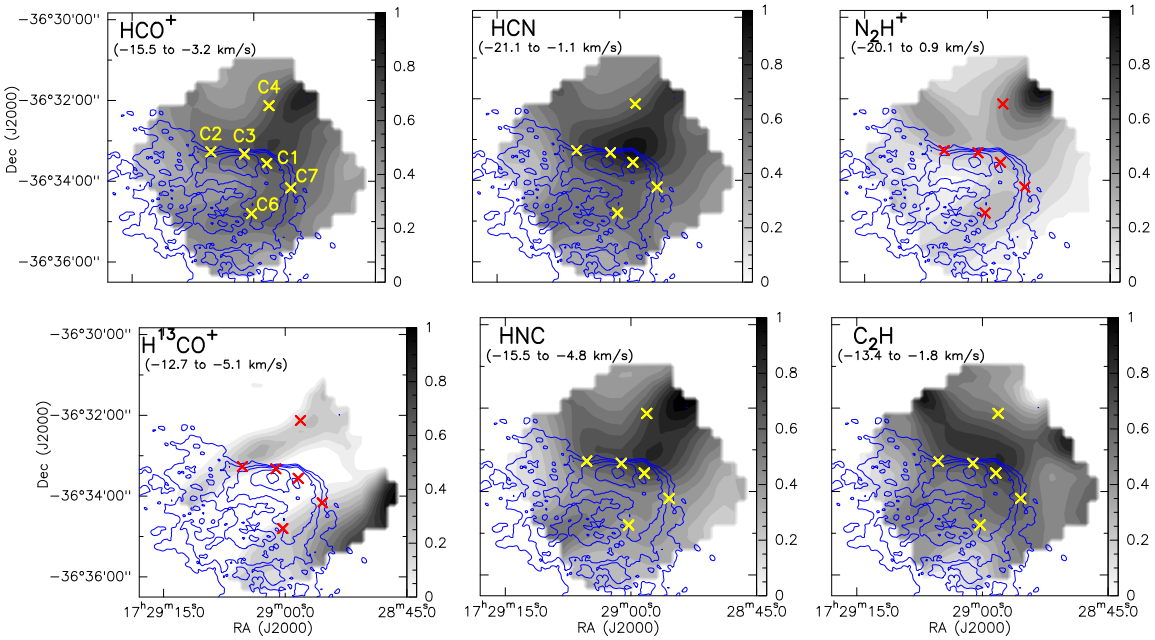

Figure 5.15: Integrated intensity maps of MALT90 molecular species detected towards IRAS 17256–3631 (HCO^+, HCN, N_2H^+, $H^{13}CO^+$, HNC and C_2H). The levels are represented in terms of percentage of peak where the peak values for HCO^+, HCN, N_2H^+, $H^{13}CO^+$, HNC and C_2H molecules are 9.6, 13.7, 13.9, 3.1, 12.2 and 4.1 K km/s respectively. The images are overlaid with 1280 MHz radio continuum contours. Also marked are the peak positions of all the clumps that are in the field of view of MALT90 data. The range of velocities used for constructing moment map of individual species are also given in the panels.

HCO^+ and $H^{13}CO^+$ (Formylium)

In IRAS 17256–3631, we observe extended emission in HCO^+ towards north-west of the radio emission. The emission shows two peaks and one of these lie close to the radio peak (angular separation $\sim 50''$). This peak lies near the brightest cold dust clump C1. The second peak lies in the vicinity of clump C4. We also detect diffuse emission that is extended towards south-west. In Sect. 5.3.3, we have estimated the HCO^+ abundance $\chi(HCO^+)$ as 7.2×10^{-8} towards clump C2, that is classified as an active/evolved clump Chapter 4. This is comparable to the median value of 5.7×10^{-8} determined by (Sanhueza et al., 2012) for a sample of evolved clumps in 37 infrared dark clouds. The

median values of $\chi(HCO^+)$ for intermediate and quiescent clouds are lower by a factor of 3 than our estimate, implying that C2 is at a later evolutionary stage as proposed in Chapter 4.

We detected a weak $H^{13}CO^+$ emission towards IRAS 17256–3631. The maximum is seen towards the west of the clumps C7 and C6 and could be a result of edge effects. We detect a peak near clump C2. A local peak is also observed towards clump C4. In the H $^{13}CO^+$ spectrum towards C4, we see a double peaked profile that could be due to two components or due to a self-absorbed profile. This could also arise from noise effects. There is no emission towards the radio continuum peak unlike the HCO^+ counterpart. The difference in morphology with respect to HCO^+ emission is likely to be due to poor SNR of the $H^{13}CO^+$ emission.

A comparative study on the fractional abundance of HCO^+ and $H^{13}CO^+$ towards shielded cores and UV irradiated cloud edges in the Horsehead nebula shows that the abundances towards PDR regions are a factor of 4 lower than that in the shielded cores (Goicoechea et al., 2009). This could explain the absence of $H^{13}CO^+$ towards the edges of the cometary H II region IRAS 17256–3631, whereas the lack of emission inside the H II region could be attributed to the destruction of this species by high density electrons ($n_e \sim 10^2$ cm^{-3}). The HCO^+ molecule on the other hand, is relatively strong (by a factor of $\sim$50), so that it is still detected within the H II region.

HCN (Hydrogen cyanide) and HNC (Hydrogen isocyanide)

HCN and HNC have hyperfine structures with three hyperfine components due to the nuclear quadrupole moment of ^{14}N. The HCN molecule and its metastable geometrical isomer HNC are mainly formed through the dissociative recombination reaction $HCNH^+ + e^- \rightarrow$ HCN + H or HNC + H (Herbst, 1978). The distribution of HCN emission is similar to HCO^+ but we discern a single peak that is near clump C1. Most of the emission is concentrated towards north of the H II region above the clumps C1, C2 and C3. We detect weak emission towards the radio peak with the emission displaying a southward extension. The overall morphology of HNC emission is similar to that of HCN. In the integrated intensity map, we also detect a second peak towards C4 similar to the case of HCO^+.

N_2H^+ (Diazenylium)

The morphology of N_2H^+ emission towards IRAS 17256–3631 is mostly distributed north of the cometary H II region although it differs in the pattern of peak emission with the other species discussed. We see a a strong peak near C4 similar to what we observe towards HCO^+ and HNC molecules. However, the peak towards C1 observed in the HCO^+, HCN and HNC lines is not perceived. In addition, we see another peak near clump C2 like the $H^{13}CO^+$. As N_2H^+ and $H^{13}CO^+$ molecules trace the optically thin, high density gas, the seconday peak near C2 implies the presence of high density material in the proximity of C2. We also identify a weak, local enhancement in N_2H^+ emission near the clump C6.

C_2H (Ethynyl)

The C_2H emission towards our region of interest displays a different morphology from the other species. However, a common attribute is the detection of peak emission close to C1. We also detect two additional peaks to the north-west and north-east of C1, that are not correlated with the dust clumps or emission from the other species. C_2H is believed to form through the photodissociation of acetylene molecule $C_2H_2 + h\nu \rightarrow C_2H + H$ (Fuente et al., 1993). C_2H is considered to be a good tracer of PDRs (Ginard et al., 2012). However, Beuther et al. (2008) suggested that C_2H could trace dense gas in the early stages of star formation but it is converted into other molecules in the hot-core phase. In the IRAS 17256–3631 region, as the peak near C1 is observed with high density gas tracers such as HCO^+, HCN and HNC, we assert that the C_2H emission close to C1 could possibly be originating from the molecular cloud and not from the PDR. Also, most of the emission is distributed to the north of the cometary head and reduces considerably as we move further north. We interpret that this emission close to the ionization front could have contributions from both, the dense molecular gas as well as the PDR.

In a nutshell, the six different molecular species identified in this region are distributed mostly towards the north and north-west of the radio peak consistent with the cold dust emission detected towards this region. Most of these molecules are high den-

sity tracers and the emission is clumpy in nature. This further confirms the presence of local density inhomogeneities within this region. The high density cloud material appears to constrict the flow of ionized gas beyond the cometary head. The ionized plasma is more extended in the regions of low molecular gas density i.e., towards the south-east. We compare the kinematics and distribution of molecular gas with that of ionized gas in the next section.

5.4 Kinematic models of the H II regions

5.4.1 Kinematics of IRAS 17256–3631: Bow shock or champagne flow?

In this section, we analyze the velocity structure of IRAS 17256–3631 using the RRL as well as molecular line data. We correlate the kinematics with the existing models to gain an insight into the origin of the cometary morphology. The velocity structures of ionized and molecular gas across the cometary axis are disparate in the prominent models. The champagne flow model (Tenorio-Tagle, 1979; Yorke et al., 1983) explains the cometary morphology as an outcome of the asymmetrical expansion of the H II region within a dense cloud, towards a region of lower gas density. In this model, as the ionizing star is stationary, the velocity of cometary head is expected to be the same as that of the molecular cloud whereas a gradual increase in velocity is expected towards the cometary tail. The ionized gas can attain large velocities of the order of $\sim$30 km/s as the ionized gas is accelerated by a strong pressure through the nozzle (Bodenheimer et al., 1979).

In the bow shock model (van Buren et al., 1990; Mac Low et al., 1991), the cometary morphology is explained as bow shocks of ionizing stars with strong stellar winds moving supersonically through the molecular cloud. In this model, as the star is moving at large velocities with respect to the molecular cloud, the velocity of the cometary head is expected to be high. As we move towards the tail region, the ionized gas velocity is expected to be similar to the velocity of the molecular cloud. Thus, the velocity structure in this case is the reverse of what is expected for the champagne flow model. We have presented the schematic of velocity fields in these models in Fig. 5.16 (Cyganowski

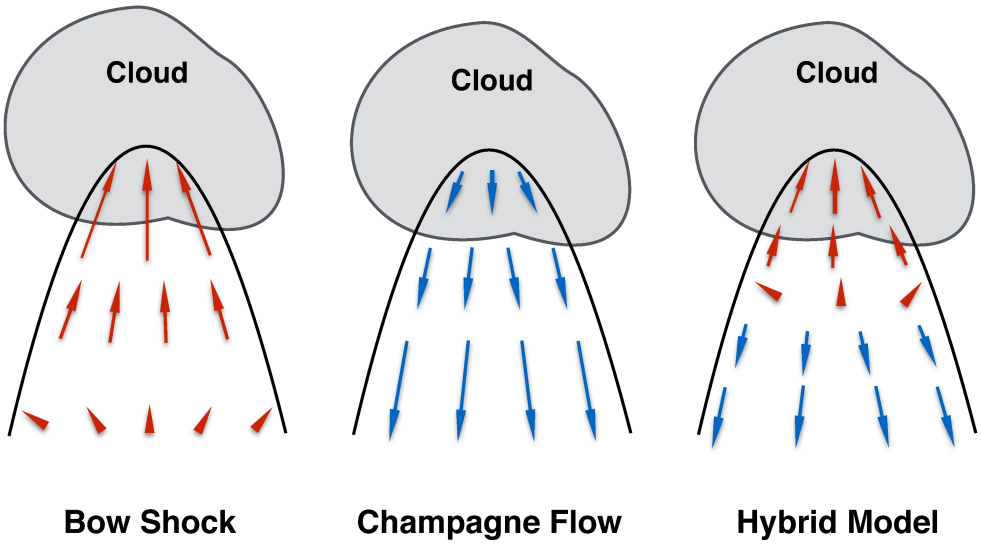

Figure 5.16: Schematic representations of velocity fields in cometary H II regions for three models : (left) bow shock, (middle) champagne flow, (right) hybrid model (adapted from Cyganowski et al., 2003). The velocities are with respect to that of ambient molecular cloud velocity.

et al., 2003).

Apart from the pure bow shock and champagne flow models, there are "hybrid" models that incorporate the effect of stellar winds into existing models (Gaume et al., 1994; Arthur & Hoare, 2006). Arthur & Hoare (2006) present the radiation-hydrodynamic simulations for various conditions such as pure bow shocks, pure champagne flows with steep and shallow density gradients, champagne flows with stellar winds, champagne flows with stellar winds and stellar motion etc. These models predict different velocity structures as compared to bow shock and champagne flow models. Cyganowski et al. (2003) investigated the gas kinematics towards the cometary H II regions in DR21 region and they found large velocities at the cometary heads suggestive of bow shocks. They also reported an increase in velocity towards the ionized tail of the southern H II region, that is consistent with the champagne flow model. They concluded that the gas kinematics is indicative of a "hybrid" model where gas flow is bow shock-like in the cometary head whereas it is champagne flow-like in the cometary tail. This hy-

brid model scenario was further confirmed with sensitive H66α observations by Immer et al. (2014). The representative hybrid velocity structure is also displayed in Fig. 5.16.

The MALT90 molecular line data shows that the velocity of the HCO^+ molecular line is -8.3 km/s. This is consistent with velocities of $C^{17}O$ (1–0) and $C^{17}O$ (2–1) lines (-8.1 and -8.5 km/s respectively; Fontani et al., 2005). Our analysis of RRL velocities using apertures (Sect. 5.2.3) shows that there exists a velocity gradient across the cometary axis of IRAS 17256–3631. The molecular line data on the other hand shows a nearly constant velocity across the entire cloud. The velocity of the molecular medium is consistent with the velocity of ionized gas near the cometary head (-8.6 km/s) from aperture S1. As we move towards the tail i.e. towards apertures S2, S3, etc, there is an increase in the velocity of ionized gas. Near aperture S5, the velocity difference between ionized and molecular gas is as large as $\sim$8 km/s. This favours the champagne flow model. This corroborates with our results from Chapter 4. While the models predict velocity gradients as large as 30 km/s between the cometary head and tail in champagne flows (Bodenheimer et al., 1979), other observational studies have reported velocity gradients of the order of $\sim$10 km/s (e.g. Garay et al., 1994) towards cometary H II regions.

We would like to note that although we have attributed the cometary morphology to a simple champagne flow model, we cannot neglect the possibility of a stellar wind emanating from the ionizing source. In our earlier work, we detected near-infrared H_2 emission near the cometary head, believed to be signatures of shocked gas (see Chapter 4). This could be due to the stellar wind interacting with the ambient medium. However, the possibility of shocked gas due to the expansion of the H II region cannot be ruled out. As the velocity information from RRL close to the cometary head suffers from poor SNR, it is difficult to distinguish between these two possibilities. In order to investigate this further, sensitive, high angular resolution information is required.

A schematic that represents our understanding for the formation of the cometary H II region towards IRAS 17256–3631 is shown in Fig. 5.17. This scenario is consistent with what was speculated in Chapter 4. Here, we briefly explain this using a figure. The ionizing star IRS1, shown in Fig. 5.3(a) and depicted as an asterisk is believed to be responsible for the H II region (Chpater 4). The expansion of the H II region is hindered by the presence of dense clumps such as C2, C3, C1 and C7 towards the northern

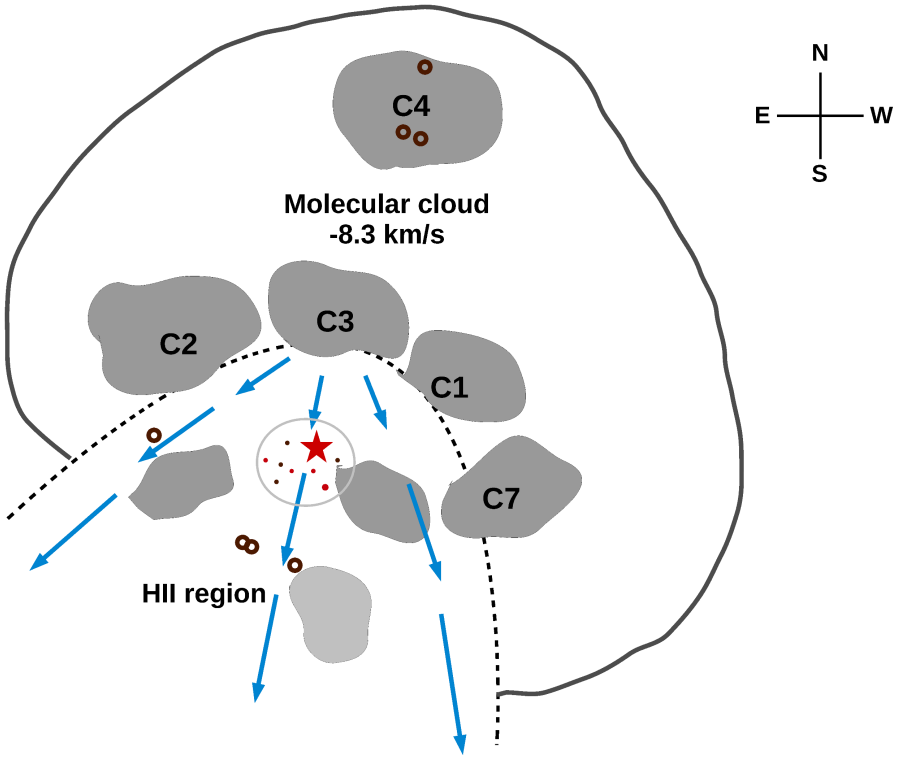

Figure 5.17: The champagne flow model for IRAS 17256–3631. The velocity field of RRL line with respect to molecular cloud is represented with blue arrows within the cometary H II region (dotted line). The molecular cloud with a central velocity of -8.3 km/s is shown (solid line) along with the locations of high density clumps (grey). Open circles mark the positions of detected H_2 knots (see Paper I). The dots represent the near-infrared cluster along with an asterisk denoting IRS-1, the brightest star in the cluster. The image is not to scale.

region. The velocity of the molecular and ionized gas are similar here. Towards the south, the density of molecular gas is low, that is evident from the dust continuum as well as the molecular line emission maps. The infrared cluster that lies in this region is also shown in the schematic. As the ionized gas expands out, it expands to regions of lower density, towards the south-east where there are fewer clumps than that of the head region. The freely flowing ionized gas accelerates here leading to relative velocities as high as 12 km/s (evident from the first moment map). We have also marked on the figure, the approximate location of few H_2 knots detected in this region. Thus, the density gradients drive the formation of the cometary head of the H II region towards

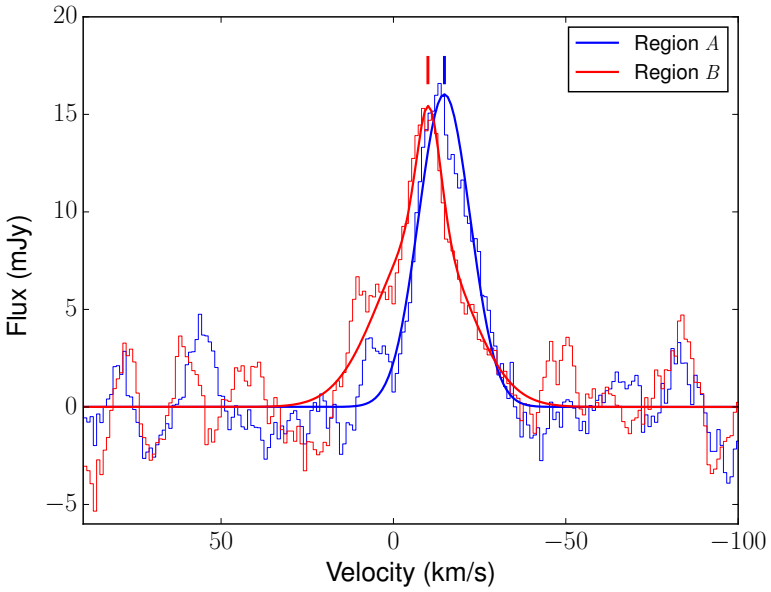

Figure 5.18: Overlay of the H172α RRL spectrum towards IRAS 17258–3637 *A* and *B* (see Fig. 5.7). To compare the spectra of the two regions, we have scaled the spectrum of region *B* by a factor of 3.2. The central velocities of both the regions are marked with vertical lines. The velocities of the two regions differ by 4.8 km/s.

IRAS 17256–3631.

5.4.2 Bipolar nature of IRAS 17258–3637

In order to understand the kinematics of IRAS 17258–3637, a comparison of the velocities of both, ionized and molecular gas, is vital. In the absence of MALT90, we use the molecular line information from earlier single pointing observations. The molecular line velocity is -12.0 km/s for CO and -11.7 km/s for CS observations, towards IRAS 17258–3637 (Batchelor et al., 1977; Whiteoak et al., 1982). However, being single dish and single pointing observations, its is difficult to segregate the emission from *A* and *B* regions. In our case, we clearly see a distinction in the RRL velocity components towards these two regions and the difference between the LSR velocities integrated over the regions is 4.8 km/s (Fig. 5.18). . Towards *A*, the velocity close to the peak emission is -11 km/s from the first moment map. Towards the extended envelope, the velocity appears to increase upto -16 km/s. Assuming that the molecular line velocity towards *A* is ~ -12 km/s, then the ionized gas velocity would appear blue shifted towards the

outer regions. This could be interpreted as a champagne flow due to density gradients in the region. Towards region *B*, the velocity structure is different compared to region *A*. The overall velocity structure is red shifted compared to that of *A*. In addition, we see a gradient in the north-south direction, i.e. as we proceed from the southern end of region B towards the northern side, the velocity gets red shifted by ~ 5 km/s. A pictorial representation of the velocity field is shown in Fig. 5.19 (Left).

In order to comprehend the velocity field better and compare it with the morphology of the molecular cloud, we have used the dust continuum map at 870 μm from ATLASGAL. Fig. 5.3(b) presents the overlay of 1280 MHz radio continuum contours over the cold dust emission at 870 μm. The extent of dust emission is larger and than the ionized gas emission although we see ionized gas emission pockets to the north-west and south-west where there is little cold dust emission. In addition, we observe that the morphology of dust emission towards the central region near the peak is flattened in a direction that is approximately perpendicular to the ionized gas distribution. Our group's earlier work on this region attributed this morphology to the champagne flow model, where the bipolar nature of ionized gas towards IRAS 17258–3637 is constrained to move towards the low density regions, perpendicular to the direction of flattening (Vig et al., 2014).

Based on the above, we arrive at the following schematic of the H II region IRAS 17258–3637, shown in Fig. 5.19 (Right). We assume that regions *A* and *B* belong to the same molecular cloud and the kinematics can be understood in terms of (i) density distribution, and (ii) projection effects. We are of the opinion that the exciting star lies within the region *A*, at the location of the ionized gas peak emission that is close to the dust continuum peaks. This is shown as an asterisk in Fig. 5.19 (Left). The H II region is believed to be inclined with respect to the observer's line-of-sight, with region *B* located farther away. As *B* is located at the farther end of the molecular cloud, then the ionized gas from *B* is likely to expand away from the observer. This would give rise to the red-shifted components in the velocity field. The region *A*, on the other hand, is relatively blue-shifted with respect to the cloud and hence it is possibly located near the edge of the cloud closer to the observer. This would explain the relative blue-shifted emission towards the observer. In this scenario, due to the inclination with respect to the observer's line-of-sight, the observer sees emission that would be increasingly blue-shifted towards one side with respect to the other side. This could explain the

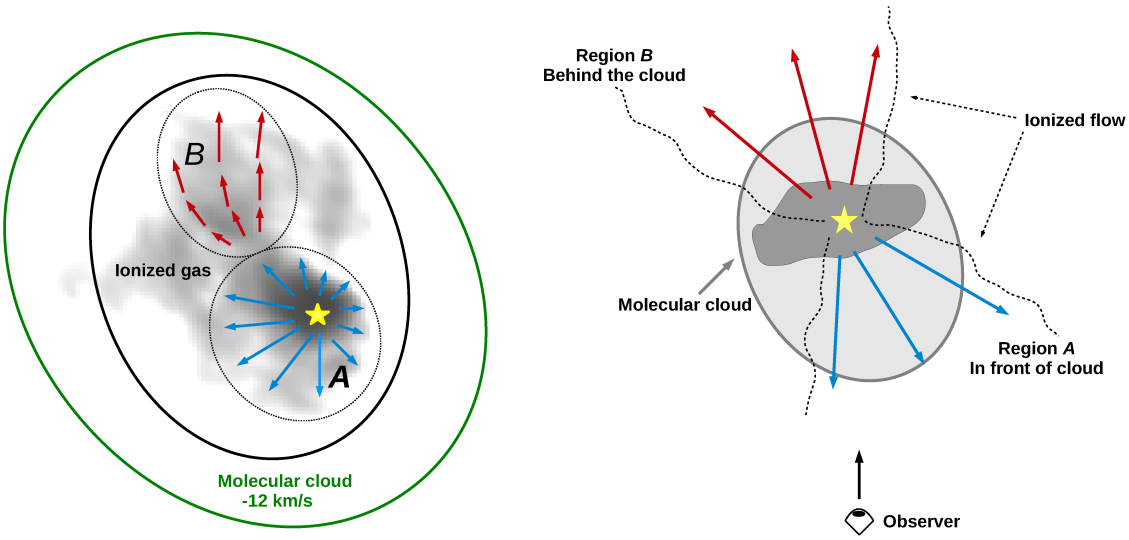

Figure 5.19: (Left) The pictorial representation of RRL velocity field observed towards IRAS 17258–3637. The molecular cloud is represented with a green ellipse and ionized gas encircled with a black ellipse. The dashed ellipses encircle regions A and B, which are overlaid on 1280 MHz greyscale image. The blue arrows represent velocities that are blue shifted with respect to the molecular cloud. Similarly, red arrows denote the red shifted velocities. The location of radio peak is marked as an asterisk. (Right) Schematic diagram showing the orientation of IRAS 17258–3637 with respect to the observer. The bipolar H II region is aligned at an angle to the observer's line-of-sight so that the expansion of H II region is not exactly directed to the observer. The images are not to scale.

larger blue-shift in emission from the east and south-east as compared to the western edge. This would also be consistent with the larger red-shift observed towards the north-western edge of region *B*. Thus, the kinematics of the bipolar H II region IRAS 17258–3637 has origins in the champagne flow of ionized gas out of a flat molecular cloud and the direction of the density gradient is responsible for the H II region silhouette. However, this proposed qualitative model although consistent with observations, is not exclusive and we cannot rule out the presence of local velocity gradients due to the clumpy medium. High resolution molecular line observations would aid immensely in confirming the scenario.

5.5 Summary

In this chapter, we examined the cometary and bipolar morphology of two H II regions: IRAS 17256–3631 and IRAS 17258–3637. For this, low frequency RRLs and molecular line data are used simultaneously. This is the first RRL mapping study of H II regions at low frequency bands. Our analysis suggests that the density gradients within molecular clouds play a dominant role in the observed morphologies of these H II regions.

Chapter 6

Non-thermal Emission from Massive Star Forming Regions: Unveiling a New SNR Candidate G351.7–1.2

The massive stars and OB clusters profoundly affect their environments through extreme UV radiation, stellar winds, and eventually by supernova explosions. Such events have destructive effects in the immediate surroundings, as they tend to disrupt the parental molecular cloud, thus terminating the ongoing/future star formation processes. However, massive stars could also drive an intense burst of star formation when an ionization front from a massive star sweeps up surrounding cloud material into a dense shell, which then fragments and trigger the formation of next generation of stars. Such triggered star formation could also be initiated by blast waves from supernova explosions where a part of the molecular cloud is dense enough to survive the explosion. Such systems provide a great opportunity to study the complex interaction mechanisms between the supernova blast wave and the ambient cloud. There are $\sim$ 70 Galactic SNRs that are found to be associated with star forming regions (Jiang et al., 2010), and examples include W44, G54.1+0.3 and IC443 (Wootten, 1978; Koo et al., 2008; Xu et al., 2011).

According to the SNR catalog of Green (2017), there are 295 known Galactic SNRs and almost 90% of these SNRs have been detected in radio surveys. However, statistical calculations suggest that more than 700 SNRs remains undetected and the reasons include inconsistent observational coverage of the Galactic plane, different sensitivities of surveys, confusion with H II regions etc. (Driessen et al., 2017). New SNRs are often identified at radio wavelength bands (Trushkin, 1999; Green, 2001; Crawford et al., 2001; de Gasperin et al., 2014). According to Green (2014), $\sim$93% of the catalogued Galactic SNRs are detected in radio, $\sim$40% are detected in X-ray and $\sim$30% are detected in optical. Recently, many new SNR candidates have been also discovered in γ-ray wavebands (e.g., Tian et al., 2008; Gottschall et al., 2017). The confusion with other Galactic thermal sources remains a major limiting factor in the detection of SNRs. Additional criteria have been applied to reinforce the detection of new SNRs. According to Anderson et al. (2017), these criteria include: i) Non-thermal emission inferred

from negative spectral indices ($\alpha \sim -0.5$ or lower), ii) detection of polarised emission from the radio source, iii) association with X-ray and/or cosmic ray emission, and iv) weak or no infrared emission unless they are associated with H II regions. An alternative probe is the presence of optical emission, particularly the Hα line, that is perceived in conjunction with the radio emission (e.g., Boumis et al., 2005; Stupar et al., 2008).

In this work, we report the presence of a new SNR candidate G351.7–1.2 that is associated with massive star forming complexes in its vicnity. The massive star forming complex include the two H II regions: IRAS 17258–3637 and IRAS 17256–3631 discussed earlier (Chapters 4 and 5). Both these regions are active sites of high mass star formation that harbour young embedded clusters. The low frequency radio continuum map of this region at 325 MHz revealed the presence of large scale diffuse emission connecting both IRAS 17256–3631 and IRAS 17258–3637, seen in Fig. 5.1. In order to examine the nature of this large scale emission, we have probed this region again with improved sensitivity and larger bandwidth at low radio frequencies.

In this chapter, we present the wideband radio observations of the star forming complexes in the vicinity of G351.7–1.2 carried out with the upgraded facilities of Giant Metrewave Radio Telescope (GMRT). We use the $300 - 500$ MHz band to map the large scale diffuse emission as well as to study the variation of spectral indices across the star forming regions. Combining this with the optical, infrared and submillimeter data, we present a multiwavelength investigation of the region that spans $15'$ in size.

6.1 Ionised radio shell

The ionized gas emission from the region associated with G351.7–1.2 is mapped using upgraded GMRT (uGMRT Gupta et al., 2017). The bandwidth of observation was 200 MHz, between $300 - 500$ MHz. The angular scale of the largest structure observable with uGMRT at 300 MHz is $\sim 35'$. The data reduction was carried out using AIPS (see Chapter 2). The calibrated target data were split into 6 files each of bandwidth of $\sim$32 MHz. The resulting central frequencies are 321, 351, 385, 418, 450 and 480 MHz. These were deconvolved separately and several iterations of self-calibration were applied to minimize the amplitude and phase errors. Thus, we have constructed 6 radio maps at the above mentioned frequencies by limiting the UV range between

0.1 and 21 kλ with a beam matching of $19.9'' \times 10.5''$, the largest beam among the 6 frequencies considered.

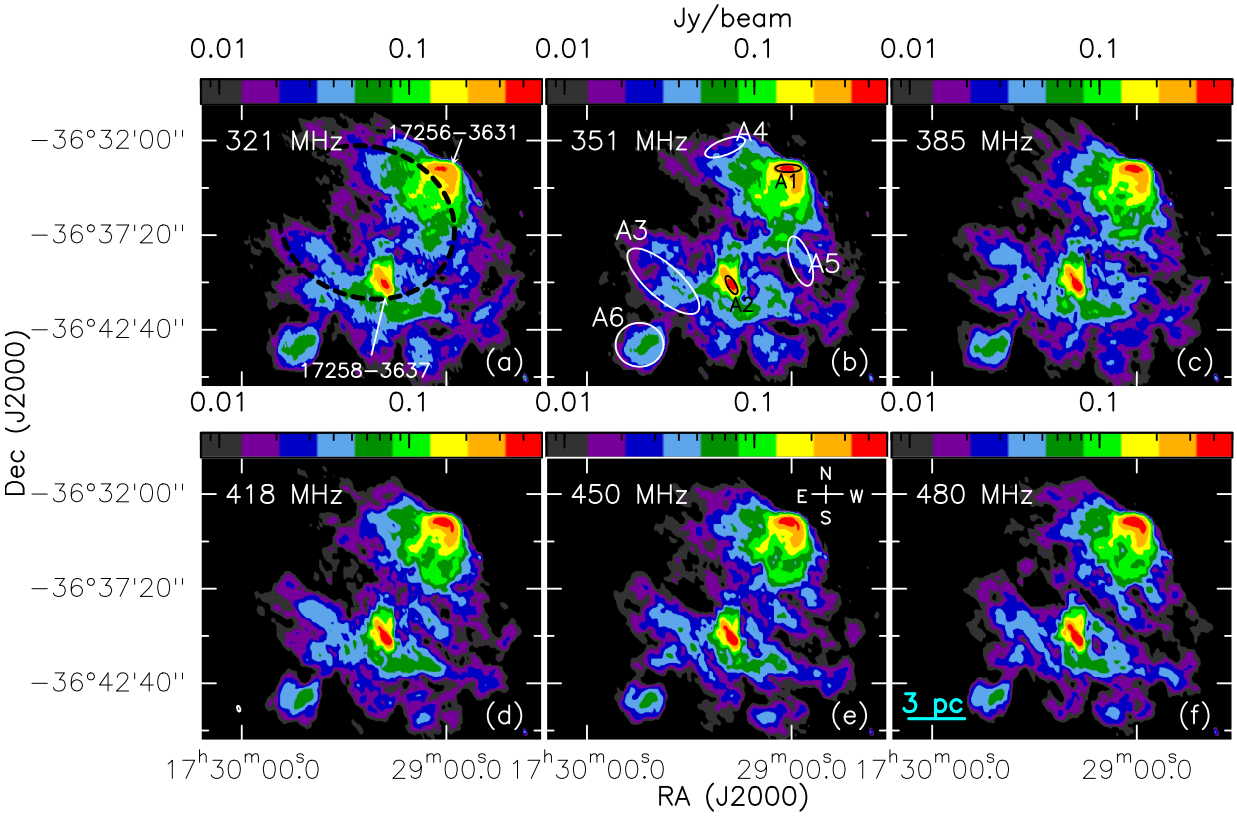

Figure 6.1: Radio continuum maps of the star forming complex G351.7–1.2 at 321, 351, 385, 418, 450 and 480 MHz. The two H II regions associated with this complex, IRAS 17256–3631 and IRAS 17258–3637 are marked and labelled in panel (a). Arc shows the approximate position of diffuse ionised shell. Panel (b) shows 6 apertures whose spectral indices are listed in Table 6.1 .The beam is shown as an ellipse in the bottom left corner of panel (d).

The radio continuum maps of G351.7–1.2 at all the six frequencies are shown in Fig. 6.1. The H II regions IRAS 17256–3631 and IRAS 17258–3637 are marked and labelled in the images. Apart from the H II regions, the low frequency radio maps also reveal a large broken shell-like structure, highlighted with a dashed curve in the figure. This radio shell has not been identified in any of the previous Galactic plane surveys. The shell is $\sim 14'$ in diameter, and has an opening towards the north-east. The physical size of the shell is 8.1 pc considering the distance to be $\sim$2 kpc. The latter is based on the assumption that the shell is located at the same distance as the H II regions (2 kpc, Vig et al., 2014; Veena et al., 2016). At this distance, the shell is $\sim$ 43 pc below the

Galactic plane. The emission from the radio shell is highly clumpy and fragmented in nature. A striking feature is that the emission from the shell is more prominent at lower frequencies ($\nu \leq 385$ MHz) unlike the emission from H II regions that become brighter as we move towards the high frequency bands. In order to closely examine the nature of emission from the newly discovered radio shell, we carried out a spectral index analysis.

6.2 Spectral index

The spectral index analysis is a useful tool to probe the processes responsible for radio emission. The spectral index α is defined as S_ν=ν^α, where S_ν is the flux density at frequency ν. The radiation process in H II regions is dominated by thermal bremsstrahlung and H II regions are often referred to as thermal sources. For a homoegenous, spherically symmetric HII region, the flux density due to thermal bremsstrahlung radiation is expected to increase with frequency ν ($\alpha = 2$) until a turnover frequency ν_c after which, the flux is nearly constant ($\alpha = -0.1$). ν_c represents the turnover frequency where the optical depth is unity. At frequencies below ν_c, the emission is optically thick while it is optically thin above ν_c, in the domain of flat spectral index. Rodriguez et al. (1993) have shown that for thermal free-free emission, spectral index will always be $\alpha \geq -0.1$ irrespective of the source characteristics such as temperature and electron density. Steep negative spectral indices ($\alpha < -0.4$), on the other hand, are often indicative of non-thermal processes (Israel & de Bruyn, 1988; Kobulnicky & Johnson, 1999).

In order to examine the nature of the radio emission, we estimated the spectral indices towards six apertures shown in Fig. 6.1. These elliptical apertures encompass the H II regions as well as other arbitrary regions in the diffuse emission (see Figure 6.2). We determined the flux densities in the apertures at all the frequencies under consideration and fitted their radio SEDs with the power-law, S_ν=ν^α, by the least-square fitting method. The spectral indices obtained towards the apertures are listed in Table 6.1. Towards apertures A1 and A2, that correspond to IRAS 17256–3631 and IRAS 17258–3637, the spectral indices are positive signifying thermal free-free emission. However, towards apertures A3, A4, A5 and A6, the spectral indices are steep and negative (< -0.5) confirming the presence of non-thermal emission. We have also evaluated

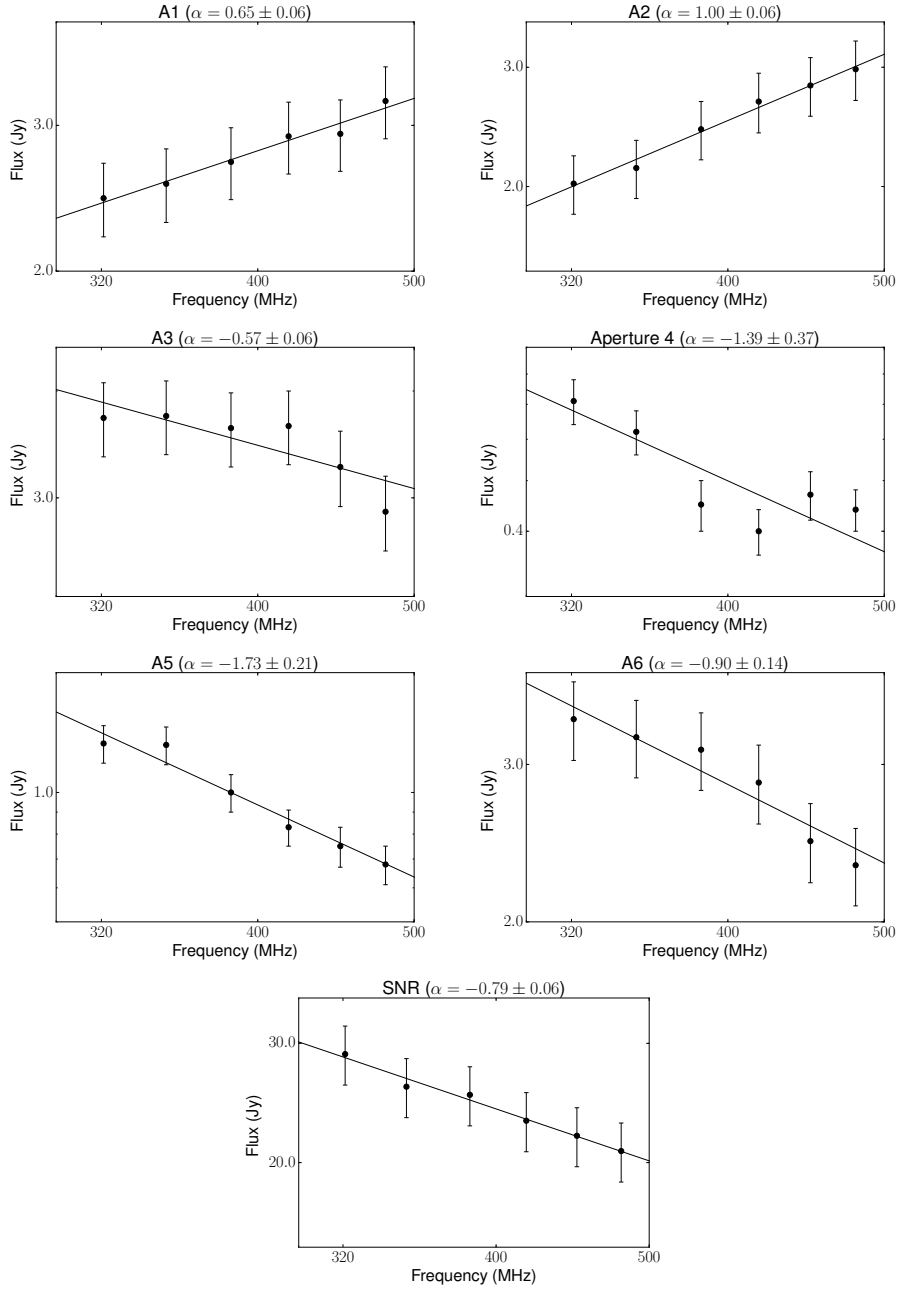

Figure 6.2: Radio spectra of the 6 apertures and the full radio shell using fluxes at 321, 351, 385, 418, 450 and 480 MHz. The corresponding apertures are shown in Fig. 6.1. Dotted lines in the figures are used to indicate the curvature in the radio spectra.

the spectral index of the full radio shell (centered on $\alpha_{\rm J2000}$: $17^h29^m18.5^s$, $\delta_{\rm J2000}$: -36°37′22.0″) excluding the two H II regions, and the value is -0.79 ± 0.06, consistent with non-thermal emission. A number of studies have reported similar spectral indices in shell-like SNRs ($\alpha \sim -0.6$ to -0.8; Gaensler et al., 1998; Combi et al., 2001; Green, 2014). The morphology as well as the spectral indices suggest that this large scale

Table 6.1: Flux densities and spectral indices of 6 apertures estimated from least square fit to the fluxes at 6 frequency bands.

Aperture	321 MHz F(Jy)	351 MHz F(Jy)	385 MHz F(Jy)	418 MHz F(Jy)	450 MHz F(Jy)	480 MHz F(Jy)	Spectral index (α)
A1 (IRAS 17256–3631)	2.45 ± 0.25	2.55 ± 0.26	2.71 ± 0.27	2.91 ± 0.29	2.93 ± 0.29	3.21 ± 0.32	0.65 ± 0.06
A2 (IRAS 17258–3637)	2.02 ± 0.20	2.13 ± 0.21	2.43 ± 0.24	2.67 ± 0.27	2.82 ± 0.28	2.98 ± 0.30	1.00 ± 0.06
A3	3.72 ± 0.37	3.74 ± 0.37	3.62 ± 0.36	3.64 ± 0.36	3.26 ± 0.33	2.89 ± 0.29	-0.57 ± 0.17
A4	0.71 ± 0.07	0.62 ± 0.06	0.45 ± 0.05	0.40 ± 0.04	0.47 ± 0.05	0.44 ± 0.04	-1.39 ± 0.37
A5	1.30 ± 0.13	1.29 ± 0.13	1.00 ± 0.10	0.83 ± 0.08	0.75 ± 0.08	0.68 ± 0.07	-1.73 ± 0.21
A6	3.37 ± 0.34	3.22 ± 0.32	3.12 ± 0.31	2.86 ± 0.29	2.46 ± 0.25	2.31 ± 0.23	-0.90 ± 0.14
Full SNR	28.92 ± 2.89	25.89 ± 2.59	25.18 ± 2.52	23.06 ± 2.31	21.91 ± 2.19	20.80 ± 2.08	-0.79 ± 0.06

non-thermal emission is plausibly related to a previously unknown SNR G351.7–1.2 (hereafter, SNR G351.7).

The spectral indices of emission in apertures A4 and A5 are -1.4 and -1.7, respectively. These are steeper than the value of the mean spectral index ($\alpha \sim -0.8$) of the radio shell. Steep spectral indices ($\alpha \leq -0.5$) are expected in regions where the effect of synchrotron losses are significant (Reynolds, 2009). Steep spectral indices are also observed in regions where shocks are decelerated due to collision with dense clouds as seen in the case of Puppis A (Dubner et al., 1991). It is worth noting that we have considered a few arbitrary apertures in the present study and the variation of spectral indices as well as radio spectra along different apertures point towards the complexity of this region.

6.2.1 Spectral tomography

We also use an additional technique called the spectral tomography to probe the emission from SNR G351.7. This technique is beneficial in regions where the emission consists of overlapping thermal and non-thermal structures. In our case, these correspond to the two H II regions 17256–3631 and 17258–3637 as well as emission from the SNR. Initially used to analyse the spectra of radio galaxies (Katz-Stone & Rudnick, 1997), this method has been recently applied to various SNRs (Katz-Stone et al., 2000; DeLaney et al., 2002). The tomography method involves the construction of a set of tomography images in which intensity images are created according to the following

expression:

$$I_t(\alpha_t) \equiv I_{321} - \left(\frac{321}{480}\right)^{\alpha_t} I_{480} \tag{6.1}$$

Here, $I_t(\alpha_t)$ is the tomographic image corresponding to the threshold spectral index α_t. I_{321} and I_{480} are the images at 321 and 480 MHz respectively. If a component has spectral index α_t, it gets subtracted from the image I_t. If a component has spectral index greater than the threshold spectral index, it will be oversubtracted from the image whereas regions having spectral indices lower than α_t will be undersubtracted and will thus have positive brightness. We have applied this method to our region of interest. In constructing the images, we have only considered those pixels whose intensity is greater than 3σ, where σ is the rms noise of the image.

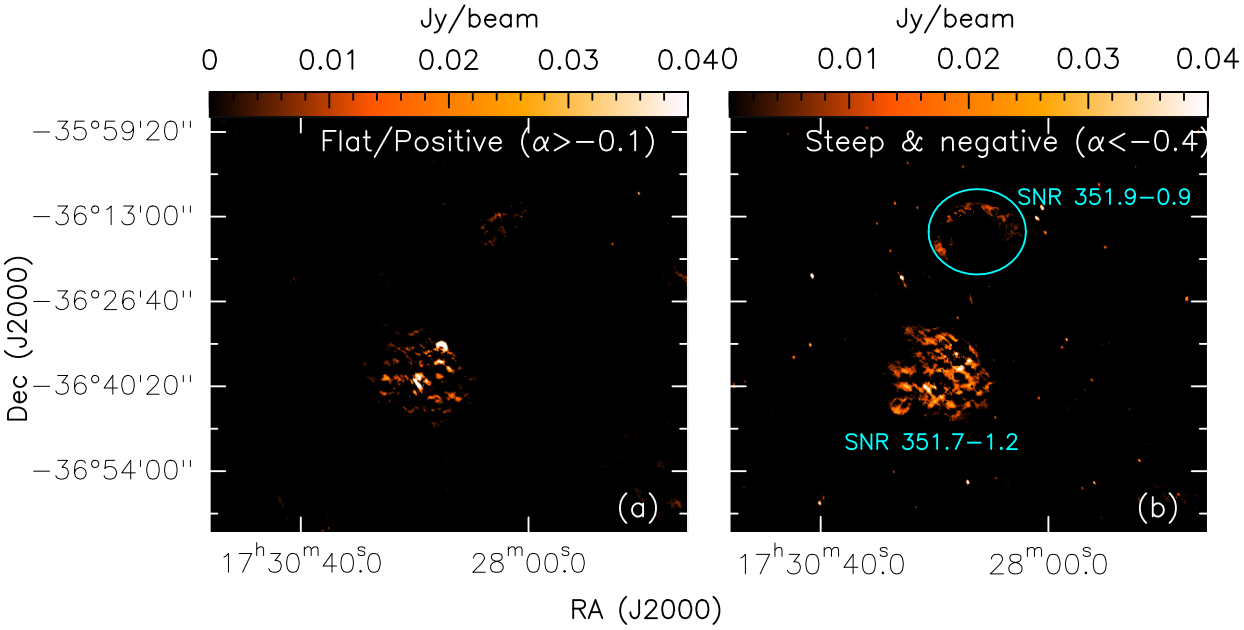

Figure 6.3: Spectral tomography images between 321 and 480 MHz. (a) Intensity scale is reversed to show bright areas that have spectral indices flatter than -0.1. The locations of two H II regions are indicated with arrows. (b) Tomography map showing regions whose spectral indices are steeper than -0.4, which is predominantly non-thermal.

We have considered regions with $\alpha_t > -0.1$ to be those associated with thermal emission. For inferring about non-thermal emission, we have constructed a tomographic image with $\alpha_t < -0.4$. Locations with spectral indices $-0.4 < \alpha < -0.1$ are assumed to have contributions from thermal as well as non-thermal emission. The tomographic

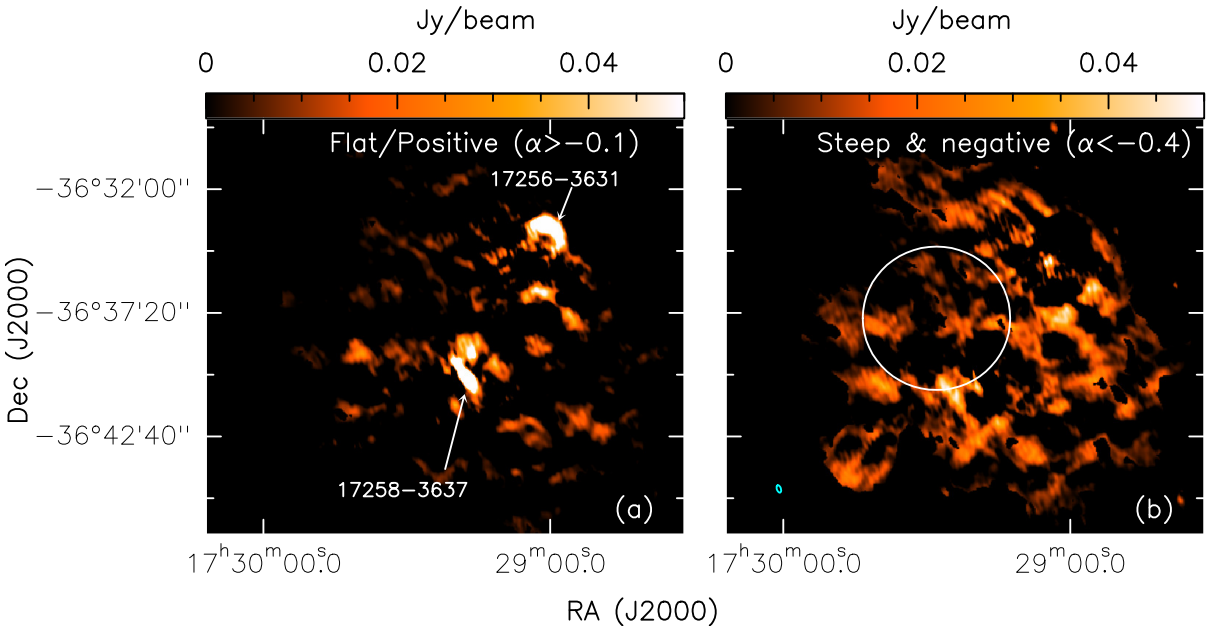

Figure 6.4: Enlarged spectral tomography images of SNR G351.7 shown in Fig. 6.3. (a) Intensity scale is reversed to show bright areas that have spectral indices flatter than -0.1. The locations of two H II regions are indicated with arrows. (b) Tomography map showing regions whose spectral indices are steeper than -0.4, which is predominantly non-thermal. Circle denotes the approximate location of Hα shell. The beam is shown as an ellipse in the bottom left corner of the image.

map showing thermal emission is displayed in panel (a) of Fig. 6.3.The color scale is inverted so that the regions whose spectral indices are more positive than -0.1 are seen as bright emission. Prominent features in the image include the two H II regions whose enlarged image is shown in panel (a) of Fig. 6.4. Panels (b) of Figs. 6.3 and 6.4 refer to non-thermal tomographic maps constructed using a threshold spectral index $\alpha_t = -0.4$, thus pointing towards regions where synchrotron emission dominates. We clearly discern a spherical distribution in the non-thermal emission map. However, the emission is filamentary in nature that is reminiscent of plerion SNRs, and limb-brightening , a characteristic of shell SNRs is not manifested in the map. In the following sections, we provide details of supporting evidence regarding the SNR. We also notice an arc-like feature to the north of the SNR G351.7, marked in Fig. 6.3(b). This prominent shell-like arc has been previously identified as SNR G351.9–0.9 catalogued by (Green, 2014) and we discuss more about this SNR later, in Sect. 3.7.

6.3 Optical emission towards G351.7

We gathered that the observed radio shell is a SNR candidate from the previous subsections. Observational studies show that ~ 30 percent of the Galactic SNRs are associated with optical emission (Green, 2014). As the SNR blast wave propagates into the cool and dense ambient ISM, shock excited radiation can develop at the interface. This is observed as Hα, other Balmer lines as well as forbidden transitions such as [SII], [NII], [OIII] etc. In addition to the shocked interface, strong optical emission is also observed in cooling and recombination zones posterior to the shock itself (e.g., Dubner et al., 2000; Dopita et al., 2010). These are the regions where inelastic collisional processes cool the gas to lower temperatures.

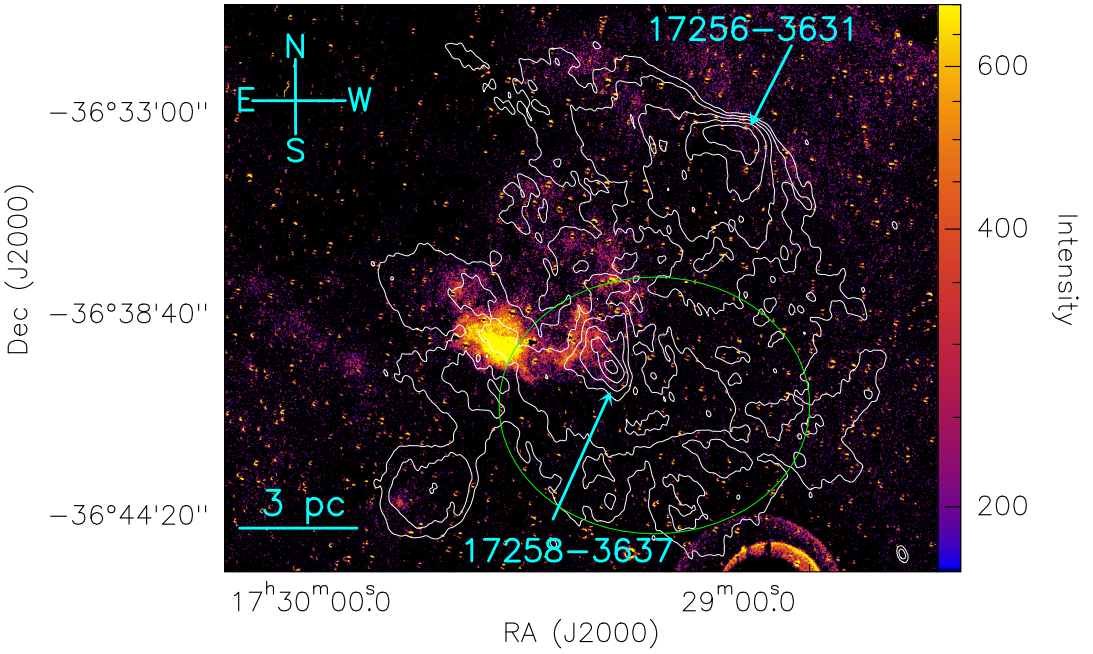

Figure 6.5: Hα image of SNRG351.7 overlaid with 321 MHz radio contours. Contour levels are 15, 36, 75, 150, 250 and 350 mJy/beam. The two H II regions associated with this complex, IRAS 17256–3631 and IRAS 17258–3637 are also marked and labelled. Ellipse denotes the location of *Fermi*-LAT γ-ray source (95%) confidence level.

In the quest for more evidence, we have searched for a possible counterpart to the radio emission in the optical wavebands towards the SNR candidate G351.7. We utilized the superCOSMOS H-alpha survey image for this purpose and subtracted the continuum emission using a scaled R-band image from the same survey. The Hα image displays considerable optical emission in the form of a shell-like feature. The optical Hα emis-

sion towards G351.7 is shown in Fig. 6.5, overlaid with contours of radio emission at 321 MHz. The Hα shell overlaps with the inner edge of the radio shell. A striking feature is the opening towards the north-east, in the same direction as the gap in the radio emission. The diameter of the Hα shell is $\sim 5.6'$, that corresponds to 3.3 pc for a distance of 2 kpc. The Hα brightness is not uniform across the rim of the shell. It is brighter towards the south-east and regions of low brightness across the shell appear filamentary. We also notice that Hα emission is not detected in the regions where the radio brightness of the two H II regions peak.

6.4 Infrared emission towards G351.7

Using mid-infrared and submillimeter data, we have investigated the dust environment of SNR G351.7. Fig. 6.6 shows the emission at six wavelength bands from 8.28 to 350 μm. The mid-infrared maps (from *Spitzer*-IRAC and MSX) reveal two bright sources that correspond to the H II regions IRAS 17256–3631 and IRAS 17258–3637. In addition, emission associated with with four IRAS sources is also discerned. These are marked in Fig. 6.6(d). We interpret the mid-infrared emission from these sources as tracing the ongoing star formating activity. The 12.13, 14.65 and 21.3 μm MSX maps (panels (c) and (d) of Fig. 6.6) show the presence of bright, arc-like features, highlighted by a dashed curve. These lie on the outer periphery of the Hα shell (represented as a circle in the figure) and we construe these as shock heated dust plausibly swept up by the supernova blast wave (Gomez et al., 2012). The fact that these features are seen prominently in mid-infrared ($12-21$ μm) could be related to the size of dust grains that survive the blast-wave and are shock-heated (e.g., Williams et al., 2006; Arendt et al., 2010). We again distinguish the lack of infrared emission towards the north-east.

Cold dust emission associated with molecular clouds is clearly perceived using the longer wavelength far-infrared bands. The regions of bright emission correspond to the two H II regions, with diffuse emission observed prominently to the west and south-western sides of the Hα emission. There is no noticeable emission towards the eastern and north-eastern sides of the SNR candidate. The shock-heated arc-like features perceived in the mid-infrared are located between the outer edge of the Hα emission and the inner regions of cold dust emission. This suggests strong interaction of the SNR

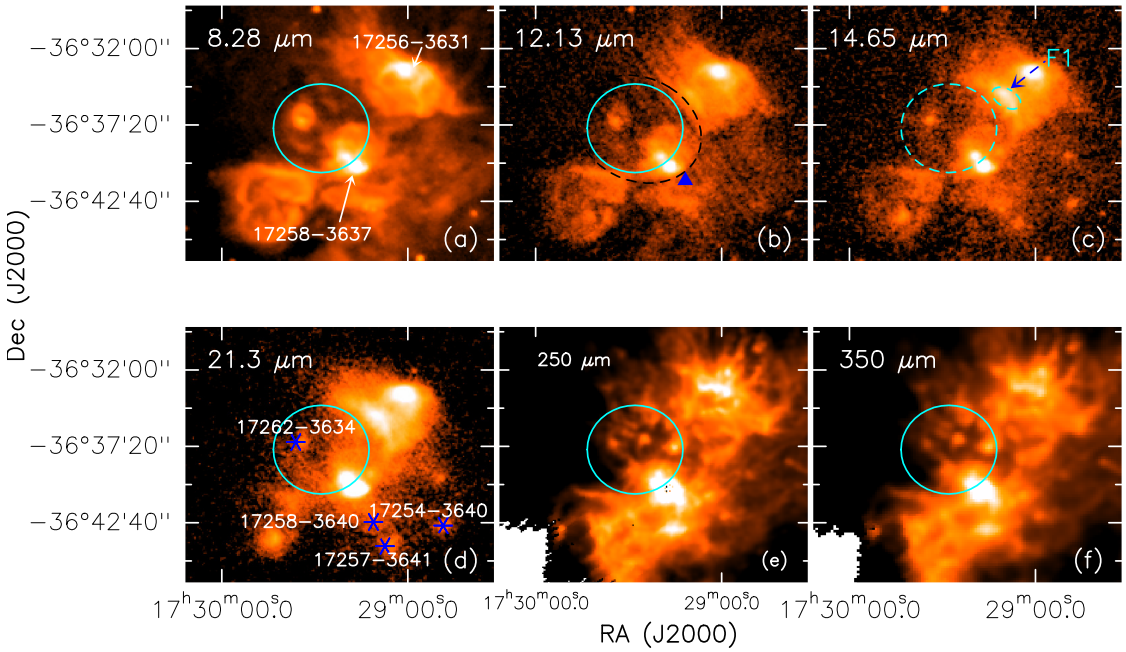

Figure 6.6: Multiwavelength view of SNR G351.7 and its surroundings. Panels (a), (b), (c) and (d) corresponds to mid-infrared emission from MSX at 4.3, 8.28, 12.13, 14.65, and 21.3 μm. Panels (e) and (f) shows cold dust emission mapped using *Herschel* at 250 and 350 μm. Circle denotes the approximate location of Hα shell. Triangle in panel (b) shows the location of the γ-ray source. Arrow in panel (c) point towards bright arc-like feature F1 seen in the periphery of Hα shell. Other IRAS sources in the field are marked as asterisks in panel (d).

with the surrounding high density cloud.

6.4.1 Spectral Energy Distribution towards F1

We estimate the temperature of the warm dust in the arc-like structure. The temperature is estimated from the infrared-submillimeter SED towards the arc-like feature F1 (shown in panel (c) of Fig. 6.6). The flux densities from MSX, IRAS, *Herschel* and ATLASGAL+Planck at 11 wavelength bands (8.28, 12.13, 14.65, 21.3, 25, 60, 100, 250, 350, 500 and 850 μm) are estimated by integrating the intensities within an elliptical aperture of size $124'' \times 74''$ oriented along the arc. The SED is displayed in Fig. 6.7 and exhibits characteristics of two dust components. Consequently, the flux densities in the SED are fitted with a function of the form shown in Eqn. (2). This equation is

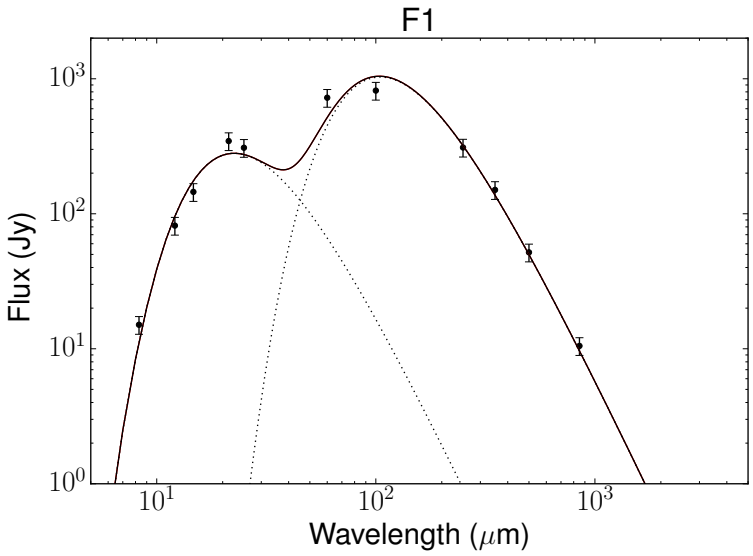

Figure 6.7: The infrared-submillimeter ($8.3 - 850$ μm) SED including MSX, IRAS, $Herschel$ and Apex+Planck towards F1. The two temperature blackbody fit to the thermal component is shown as solid black line.

the outcome of radiative transfer through a homogeneous absorbing medium comprised of two dust components, reflected in the two-component modified blackbody functions corresponding to temperatures T_1 and T_2.

$$F_\nu = \Omega \left[a\, B_\nu(T_1) + (1-a)\, B_\nu(T_2) \right] (1 - e^{-\tau_\nu}) \tag{6.2}$$

Here, Ω is the solid angle subtended by the clump, a is the ratio of warm dust emission to the total emission, $B_\nu(T_1)$ is the blackbody function at dust temperature T_1 and $B_\nu(T_2)$ is the blackbody function at dust temperature T_2 and τ_ν is the optical depth at frequency ν estimated using Eqn. 3.2.

The fitting is performed using the method described in Sect. 3.2 and we have set the dust temperature and column density as free parameters. We choose dust emissivity index β as 1.5 (Gomez et al., 2012). The best fits were obtained using non linear least squares Marquardt-Levenberg algorithm, considering T_1, T_2 and $N(\mathrm{H_2})$ as free parameters. We have assumed a flux density uncertainty of 15% in all bands (Veena et al., 2016, and references therein). The best fit temperatures in the filament are $T_1 = 31.6 \pm 1.9$ K and $T_2 = 153.1 \pm 7.9$ K. The presence of warm and cold dust components are also found

in other SNRs (e.g. Kepler and Tycho, Gomez et al., 2012). The presence of warm dust is likely to be due to (i) collisional heating by plasma, or (ii) radiative shocks. In the fomer case, the dust would reside in regions coincident with X-ray emission, while in the latter case, the dust emission would overlap UV/optical knots or filamentary structures (Bouchet et al., 2006). The lack of optical Hα emission in the filamentary region prompts us to consider collisional heating by the plasma as radio emission has also been detected in this region. Assuming collisional heating of dust in the shocked gas, the dust temperature of $\sim$ 150 K is consistent with a plasma of electron density $\geq$ 300 cm^{-3} (Bouchet et al., 2006). However, we note that a lack of optical emission could also be ascribed to extinction due to the cloud in this region. The heating mechanism can be reaffirmed by X-ray observations of this region.

6.5 γ-ray source 1FGLJ1729.1–3641c: Possible association with SNR

SNRs are widely believed to be a major source of Galactic cosmic rays (GCR). According to Drury et al. (1994), γ-rays are expected in SNRs that are interacting with molecular clouds and this has been confirmed observationally (e.g., Uchiyama & on behalf of the Fermi LAT collaboration, 2011; Dubner & Giacani, 2015). These γ-rays are produced as a result of hadronic interactions between cosmic rays and the dense molecular cloud. Towards G351.7, a γ-ray source 1FGLJ1729.1–3641c has been found that is located towards south-west of the radio shell (see Fig. 6.5). The origin of this γ-ray source, listed in the Fermi LAT catalog, has been speculated to be the interaction between the stellar wind from the massive star in the H II region IRAS 17258–3637, and the associated molecular cloud Massaro et al. (2015). A visual inspection towards the region enclosed within the 95% confidence level of this source location (represented as an ellipse in Fig. 6.5), shows diffuse radio emission as well as high extinction filamentary structures. Although the angular resolution ($\sim 0.1^{\circ}$) is insufficient to pinpoint its origin, we propose that the γ-ray source has a likely genesis at the site where SNR interacts with the cloud.

6.6 SNR interaction with the molecular cloud: Is the star-formation triggered by the supernova?

The multiwavelength portrayal of this region can be visualized from Fig. 6.8. In this color-composite image, radio emission is shown as red, *Spitzer* IRAC 4.5 μm as green and Hα emission as blue. The morphology of dust and consequently molecular gas in this region can be deciphered in terms of the initial density inhomogeneities present during the supernova explosion. The eastern and northern regions possibly had lower densities that could have been dispersed by the blast-wave in the initial expansion phase. On the other hand, the density of the medium towards the western and southern sides were higher. This could have led to compression and triggering of star-formation. Alternately, it is possible that star-formation activity in the molecular cloud(s) preceded the supernova explosion due to the rapid evolution of a massive star, and the clouds were dislodged by the associated pressure of the blast wave.

We attempt to estimate the age of the SNR based on simple analytic calculations. It is widely believed that after the initial supernova explosion, the ejecta expands out freely in the interstellar medium at supersonic speeds. This expansion continues until the SNR sweeps up its own mass. And once the swept up mass exceeds the ejecta mass, the object enters a second adiabatic phase that can be explained using the blast wave solutions proposed by Sedov (Sedov, 1959). For the expansion of a blast wave, the SNR age can be estimated using the expression given by Cox (e.g., 1972):

$$R\,(\mathrm{pc}) = 12.9\,(\epsilon_0/n_0)^{1/5}\,t_4^{2/5} \tag{6.3}$$

Here, R is the radius of the SNR, ϵ_0 is the explosion energy in units of 0.7×10^{51} erg, n_0 is the ambient density in units of cm^{-3} and t_4 is the age of the remnant in 10^4 yr. For a distance of 2 kpc, we consider the mean radius of SNR as 4 pc. For an average ambient density of 10 cm^{-3} and ϵ_0=1, we estimate the age of the SNR as 2.4×10^3 yr. Considering an electron density of $n_e = 300$ cm^{-3}, temperature of the warm dust component residing in plasma (Sect. 3.4.1) as the ambient density, the age estimate is larger by a fraction of $\sim$5, i.e. 9.4×10^3 yr. A further increase in an order of magnitude in density, i.e 10^4 cm^{-3} leads to an age estimate of 3.8×10^4 yr. Although there are

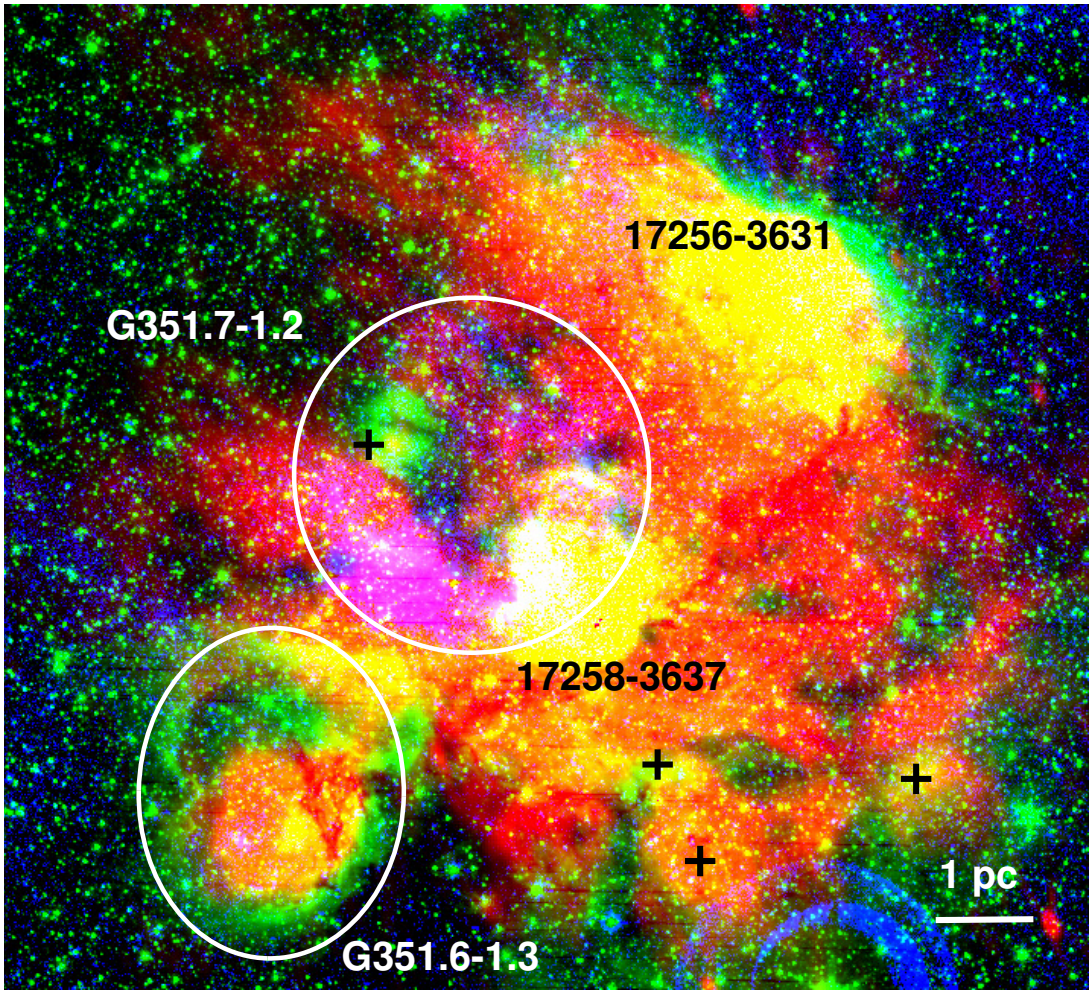

Figure 6.8: Three color composite image of the SNR G351.7–1.2. The 321 MHz radio map is shown in red, 4.5 μm infrared map in green and optical (Hα) image in blue. The two H II regions IRAS 17256–3631 and IRAS 17258–3637 are labelled. The SNR shell is evident in the image. The Hα shell and the bubble G351.6–1.3 (discussed in Sect. 3.7) are marked as circles. Also shown are the locations of the IRAS sources in the field of view (crosses).

uncertainties involved in the density estimates, we presume that the age of this SNR is a few thousands of years.

Considering the close proximity of the embedded clusters and H II regions, we next investigate whether the star formation in IRAS 17256–3631 and IRAS 17258–3637 could have been triggered by the supernova or not. These H II regions appear embedded in the radio emission from the SNR. If the H II regions are triggered by this SNR, the remnant ought to be much older than the H II region itself. A typical lower limit to the

age of the ultracompact H II regions based on chemical clocks is $\sim 10^5$ yr (Treviño-Morales et al., 2014) and for later stages such as compact H II regions, it is even larger. This is an order of magnitude larger than the age estimate of this SNR. The age of young stellar objects towards IRAS 17256-3631 is found to be the order of $10^5 - 10^6$ yrs (Veena et al., 2016). Thus, it appears that the star-formation in the H II regions are unlikely to have been triggered by the supernova explosion. The SNR progenitor is likely to have been an older generation star in the giant molecular cloud associated with the nearby star forming complexes. In order to find the progenitor of the SNR, we have searched for possible pulsars associated with the SNR in the ATNF pulsar catalog (Hobbs et al., 2004). However, we could not find any pulsar that has been detected in this region.

6.6.1 Alternate explanations for SNR G351.7–1.2

We have attributed the emission from this region to a previously unknown SNR G351.7–1.2. In this section, we explore alternate scenarios that could give rise to the observed radio, infrared and optical emission. Apart from SNRs, emission from H II regions, planetary nebulae and stellar wind bubbles can also produce emission in optical to radio wavebands. A major tool to distinguish the different classes of objects is based on analysing the emission spectra. For example, the radio spectra of planetary nebulae and H II regions are predominantly thermal (e.g., Terzian, 1968). The non-thermal radio spectral index of -0.8 rule out the H II region and planetary nebula hypotheses. In the case of a stellar wind bubble, the central star is most likely to be a Wolf-Rayet star (Inglis & Kitchin, 1990) and non-thermal radio emission has been reported around many Wolf-Rayet stars (e.g., Chapman et al., 1999). If the radio and optical emission is due to a Wolf-Rayet star, one would expect its central star to be observable (apparent magnitude < 10 at a distance of 2 kpc). The optical magnitudes of all stars that are located within $30''$ of the Hα shell are 14 magnitudes or fainter. Either the emission from central star is heavily obscured by the foreground ISM, or it is likely to be SNR. Based on our observational analysis and possible association with γ-ray source, we adhere to the SNR hypothesis. Follow up optical spectral line observations are envisaged to ascertain the SNR nature of this source.

6.7 Other SNR/SNR candidates in the field of view

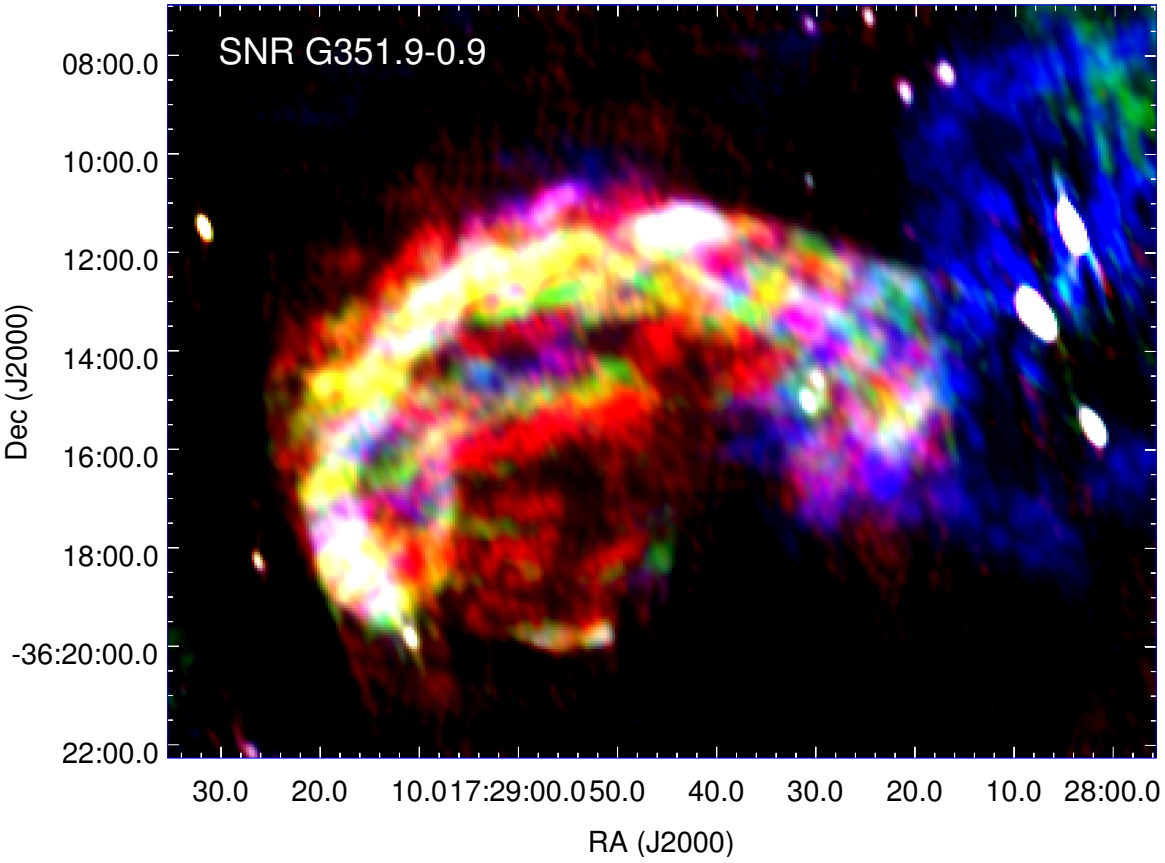

Figure 6.9: Three color composite image of the SNR G351.9–0.9. The 321 MHz radio map is shown in red, 385 MHz map in green and 450 MHz map in blue.

Apart from SNR G351.7, we have detected other SNR candidate(s) in the field of view. These are briefly discussed in this section.

SNR G351.9–0.9 has been previously catalogued as a Galactic SNR (Green, 2014). This SNR is located to the north of ($\sim 25'$ away) SNR G351.7. The 321 MHz image of this SNR is shown in Fig. 6.9. This SNR exhibits a shell morphology consistent with the morphological classification given in the catalogue. The radio emission spans a region $13.0' \times 8.4'$. A bright arc-like feature is visible in the north-east direction where the SNR exhibits a sharp boundary. The emission appears to be patchy towards the interior of the arc. The flux density of this source at 321 MHz is 10.7 Jy. From the spectral tomography map discussed in Sect. 3.2.1, we have identified steeper spectral index features ($\alpha < -0.4$) in this SNR. This is consistent with non-thermal emission expected from the SNR.

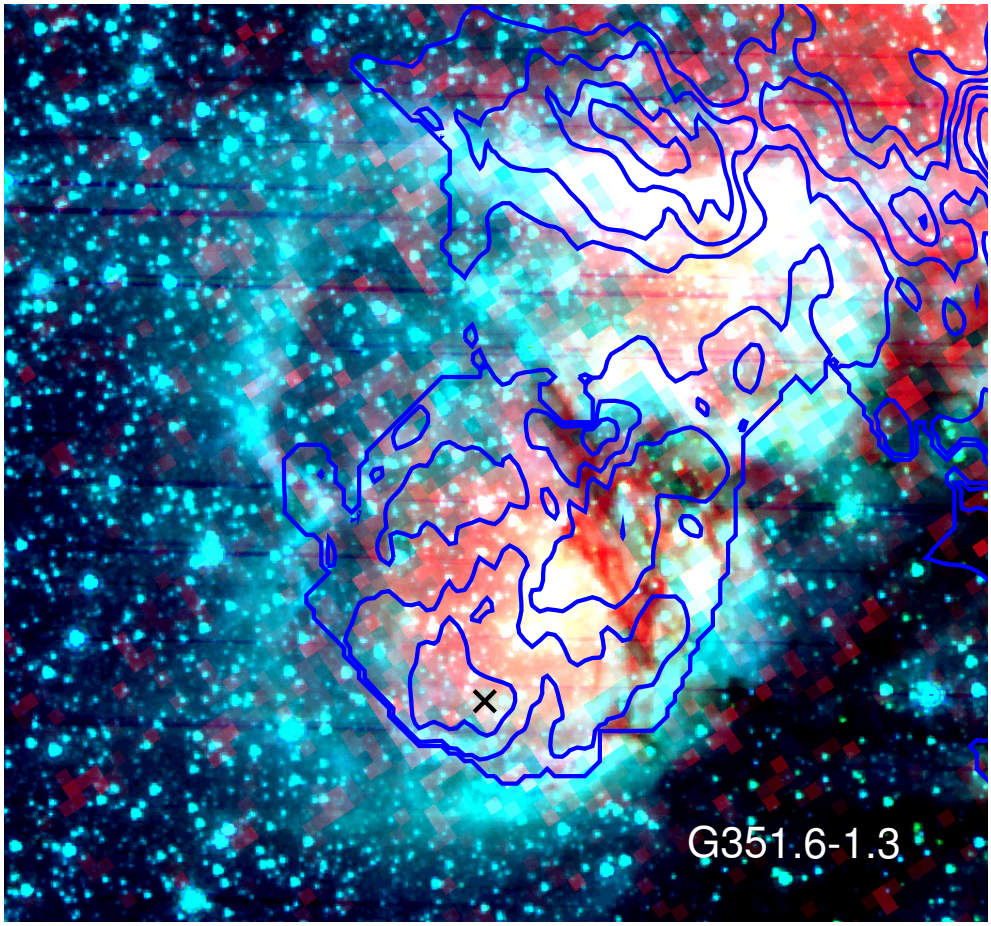

Figure 6.10: Three color composite image of the bubble G351.6–1.3. The MSX 21.3 μm map tracing warm dust is shown in red, *Spitzer IRAC* 4.5 μm and 3.6 μm maps in green and blue. Overlaid is the 321–480 steep spectral tomography image ($\alpha < -0.4$).

An alternate spherical structure visible in the radio bands is the source G351.6–1.3, that is located towards the south-east of the SNR G351.7 (enclosed within aperture A6). This source is nearly spherical with an angular diameter of $1.5'$. As no distance information is available for this region ,we could not calculate the physical size of the source. The spectral index analysis of this region shows steep negative spectral index of $\alpha = -0.90$ indicating the presence of non-thermal emission. From the color composite image shown in Fig. 6.8, we identify significant infrared emission associated with the radio source in the form of filamentary structures encompassing the radio source. We also detect infrared emission towards the centre of the object. The submillimeter images at 250 and 350 μm reveal a bubble like structure in the cold dust. No optical emission has been detected towards this region. An enlarged view of this source is presented in Fig. 6.10. In the image, the MSX 21.3 μm is shown in red, *Spitzer* IRAC 4.5 μm in

green and 3.6 μm in blue. Here, we again see prominent features in mid-infrared towards the centre of the source surrounded by bright filamentary structures. If this object has an supernova origin similar to SNR G351.7–1.2, the infrared emission is expected to be weak. But in this case, we detect strong mid-infrared emission in the outer rim of radio emission as well as towards the center. Similar structures are often associated with OB stars whose stellar winds and ionising pressure induce formation of shell/bubble like structures (Weaver et al., 1977; Shull, 1980). Thus, it is likely that the object is an expanding stellar bubble. We have also overlaid the spectral tomography contours on the color composite image to identify regions whose spectral index is negative steeper than -0.4 (non-thermal emission). The contours show a spherical structure with an extended tail towards the north, pointing to the SNR. The peak of the tomography image is shifted southward of the radio continuum peak. The source could possibly be a bubble showing signatures of non-thermal emission similar to other stellar bubbles where previous studies have reported signatures of non-thermal emission (e.g., Nandakumar et al., 2016; Das et al., 2017). The non-thermal emission from such sources has been attributed to shocks induced by outflows and/or winds (e.g., Garay et al., 1996). Alternatively, this source could be a non-thermal source in the foreground/background of the bubble or a supernova within a wind blown bubble as in the case of RCW86 (Williams et al., 2011).

6.8 Summary

Using the low frequency wide band observations, we mapped the large scale diffuse emission associated with a massive star forming complex. The diffuse radio emission possess broken shell morphology. Spectral index analysis affirm the non-thermal nature of this shell. From our analysis that includes radio as well as complementary archival data (γ-ray to submillimeter), we conclude that the radio shell is a previously unknown SNR G351.7–1.2.

Chapter 7

Conclusions and Future Work

7.1 Conclusions

The aim of this thesis has been to investigate the structure, evolution and kinematics of massive star forming regions. This has been undertaken by the study of few southern massive star forming regions through continuum and spectral line observations across a wide range of wavelength bands: from optical to radio wavelengths. The key findings from each of the chapters are summarised below.

The star formation activity of the southern filamentary IRDC G333.73+0.37 is analysed in Chapter 3. This region contains two distinct mid-infrared sources S1 and S2 connected by dark lanes of gas and dust. In order to study the properties of the molecular cloud, we created dust temperature and column density maps of this region. The 4700 $M_{\odot}$ filament is fragmented into 10 clumps. We have estimated the properties of these clumps such as temperature: $14.3 - 22.3$ K and mass: $87 - 1530$ $M_{\odot}$ by fitting a modified blackbody to the SED of each clump between 160 μm and 1.2 mm. The molecular line emission from the clump associated with infrared source S1 show infall signatures and we have modelled the infall profile of HCO^+ using the optically thin isotopologue $H^{13}CO^+$. From the low frequency radio continuum observations, we identify a shell-like H II region associated with S1. We also detect compact radio emission towards S2. The spectral types of these sources are consistent with late O or early B type stars. Photometric analysis of near and mid-infrared point sources unveil the YSO population associated with this cloud. Using the fragmentation analysis, we affirm the supercritical nature of this cloud. A large scale velocity gradient is observed along the filament that has likely origins due to an accretion flow. Our analysis reveal multiple objects in different evolutionary stages associated with this IRDC, such as millimeter cores, H II regions and YSOs. The expanding H II region S1 is in the process of dispersing the cloud in its immediate vicinity. According to the classification scheme of (Jackson et al., 2010), IRDC G333.73+0.37 is in intermediate phase compared to prestellar

filamentary clouds and highly evolved regions that harbour massive star clusters in the Milky Way. Based on various estimates obtained for objects in different evolutionary stages, we find a lower limit to the age of this IRDC as $1 - 2$ Myr.

In Chapter 4, we investigated a relatively evolved star forming region IRAS 17256–3631. The low frequency radio continuum emission from this region exhibits a cometary morphology. Spectral type of the ionising source estimated from 1372 MHz radio map is O7-O7.5. The radio spectral index maps indicate the presence of thermal as well as non-thermal emission in this region. Narrow band Brγ emission from the ionised gas at near-infrared wavelengths is also detected in this region and is consistent with radio emission. The narrow band H_2 image shows emission in the form of filamentary structures. These indicate the presence of highly excited molecular gas. We have identified a partially embedded infrared cluster associated with this region and the near-infrared spectroscopic study of the brightest star in the cluster, IRS-1, indicates that it is a late O or an early B-type star. Apart from the near-infrared cluster, we have also identified 18 mid-infrared YSO candidates in the region along with an extended green object: EGO-1, likely to be a massive protostellar candidate. The parent cloud is massive (6700 $M_\odot$) and is clumpy in nature. We have identified 18 cold dust clumps whose properties has been probed in detail. The temperature in these clumps range from 14.2 to 33.2 K whereas the mass ranges from 100 to 1200 $M_\odot$. Using various star formation tracers, we examined the evolutionary stages of these clumps. We have also analytically examined the origin of cometary morphology of the H II region. The radio emission is density bounded towards the north-west and is ionisation bounded towards south-west. Several high density clumps are located along the cometary head of the ionised emission. The morphology of IRAS 17256–3631 is explained with the champagne flow model.

The structure and kinematics of the H II region IRAS 17256–3631 and its neighbour IRAS 17258–3637 is probed using low frequency RRLs in Chapter 5. The latter is a bipolar H II region. The hydrogen H172α RRL from these regions are mapped using GMRT, India. We have also detected carbon (C172α) RRL towards these regions. The effects of various line broadening mechanisms on the line width of H172α RRL has been carried out. The H172α RRL from both H II regions display the effects of pressure and dynamical broadening in the line profiles, with the dynamical broadening playing a major role in IRAS 17256–3631. The kinematics of ionised gas in IRAS 17256–3631 is compared with that of molecular cloud. For this, we have used molecular line

data from MALT90 pilot survey. A velocity gradient across the cometary axis of the H II region has been detected and the ionised gas at the cometary tail is blue shifted atleast 8 km s^{-1} with respect to the molecular cloud, consistent with champagne flow model proposed in Chapter 4. The relative velocity of 5 km s^{-1} detected between the northern and southern lobes of the bipolar H II region IRAS 17258–3637 is consistent with the premise that the bipolar morphology is a result of the expanding ionised gas lobes within a flat molecular cloud.

The large scale radio emission associated with the star forming complex comprising of the two H II regions IRAS 17256–3631 and IRAS 17258–3637 is analysed in Chapter 6. We carried out low frequency wideband observations (bandwidth = 200 MHz) using upgraded GMRT to map the large scale diffuse emission from this region. Combining this with the optical, infrared and submillimeter data, we carried out a multiwavelength investigation of the diffuse emission to get a larger picture about the structure and evolution of this star forming complex. We detected a broken radio shell spanning a region $\sim 14'$, that encompasses the two H II regions. The radio spectral index of the shell is -0.8, indicating non-thermal emission. Hα emission that mimics the morphology of the radio shell on a smaller scale is also detected here. We classify this radio shell and its optical counterpart as a previously unknown supernova remnant SNR G351.7–1.2. A γ-ray source detected by $Fermi$ LAT (1FGLJ1729.1–3641c) is located towards the south-west of the radio shell and could have a possible origin in the interaction between high velocity particles from the SNR and the ambient molecular cloud.

From our detailed analysis on the evolution and structure of three star forming regions, we arrive at the following conclusions. The analysis of star formation activity towards IRDC G333.73+0.37 and IRAS 17256–3631 has shown that the regions are currently undergoing a star formation flurry. The clumps in these regions range from active/evolved with ultracompact and compact H II regions and associated infrared clusters to YSOs and EGOs prior to the formation of H II regions and to starless clumps that are devoid of any signatures of star formation. Of the 10 clumps in the IRDC G333.73, 40$\%$ are exhibiting signatures of star formation activity whereas 60$\%$ are quiescent clumps. In case of the cloud associated with the cometary H II region IRAS 17256–3631, there are 18 identified clumps of which 33.3$\%$ are star forming clumps and 66.7$\%$ are quiescent clumps. The temperature of the dust clumps in these regions lie in the range $14 - 33$ K and we find that the clump temperature changes with the

evolution. On the average, the temperatures of the active/evolved clumps are higher ($\Delta T \gtrsim 5$K) than that of the quiescent clumps. The average clump temperature in the IRDC G333.73 (17 K) is lower than that of the H II region IRAS 17256–3631 (23 K). This is expected as the IRDC as a whole, is in an early evolutionary stage compared to the star forming region IRAS 17256–3631. The latter already harbour an infrared cluster that contain one or more massive stars. The radiation from the partially embedded cluster is heating up the ambient gas and dust and is in the process of dispersing the natal cloud. The typical column densities of the clumps in these regions are of the order of 10^{22} cm^{-2} and the masses range from $\sim 100 - 1500$ M$_{\odot}$.

We have also probed the morphology and gas kinematics of the H II regions associated with these regions. The origin of specific morphologies in H II regions is still a matter of debate and several models are proposed to explain the diverse morphological classes. In this thesis, we study the morphology of three H II regions: the cometary H II region IRAS 17256–3631, bipolar H II region IRAS 17258–3637 and shell-like H II region S1 in the IRDC G333.73. Based on our analysis using continuum and spectral line data, we find that the effects of density gradients play a major role in IRAS 17256–3631 and IRAS 17258–3637 whereas in the case of S1, a combination of stellar wind and density gradient is responsible for the observed structure. Additionally, we also investigated the origin of mid-infrared arc-like emission around the compact radio source S2 and concluded that this is a result of stellar wind bow shock and density gradients. Irrespective of the morphological class, all of them show strong interaction with the ambient cloud. This is the first RRL mapping study of H II regions at low frequency bands ($\nu \lesssim 1$ GHz). We emphasise on the importance of RRL and molecular line mapping studies to constrain the kinematic models of H II regions that are in their early stages of evolution.

Using low frequency radio continuum observations and complementary archival data, we have identified a prospective SNR candidate SNR G351.7–1.2 interacting with the molecular cloud associated with the H II regions IRAS 17256–3631 and IRAS 17256–3637. This is an important finding considering the fact that there are only a limited number of Galactic systems where there are SNR/molecular cloud interactions. Such systems are crucial in understanding the physics of shock/cloud interactions. The study also accentuates the importance of low frequency radio observations in identifying and segregating SNRs that are associated with H II regions and molecular clouds.

The work provides a larger picture on the evolution of this star forming complex and how the shock waves from the dying massive star could affect the ambient medium and the formation of future massive stars.

7.2 Future work

We have used molecular line archival data to study the kinematics of a IRDC filament. Due to the limited resolution ($\sim$1$'$) of the surveys and lack of higher order transitions that better trace the kinematics of the cloud, we are not able to obtain an accurate picture of the velocity structure as well as the properties of this filament. It is therefore instructive to carry out follow up high resolution spectral line observations to sample the velocity structure of the entire filament while probing the infall and outflow activity of the central clump. As a continuation of the thesis work, we intend to carry out high resolution molecular line mapping towards a sample of IRDC filaments. At high angular resolutions, the sub-structures on these filaments at scales of cores ($\sim$10,000 AU) can be probed in detail. Such investigations can reveal whether the cores in the filaments are likely to produce a single high-mass star or a cluster of low-mass stars. Furthermore, the high resolution molecular line data can trace the star forming activity of sub-parsec cores such as infalls/outflows. Molecular line mapping of these filaments will also provide insights on the chemistry and kinematics of these filaments and how it changes with evolution. The kinematic study is particularly important in the case of filaments having accretion flows within them. The high resolution millimeter observations can be complemented with radio frequency observations and archival data from various surveys.

Even though the combination of RRLs and submillimeter molecular line data is an efficient tool to probe the morphology and kinematics of H II regions, velocity mapping studies using RRLs remain limited. Hence, observational work towards a sample of H II regions with diverse morphologies are essential in perceiving the complex interaction mechanisms existing in massive star forming regions. A comparative study of the centimetre and millimeter RRLs originating from the same star forming region is helpful in analysing various effects of line broadening mechanisms and to detect the velocity difference between high and low density gas, if present. This is possible because high

frequency RRLs sample regions of high density whereas low frequency RRLs have contributions from both high and low density gas.

REFERENCES

1. Aannestad, P. A. 1975, ApJ, 200, 30
2. Abreu-Vicente, J., Ragan, S., Kainulainen, J., et al. 2016, A&A, 590, A131
3. Adams, F. C., Lada, C. J., & Shu, F. H. 1987, ApJ, 312, 788
4. Allen, L. E., Calvet, N., D'Alessio, P., et al. 2004, ApJS, 154, 363
5. Anderson, L. D., Zavagno, A., Rodón, J. A., et al. 2010, A&A, 518, L99
6. Anderson, L. D., Zavagno, A., Deharveng, L., et al. 2012, A&A, 542, A10
7. Anderson, L. D., Wang, Y., Bihr, S., et al. 2017, A&A, 605, A58
8. André, P., Men'shchikov, A., Bontemps, S., et al. 2010, A&A, 518, L102
9. Aniano, G., Draine, B. T., Gordon, K. D., & Sandstrom, K. 2011, PASP, 123, 1218
10. Arendt, R. G., Dwek, E., Blair, W. P., et al. 2010, ApJ, 725, 585
11. Arquilla, R., & Goldsmith, P. F. 1986, ApJ, 303, 356
12. Arthur, S. J., & Hoare, M. G. 2006, ApJS, 165, 283
13. Aumann, H. H., Fowler, J. W., & Melnyk, M. 1990, AJ, 99, 1674
14. Azimlu, M., Fich, M., & McCoey, C. 2009, AJ, 137, 4897
15. Ballesteros-Paredes, J. 2006, MNRAS, 372, 443
16. Barbá, R. H., Walborn, N. R., & Rubio, M. 1999, in Revista Mexicana de Astronomia y Astrofisica, vol. 27, Vol. 8, Revista Mexicana de Astronomia y Astrofisica Conference Series, ed. N. I. Morrell, V. S. Niemela, & R. H. Barbá, 161–169
17. Barnes, P. J., Muller, E., Indermuehle, B., et al. 2015, ApJ, 812, 6
18. Bastian, N., & Goodwin, S. P. 2006, MNRAS, 369, L9

19. Batchelor, R. A., Gardner, F. F., Knowles, S. H., & Mebold, U. 1977, Proceedings of the Astronomical Society of Australia, 3, 152

20. Bate, M. R. 2009, MNRAS, 392, 1363

21. Battersby, C., Bally, J., Jackson, J. M., et al. 2010, ApJ, 721, 222

22. Battersby, C., Bally, J., & Svoboda, B. 2017, ApJ, 835, 263

23. Battersby, C., Ginsburg, A., Bally, J., et al. 2014, ApJ, 787, 113

24. Battersby, C., Bally, J., Ginsburg, A., et al. 2011, A&A, 535, A128

25. Baumgardt, H., & Klessen, R. S. 2011, MNRAS, 413, 1810

26. Beltrán, M. T., Brand, J., Cesaroni, R., et al. 2006, A&A, 447, 221

27. Benaglia, P., Koribalski, B., Peri, C. S., et al. 2013, A&A, 559, A31

28. Benjamin, R. A., Churchwell, E., Babler, B. L., et al. 2003, PASP, 115, 953

29. Bergin, E. A., & Langer, W. D. 1997, ApJ, 486, 316

30. Berry, D. S. 2015, Astronomy and Computing, 10, 22

31. Bertin, E., & Arnouts, S. 1996, A&AS, 117, 393

32. Bessell, M. S., & Brett, J. M. 1988, PASP, 100, 1134

33. Beuther, H., Churchwell, E. B., McKee, C. F., & Tan, J. C. 2007, Protostars and Planets V, 165

34. Beuther, H., Schilke, P., Sridharan, T. K., et al. 2002a, A&A, 383, 892

35. Beuther, H., Semenov, D., Henning, T., & Linz, H. 2008, ApJL, 675, L33

36. Beuther, H., & Sridharan, T. K. 2007, ApJ, 668, 348

37. Beuther, H., Walsh, A., Schilke, P., et al. 2002b, A&A, 390, 289

38. Beuther, H., Linz, H., Tackenberg, J., et al. 2013, A&A, 553, A115

39. Bica, E., Dutra, C. M., Soares, J., & Barbuy, B. 2003, A&A, 404, 223

40. Bik, A., Kaper, L., Hanson, M. M., & Smits, M. 2005, A&A, 440, 121

41. Black, J. H., & Dalgarno, A. 1976, ApJ, 203, 132

42. Blake, G. A., Sutton, E. C., Masson, C. R., & Phillips, T. G. 1987, ApJ, 315, 621

43. Bloomer, J. D., Watson, D. M., Pipher, J. L., et al. 1998, ApJ, 506, 727

44. Bodenheimer, P., Tenorio-Tagle, G., & Yorke, H. W. 1979, ApJ, 233, 85

45. Bohlin, R. C., Savage, B. D., & Drake, J. F. 1978, ApJ, 224, 132

46. Bonnell, I. A. 2002, in Astronomical Society of the Pacific Conference Series, Vol. 267, Hot Star Workshop III: The Earliest Phases of Massive Star Birth, ed. P. Crowther, 193

47. Bonnell, I. A., & Bate, M. R. 2006, MNRAS, 370, 488

48. Bonnell, I. A., Bate, M. R., Clarke, C. J., & Pringle, J. E. 2001, MNRAS, 323, 785

49. Bonnell, I. A., Bate, M. R., & Zinnecker, H. 1998, MNRAS, 298, 93

50. Bosch, G., Terlevich, E., & Terlevich, R. 2009, AJ, 137, 3437

51. Bouchet, P., Dwek, E., Danziger, J., et al. 2006, ApJ, 650, 212

52. Boumis, P., Mavromatakis, F., Xilouris, E. M., et al. 2005, A&A, 443, 175

53. Braz, M. A., Gregorio Hetem, J. C., Scalise, Jr., E., Monteiro Do Vale, J. L., & Gaylard, M. 1989, A&AS, 77, 465

54. Bronfman, L., Nyman, L.-A., & May, J. 1996, A&AS, 115, 81

55. Brooks, K. J., Garay, G., Nielbock, M., Smith, N., & Cox, P. 2005, ApJ, 634, 436

56. Brown, A. G. A. 2001, in Revista Mexicana de Astronomia y Astrofisica Conference Series, Vol. 11, Revista Mexicana de Astronomia y Astrofisica Conference Series, 89

57. Brown, R. L., Lockman, F. J., & Knapp, G. R. 1978, ARA&A, 16, 445

58. Busquet, G., Estalella, R., Palau, A., et al. 2016, ApJ, 819, 139

59. Camps-Fariña, A., Beckman, J. E., Font, J., et al. 2016, MNRAS, 461, L87

60. Cappa, C., Niemela, V. S., Martín, M. C., & McClure-Griffiths, N. M. 2005, A&A, 436, 155

61. Cappa, C. E., Barbá, R. H., Arnal, M., et al. 2007, in IAU Symposium, Vol. 237, Triggered Star Formation in a Turbulent ISM, ed. B. G. Elmegreen & J. Palous, 400–400

62. Carey, S. J., Feldman, P. A., Redman, R. O., et al. 2000, ApJL, 543, L157

63. Carey, S. J., Noriega-Crespo, A., Mizuno, D. R., et al. 2009, PASP, 121, 76

64. Carpenter, J. M. 2001, AJ, 121, 2851

65. Carroll, B. W., & Ostlie, D. A. 1996, An Introduction to Modern Astrophysics

66. Casali, M., Adamson, A., Alves de Oliveira, C., et al. 2007, A&A, 467, 777

67. Castor, J., McCray, R., & Weaver, R. 1975, ApJL, 200, L107

68. Caux, E., Bottinelli, S., Vastel, C., & Glorian, J. M. 2011, in IAU Symposium, Vol. 280, The Molecular Universe, ed. J. Cernicharo & R. Bachiller

69. Chaisson, E. J., Black, J. H., Dupree, A. K., & Cesarsky, D. A. 1972, ApJL, 173, L131

70. Chambers, E. T., Jackson, J. M., Rathborne, J. M., & Simon, R. 2009, ApJS, 181, 360

71. Chandrasekhar, S., & Fermi, E. 1953, ApJ, 118, 116

72. Chapman, J. M., Leitherer, C., & Koribalski, B. 1999, in IAU Symposium, Vol. 193, Wolf-Rayet Phenomena in Massive Stars and Starburst Galaxies, ed. K. A. van der Hucht, G. Koenigsberger, & P. R. J. Eenens, 59

73. Charnley, S. B. 1997, MNRAS, 291, 455

74. Chini, R., Kruegel, E., & Wargau, W. 1987, A&A, 181, 378

75. Chira, R.-A., Beuther, H., Linz, H., et al. 2013, A&A, 552, A40

76. Chira, R.-A., Smith, R. J., Klessen, R. S., Stutz, A. M., & Shetty, R. 2014, MNRAS, 444, 874

77. Chu, Y.-H., & Gruendl, R. A. 2011, Bulletin de la Societe Royale des Sciences de Liege, 80, 297

78. Churchwell, E. 2002, ARA&A, 40, 27

79. Churchwell, E., Smith, L. F., Mathis, J., Mezger, P. G., & Huchtmeier, W. 1978, A&A, 70, 719

80. Churchwell, E., Babler, B. L., Meade, M. R., et al. 2009, PASP, 121, 213

81. Codella, C., Bachiller, R., Nisini, B., Saraceno, P., & Testi, L. 2001, A&A, 376, 271

82. Combi, J. A., Romero, G. E., Benaglia, P., & Jonas, J. L. 2001, A&A, 366, 1047

83. Comerón, F., & Pasquali, A. 2007, Astronomy & Astrophysics, 467, L23

84. Compiègne, M., Flagey, N., Noriega-Crespo, A., et al. 2010, ApJL, 724, L44

85. Contreras, Y., Garay, G., Rathborne, J. M., & Sanhueza, P. 2016, MNRAS, 456, 2041

86. Contreras, Y., Rathborne, J. M., Guzman, A., et al. 2017, MNRAS, 466, 340

87. Cox, D. P. 1972, ApJ, 178, 159

88. Cox, N. L. J., Kerschbaum, F., van Marle, A.-J., et al. 2012, A&A, 537, A35

89. Crawford, F., Gaensler, B. M., Kaspi, V. M., et al. 2001, ApJ, 554, 152

90. Crowther, P. A., Schnurr, O., Hirschi, R., et al. 2010, MNRAS, 408, 731

91. Crusius-Watzel, A. R. 1990, ApJL, 361, L49

92. Csengeri, T., Weiss, A., Wyrowski, F., et al. 2016, A&A, 585, A104

93. Cunningham, N. 2015, PhD thesis, University of Leeds

94. Curiel, S., Rodriguez, L. F., Moran, J. M., & Canto, J. 1993, ApJ, 415, 191

95. Cutri, R. M., & et al. 2012, VizieR Online Data Catalog, 2311

96. Cyganowski, C., Whitney, B., Holden, E., et al. 2008, The Astronomical Journal, 136, 2391

97. Cyganowski, C. J., Brogan, C. L., Hunter, T. R., & Churchwell, E. 2009, ApJ, 702, 1615

98. Cyganowski, C. J., Brogan, C. L., Hunter, T. R., Churchwell, E., & Zhang, Q. 2011, ApJ, 729, 124

99. Cyganowski, C. J., Reid, M. J., Fish, V. L., & Ho, P. T. P. 2003, ApJ, 596, 344

100. Dame, T. M., Hartmann, D., & Thaddeus, P. 2001, ApJ, 547, 792

101. Das, S. R., Tej, A., Vig, S., et al. 2017, MNRAS, 472, 4750

102. Davis, C. J., Kumar, M. S. N., Sandell, G., et al. 2007, MNRAS, 374, 29

103. De Buizer, J. M., Radomski, J. T., Telesco, C. M., & Piña, R. K. 2003, ApJ, 598, 1127

104. de Gasperin, F., Evoli, C., Brüggen, M., et al. 2014, A&A, 568, A107

105. de Pree, C., Geballe, T., Goss, W. M., Mehringer, D., & Cecil, G. 1994, in Bulletin of the American Astronomical Society, Vol. 26, American Astronomical Society Meeting Abstracts, 1459

106. De Pree, C. G., Wilner, D. J., Deblasio, J., Mercer, A. J., & Davis, L. E. 2005, ApJL, 624, L101

107. de Wit, W. J., Testi, L., Palla, F., & Zinnecker, H. 2005, A&A, 437, 247

108. Decin, L., Cox, N. L. J., Royer, P., et al. 2012, A&A, 548, A113

109. Deharveng, L., Lefloch, B., Zavagno, A., et al. 2003, A&A, 408, L25

110. Deharveng, L., Schuller, F., Anderson, L. D., et al. 2010, A&A, 523, A6

111. Deharveng, L., Zavagno, A., Samal, M. R., et al. 2015, A&A, 582, A1

112. DeLaney, T., Koralesky, B., Rudnick, L., & Dickel, J. R. 2002, ApJ, 580, 914

113. Désert, F.-X., Macías-Pérez, J. F., Mayet, F., et al. 2008, A&A, 481, 411

114. Dickey, J. M., Hanson, M. M., & Helou, G. 1990, ApJ, 352, 522

115. Dobbs, C. L., Krumholz, M. R., Ballesteros-Paredes, J., et al. 2014, Protostars and Planets VI, 3

116. Dopita, M. A., Blair, W. P., Long, K. S., et al. 2010, ApJ, 710, 964

117. Driessen, L. N., Domček, V., Vink, J., et al. 2017, ArXiv e-prints, arXiv:1706.08826

118. Drury, L. O., Aharonian, F. A., & Voelk, H. J. 1994, A&A, 287, 959

119. Duarte-Cabral, A., & Dobbs, C. L. 2017, MNRAS, 470, 4261

120. Dubner, G., & Giacani, E. 2015, A&ARv, 23, 3

121. Dubner, G. M., Braun, R., Winkler, P. F., & Goss, W. M. 1991, AJ, 101, 1466

122. Dubner, G. M., Velázquez, P. F., Goss, W. M., & Holdaway, M. A. 2000, AJ, 120, 1933

123. Dunham, M. K., Rosolowsky, E., Evans, II, N. J., et al. 2010, ApJ, 717, 1157

124. Dunham, M. M., Arce, H. G., Mardones, D., et al. 2014, ApJ, 783, 29

125. Dunham, M. M., Crapsi, A., Evans, II, N. J., et al. 2008, ApJS, 179, 249

126. Dupac, X., Bernard, J.-P., Boudet, N., et al. 2003, A&A, 404, L11

127. Dyson, J. E., & Williams, D. A. 1980, Physics of the interstellar medium

128. Edelmann, H., Napiwotzki, R., Heber, U., Christlieb, N., & Reimers, D. 2005, ApJL, 634, L181

129. Egan, M. P., Shipman, R. F., Price, S. D., et al. 1998, ApJL, 494, L199

130. Elmegreen, B. G. 1994, ApJ, 433, 39

131. Elmegreen, B. G., & Lada, C. J. 1977, ApJ, 214, 725

132. Epchtein, N. 1998, in IAU Symposium, Vol. 179, New Horizons from Multi-Wavelength Sky Surveys, ed. B. J. McLean, D. A. Golombek, J. J. E. Hayes, & H. E. Payne, 106

133. Falgarone, E., & Phillips, T. G. 1990, ApJ, 359, 344

134. Fallscheer, C., Reid, M. A., Di Francesco, J., et al. 2013, ApJ, 773, 102

135. Faúndez, S., Bronfman, L., Garay, G., et al. 2004, A&A, 426, 97

136. Fazio, G. G., Hora, J. L., Allen, L. E., et al. 2004, ApJS, 154, 10

137. Felli, M., Churchwell, E., Wilson, T. L., & Taylor, G. 1993, Astronomy and Astrophysics Supplement Series, 98, 137

138. Fich, M., Blitz, L., & Stark, A. A. 1989, ApJ, 342, 272

139. Fontani, F., Beltrán, M. T., Brand, J., et al. 2005, A&A, 432, 921

140. Foster, J. B., Jackson, J. M., Barnes, P. J., et al. 2011, ApJS, 197, 25

141. Foster, T. J., Kothes, R., Kerton, C. R., & Arvidsson, K. 2007, ApJ, 667, 248

142. France, K., McCandliss, S. R., & Lupu, R. E. 2007, ApJ, 655, 920

143. Fuente, A., Martin-Pintado, J., Cernicharo, J., & Bachiller, R. 1993, A&A, 276, 473

144. Fuller, G. A., Williams, S. J., & Sridharan, T. K. 2005, A&A, 442, 949

145. Gaensler, B. M., Manchester, R. N., & Green, A. J. 1998, MNRAS, 296, 813

146. Galván-Madrid, R., Keto, E., Zhang, Q., et al. 2009, ApJ, 706, 1036

147. Garay, G., & Lizano, S. 1999, PASP, 111, 1049

148. Garay, G., Lizano, S., & Gomez, Y. 1994, ApJ, 429, 268

149. Garay, G., Lizano, S., Gómez, Y., & Brown, R. L. 1998, ApJ, 501, 710

150. Garay, G., Mardones, D., Brooks, K. J., Videla, L., & Contreras, Y. 2007, The Astrophysical Journal, 666, 309

151. Garay, G., Ramirez, S., Rodriguez, L. F., Curiel, S., & Torrelles, J. M. 1996, ApJ, 459, 193

152. Garay, G., Rodriguez, L. F., & van Gorkom, J. H. 1986, ApJ, 309, 553

153. Gardner, F. F., & Whiteoak, J. B. 1978, MNRAS, 183, 711

154. Garmany, C. D. 1991, in Astronomical Society of the Pacific Conference Series, Vol. 13, The Formation and Evolution of Star Clusters, ed. K. Janes, 23–34

155. Garmany, C. D. 1994, PASP, 106, 25

156. Gaume, R. A., Fey, A. L., & Claussen, M. J. 1994, ApJ, 432, 648

157. Giannetti, A., Brand, J., Sánchez-Monge, Á., et al. 2013, A&A, 556, A16

158. Gies, D. R. 1987, ApJS, 64, 545

159. Ginard, D., González-García, M., Fuente, A., et al. 2012, A&A, 543, A27

160. Goicoechea, J. R., Pety, J., Gerin, M., Hily-Blant, P., & Le Bourlot, J. 2009, A&A, 498, 771

161. Gomez, H. L., Clark, C. J. R., Nozawa, T., et al. 2012, MNRAS, 420, 3557

162. Gomez, Y., Garay, G., & Lizano, S. 1995, ApJ, 453, 727

163. Goodman, A. A., Benson, P. J., Fuller, G. A., & Myers, P. C. 1993, ApJ, 406, 528

164. Goodman, A. A., Alves, J., Beaumont, C. N., et al. 2014, ApJ, 797, 53

165. Gordon, M. A. 1987, ApJ, 316, 258

166. Gordon, M. A., & Burton, W. B. 1976, ApJ, 208, 346

167. Gorti, U., & Hollenbach, D. 2002, ApJ, 573, 215

168. Gottschall, D., Capasso, M., Deil, C., et al. 2017, in American Institute of Physics Conference Series, Vol. 1792, 6th International Symposium on High Energy Gamma-Ray Astronomy, 040030

169. Green, D. A. 2001, MNRAS, 326, 283

170. —. 2014, Bulletin of the Astronomical Society of India, 42, 47

171. —. 2017, VizieR Online Data Catalog, 7278

172. Gregersen, E. M., Evans, II, N. J., Zhou, S., & Choi, M. 1997, ApJ, 484, 256

173. Griem, H. R. 1967, ApJ, 148, 547

174. Griffin, M. J., Abergel, A., Abreu, A., et al. 2010, A&A, 518, L3

175. Gupta, Y., Ajithkumar, B., Kale, H., et al. 2017, Current Science, 113, 707

176. Gutermuth, R. A., & Heyer, M. 2015, AJ, 149, 64

177. Gutermuth, R. A., Myers, P. C., Megeath, S. T., et al. 2008, ApJ, 674, 336

178. Güver, T., & Özel, F. 2009, MNRAS, 400, 2050

179. Guzmán, A. E., May, J., Alvarez, H., & Maeda, K. 2011, A&A, 525, A138

180. Gvaramadze, V., Kniazev, A., Kroupa, P., & Oh, S. 2011, Astronomy & Astrophysics, 535, A29

181. Haikala, L. K., Harju, J., Mattila, K., & Toriseva, M. 2005, A&A, 431, 149

182. Haisch, Jr., K. E., Lada, E. A., & Lada, C. J. 2000, in Bulletin of the American Astronomical Society, Vol. 32, American Astronomical Society Meeting Abstracts, 1440

183. Haisch, Jr., K. E., Lada, E. A., & Lada, C. J. 2001, ApJL, 553, L153

184. Hambly, N. C., Collins, R. S., Cross, N. J. G., et al. 2008, MNRAS, 384, 637

185. Hanson, M. M., Conti, P. S., & Rieke, M. J. 1996, ApJS, 107, 281

186. Hanson, M. M., Howarth, I. D., & Conti, P. S. 1997, ApJ, 489, 698

187. Harper-Clark, E., & Murray, N. 2009, ApJ, 693, 1696

188. Hartmann, L., Megeath, S. T., Allen, L., et al. 2005, ApJ, 629, 881

189. Haslam, C. G. T., Salter, C. J., Stoffel, H., & Wilson, W. E. 1982, A&AS, 47, 1

190. He, Y.-X., Zhou, J.-J., Esimbek, J., et al. 2015, MNRAS, 450, 1926

191. Heap, S. R., Altner, B., Ebbets, D., et al. 1991, ApJL, 377, L29

192. Helmich, F. P., Jansen, D. J., de Graauw, T., Groesbeck, T. D., & van Dishoeck, E. F. 1994, A&A, 283, 626

193. Henriksen, R. N., Mirabel, I. F., & Ptuskin, V. S. 1991, A&A, 248, 221

194. Herbst, E. 1978, ApJ, 222, 508

195. Herbst, E., & Klemperer, W. 1973, ApJ, 185, 505

196. Herpin, F., Marseille, M., Wakelam, V., Bontemps, S., & Lis, D. C. 2009, A&A, 504, 853

197. Heyer, M., Krawczyk, C., Duval, J., & Jackson, J. M. 2009, ApJ, 699, 1092

198. Hildebrand, R. H. 1983, QJRAS, 24, 267

199. Hillenbrand, L. A. 1997, AJ, 113, 1733

200. Hjellming, R. M., & Davies, R. D. 1970, A&A, 5, 53

201. Hoare, M. G., Kurtz, S. E., Lizano, S., Keto, E., & Hofner, P. 2007, Protostars and Planets V, 181

202. Hoare, M. G., Roche, P. F., & Glencross, W. M. 1991, MNRAS, 251, 584

203. Hobbs, G., Manchester, R., Teoh, A., & Hobbs, M. 2004, in IAU Symposium, Vol. 218, Young Neutron Stars and Their Environments, ed. F. Camilo & B. M. Gaensler, 139

204. Hodgkin, S. T., Irwin, M. J., Hewett, P. C., & Warren, S. J. 2009, MNRAS, 394, 675

205. Högbom, J. A. 1974, A&AS, 15, 417

206. Hoq, S., Jackson, J. M., Foster, J. B., et al. 2013, ApJ, 777, 157

207. Hosokawa, T., & Omukai, K. 2009, ApJ, 691, 823

208. Hosokawa, T., Yorke, H. W., & Omukai, K. 2010, ApJ, 721, 478

209. Immer, K., Cyganowski, C., Reid, M. J., & Menten, K. M. 2014, A&A, 563, A39

210. Inglis, M. D., & Kitchin, C. R. 1990, MNRAS, 246, 358

211. Israel, F. P. 1978, A&A, 70, 769

212. Israel, F. P., & de Bruyn, A. G. 1988, A&A, 198, 109

213. Issa, M., MacLaren, I., & Wolfendale, A. W. 1990, ApJ, 352, 132

214. Jackson, J. M., Finn, S. C., Chambers, E. T., Rathborne, J. M., & Simon, R. 2010, ApJL, 719, L185

215. Jackson, J. M., Rathborne, J. M., Foster, J. B., et al. 2013, PASA, 30, e057

216. Jiang, B., Chen, Y., Wang, J., et al. 2010, in COSPAR Meeting, Vol. 38, 38th COSPAR Scientific Assembly, 8

217. Jiménez-Serra, I., Caselli, P., Fontani, F., et al. 2014, MNRAS, 439, 1996

218. Jin, M., Lee, J.-E., Kim, K.-T., & Evans, II, N. J. 2016, ApJS, 225, 21

219. Kahn, F. D. 1974, A&A, 37, 149

220. Kantharia, N. G., Anantharamaiah, K. R., & Goss, W. M. 1998a, ApJ, 504, 375

221. Kantharia, N. G., Anantharamaiah, K. R., & Payne, H. E. 1998b, ApJ, 506, 758

222. Kaper, L., van Loon, J. T., Augusteijn, T., et al. 1997, ApJL, 475, L37

223. Katz-Stone, D. M., Kassim, N. E., Lazio, T. J. W., & O'Donnell, R. 2000, ApJ, 529, 453

224. Katz-Stone, D. M., & Rudnick, L. 1997, ApJ, 488, 146

225. Kauffmann, J., Pillai, T., & Goldsmith, P. F. 2013, ApJ, 779, 185

226. Kerton, C. R., Arvidsson, K., & Alexander, M. J. 2013, AJ, 145, 78

227. Keto, E., & Klaassen, P. 2008, ApJL, 678, L109

228. Keto, E., Zhang, Q., & Kurtz, S. 2008, ApJ, 672, 423

229. Keto, E. R., Welch, W. J., Reid, M. J., & Ho, P. T. P. 1995, ApJ, 444, 765

230. Kim, K.-T., & Koo, B.-C. 2001, ApJ, 549, 979

231. Kirk, H., Myers, P. C., Bourke, T. L., et al. 2013, ApJ, 766, 115

232. Klaassen, P. D., & Wilson, C. D. 2007, ApJ, 663, 1092

233. Kobulnicky, H. A., & Johnson, K. E. 1999, ApJ, 527, 154

234. Kobulnicky, H. A., Chick, W. T., Schurhammer, D. P., et al. 2016, ApJS, 227, 18

235. Koenig, X. P., Allen, L. E., Gutermuth, R. A., et al. 2008, ApJ, 688, 1142

236. Koenig, X. P., Leisawitz, D. T., Benford, D. J., et al. 2012, ApJ, 744, 130

237. Konovalenko, A. A., & Stepkin, S. V. 2005, in EAS Publications Series, Vol. 15, EAS Publications Series, ed. L. I. Gurvits, S. Frey, & S. Rawlings, 271–295

238. Koo, B.-C., McKee, C. F., Lee, J.-J., et al. 2008, ApJL, 673, L147

239. Kroupa, P. 2001, MNRAS, 322, 231

240. Kroupa, P., Aarseth, S., & Hurley, J. 2001, MNRAS, 321, 699

241. Krumholz, M. R., Klein, R. I., & McKee, C. F. 2005a, in IAU Symposium, Vol. 227, Massive Star Birth: A Crossroads of Astrophysics, ed. R. Cesaroni, M. Felli, E. Churchwell, & M. Walmsley, 231–236

242. Krumholz, M. R., & McKee, C. F. 2008, Natur, 451, 1082

243. Krumholz, M. R., McKee, C. F., & Klein, R. I. 2005b, ApJL, 618, L33

244. —. 2005c, Natur, 438, 332

245. Krumholz, M. R., Bate, M. R., Arce, H. G., et al. 2014, Protostars and Planets VI, 243

246. Kuan, Y.-J., Mehringer, D. M., & Snyder, L. E. 1996, ApJ, 459, 619

247. Kurtz, S. 2002, in Astronomical Society of the Pacific Conference Series, Vol. 267, Hot Star Workshop III: The Earliest Phases of Massive Star Birth, ed. P. Crowther, 81

248. Kurtz, S., Cesaroni, R., Churchwell, E., Hofner, P., & Walmsley, C. M. 2000, Protostars and Planets IV, 299

249. Kurtz, S., Churchwell, E., & Wood, D. O. S. 1994, ApJS, 91, 659

250. Kurtz, S., & Franco, J. 2002, in Revista Mexicana de Astronomia y Astrofisica Conference Series, Vol. 12, Revista Mexicana de Astronomia y Astrofisica Conference Series, ed. W. J. Henney, J. Franco, & M. Martos, 16–21

251. Lada, C. J., & Adams, F. C. 1992, ApJ, 393, 278

252. Lada, C. J., & Lada, E. A. 2003, ARA&A, 41, 57

253. Lada, C. J., Muench, A. A., Haisch, Jr., K. E., et al. 2000, AJ, 120, 3162

254. Lada, C. J., Muench, A. A., Rathborne, J., Alves, J. F., & Lombardi, M. 2008, ApJ, 672, 410

255. Lada, C. J., Muench, A. A., Luhman, K. L., et al. 2006, AJ, 131, 1574

256. Ladd, N., Purcell, C., Wong, T., & Robertson, S. 2005, PASA, 22, 62

257. Lang, C. C., Goss, W. M., & Morris, M. 2001, AJ, 121, 2681

258. Langer, W. D., Graedel, T. E., Frerking, M. A., & Armentrout, P. B. 1984, ApJ, 277, 581

259. Launhardt, R., Stutz, A. M., Schmiedeke, A., et al. 2013, A&A, 551, A98

260. Leger, A., & Puget, J. L. 1984, A&A, 137, L5

261. Leisawitz, D., Bash, F. N., & Thaddeus, P. 1989, ApJS, 70, 731

262. Li, G.-X., Urquhart, J. S., Leurini, S., et al. 2016, A&A, 591, A5

263. Liu, T., Wu, Y., & Zhang, H. 2013a, ApJ, 776, 29

264. Liu, X.-L., Wang, J.-J., & Xu, J.-L. 2013b, MNRAS, 431, 27

265. Lopez, L. A., Krumholz, M. R., Bolatto, A. D., Prochaska, J. X., & Ramirez-Ruiz, E. 2011, ApJ, 731, 91

266. López-Sepulcre, A., Cesaroni, R., & Walmsley, C. M. 2010, A&A, 517, A66

267. Lumsden, S. L., & Hoare, M. G. 1999, MNRAS, 305, 701

268. Luna, A., Bronfman, L., Carrasco, L., & May, J. 2006, ApJ, 641, 938

269. Mac Low, M.-M., & Klessen, R. S. 2004, Reviews of Modern Physics, 76, 125

270. Mac Low, M.-M., van Buren, D., Wood, D. O. S., & Churchwell, E. 1991, ApJ, 369, 395

271. MacLaren, I., Richardson, K. M., & Wolfendale, A. W. 1988, ApJ, 333, 821

272. MacLeod, G. C., van der Walt, D. J., North, A., et al. 1998, AJ, 116, 2936

273. Maeder, A. 2009, Physics, Formation and Evolution of Rotating Stars, doi:10.1007/978-3-540-76949-1

274. Mardones, D., Myers, P. C., Tafalla, M., et al. 1997, ApJ, 489, 719

275. Martin, S. C. 1996, ApJ, 473, 1051

276. Massaro, F., D'Abrusco, R., Landoni, M., et al. 2015, ApJS, 217, 2

277. Mathis, J. S., & Whiffen, G. 1989, ApJ, 341, 808

278. Maud, L. T., Moore, T. J. T., Lumsden, S. L., et al. 2015, MNRAS, 453, 645

279. McKee, C. F., & Ostriker, E. C. 2007, ARA&A, 45, 565

280. McKee, C. F., & Tan, J. C. 2002, Natur, 416, 59

281. —. 2003, ApJ, 585, 850

282. Megeath, S. T., Allen, L. E., Gutermuth, R. A., et al. 2004, ApJS, 154, 367

283. Mehringer, D. M. 1994, ApJS, 91, 713

284. Meyer, M. R., Calvet, N., & Hillenbrand, L. A. 1997, AJ, 114, 288

285. Mezger, P. G., & Henderson, A. P. 1967, ApJ, 147, 471

286. Miettinen, O. 2012, A&A, 540, A104

287. —. 2014, A&A, 562, A3

288. Miettinen, O., & Harju, J. 2010, A&A, 520, A102

289. Minier, V., Conway, J. E., & Booth, R. S. 2001, A&A, 369, 278

290. Molinari, S., Brand, J., Cesaroni, R., & Palla, F. 1996, A&A, 308, 573

291. Molinari, S., Pezzuto, S., Cesaroni, R., et al. 2008, A&A, 481, 345

292. Molinari, S., Swinyard, B., Bally, J., et al. 2010a, A&A, 518, L100

293. —. 2010b, PASP, 122, 314

294. Monet, D. 1998, USNO-A2.0

295. Motte, F., Bontemps, S., & Louvet, F. 2017, ArXiv e-prints, arXiv:1706.00118

296. Motte, F., Bontemps, S., Schilke, P., et al. 2007, A&A, 476, 1243

297. Mücke, A., Koribalski, B. S., Moffat, A. F. J., Corcoran, M. F., & Stevens, I. R. 2002, ApJ, 571, 366

298. Mueller, K. E., Shirley, Y. L., Evans, II, N. J., & Jacobson, H. R. 2002, ApJS, 143, 469

299. Murray, N. 2011, ApJ, 729, 133

300. Myers, P. C. 2009, ApJ, 700, 1609

301. Nakashima, J.-i., Ladeyschikov, D. A., Sobolev, A. M., et al. 2016, ApJ, 825, 16

302. Nandakumar, G., Veena, V. S., Vig, S., et al. 2016, AJ, 152, 146

303. Noriega-Crespo, A., van Buren, D., & Dgani, R. 1997, The Astronomical Journal, 113, 780

304. Noriega-Crespo, A., Morris, P., Marleau, F. R., et al. 2004, ApJS, 154, 352

305. Ochsendorf, B. B., Cox, N. L. J., Krijt, S., et al. 2014a, A&A, 563, A65

306. Ochsendorf, B. B., Verdolini, S., Cox, N. L. J., et al. 2014b, A&A, 566, A75

307. Oey, M. S., & Clarke, C. J. 2007, ArXiv Astrophysics e-prints, astro-ph/0703036

308. Olnon, F. M. 1975, A&A, 39, 217

309. Osterbrock, D. E. 1989, Astrophysics of gaseous nebulae and active galactic nuclei (Mill Valley, CA (US); University Science Books)

310. Palla, F., Brand, J., Comoretto, G., Felli, M., & Cesaroni, R. 1991, A&A, 246, 249

311. Palla, F., & Stahler, S. W. 1993, ApJ, 418, 414

312. Panagia, N. 1973, AJ, 78, 929

313. Panagia, N., & Felli, M. 1975, A&A, 39, 1

314. Pankonin, V. 1980, in Astrophysics and Space Science Library, Vol. 80, Radio Recombination Lines, ed. P. A. Shaver, 111–125

315. Pankonin, V., Walmsley, C. M., & Harwit, M. 1979, A&A, 75, 34

316. Pankonin, V., Walmsley, C. M., Wilson, T. L., & Thomasson, P. 1977, A&A, 57, 341

317. Paradis, D., Veneziani, M., Noriega-Crespo, A., et al. 2010, A&A, 520, L8

318. Parker, Q. A., Phillipps, S., Pierce, M. J., et al. 2005, MNRAS, 362, 689

319. Pearson, T. J., & Readhead, A. C. S. 1984, ARA&A, 22, 97

320. Perault, M., Omont, A., Simon, G., et al. 1996, A&A, 315, L165

321. Peri, C. S., Benaglia, P., Brookes, D. P., Stevens, I. R., & Isequilla, N. L. 2012, A&A, 538, A108

322. Peri, C. S., Benaglia, P., & Isequilla, N. L. 2015, A&A, 578, A45

323. Pilbratt, G. L., Riedinger, J. R., Passvogel, T., et al. 2010, A&A, 518, L1

324. Poglitsch, A., Waelkens, C., Geis, N., et al. 2010, A&A, 518, L2

325. Portegies Zwart, S. F., McMillan, S. L. W., & Gieles, M. 2010, ARA&A, 48, 431

326. Povich, M. S., Benjamin, R. A., Whitney, B. A., et al. 2008, ApJ, 689, 242

327. Price, S. D., Egan, M. P., Carey, S. J., Mizuno, D. R., & Kuchar, T. A. 2001, The Astronomical Journal, 121, 2819

328. Purcell, C. R., Balasubramanyam, R., Burton, M. G., et al. 2006, MNRAS, 367, 553

329. Quireza, C., Rood, R. T., Balser, D. S., & Bania, T. M. 2006a, ApJS, 165, 338

330. Quireza, C., Rood, R. T., Bania, T. M., Balser, D. S., & Maciel, W. J. 2006b, ApJ, 653, 1226

331. Ragan, S., Henning, T., Krause, O., et al. 2012a, A&A, 547, A49

332. Ragan, S. E., Heitsch, F., Bergin, E. A., & Wilner, D. 2012b, ApJ, 746, 174

333. Ragan, S. E., Henning, T., Tackenberg, J., et al. 2014, A&A, 568, A73

334. Ramspeck, M., Heber, U., & Moehler, S. 2001, A&A, 378, 907

335. Rathborne, J., Jackson, J., Chambers, E., et al. 2010, The Astrophysical Journal, 715, 310

336. Rathborne, J. M., Jackson, J. M., & Simon, R. 2006, ApJ, 641, 389

337. Redman, M. P., Keto, E., Rawlings, J. M. C., & Williams, D. A. 2004, MNRAS, 352, 1365

338. Reid, M. J., & Ho, P. T. P. 1985, ApJL, 288, L17

339. Reiter, M., Shirley, Y. L., Wu, J., et al. 2011, ApJS, 195, 1

340. Reynolds, S. P. 1986, ApJ, 304, 713

341. —. 2009, ApJ, 703, 662

342. Rho, J., Reach, W. T., Lefloch, B., & Fazio, G. G. 2006, ApJ, 643, 965

343. Rieke, G. H., & Lebofsky, M. J. 1985, ApJ, 288, 618

344. Robitaille, T. P., Whitney, B. A., Indebetouw, R., & Wood, K. 2007, ApJS, 169, 328

345. Robitaille, T. P., Whitney, B. A., Indebetouw, R., Wood, K., & Denzmore, P. 2006, ApJS, 167, 256

346. Rodriguez, L. F., Marti, J., Canto, J., Moran, J. M., & Curiel, S. 1993, RMxAA, 25, 23

347. Roger, R. S., Costain, C. H., Landecker, T. L., & Swerdlyk, C. M. 1999, A&AS, 137, 7

348. Roshi, D. A., Goss, W. M., Anantharamaiah, K. R., & Jeyakumar, S. 2005, ApJ, 626, 253

349. Rosolowsky, E. W., Pineda, J. E., Kauffmann, J., & Goodman, A. A. 2008, ApJ, 679, 1338

350. Russeil, D., Schneider, N., Anderson, L. D., et al. 2013, A&A, 554, A42

351. Rygl, K. L. J., Wyrowski, F., Schuller, F., & Menten, K. M. 2013, A&A, 549, A5

352. Sánchez-Monge, Á., Beltrán, M. T., Cesaroni, R., et al. 2013, A&A, 550, A21

353. Sanhueza, P., Jackson, J. M., Foster, J. B., et al. 2012, ApJ, 756, 60

354. Sanhueza, P., Jackson, J. M., Zhang, Q., et al. 2017, ArXiv e-prints, arXiv:1704.08264

355. Saurin, T. A., Bica, E., & Bonatto, C. 2012, MNRAS, 421, 3206

356. Schisano, E., Rygl, K. L. J., Molinari, S., et al. 2014, ApJ, 791, 27

357. Schmeja, S. 2010, in Astronomical Society of India Conference Series, Vol. 1, Astronomical Society of India Conference Series, 27–35

358. Schmeja, S., Kumar, M., & Ferreira, B. 2008, Monthly Notices of the Royal Astronomical Society, 389, 1209

359. Schmiedeke, A., Schilke, P., Möller, T., et al. 2016, A&A, 588, A143

360. Schuller, F., Menten, K. M., Contreras, Y., et al. 2009, A&A, 504, 415

361. Schutte, A. J., van der Walt, D. J., Gaylard, M. J., & MacLeod, G. C. 1993, MNRAS, 261, 783

362. Scoville, N. Z., & Solomon, P. M. 1975, ApJL, 199, L105

363. Sedov, L. I. 1959, Similarity and Dimensional Methods in Mechanics

364. Sewilo, M., Churchwell, E., Kurtz, S., Goss, W. M., & Hofner, P. 2004, ApJ, 605, 285

365. Sewiło, M., Churchwell, E., Kurtz, S., Goss, W. M., & Hofner, P. 2008, ApJ, 681, 350

366. Shaver, P. A. 1980, A&A, 91, 279

367. Shetty, R., Kauffmann, J., Schnee, S., & Goodman, A. A. 2009, ApJ, 696, 676

368. Shima, K., Tasker, E. J., & Habe, A. 2017, MNRAS, 467, 512

369. Shipman, R. F., van der Tak, F. F. S., Wyrowski, F., Herpin, F., & Frieswijk, W. 2014, A&A, 570, A51

370. Shu, F. H., Adams, F. C., & Lizano, S. 1987, ARA&A, 25, 23

371. Shull, J. M. 1980, ApJ, 238, 860

372. Silverglate, P. R. 1984, ApJ, 278, 604

373. Simon, J. D., Bolatto, A. D., Whitney, B. A., et al. 2007, ApJ, 669, 327

374. Simpson, J. P. 1973, Ap&SS, 20, 187

375. Simpson, R. J., Povich, M. S., Kendrew, S., et al. 2012, MNRAS, 424, 2442

376. Smith, M. D. 1995, A&A, 296, 789

377. Smith, M. G. 1973, ApJ, 182, 111

378. Smith, R. J., Glover, S. C. O., Bonnell, I. A., Clark, P. C., & Klessen, R. S. 2011, MNRAS, 411, 1354

379. Smith, R. J., Shetty, R., Beuther, H., Klessen, R. S., & Bonnell, I. A. 2013, ApJ, 771, 24

380. Sodroski, T. J. 1991, ApJ, 366, 95

381. Sokolov, V., Wang, K., Pineda, J. E., et al. 2017, A&A, 606, A133

382. Solomon, P. M., Rivolo, A. R., Barrett, J., & Yahil, A. 1987, ApJ, 319, 730

383. Sridharan, T. K., Beuther, H., Schilke, P., Menten, K. M., & Wyrowski, F. 2002, ApJ, 566, 931

384. Stahler, S. W., & Palla, F. 2005, The Formation of Stars, 865

385. Stupar, M., Parker, Q. A., & Filipović, M. D. 2008, MNRAS, 390, 1037

386. Sugitani, K., Tamura, M., Nakajima, Y., et al. 2002, ApJL, 565, L25

387. Sun, Y., & Gao, Y. 2009, MNRAS, 392, 170

388. Svoboda, B. E., Shirley, Y. L., Battersby, C., et al. 2016, ApJ, 822, 59

389. Swarup, G., Ananthakrishnan, S., Kapahi, V. K., et al. 1991, Current Science, Vol. 60, NO.2/JAN25, P. 95, 1991, 60, 95

390. Tackenberg, J., Beuther, H., Henning, T., et al. 2014, A&A, 565, A101

391. Takahira, K., Tasker, E. J., & Habe, A. 2014, ApJ, 792, 63

392. Takami, M., Karr, J. L., Koh, H., Chen, H.-H., & Lee, H.-T. 2010, ApJ, 720, 155

393. Tan, J. C., Beltrán, M. T., Caselli, P., et al. 2014, Protostars and Planets VI, 149

394. Tan, J. C., Krumholz, M. R., & McKee, C. F. 2006, ApJL, 641, L121

395. Tan, J. C., Shaske, S. N., & Van Loo, S. 2013, in IAU Symposium, Vol. 292, Molecular Gas, Dust, and Star Formation in Galaxies, ed. T. Wong & J. Ott, 19–28

396. Teixeira, P. S., Fernandes, S. R., Alves, J. F., et al. 2004, A&A, 413, L1

397. Tej, A., Ojha, D. K., Ghosh, S. K., et al. 2006, A&A, 452, 203

398. Tenorio-Tagle, G. 1979, A&A, 71, 59

399. Terzian, Y. 1968, in IAU Symposium, Vol. 34, Planetary Nebulae, ed. D. E. Osterbrock & C. R. O'dell, 87

400. Thompson, M., Beuther, H., Dickinson, C., et al. 2015, Advancing Astrophysics with the Square Kilometre Array (AASKA14), 126

401. Thompson, M. A., Hatchell, J., Walsh, A. J., MacDonald, G. H., & Millar, T. J. 2006, A&A, 453, 1003

402. Tian, W. W., Leahy, D. A., Haverkorn, M., & Jiang, B. 2008, ApJL, 679, L85

403. Timmermann, R., Bertoldi, F., Wright, C. M., et al. 1996, A&A, 315, L281

404. Tobin, J. J., Hartmann, L., Bergin, E., et al. 2012, ApJ, 748, 16

405. Tody, D. 1986, in Society of Photo-Optical Instrumentation Engineers (SPIE) Conference Series, Vol. 627, Instrumentation in astronomy VI, ed. D. L. Crawford, 733

406. Townes, C. H., & Schawlow, A. L. 1975, ApL, 16, 184

407. Treviño-Morales, S. P., Pilleri, P., Fuente, A., et al. 2014, A&A, 569, A19

408. Trushkin, S. A. 1999, A&A, 352, L103

409. Turner, B. E. 1991, ApJS, 76, 617

410. Turner, B. E., & Matthews, H. E. 1984, ApJ, 277, 164

411. Uchiyama, Y., & on behalf of the Fermi LAT collaboration. 2011, ArXiv e-prints, arXiv:1104.1197

412. Urban, A., Martel, H., & Evans, II, N. J. 2010, ApJ, 710, 1343

413. van Buren, D., & Mac Low, M.-M. 1992, ApJ, 394, 534

414. van Buren, D., Mac Low, M.-M., Wood, D. O. S., & Churchwell, E. 1990, ApJ, 353, 570

415. van der Tak, F. F. S. 2004, in IAU Symposium, Vol. 221, Star Formation at High Angular Resolution, ed. M. G. Burton, R. Jayawardhana, & T. L. Bourke, 59

416. van der Tak, F. F. S., van Dishoeck, E. F., Evans, II, N. J., & Blake, G. A. 2000, ApJ, 537, 283

417. Vanhala, H. A. T., & Cameron, A. G. W. 1998, ApJ, 508, 291

418. Varricatt, W. P., Davis, C. J., & Adamson, A. J. 2005, MNRAS, 359, 2

419. Varricatt, W. P., Davis, C. J., Ramsay, S., & Todd, S. P. 2010, MNRAS, 404, 661

420. Veena, V. S., Vig, S., Tej, A., Kantharia, N. G., & Ghosh, S. K. 2017, MNRAS, 465, 4219

421. Veena, V. S., Vig, S., Tej, A., et al. 2016, MNRAS, 456, 2425

422. Velusamy, T., Peng, R., Li, D., Goldsmith, P. F., & Langer, W. D. 2008, ApJL, 688, L87

423. Vig, S., Ghosh, S. K., Ojha, D. K., Verma, R. P., & Tamura, M. 2014, MNRAS, 440, 3078 (Paper II)

424. Vig, S., Testi, L., Walmsley, M., et al. 2007, A&A, 470, 977

425. von Procházka, A. A., Remijan, A. J., Balser, D. S., et al. 2010, PASP, 122, 354

426. Walker, C. K., Narayanan, G., & Boss, A. P. 1994, ApJ, 431, 767

427. Walsh, A. J., Hyland, A. R., Robinson, G., & Burton, M. G. 1997, MNRAS, 291, 261

428. Wang, K., Testi, L., Burkert, A., et al. 2016, ApJS, 226, 9

429. Wang, K., Testi, L., Ginsburg, A., et al. 2015, MNRAS, 450, 4043

430. Wang, K., Zhang, Q., Testi, L., et al. 2014, MNRAS, 439, 3275

431. Ward-Thompson, D., André, P., & Kirk, J. M. 2002, MNRAS, 329, 257

432. Ward-Thompson, D., & Robson, E. I. 1990, MNRAS, 244, 458

433. Ward-Thompson, D., Kirk, J. M., André, P., et al. 2010, A&A, 518, L92

434. Watson, C., Corn, T., Churchwell, E. B., et al. 2009, ApJ, 694, 546

435. Watson, C., Povich, M. S., Churchwell, E. B., et al. 2008, ApJ, 681, 1341

436. Weaver, R., McCray, R., Castor, J., Shapiro, P., & Moore, R. 1977, ApJ, 218, 377

437. Whiteoak, J. B., Otrupcek, R. E., & Rennie, C. J. 1982, Proceedings of the Astronomical Society of Australia, 4, 434

438. Whiteoak, J. B. Z., & Uchida, K. I. 1997, A&A, 317, 563

439. Whitworth, A. P., Bhattal, A. S., Chapman, S. J., Disney, M. J., & Turner, J. A. 1994, A&A, 290, 421

440. Wilkin, F. P. 1996, ApJL, 459, L31

441. —. 2000, ApJ, 532, 400

442. Williams, B. J., Borkowski, K. J., Reynolds, S. P., et al. 2006, ApJL, 652, L33

443. Williams, B. J., Blair, W. P., Blondin, J. M., et al. 2011, ApJ, 741, 96

444. Williams, J. P., Blitz, L., & McKee, C. F. 2000, Protostars and Planets IV, 97

445. Williams, J. P., de Geus, E. J., & Blitz, L. 1994, ApJ, 428, 693

446. Williams, J. P., & McKee, C. F. 1997, ApJ, 476, 166

447. Wolfire, M. G., & Cassinelli, J. P. 1987, ApJ, 319, 850

448. Wood, D. O. S., & Churchwell, E. 1989, ApJS, 69, 831

449. Wootten, A. 1978, Moon and Planets, 19, 163

450. Wright, E. L., Eisenhardt, P. R., Mainzer, A. K., et al. 2010, The Astronomical Journal, 140, 1868

451. Xu, J.-L., Li, D., Zhang, C.-P., et al. 2016, ApJ, 819, 117

452. Xu, J.-L., Wang, J.-J., & Miller, M. 2011, ApJ, 727, 81

453. Xu, J.-L., Wang, J.-J., Ning, C.-C., & Zhang, C.-P. 2014, Research in Astronomy and Astrophysics, 14, 47

454. Xu, J.-L., Xu, Y., Zhang, C.-P., et al. 2017, ArXiv e-prints, arXiv:1708.09098

455. Yorke, H. W., Tenorio-Tagle, G., & Bodenheimer, P. 1983, A&A, 127, 313

456. Yu, N., & Wang, J.-J. 2015, MNRAS, 451, 2507

457. Yu, N.-P., & Wang, J.-J. 2013, Research in Astronomy and Astrophysics, 13, 28

458. Yuan, J., Li, J.-Z., Wu, Y., et al. 2018, ApJ, 852, 12

459. Zavagno, A., Deharveng, L., Comerón, F., et al. 2006, A&A, 446, 171

460. Zernickel, A., Schilke, P., Schmiedeke, A., et al. 2012, A&A, 546, A87

461. Zhang, C.-P., Yuan, J.-H., Li, G.-X., Zhou, J.-J., & Wang, J.-J. 2016, ArXiv e-prints, arXiv:1611.08794

462. Zhu, L., Wright, M. C. H., Zhao, J.-H., & Wu, Y. 2010, ApJ, 712, 674

463. Zinnecker, H., & Yorke, H. W. 2007, ARA&A, 45, 481

464. Zucker, C., Battersby, C., & Goodman, A. 2015, ApJ, 815, 23

Publications based on the Thesis

1. **Probing the massive star forming environment - a multiwavelength investigation of the filamentary IRDC G333.73+0.37**, V. S. Veena, S. Vig, B. Mookerjea, A. Sánchez-Monge, A.Tej, C. H. Ishwara-Chandra, ApJ , 2018, 852, 93

2. **Gas kinematics in the H II regions G351.69–1.15 and G351.63–1.25**, V. S. Veena, S. Vig, A.Tej, N. G. Kantharia, S. K. Ghosh, MNRAS , 2017, 465, 4219

3. **Star formation towards the southern cometary H II region IRAS 17256–3631**, V. S. Veena, S. Vig, A.Tej, W. P. Varricatt, S. K. Ghosh, T. Chandrasekhar, N. M. Ashok, MNRAS , 2016, 456, 2425

4. **Non-thermal emission from massive star forming regions: Unveiling a new SNR candidate G351.7–1.2**, V. S. Veena, S. Vig, B. Sebastian, D. V. Lal, A. Tej, S. K. Ghosh (MNRAS, under revision)